

Experimental and *first-principles* theoretical
investigations of the growth and properties of
pristine and Magnesium doped GaN nanostructures

A Thesis
Submitted For The Degree of
Doctor of Philosophy
in The Faculty of Science

by
Sanjay Kumar Nayak



Chemistry and Physics of Materials Unit
Jawaharlal Nehru Centre for Advanced Scientific Research
Bangalore - 560 064, India

March 2018

To my Niece

DECLARATION

I hereby declare that the matter embodied in the thesis entitled “**Experimental and *first-principles* theoretical investigations of the growth and properties of pristine and Magnesium doped GaN nanostructures**” is the result of investigations carried out by me at the Chemistry and Physics of Materials Unit, Jawaharlal Nehru Centre for Advanced Scientific Research, Bangalore, India under the supervision of **Prof. S. M. Shivaprasad** and that it has not been submitted elsewhere for the award of any degree or diploma.

In keeping with the general practice in reporting scientific observations, due acknowledgement has been made whenever the work described is based on the findings of other investigators. Any omission that might have occurred by oversight or error of judgement is regretted.

Sanjay Kumar Nayak

Date:

Place: Bangalore, India

CERTIFICATE

I hereby certify that the matter embodied in this thesis entitled “**Experimental and *first-principles* theoretical investigations of the growth and properties of pristine and Magnesium doped GaN nanostructures**” has been carried out by Mr. **Sanjay Kumar Nayak** at the Chemistry and Physics of Materials Unit, Jawaharlal Nehru Centre for Advanced Scientific Research, Bangalore, India under my supervision and that it has not been submitted elsewhere for the award of any degree or diploma.

Prof. S. M. Shivaprasad
(Research Supervisor)

Date:

Place: Bangalore, India

Acknowledgements

Firstly, I would like to express my sincere gratitude to my advisor Prof. S. M. Shivaprasad for the continuous support of my Ph.D study and related research, for his patience, motivation, and immense knowledge. His guidance helped me in all the time of research and writing of this thesis.

Besides my advisor, I would like to thank Prof. Umesh V. Waghmare for his encouragement, insightful suggestions, and computational facilities during this thesis work. I also sincerely acknowledge Prof. Manish Jain and Mit Naik (IISc, Bangalore) and Dr. Mukul Gupta (UGC-DAE, Indore) for fruitful collaborations. I would like to express my gratitude to Bharat Ratna Prof. C. N. R. Rao for his endless support and motivations.

I would like to thank the present and past chairman of CPMU Prof. Chandrabhas Narayana and Prof. S. Balasubramaniam for all the support. I also express my sincere gratitude to Prof. N. S. Vidhyadhiraja, Prof. S.M. Shivaprasad, Prof. Umesh V. Waghmare, Prof. Shobana Narasimhan and Prof. Chandrabhas Narayana for the one year course work, where I gained basic concepts of theoretical and experimental material science, which have been very useful for my Ph.D. work.

I greatly appreciate the patience and diligent effort of Mr. Srinath for helping in the maintaince of MBE system, without which successful experiments would not have been possible. I am indebted to Dr. Jay Ghatak for helping in TEM measurements and his insight in the analysis of data. I also thank Jagadeesh and Prajwal for all the technical help. All the help provided by Academic section, Administrative section, Library, Complab and Hostel authority are also greatly appreciated.

I am also thankful to all my present and past lab-mates Dr. Malleswararao Tangi, Dr. Satish Shetty, Dr. Varun Thakur, Dr. Arpan De, Dr. Nagaraja KK, Dr. Sashidhar, Dr. Anjan Bhukta, Dr. Saraswathi, Abhijit, Shivaram, Rajendra and Sachin for creating

a friendly working atmosphere in the lab and for their help and valuable inputs to my work.

I am grateful to my friends Sridhar, Dheeraj, Sunil, Vikas, Shantanu, Somnath, Chandan De, Abhijit, Sisir, Saikat, Narendra and Subrat for their help and motivations during my Ph.D. work. I greatly acknowledge my friends Dr. Chandan Mishra, Dr. Devendra Singh Negi and Dr. Anshul Deep Singh Parmar for their endless support in many aspects of life and for arranging beautiful trips.

I would like to gratefully and sincerely thank Mr. Sanjay Prasad Pattnaik and other faculty members of Gangadhar Meher University (Sambalpur, Odisha) for their support and motivations over the years to pursue science as career.

I acknowledge Chemistry and Physics of Materials Unit and International Center for Materials Science, JNCASR for the support and equipment I have needed to produce and complete my thesis and the DST, Govt. of India for Junior Research Fellowship and Senior Research Fellowship.

Finally, I wish to thank my parents for their love and encouragement, without whom I would never have enjoyed so many opportunities. I also like to thank my brothers and sister-in-law for their support, encouragement and concern for me.

Synopsis

III-Nitrides (InN, GaN, AlN and their alloys) form an important group in the family of semiconductors. The applications of these materials are widespread, due to their direct and tunable band gaps, chemical robustness and sustainability under high current and high temperature. In this modern era of science and technology, this family of material has proven to be essential building block for the next generation devices; the optoelectronics, high power and frequency transistors and chemical and biological sensors are few of many such important applications. The astronomical amount of research work carried by scientists and engineers, both in material science and their industrial applications in the past two decades has led to extensive commercialization of nitride based devices. However, due to some unresolved material related issues, full potential of III-nitrides is yet to be realized. Purpose of this dissertation is to shed light upon such issues and proposed methods to overcome the same by using experimental and *in silico* techniques. A brief account on these issues and results from this dissertation work is given here.

Due to the unavailability of large sized wafers as substrates for homoepitaxial growth of GaN, it is grown over foreign substrates such as sapphire and silicon. It is well known that heteroepitaxial growth leads to a large interfacial strain, which is released by the formation of dislocations in the overgrown films. Further, these dislocations play a crucial role in determining the device performance. These dislocations act as scattering sites for charge carriers and as non-radiative recombination centers, both are deleterious for high perform optoelectronic device applications. Several methods have been proposed to improve the crystallinity of films by minimizing dislocations; among these methods the nanostructuring of material has proven to be largely effective. Since surface free energy drives dislocations to terminate early at the side-walls in nanostructures their density reduces significantly as the structure grows, and also their small contact area

on the substrate enable minimization of the lattice mismatch induced stress by local rearrangement of atoms.

Low light extraction efficiencies (LEE) of III-nitrides have been a serious issue for the fabrication of high brightness LEDs. It is estimated for flat GaN based LEDs that only about 4% of the generated light falls within the ‘escape cone’ and come out from the material, due to a large mismatch between the refractive indices of GaN and ambient. To overcome such problems, various techniques have been adopted. LEE of GaN can be enhanced significantly by the use of nano/micro-porous structures that make the geometry conducive to light extraction. Most of the porous films are formed by chemical etching or ion bombardment methods, which have their own limitations and consequent adverse effects on the grown films. Recently, it has been shown that the single crystalline porous GaN in the form of nanowall network (NWN) can be synthesized by epitaxial growth techniques. However, role of their pore dimension on the luminescence properties have not been addressed adequately and also the growth mechanism underlying the formation of such porous structures is still ambiguous, which is in fact one of the central aspect of our research theme.

The background carrier doping ($n = 10^{17} - 10^{19} \text{ cm}^{-3}$) of GaN has hindered the fabrication of efficient optoelectronic devices. Since optimization of GaN-based electronic and optoelectronic devices requires control over the doping concentration, it is essential to understand its atomistic origin to control the doping concentration. For the determination of dominant defect(s) concentration in materials, we rely on the formation energies of defects, estimated by *first-principles* calculations, which also vary with the numerical parameters used in the calculations. Since nanostructure has a very high surface to volume ratio, it is expected that surface electronic structure will dominate over its bulk counterpart. Throughout the literature the formation energies and corresponding electronic structure of various defects in bulk w-GaN is thoroughly discussed, whereas the energetics and corresponding electronic structure of defects at surfaces is not available. By *first-principles* DFT calculations here we establish the difference in energetics, stability and electronic structure of native defects (both in neutral and various charged state) between bulk and surface configuration. In the synthesis of efficient p-GaN, along with this native n-type character, the high ionization energy of dopants is the main hindrance.

At $T=300$ K only about 1% of incorporated Mg get ionized and contribute in hole generation. Adding to that, overcome of self-compensation effect remains a major challenge too. Experiments reveal that the concentration of incorporated Mg on the surface is higher than in the bulk suggesting that the higher surface area GaN structure may enable higher incorporation of Mg. Thus, GaN nanostructures having a very high surface to volume ratio can be potential candidates for achieving higher incorporation of Mg, by increasing the solubility limit of Mg in GaN.

In order to potentially integrate GaN based microelectronics and optoelectronics with already well-established and mature Si technology, the growth of GaN on silicon substrates attracts a lot of attention. Moreover, GaN-on-silicon is a low-cost alternative to the growth on sapphire or silicon carbide substrate. However, there are important problems that need to be addressed in order to realize the integration, which are discussed extensively in the thesis. One of the solutions of most of the problems discussed here is the potential of nanomanifestation.

To address these fundamental problems, various experiments and relevant simulations have been carried out in the proposed thesis of the research work. Summary of various projects has been divided into the following eight chapters.

Chapter 1 gives an introduction to some of the key nature of III-nitride compound semiconductors and its applications which make these materials both fundamentally and technologically important. Some inherent limitations and difficulties such as unavailability of larger native substrates, formation of various types of defects and their consequences are discussed. Finally, mechanisms of thin film growth such as nucleation and formation of 2D and 3D islands and epitaxial nanostructures are explained.

Chapter 2 provides a brief literature survey on the fundamental limitations of employing both pristine and doped GaN for device applications, which include low light extraction efficiency, high background native carrier concentration, formation energy and stability of various defect configurations, limitation in p-doping and different luminescence centres in doped GaN. A brief discussion on the growth of GaN on Si surface and its structural properties are also mentioned. This chapter summarizes the improvements made over the years to overcome these limitations.

Chapter 3 involves the details of the experimental and computational techniques employed during this work. Plasma assisted molecular beam epitaxy growth system, equipped with various *in-situ* characterization tools *e.g.* RHEED, RGA, Ellipsometer etc., has been used for the synthesis of single crystal thin films. For *ex-situ* characterization of grown samples we have used FESEM, AFM, HR-XRD, PL, Raman spectroscopy, HR-TEM, XAS, XPS and SIMS. A brief background of the theoretical calculations used (*e.g.* FDTD, DFT and Multi Scattering Theory) to understand the material properties are also discussed.

Chapter 4 discusses the growth and characterization of GaN nanowall network (NWN) with different pore sizes/porosity and their impact on the optical properties of thin films. FDTD simulations have been carried out to correlate the pore size and the recorded PL intensity of the samples. We find that the luminescence intensity is sensitive to the mean pore dimensions. Based on the experimentally observed evolution of surface morphology and *first-principles* DFT calculations a growth mechanism of GaN NWN is proposed where for the first time we identify that the structure dependent attachment kinetics (SDAK) instabilities is responsible for the formation of NWN.

Chapter 5 presents atomic and electronic structure, formation energies and stability of Ga and N vacancy in bulk as well as at $(10\bar{1}0)$ surface of GaN. Further, the results obtained from the simulations are correlated with the data obtained from electron energy loss spectroscopy (EELS). We find that unlike in bulk configuration, nitrogen vacancy can form spontaneously which majorly contribute to high background carrier density. Experimentally recorded high conductivity of the GaN NWN is correlated with the N-vacancies on the side wall surfaces of NWN.

Chapter 6 gives a brief discussion on the growth and characterization of Mg incorporated GaN NWN. Various complementary characterization methods are used to study the structural, optical and electronic properties. p-doped GaN NWN is shown to be an efficient material for various applications due to its high surface to volume ratio. At the end, a combined experimental and *first-principles* calculation based analysis is presented to understand the atomistic origin of the blue luminescence

peak in PL spectra and self-compensation effect in heavily doped GaN. Further, based on these results, an epitaxial growth process is identified to achieve high hole concentrations in Mg doped GaN.

Chapter 7 contains the growth and characterization of GaN Nanorods (NRs) grown on Si (111) surface. The investigation of the enhanced radial growth of NRs upon Mg incorporation is carried out by using both electron microscopies and *first-principles* based analysis. First-principles calculation reveals that presence of Mg at surface favors the adsorptions of Ga adatoms results into higher growth rate of side wall facets of GaN NRs. Further, the structural, optical and electronic properties of the samples are studied with the help of X-ray diffraction and various spectroscopic techniques.

Chapter 8 summarizes the content of the present thesis and draws conclusions from the observed results. Overall, the thesis is a systematic study to understand various properties of pristine and Mg doped GaN nanostructure as well as the role of different defect configurations on the structural, optical and electronic properties of the same. This chapter also provides a brief direction for future research that has emerged as the outcome of the present work.

List of Publications

1. **Sanjay Nayak**, Rajendra Kumar, Nidhi Pandey, KK Nagaraja, Mukul Gupta and S. M. Shivaprasad, “Enhanced Radial growth of Mg doped GaN Nanorods: A combined experiment and first-principles based analysis” Accepted in **Journal of Applied Physics** (2018)
arXiv preprint arXiv:1709.04479 (2017)
2. **Sanjay Nayak**, Rajendra Kumar, and S. M. Shivaprasad, “Edge enhanced growth induced shape transition in the formation of GaN Nanowall Network”, **Journal of Applied Physics**, 123, 014302 (2018)
3. **Sanjay Kumar Nayak**, Mukul Gupta, and S. M. Shivaprasad, “Structural, optical and electronic properties of a Mg incorporated GaN nanowall network”, **RSC Advances** 7 (42), 25998-26005 (2017)
4. **Sanjay Kumar Nayak**, Danish Shamoon, Jay Ghatak, and S. M. Shivaprasad, “Nanostructuring GaN thin film for enhanced light emission and extraction”, **Physica Status Solidi (A)** 214, 1600300 (2017)
5. **Sanjay Nayak**, Mukul Gupta, Umesh V. Waghmare, and S. M. Shivaprasad, “On the origin of Blue Luminescence in Mg doped GaN”, **arXiv preprint arXiv:1708.04036 (2017)**
6. **Sanjay Nayak**, Mit H. Naik, Manish Jain, Umesh V Waghmare, and S. M. Shivaprasad, “Vacancy Defect in bulk and at $(10\bar{1}0)$ surface of GaN: A combined first-principles calculations and experimental analysis” **arXiv:1710.05670v2 (2017)**
7. Varun Thakur, **Sanjay Kumar Nayak**, KK Nagaraja, and S. M. Shivaprasad “Surface modification induced photoluminescence enhancement of GaN nanowall network grown on c-sapphire” **Electronic Materials Letters** 11 (3), 398-403 (2015)
8. Varun Thakur, **Sanjay Kumar Nayak**, KK Nagaraja, and S. M. Shivaprasad “Improved structural quality of GaN nanowall network grown on pre-nitrided c-sapphire” **2014 IEEE 2nd International Conference on Emerging Electronics (ICEE), Bangalore, 2014**, pp. 1-4, doi: 10.1109/ICEmElec.2014.7151177

Contents

Acknowledgements	v
Synopsis	vii
List of publications	xiii
Contents	xv
Acronyms	xix
1 Introduction and Motivation	1
1.1 Introduction	1
1.2 Brief history of III-Nitrides	3
1.3 Applications of III-Nitrides	5
1.3.1 Light Emitting Diode (LEDs)	5
1.3.2 Laser Diodes (LDs)	7
1.3.3 High Electron Mobility Transistor (HEMT)	7
1.3.4 Photovoltaics	9
1.3.5 Chemical and Biological Sensors	11
1.3.6 Dilute Magnetic Semiconductor	12
1.4 Crystal structure of III-Nitrides	13
1.5 Substrates used for III-nitride growth	15
1.6 Structural Defects	17
1.6.1 Point defects	18
1.6.2 Line Defects or Dislocations	19
1.6.3 Planar and Volume defects	20

1.7	Growth process of thin films and Nanostructures	21
1.7.1	Growth Modes of Thin films	22
2	Literature Overview	25
2.1	Growth of GaN Nanostructures	25
2.2	Unintentional n-type doping	30
2.3	Issues with p-doping in GaN	33
2.4	Growth of p-GaN on silicon substrate	35
3	Experimental and Simulation Techniques	39
3.1	Crystal Growth: Molecular Beam Epitaxy	39
3.1.1	Effusion Cells	41
3.1.2	Nitrogen Plasma Source	44
3.1.3	Residual Gas Analyser	47
3.2	Characterization Techniques	48
3.2.1	Reflection High Energy Electron Diffraction (RHEED)	48
3.2.2	Field Emission Scanning Electron Microscopy (FESEM)	51
3.2.3	High Resolution X-ray Diffraction (HRXRD)	52
3.2.4	Photoluminescence (PL) and Cathodoluminescence (CL)	55
3.2.5	Raman Spectroscopy	56
3.2.6	X-ray photoelectron spectroscopy (XPS)	59
3.2.7	Transmission Electron Microscopy (TEM)	62
3.2.8	X-ray Absorption Near Edge Spectroscopy (XANES)	67
3.2.9	Secondary Ion Mass Spectrometry (SIMS)	69
3.3	Simulation Techniques	70
3.3.1	Finite Difference Time Domain (FDTD) method	70
3.3.2	Density Functional Theory (DFT)	71
3.3.3	Full Multi Scattering (FMS) Theory	74
4	Growth and Characterization of GaN Nanowall Network	77
4.1	Growth, Structural and Optical Properties of GaN NWN	77
4.1.1	Introduction	77
4.1.2	Experimental Details	78

4.1.3	Results and Discussion	79
4.1.4	Summary	90
4.2	Growth Mechanism of GaN NWN	91
4.2.1	Introduction	91
4.2.2	Methods	92
4.2.3	Results	93
4.2.4	Discussion	97
4.2.5	Summary	101
5	Energetics, stability and electronic structure of vacancy defect	103
5.1	Introduction	103
5.2	HR-TEM and HR-EELS study of NWN	105
5.3	Computational Details	106
5.4	Results and Discussion	108
5.4.1	Atomic and Electronic structure of bulk <i>w</i> -GaN	108
5.4.2	Atomic and Electronic structure of Ga vacancies in bulk <i>w</i> -GaN	110
5.4.3	Atomic and Electronic structure of N vacancies in bulk <i>w</i> -GaN	112
5.4.4	Atomic and Electronic structure of Pristine (10 $\bar{1}$ 0) surface	115
5.4.5	Atomic and Electronic structure of Ga-vacancies at (10 $\bar{1}$ 0) surface	119
5.4.6	Atomic and Electronic structure of N-vacancies at (10 $\bar{1}$ 0) surface	122
5.5	Summary	128
6	Magnesium doping in GaN Nanowall Network	131
6.1	Issues related to Mg doping in GaN	131
6.1.1	Introduction	131
6.1.2	Experimental Details	132
6.1.3	Results and Discussion	133
6.1.4	Summary	147
6.2	Origin of Blue luminescence in Mg doped GaN	148
6.2.1	Introduction	148
6.2.2	Experimental Details	148
6.2.3	Simulation Details	149

6.2.4	Experimental Results	150
6.2.5	Theoretical Analysis and Discussion	153
6.2.6	Summary	160
7	Magnesium doping in GaN Nanorods grown over Si (111) substrate	161
7.1	Enhanced Radial Growth	161
7.1.1	Introduction	161
7.1.2	Methods	162
7.1.3	Results and Discussion	164
7.1.4	Summary	172
7.2	Structural, Optical and Electronic properties	172
7.2.1	Experimental Details	172
7.2.2	Structural Properties	173
7.2.3	Optical Properties	174
7.2.4	Electronic Properties	178
7.2.5	Summary	180
8	Conclusions	181
8.1	Summary and Conclusions	181
8.2	Highlights of the work	187
8.3	Limitations of the work and Future directions	189
	Bibliography	191

Acronyms

AES	Auger Electron Spectroscopy
AFM	Atomic Force Microscopy
ARUPS	Angle Resolved Ultraviolet Photoelectron Spectroscopy
BE	Binding Energy
BEP	Beam Equivalent Pressure
BPE	Branch Point Energy
CBM	Conduction Band Minimum
CL	Core level
CL	Cathodoluminescence
CNL	Charge Neutrality Level
CPS	Counts Per Second
CVD	Chemical Vapor Deposition
DAS	Dimer Adatom Stacking Fault (Model)
DD	Double Domain
DFT	Density Functional Theory
DME	Domain Matching Epitaxy
DOS	Density Of State
EEELS	Electron Energy Loss Spectroscopy
ELOG	Epitaxial Lateral Overlayer Growth
ESCA	Electron Spectroscopy for Chemical Analysis
FESEM	Field Emission Scanning Electron Microscopy
FM	Frank van-der Merwe (growth mode)
FWHM	Full width at Half Maximum
HBT	Hetero-junction Bipolar Transistor

HREELS	High Resolution Electron Energy Loss Spectroscopy
HRXRD	High Resolution X-ray Diffraction
HT	High Temperature
HVPE	Hydride Vapor Phase Epitaxy
IMFP	Inelastic Mean Free Path
IL	Intermediate Layer
IRS	Infrared Spectroscopy
LD	Laser Diode
LEO	Lateral Epitaxial Overlayer Growth
LED	Light Emitting Diode
LEE	Light Extraction Efficiency
LEED	Low Energy Electron Diffraction
LME	Lattice Matching Epitaxy
LT	Low Temperature
MBE	Molecular Beam Epitaxy
ML	Monolayer
MOCVD	Metal Organic Vapor Phase Epitaxy
MOSFET	Metal Oxide Semiconductor Field Effect Transistor
PES	Photoelectron Spectroscopy
PVD	Physical Vapor Deposition
PL	Photoluminescence
RHEED	Reflection High Energy Electron Diffraction
RMS	Root Mean Square
RT	Room Temperature
RTD	Residual Thermal Desorption
SAG	Selective Area Growth
SEM	Scanning Electron Microscopy
SK	Stranski-Krastonov (growth mode)
STM	Scanning Tunneling Microscopy
SXPS	Synchrotron X-ray Photoelectron Spectroscopy
TDS	Thermal Desorption Spectroscopy
TEM	Transmission Electron Microscopy
UHV	Ultra High Vacuum _{xx}

Chapter 1

Introduction and Motivation

This chapter describes some of the fundamental aspects of III-nitride compound semiconductors, which make these materials technologically important for various applications. The crystal structure and chemical nature of the III-nitrides are presented briefly. Critical limitations and difficulties such as unavailability of large native substrates and its consequences are also discussed. Finally, mechanisms of the formation of island and its nucleation that determine thin film growth are described.

1.1 Introduction

Modern human civilization is founded on the consumption of vast quantities of energy, and thus an appropriate and efficient utilization of resources is essential to sustain the growth in the coming days. Most commonly used non-renewable natural energy resources (such as fossil fuels) are identified to be primarily responsible for enormous damage to earth's climate causing global warming which melts the polar ice and can result in extinction of many species. Therefore, it is inevitable to find alternative energy sources (*i.e.* renewable resources). Currently, the cheapest and efficient renewable energy resources available to us are wind, water and sunlight. It has been estimated that the power density of sunlight on earth is $\approx 1.4 \text{ kW/m}^2$, *i.e.* about 6000 times more than the requirement. Thus, the use of the solar power to overcome the energy crisis is perceived as one of the best alternatives¹. Developing energy efficient devices such as light emitting diodes (LEDs) is also one the key requirement to conserve energy in addition to the

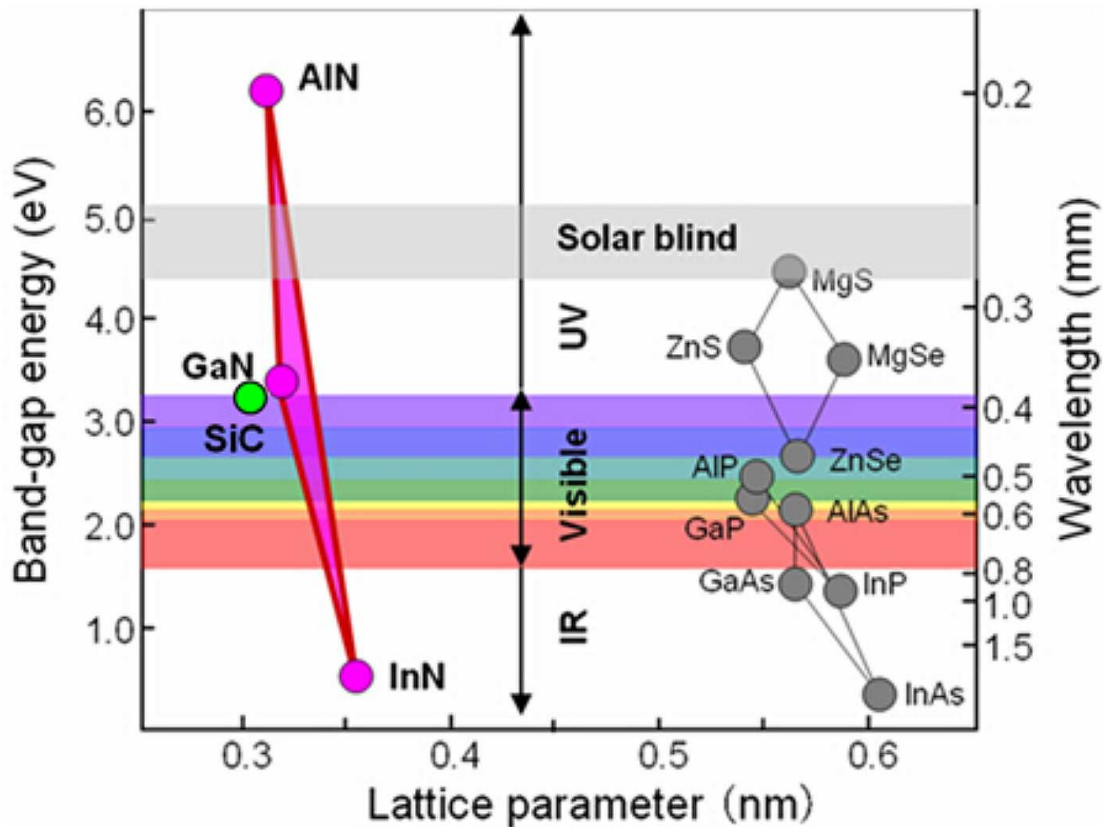


Figure 1.1: Plot of in-plane lattice constant vs. band gap *

production of renewable energy sources.

Semiconducting materials are the basic building blocks of any modern day electronic and optoelectronic devices. The naturally available elemental semiconductors are silicon (Si) and germanium (Ge). However, due to their certain inherent characteristics such as indirect band gap, lower electron mobility, lower breakdown voltage, inability to perform in harsh environment etc., these semiconductors are not desirable for several applications. As correctly said in the famous English proverb “Necessity is the mother of invention”, alternatives to elemental semiconductors, which can overcome the limitations of Si and Ge, have been intensively explored in last few decades. There are many compound semiconductors available now, such as binary and ternary compounds; composed of group III and V elements or group II and VI elements of the periodic table. In the III-V compound semiconductor group, nitrides, arsenides and phosphides are intensively investigated in the past. It is evident from Fig. 1.1 that the entire visible solar spectrum (390-700 nm)

*<http://www-opto.e-technik.uni-ulm.de/lehre/cs/>

can be accessible by suitably alloying the nitride semiconductors alone. This makes nitrides a very exciting candidate for research and applications. The three most important members of III-nitride family are indium nitride (InN), gallium nitride (GaN) and aluminum nitride (AlN). The direct band gap (at $T=2$ K) of InN, GaN and AlN are 0.69, 3.51 and 6.25 electron volt (eV), respectively². The greatest advantage of the III-nitride materials is the possibility of band gap engineering achieved by alloying them, making them ideal candidates for opto-electronic devices, operating within the range of near Infra Red (IR) to deep Ultra Violet (UV), such as Laser diodes, UV lasers, IR detectors, High Electron Mobility Transistors etc.

Major scientific and technological advancement in III-nitride semiconductors led to commercialization of LEDs that emit various wavelengths of light. The synthesis of efficient and bright blue LEDs, independently by Shuji Nakamura (in 1992) and by Hiroshi Amano and Isamu Akasaki (in 1989), has led to major breakthrough in obtaining a white light LED, for which the three were awarded the most prestigious Nobel Prize in Physics in 2014. The main advantages of LEDs over incandescent light are higher brightness, longer lifetime and low consumption of power for the same luminous flux. The solid state lighting applications of LEDs are not confined to home lighting alone, but also extended to traffic signals, full colour displays, flash light in mobile phones and for indoor farming. Despite great success in the manufacturing of nitride based LEDs, there are several fundamental issues which need to be addressed for efficient use of nitride semiconductors; some of which will be discussed in the following sections.

1.2 Brief history of III-Nitrides

Unlike elemental semiconductors, nitrides are not abundant and are not readily available naturally, making chemical reaction as the exclusive way to synthesis them. The first successful synthesis of GaN took place way back in 1938 by Juza *et al.*³ by passing ammonia over hot gallium forming GaN needles. The primary objective of their work was to estimate the lattice parameters of GaN. Later on similar technique was used by Grimmeiss *et al.* in 1959⁴ to obtain small crystals of GaN. The revolutionary use of GaN in the field of solid state lighting started in 1969 by the successful deposition of single crystalline GaN

on sapphire substrates by Maruska *et al.*⁵ at Radio Corporation of America Laboratories (New York, USA). Following this work, GaN has gone through a huge revolution in the field of optoelectronics. Meanwhile various advanced techniques such as Metal-Organic Chemical Vapour Deposition (MOCVD), Metalorganic Vapour Phase Epitaxy (MOVPE), Chemical Vapour Deposition (CVD), Pulsed Laser Deposition (PLD), Molecular Beam epitaxy (MBE), Laser Molecular Beam Epitaxy (L-MBE) etc., have been developed to fabricate high crystalline quality material. Many interesting and ground breaking properties of GaN were discovered during 1970s⁶⁻⁹. In 1971 Pankove *et al.* showed blue electroluminescence¹⁰ (2.6 eV) in Zn doped GaN, when the applied voltage was higher than 60 V. However, it was not a conventional p-n junction device but rather a metal-insulator-semiconductor (MIS) diode, where the output power was of the order of 1-5 μW . Until late 1970s the crystalline quality of GaN was not good and hence optical and electrical properties were not reproducible. The first device quality thin film growth was reported by Yoshida *et al.*¹¹ in 1983, where they used a two step growth method by using Reactive Molecular Beam Epitaxy technique and for the first time an AlN buffer layer was deposited on sapphire prior to GaN. First report on the growth of GaN by MOCVD was published in 1986 by Amano *et al.*¹², where a mirror like surface morphology and residual carrier concentration of 10^{17} cm^{-3} was observed. In 1991, Shuji Nakamura used low temperature GaN buffer layer, prior to growth of high quality GaN on sapphire¹³, and subsequently observed an electron mobility of $900 \text{ cm}^2/V.s$ at room temperature.

Despite all these advancements, a few difficulties and issues such as fabrication of p-type GaN, presence of native n-type unintentional background doping and making of good ohmic contacts to GaN, still remain challenging. In 1988-89 Amano *et al.*^{14,15} demonstrated the p-type conductivity in GaN by Low Energy Electron Beam Irradiation (LEEBI) on as grown samples. Nakamura *et al.*^{16,17} also observed p-type conductivity by thermally annealing the as grown samples by MOCVD. They attributed the hole compensation mechanism to hydrogen passivation¹⁸, which was further supported by *first-principles* calculations by Van De Walle *et al.*^{19,20}. In 1991, Shuji Nakamura demonstrated the fabrication of p-n junction based LED by using III-Nitride semiconductors, whose output power and the external quantum efficiency (EQE) were $42 \mu W$ and 0.18%, respectively, with peak emission wavelength at 430 nm for 20 mA input current, with a

forward biased voltage of 4V. Soon after this, it was realized that a single p-n junction based LEDs might not be efficient enough for commercial applications.

It is evident that, spanning of the entire solar spectrum can be achieved only when the band gap of the active layer is lower than GaN. Thus in 1992, Nakamura and Mukai demonstrated fabrication of hetero-structure of InGaN on GaN template grown on sapphire substrate and observed luminescence spectra from a band to band transitions for the first time. Later, Nakamura *et al.* fabricated GaN/InGaN and InGaN/AlGaN based double hetero-structures²¹⁻²³. Until 1995, the recorded output power (external quantum efficiency) of blue and green MQW based first generation LEDs were 5mW (9.1%) and 3mW (6.3%), respectively. The first p-n junction based III-nitride LED was commercialized by Nichia Chemical Industries Ltd. in late 1993.

1.3 Applications of III-Nitrides

1.3.1 Light Emitting Diode (LEDs)

The demonstration of first solid state lighting started in 1962 when Jacques Pankove reported infrared electroluminescence from GaAs²⁴, followed by the first observation of visible light emission from GaAsP junctions²⁵, in same year.

In principle, suitability of semiconductors for LEDs application requires a few intrinsic properties such as:

- **Direct band gap:** To minimize thermal loss
- **Band gap tunability:** To obtain different desired wavelength of light
- **Efficient radiative recombination:** For high luminous intensity

The direct band gap and band gap tunability by alloying other elements of the same family (iso-structures) of III-nitride semiconductors makes them an obvious candidate for LED application.

The primary goal for fabrication of LED has been to mimic the natural sunlight or white light. There are three most popular and well established methods to generate white light by using LEDs : a blue LED with yellow phosphors; a UV LED with blue

and yellow phosphors; and a device that combines LEDs having red, green and blue emissions separately. Currently, the blue GaN LEDs with yellow phosphor dominates commercial white light LEDs industry which is based on the principle of the absorption and re-emission of light. The most commonly used phosphors are cerium doped yttrium aluminium garnet (YAG), ($Y_3Al_5O_{12}:Ce$) and rare-earth (RE) doped YAG ($Y_3Al_5O_{12}:RE$). The ease of manufacturing of GaN based blue LEDs with yellow phosphor with high efficacy make them attractive for production of low cost bright white LEDs. The big disadvantage of this method is, lower color rendering index (CRI) value, which is a measure of how closely a light source can replicate the true color of an object and it largely depends upon the spectral power distribution (SPD) of the light source. To resolve this issue, additional phosphors such as red or green were coated, resulting in a broader spectral emission and hence, higher CRI values. However, a poorer efficacy is trivial in this case^{26,27}. White LEDs obtained using blue LEDs plus phosphors were developed in 1996 and in the year 2006 a luminous efficacy of 116 lm/W was reported²⁸.

For dynamic control of white light, the final and essential approach is a combination of three (or more) LEDs of different wavelengths which will enable higher efficacies than phosphor based LEDs. However, at present comes with a high manufacturing cost, until further advances are made. The concept of the phosphor-free LED was first proposed in 2000 by Sumitomo Electric Industries Ltd., who produced phosphor-free ZnSe-based white LEDs, which had the advantages of low power consumption, low cost and electrostatic breakdown-free behavior²⁹. They adjusted the emission wavelength of the ZnSe active layer in the 480 nm - 490 nm range and a portion of the greenish-blue emitted light was absorbed by the conductive substrate, which was then converted into yellow light, similar to the phosphor based LEDs. These two emission bands were then further combined and appeared as white light to the naked eye. However, the commercialization of these II-VI based LEDs was hindered due to short lifetime of only ≈ 1800 h at a current density of $14.5 A/cm^2$ for an i-ZnMgBeSe/p-ZnMgSe double cladding structure.

GaN-based white-light LEDs are particularly desirable because of their long lifetime, small size, and low consumption of energy. Theoretically, the entire visible wavelength band can be produced by a combination of $In_xGa_{1-x}N$, with variable Indium composition and quantum well width. However, strong quantum confinement Stark effect and the solid

phase immiscibility in the $In_xGa_{1-x}N/GaN$ material system create greater challenges for the synthesis of $In_xGa_{1-x}N/GaN$ QWs for green and red wavelengths³⁰. These two fundamental limitations are still challenging for the fabrication of high efficient white light LEDs.

1.3.2 Laser Diodes (LDs)

It is well known that, laser is a device that emits light through a process of optical amplification based on stimulated emission of electromagnetic radiation. The applications of lasers are wide spread *e.g.* as source in spectroscopy, microscopy, heat treatment, lunar laser ranging, photochemistry, laser scanner, laser cooling, nuclear fusion, in military, in medical, industrial and commercial applications, entertainment and recreation, surveying and ranging, compact disc (CD), 3D printing, feeding of fibre optics etc. Invention of Laser Diode has a great impact in last decade, where the evolution of LD technology has led to a rapid increase in data storage capacity; from CDs (650 MB) to DVDs (4.7 GB/layer) and reaching 25 GB/layer with Blu-Ray Disc. Such kind of technology requires low wavelength emitting laser (particularly 405 nm), which can be obtained only from the wide band gap semiconductors like GaN.

The semiconductor based lasers were first demonstrated in 1962 by Robert Hall³¹. The injection lasers by using III-nitride semionductors were first demonstrated in 1995 by Akasaki *et al*^{32,33}. The FWHM of the output light was 0.15 nm with current density of 3.0 kA/cm^2 . A room temperature continuous wave (CW) laser emitting at $\approx 400\text{ nm}$ with more than 6000 h lifetime was demonstrated by Nakamura in 1998³⁴. The InGaN MQWs LDs produced a luminescence peak at 417 nm with FWHM of 1.6 nm under the pulsed current injection at room temperature³⁵. A laser as narrow as 0.002 nm of FWHM with peak wavelength 400.23 nm at room temperature was further reported by Nakamura *et al.*³⁶

1.3.3 High Electron Mobility Transistor (HEMT)

With the recent upswing of the wireless communication market and continuous progress of military applications, microwave transistors are playing critical roles in many aspects of day to day life. For example, for personal mobile communication applica-

tions since the next generation cell phones require wider bandwidth and improved efficiency; similarly development of satellite communications and TV broadcasting requires amplifiers operating at higher frequencies. The need for high power and high frequency operation requires transistors to be based on semiconductor materials with both large breakdown voltage and high electron mobility(μ_e). A HEMT is a field-effect transistor incorporating a junction between two materials with different band gaps as the channel instead of a doped region that is commonly used in MOSFET. Unique properties of HEMTs, such as high breakdown voltage, high current density, high cut off frequencies and high operating temperature are the reasons behind their emergence as an alternative to standard FETs.

The effect of material parameters of semiconductors on the performance of power devices was demonstrated by Baliga *et al.* in 1982³⁷. The study suggests that the potential in the drift region resistance of unipolar power devices improves by substituting Si with other semiconductor materials like GaAs, GaAlAs, GaAsP, and InGaP. Based on these works, General Electric (GE) has developed GaAs based power devices. Later on, GaAs based Schottky power rectifiers with high breakdown voltage (≈ 200 V) is made commercially available by several other companies.

In recent years, GaN based HEMTs have attracted attention due to their high-power performance. In general, III-Nitride based HEMTs are composed of AlGaN and GaN hetero-structure. The polar nature of the nitride semiconductor is a consequence of absence of inversion symmetry, which makes it possible to form high electron density of two-dimensional electron gas (2DEG) at the AlGaN/GaN interface without any intentional doping. A smooth and abrupt AlGaN/AlN/GaN interface have shown electron mobility as high as $2000 \text{ cm}^2/\text{V.s}$ at room temperature³⁸. The high electric conductivity due to the formation of 2DEG and the high breakdown field of AlGaN/GaN materials are the key reasons behind the application of AlGaN/GaN hetero-structure for HEMTs. Strong power amplification capability of GaN based HEMTs has been demonstrated by Okamoto *et al.*³⁹, where a total output power density over 4.8 W/mm at 2GHz is observed by a single HEMT device and the latest report suggests a record high output power density over 40 W/mm at 4GHz ⁴⁰.

Efforts to expand the operation frequency of GaN HEMTs inorder to realize W-band

power amplification is still underway. In 2011, a double hetero-structure (DH) HEMT of AlN/ GaN/AlGaN with a current gain cutoff frequency and the highest oscillation frequency of 310 GHz and 364 GHz, respectively, is reported by Shinohara *et al*⁴¹. Brown *et al.*⁴² reported an AlGaN/GaN DH HEMT with the achievement of a continuous wave (CW) output power of 1023 mW at 95 GHz (W-band) and a power added efficiency (PAE) of 19.1%. Lee *et al.*⁴³ reported GaN HEMTs without AlGaN barrier layer *i.e.* InAlN/GaN DH HEMT with a gain cutoff frequency of 290-300 GHz.

1.3.4 Photovoltaics

Photovoltaic (PV) devices are capable of converting light into electricity using suitable semiconducting materials. The main objective of the research in this area is to reduce the cost and to increase the conversion efficiency of solar cells. One of the most promising techniques for improving PV efficiency is the use of multi-junction cells to absorb a wider energy range of incident photons. As it is discussed previously that $In_xGa_{1-x}N$ has the ability to cover the entire visible solar spectrum, it is the obvious choice for photovoltaics applications. Adding to that, it is theoretically predicted that efficiency of InGaN based solar cell is nearly 60%⁴⁴, which is much higher than typical Si based solar cell, where it is merely 6% for amorphous Si, 31% for single junctions and 44% for multi junction⁴⁵. It is also shown that the optical and electronic properties of $In_xGa_{1-x}N$ alloys exhibit a higher resistance to high energy (≈ 2 MeV) photon irradiation, which suggests a very robust nature of the material and thus, it has huge potential for applications in space technology. The use of InGaN as absorber is not yet mature and is still evolving. Various structures of InGaN have been employed to enhance the performance of solar cells. Some of the commonly used configurations are

- $In_xGa_{1-x}N$ p-i-n and p-n homojunction cells
- $In_xGa_{1-x}N$ /Si heterojunction
- $In_xGa_{1-x}N$ /GaN heterostructure solar cells with p-n, p-i-n, and nanorod/nanowire configurations
- $In_xGa_{1-x}N$ quantum well and quantum dots solar cells

The first successful demonstration of nitride based PV was given in 2007 by Jani *et al.*⁴⁶ and Yang *et al.*⁴⁷. Jani *et al.* fabricated the single-junction $In_{0.28}Ga_{0.72}N$ solar cell using metalorganic chemical vapor deposition (MOCVD) method and obtained a high open-circuit voltage (V_{oc}) of 2.1 V for a 100 nm thick cell, which was consistent with the band gap of $In_{0.28}Ga_{0.72}N$ at 2.5 eV, but no photoresponse was observed for the cells of thickness around 300 nm. Cai *et al.*⁴⁸ and Jampana *et al.*⁴⁹ reported comparatively good PV response with enhanced illumination, but in these cases the indium contents of their cells were limited to 17%. It was observed that increasing the indium content in the film causes poor performance of the PV. In 2010, Boney *et al.* reported high indium ($\approx 54\%$) incorporation in InGaN based solar cell⁵⁰ by using PA-MBE, but the efficiencies of these devices were very poor.

Recent development in III-nitride based solar cell is mostly dominated by the hetero junction structure *e.g.* p-GaN/ $In_xGa_{1-x}N$ /n-GaN, similar to an LED structure. Jani *et al.* measured the PV response in a p-i-n heterojunction structure with $In_xGa_{1-x}N$ ($x = 0.04 - 0.05$) layer sandwiched between GaN, with a V_{oc} of 2.4 V with very low short circuit current density (J_{sc})⁵¹. Recently Liou *et al.*⁵² has reported $In_xGa_{1-x}N$ /GaN MQWs grown over SiCN/Si substrate, which shows low dark current density (J_d) of 2.14 to 8.88 $\mu A/cm^2$, a high V_{oc} of 2.72 to 2.92 V, a high J_{sc} of 2.72 to 2.97 mA/cm^2 , and a high fill factor (FF) of 61.51 to 74.89%, alongwith a high photovoltaic efficiency of 5.95%. Al-Amri *et al.*⁵³ reported a record 31% conversion efficiency of solar cell by using stack of nano-spheres on InGaN based MQW structure. Although GaN/InGaN based heterojunction and InGaN homojunction solar cells having high Ga content have been demonstrated, their performances and efficiencies are still poor. This is the consequence of transparency loss for high band gap energy InGaN cells caused by low In composition and also for poor crystalline quality of the grown InGaN layers. Therefore, at present this is limited by the ability to produce high crystal quality InGaN with high In content. Although various efforts have been carried out towards achieving high efficiency solar cells, still there remains many challenges to attain this goal.

1.3.5 Chemical and Biological Sensors

There is always a huge demand for the development of robust solid-state sensors capable of operating in harsh environments such as in outer-space. These sensors should be capable of detecting chemicals or radiation and sending information back to ground control. The high carrier density of 2DEG of AlGa_N/Ga_N HEMTs is consequences of piezoelectric polarization of the strained AlGa_N layer and sensitive to the strain, any change in local radiation pressure directly influences device properties, which strongly indicates its consideration for pressure sensor and piezoelectric related applications. It is well known that presence of different chemicals or radiations induces changes in local environment such as pressure. Further, the sheet charge density in the 2D channel of AlGa_N/Ga_N HEMT is extremely sensitive to its chemical ambient: any change in the surface such as the adsorption of polar molecules on the surface of Ga_N affects both the surface potentials and consequently changes the device characteristics. In additions the sheet carrier concentration of the 2DEG at the interfaces of AlGa_N/Ga_N HEMTs, without any surface passivation, becomes sensitive to any manipulation of surface charge. This effect is used to build micro-sensors for the detection of applied strain and surface polarity change by polar liquids or toxic gases.

Numerous groups have demonstrated various sensors utilising the above mentioned features of Ga_N based devices. For instance AlGa_N/Ga_N HEMT structures fabricated by Kang *et al.* showed large changes in source-drain current by exposing the gate region to various block co-polymer solutions⁵⁴. The polar nature of some of these polymer chains causes a change in surface charge around gate region on the HEMT, consequently produces a change in surface potential at the interface of semiconductor and solution. Steinhoff *et al.* has observed simple Ga_N Schottky diodes exhibit strong changes in current upon exposure to hydrogen containing ambients⁵⁵.

In the past, Si based FETs have been widely used as bio-sensors, specially the Si-based Ion Sensitive Field Effect Transistor (ISFET), which is already commercialized to replace conventional electrolyte pH metres. However, there are certain drawbacks in the use of Si-based FETs; prevention of damages caused by exposure to solutions containing ions, need an ion-sensitive membrane coated over their surface and a reference electrode (usually Ag/AgCl). Special precautions must also be taken to apply those biomembranes

over the FETs so that they retain their enzymatic activity. Unlike Si, GaN-based wide energy band gap semiconductor material systems are extremely chemically stable. Adding to that, Proteins can easily attach to the GaN surface. Thus, nitride materials are very competitive candidate for application in gas and biological detection⁵⁶.

1.3.6 Dilute Magnetic Semiconductor

The observation of ferromagnetism in semiconductor which are doped with magnetic ions, specially transition metals that have partially filled *d*-states (such as Sc, Ti, V, Cr, Mn, Fe, Co, Ni, and Cu) and rare earth elements that have partially filled *f*-states (such as Eu, Gd, Er), has inspired material scientist and engineers to exploit the spin, in addition to charge of the electrons in semiconductors. There are many mechanisms that could be responsible for magnetic ordering in these cases, and thus, studies based on *first-principles* are must for better understanding. The main challenge for practical application of the DMS materials is the attainment of a high Curie temperature (T_c) preferably above room temperature (RT) to avoid data loss due to spin flipping. At the early stage, studies of DMS were largely based on II-VI compounds⁵⁷. However, the low T_c and difficulty in doping in these materials make them less attractive.

In 1998, Hideo Ohno discovered ferromagnetism in Mn doped GaAs, with a T_c of 110 K⁵⁸. In 2000, Dietl *et al.* reported for the first time that ferromagnetic state can be found even at RT for GaN:Mn⁵⁹. By using *first-principles* based calculations, Das *et al.* predicted that Cr doping in GaN can induce ferromagnetism in the system⁶⁰. There are various approaches that have been made in the past to synthesize single crystal GaN:Mn and the results indicate the presence of RT ferromagnetism in the same^{61–69}. Sonoda *et al.* found, by incorporation of 6-9% of Mn in GaN, a clear hysteresis in M vs H plot at 300 K, with coercivities of 52-85 Oe. Surprisingly, they reported the T_c value to be 940 K by using mean-field approximation to analyze the experimental data⁶³. Such high values of T_c provides a great promise for GaN to be used in spintronics devices.

1.4 Crystal structure of III-Nitrides

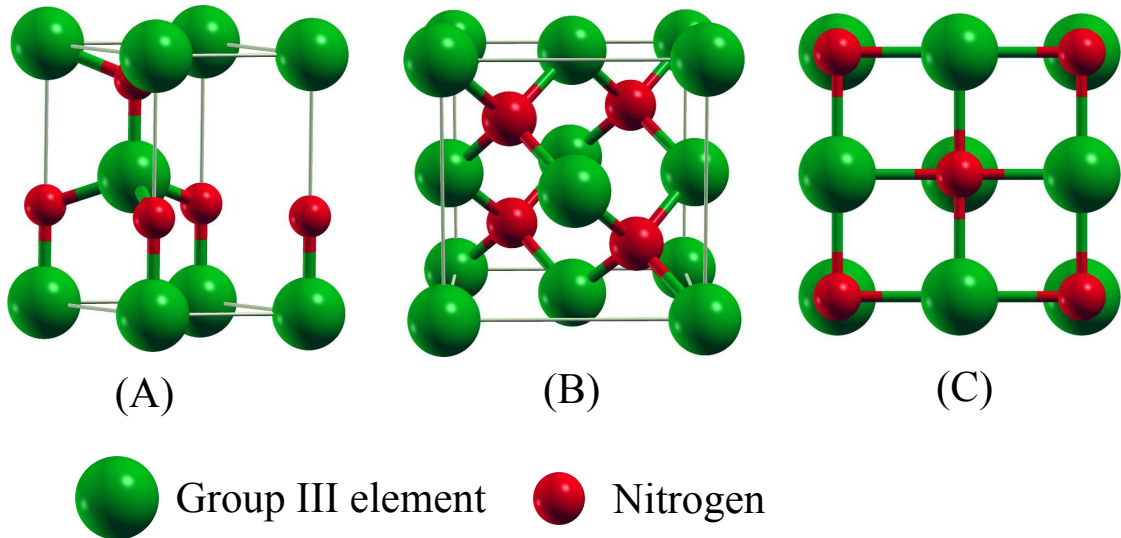


Figure 1.2: (A), (B) and (C) represent the schematic of unit cell of wurtzite, zincblende and rock-salt phase of III-nitrides.

Group III-nitrides can crystallize in three different crystal structures: Wurtzite, Zinc blende and Rocksalt, out of which Wurtzite phase is thermo-dynamically the most stable. The wurtzite phase is an example of hexagonal crystal system (or hexagonal closed packing (*hcp*) or α -phase). The wurtzite crystal structure is denoted by the Strukturbericht designation B4 and by the Pearson symbol as hP4. The space group is No.186 in International Union of Crystallography (IUCr) classification and $P6_3mc$ in Hermann-Mauguin notation. The wurtzite structure consists of two interpenetrating hexagonal sub-lattices, each with individual type of atoms, offset by $5/8$ of cell height along (0001) direction. The hcp structure of group III-nitride is ascribed by the edge length a and height c of the hexagonal prism. It contains two lattice point and two basis for each lattice in an unit cell, resulting 4 atoms in an unit cell: two metal (at $(1/3, 2/3, 0)$ and $(2/3, 1/3, 1/2)$) and two nitrogen ($(1/3, 2/3, u)$ and $(2/3, 1/3, 1/2+u)$) atoms, where u is the internal parameter defined as ratio between bond-length of Ga-N along (0001) direction and c lattice parameter. In the crystal, each metal atom is surrounded by four nitrogen atoms and vice-versa. The bond-length of Ga-N along (0001) direction is relatively higher than that along other directions in the tetrahedra. The stacking sequence of (0001) plane is AaB-bAa in [0001] direction. Lowercase and uppercase letters stand for the two different kinds

Table 1.1: Lattice parameters and Band gap of III-nitrides at RT

III-nitrides	Wurtzite Phase			Zinc-blende Phase	
	a (in Å)	c (in Å)	E_g (eV)	a (in Å)	E_g (eV)
AlN	3.1106	4.9795	6.12	4.38 ⁷⁰	5.40 (indirect) ⁷¹
GaN	3.1893	5.1852	3.42	4.50 ⁷²	3.20 ⁷²
InN	3.5376	5.7064	0.64	4.98 ⁷³	0.43-0.45 ⁷⁴

of constituents.

The zincblende phase is an example of cubic crystal system. The space group of the zincblende structure (or β -phase or sphalerite) is called $F\bar{4}3m$ in Hermann-Mauguin notation, or 216 in IUCr classification and Strukturbericht designation is B3. β -phase contains four group III-element and four nitrogen atoms in the unit-cell. The β phase consists of two interpenetrating face centered cubic (FCC) sublattices, offset by one fourth of the distance along a body diagonal. The stacking sequence for the (1 1 1) close-packed planes in this structure is AaBbCc. A detailed comparison of lattice parameters and band gaps between III-nitrides are give in Table 1.1.

The rock salt (or more commonly NaCl) structure (space group Fm3m in the Hermann-Mauguin notation and Strukturbericht designation is B1) can be obtained for III nitrides under very high pressures. The reason for the structural phase transition is the reduction of the lattice dimensions due to applied high pressure, which forces the inter ionic Coulomb interaction to favor the ionicity over the covalent nature. The structural phase transition to rock salt structure was experimentally observed at the estimated pressure of 14 GPa for AlN⁷⁵, 37 GPa for GaN⁷⁶, and 15 GPa for InN⁷⁷. However, rock salt III nitrides cannot be produced by any epitaxial growth methods.

Wurtzite III-nitrides structure lacks the inversion plane perpendicular to c-axis, which causes growth of the films with either group III-metals (+c axis) polar or N polar(-c axis) orientations. The concept of polarity in these cases is a bit tricky. Ga-polar does not necessarily mean the termination of the surfaces by Ga atoms, and same is true for N-polarity. The vector going from the metallic cation and pointing toward the anion defines the [0001] or +c direction and hence the polarity, and referred to as cation polar. It is widely observed that^{78,79} Ga polar GaN films have a rougher morphology than

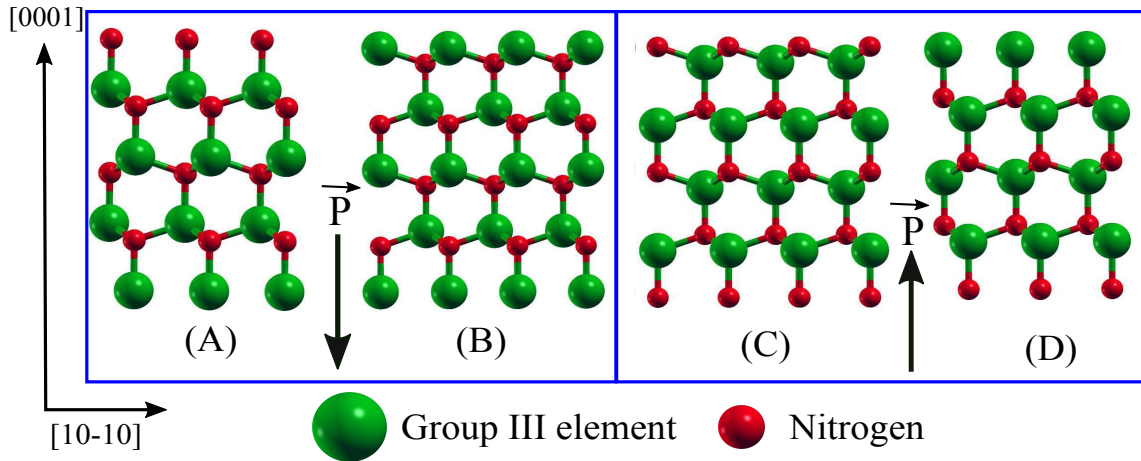


Figure 1.3: (A) and (B) represent N and Ga terminated Ga-polar arrangement, respectively. (C) and (D) represent N and Ga terminated N-polar arrangement, respectively.

N-polar films. Not only the polarity has impact on morphological properties but also on optical properties of GaN^{80,81}. Since devices are commonly fabricated on polar surfaces, their characteristics depend upon the termination of the surfaces. Therefore, it is very important to be able to determine and control the polarity of GaN for better control over device fabrication.

1.5 Substrates used for III-nitride growth

As mentioned previously, group III-nitrides are not available naturally, thus synthesis of single crystalline films requires a suitable substrate. Due to lack of availability of sufficiently large native substrate, often nitrides are grown over foreign substrate. Typical requirements to be a substrate for thin film growth are as follows:

- Low lattice mismatch between film and substrate
- Low thermal expansion co-efficient mismatch
- Structurally stability at high temperature (1000-1200 °C)
- Chemically stability
- Availability at larger dimension *i.e.* larger wafer size
- Affordable price

Over the years, several substrates have been used to grow III-nitride thin films. A list of possible substrate for III-nitrides are shown in Table 1.2^{71,82-84}. The most preferable substrate to grow GaN is sapphire (α -Al₂O₃), which has a rhombohedral crystal structure. The lattice mismatch [defined as $(a_{substrate} - a_{film})/a_{substrate}$] between sapphire and GaN is $\approx 33.1\%$ (without any reconstruction). Due to this large lattice mismatch between GaN and sapphire, there is a general tendency of III-nitride unit cells to rotate by 30° around the c-axis w.r.t. sapphire unit cell. In this rotated case the lattice mismatch is defined as $(a_{substrate} - 2a_{film}\cos\theta)/a_{substrate}$, where θ is the angle of rotation of the film unit cell w.r.t. substrate. Consequently, after this rotation the lattice mismatch reduces to $\approx 16\%$. Despite this reduction in the lattice mismatch a dislocation density in the films is of the order of 10^{10} cm^{-2} exist. Adding to that, the coefficient of thermal expansion of sapphire is greater than that of GaN, which results in the development of biaxial compressive stress in the thin film as it is cooled down from the growth temperature. Thus, growth of thin film directly over the foreign substrate may not result in good quality films. Therefore, use of buffer layers such as low and high temperature AlN and/or GaN, prior to the growth of the desired films, is necessary for device fabrication. Different surfaces of the substrates are used to obtain different orientation of the crystal in epitaxial thin film growth.

Generally, (0001) surface of sapphire is used to grow GaN along the (0001) direction. In this case, the epitaxial relations are $[0001]_{GaN} || [0001]_{Al_2O_3}$ and $[10\bar{1}0]_{GaN} || [11\bar{2}0]_{Al_2O_3}$. The growth of GaN along non-polar surface $(11\bar{2}0)$ (or commonly ‘a’ surface) can be achieved by using r-plane (*i.e.* $(1\bar{1}02)$) of sapphire substrate⁸⁶. Similarly, epitaxial growth of GaN on $(1\bar{1}00)$ surface of sapphire results in in-plane epitaxial relation $[1\bar{1}00]_{GaN} || [1\bar{1}00]_{Al_2O_3}$ in HVPE growth and $[11\bar{2}0]_{GaN} || [1\bar{1}00]_{Al_2O_3}$ in MOVPE growth⁸⁷. The (111) surface of cubic materials such as MgO, Si and GaAs can be used for epitaxial growth of w-GaN in (0001) direction. In such cases, the epitaxial relations are $[0002]_{GaN} || [111]_{MgO}$ and $[01\bar{1}0]_{GaN} || [101]_{MgO}$ ⁸⁸. Similarly for Si, the epitaxial relations are $[0002]_{GaN} || [111]_{Si}$ and $[11\bar{2}0]_{GaN} || [110]_{Si}$ ⁸⁹. Cubic phase of GaN can be obtained by using different surfaces (such as (100), (001) and (010)) of cubic materials such as Si⁹⁰, GaAs⁹¹, MgO⁹², 3C-SiC⁹³ etc.

Table 1.2: Commonly used substrate for the growth of III-Nitride.

Materials	Crystal structure	Lattice parameters (in Å)		Lattice mismatch ($\approx\%$) w.r.t			Thermal Expansion coefficient (10^{-6} K $^{-1}$)	
		a	c	GaN	InN	AlN	$\parallel a$	$\parallel c$
InN	Wurtzite	3.5378	5.7033	-11	0	-12	3.09	2.79
GaN	Wurtzite	3.1850	5.1880	0	11	-2.3	3.17	5.59
AlN	Wurtzite	3.1110	4.9800	2.3	13.7	0	4.20	5.30
α -Al ₂ O ₃	Rhombohedral	4.7650	12.9820	16	29.2	13.3	5.00	9.03
6H-SiC	Wurtzite	3.0806	15.1173	-3.1	14.8	-0.98	4.30	4.70
ZnO	Wurtzite	3.2469	5.2065	-1.9	8.95	-4.18	6.5	3.0
LaAlO ₃	Rhombohedral	5.3640	13.1100	3	-	-	-	-
MgO	Rocksalt	$a = b = c = 4.2100$		6.8	18.7	4.4	13.85	
ScN	Rocksalt	$a = b = c = 4.5776$		1.46 ⁸⁵	12.7	-0.89	-	
Si (111)	Diamond	$a = b = c = 5.4310$		19	-7.8	23.4	2.61	
GaAs	Zincblende	$a = b = c = 5.653$		20	11.7	-	6.03	

1.6 Structural Defects

It can be clearly seen from Table 1.2, that the lattice parameter and thermal expansion co-efficients of III-nitrides and those of the commonly used substrates are different. Thus, at initial stage of growth, the films grow pseudo-morphically (*i.e.* lattice parameters of the film is forced to take that of substrate, which results in high strain in the films). After achieving a critical thickness (t_c), the films attain the relaxed value of lattice parameter by accommodating structural defects within it-self. The residual strain is called tensile when $a_{substrate} > a_{film}$, while it is compressive when $a_{substrate} < a_{film}$. In addition, most of thin film growth processes happen far away from the thermal equilibrium conditions, which results in the formation of several kinds of defects in the epitaxial films.

The structural defects in overgrown thin films are generally classified in to 4 types (D=dimension)

- 0D or point defects
- 1D or line defects

- 2D or planar defects
- 3D or volume defects

1.6.1 Point defects

Point defects are where an atom is missing and/or is in an irregular place in the lattice structure or the presence of an impurity atom. Various point defects are shown in Fig.1.4. The concentration of point defects in the solid at a certain temperature can be estimated from the relation

$$N_{pd} = N \exp(-E_f/kT) \quad (1.1)$$

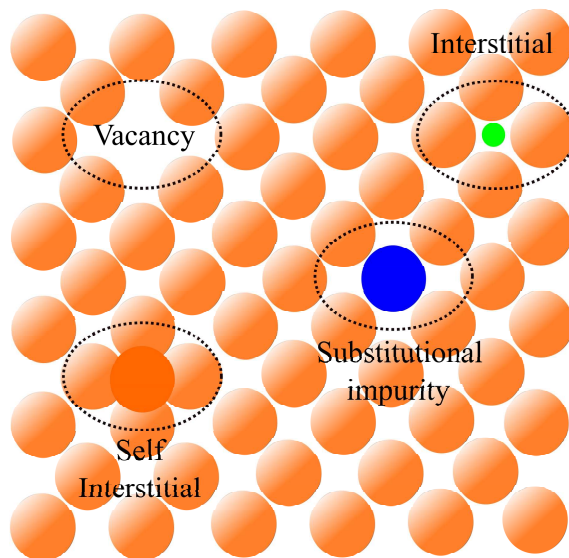


Figure 1.4: Two dimensional schematic representation of different point defects in solid.

where N is total number of atomic sites, E_f is the formation energy of the defect, T is the absolute temperature and k is the Boltzmann's constant. All crystalline solids inherently contain point defects such as vacancies, whose necessity is explained within the principles of thermodynamics; to increase the entropy of the crystal. An interstitial defect is the presence of an extra atom at the interstitial position. Self-interstitial defects are interstitial defects which contain only those atoms which are present in the ideal lattice sites. A substitutional impurity defect appears when a foreign atoms takes the lattice sites, whether incorporated intentionally or non-intentionally in the crystal.

In compound semiconductors antisite defects can be formed, if atoms occupy opposite sub-lattice sites. Presence of any kind of point defect is very much influential on the optical, electronic and electrical properties of the material. For instance, N vacancy in intrinsic GaN gives rise to background carrier doping while Ga vacancy results in p-type conductivity and yellow luminescence (2.2 eV).

1.6.2 Line Defects or Dislocations

A dislocation is a linear or one dimensional defect in which some of the atoms along it are misaligned, causing a severe change in the material properties. A dislocation can be visualized as being caused by the termination of a plane of atoms in the middle of a crystal as shown in Fig.1.5. Due to this the surrounding planes are not straight, instead they bend around the edge of the terminating plane so that the crystal structure remains ordered on either side. A dislocation is usually represented by an oriented dislocation lines \vec{l} , and characterize by the Burger vector \vec{b} .

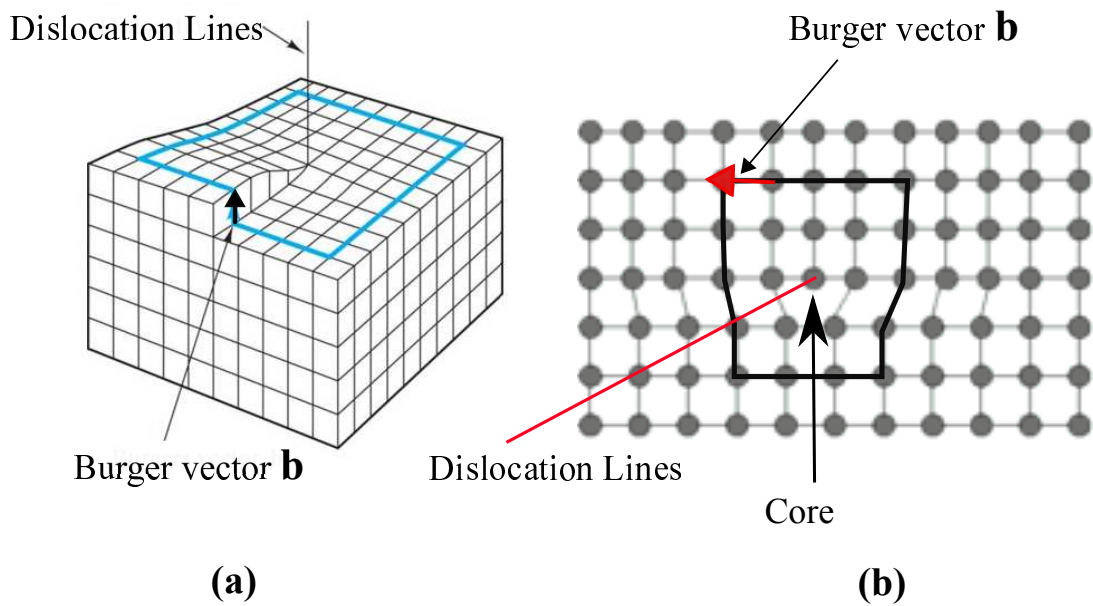


Figure 1.5: (a) screw type dislocation in which Burger vector \mathbf{b} is parallel to the dislocation line \mathbf{l} . (b) edge type dislocation in which \mathbf{b} is perpendicular to \mathbf{l} .

Mainly, there are three types of dislocations: edge dislocation, screw dislocation and mixed dislocations. In screw dislocations, the Burger vector \vec{b} is parallel to dislocation lines \vec{l} , whereas in case of edge dislocations, the Burger vector \vec{b} is perpendicular to

dislocation lines \vec{l} (see Fig.1.5). The mixed dislocation is the combination of individual edge and screw dislocation lines where $\vec{b} \not\perp \vec{l} \not\parallel \vec{b}$. In case of hexagonal lattice (such as GaN), there are three possible Burger vectors for perfect dislocations: $\langle 0001 \rangle$ or c -type, $\frac{1}{3} \langle 11\bar{2}0 \rangle$ or a type, and $\frac{1}{3} \langle 11\bar{2}3 \rangle$ or $a + c$ type.

The density of dislocations can be measured by various techniques such as TEM, AFM and XRD. In TEM we can visualize the type of dislocations directly, however, it is a destructive technique. XRD and AFM are non-destructive technique, and thus used frequently for the study of dislocations in epitaxial growth of crystal. In AFM, only dislocations that thread to the surface are measured while XRD information does not have spatial information.

1.6.3 Planar and Volume defects

The planar defects are at the interface between the homogeneous region of the materials. Below we have listed most commonly observed planar defects:

- **Grain boundaries** : A general planar defect separates the regions of different crystalline orientation (grains) in a poly-crystalline solid.
- **Twin boundaries** : Responsible for change in the crystal orientation across a twin plane, such that certain symmetry (such as mirror image) exists across the plane.
- **Stacking faults**: Created by a fault in the stacking of the layer and are generally observed in closed packed structures.

Bulk defects or volume defects occur in the crystal at a larger scale than other defects which are discussed above. Volume defects in crystals are three dimensional segregation of atoms or vacancies, categorized into four types;

- **Precipitates**: Manipulation of the small particles into a crystal by solid state reactions. Size of the particles are of the order of a fraction of a micron.
- **Dispersants**: Larger particles that behave as a second phase as well as influence the behavior of the host. Size varies from fraction of a micron to $10\text{-}100\mu\text{m}$.
- **Inclusions**: Undesirable particles that entered the system as impurities, whose sizes vary from micron to macroscopic dimension.

- **Voids or pores:** Holes in the solid, formed by trapped gases or by the segregation of vacancies. Thus become responsible for decrease in the mechanical strength of the material and hence promote fracture at small loads.

1.7 Growth process of thin films and Nanostructures: Physical deposition processes

The fabrication of thin films on a single crystal substrate is done by the deposition of individual atoms on it (bottom-up approach). There are various factors which govern the growth of the film such as substrate temperature, flux rate of the materials and the growth environment. During thin film growth, various physical and chemical phenomena take place, which essentially play a crucial role in the formation of desired crystals on the substrate. Some of these crucial phenomena are listed below and are shown in Fig.1.6.

1. Generation of the appropriate species
2. Transportation of the species on to the substrate
3. Condensation on the substrate

The species that arrived, on impacting the substrate, lose their velocity component normal to the substrate and get physically adsorbed on it with random hopping process on the substrate atomic lattice or get desorbed (re-evaporated) from the substrate depending on the potential energy surface (PES) of the substrate. Once the species get adsorbed on to the substrate, due to thermal non-equilibrium, they diffuse over the surface of the substrate, colliding into each other and form clusters (or more commonly called as *nuclei*). After reaching a critical size, the cluster becomes thermodynamically stable. This stage is called *nucleation*. Until a saturation nucleation density is achieved the critical nuclei continue to grow both in number and in size. The nucleation density and the average nucleus size depend on various parameters; the energy of the impinging species, the rate of impingement, the temperature, the activation energies of adsorption and desorption, thermal diffusion and the chemical nature of the substrate. The larger grown nuclei are called *islands*. A nucleus can grow both parallel and perpendicular to the surface of

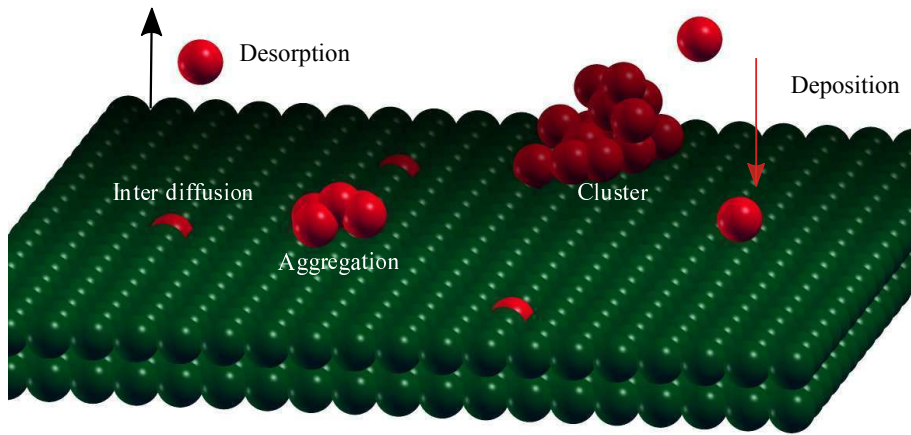


Figure 1.6: Schematic diagram of different processes that are involved in thin film growth.

the substrate. In most of the cases, the rate of lateral growth at this stage, is much higher than that of the perpendicular growth. As the island continues to grow further and possibly migrate, they can meet proximal islands and coalesce to each other to form larger islands. This process is called *agglomeration*. The agglomeration can be enhanced by increasing the mobility of adsorbed species by external kinetic parameters, such as high substrate temperature or arrival flux. As many larger islands form on the substrate and start merging, channels and holes appears on the uncovered substrate. The structure of the films at this particular stage may change from discontinuous island type to a porous network type. During growth, if the channels and the holes get filled, the outcome will be a completely continuous 2D film.

1.7.1 Growth Modes of Thin films

Depending on the initial nucleation process and interplay between elastic and plastic relaxation, the various thin films growth modes are classified in to three types; Frank van der Merwe (FM) layer by layer mode, Volmer Weber (VW) island mode and Stranski-Krastanov (SK) layer plus island mode. A brief description on three different growth mode is discussed below and their schematic is shown in Fig.1.7.

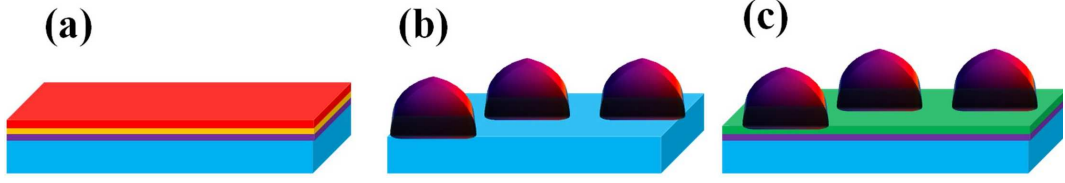


Figure 1.7: Schematic diagram of different growth modes; FM(a), VW(b) and SK(c)

1.7.1.1 Frank van der Merwe (FM) growth mode

In the FM growth mode, two dimensional (2D) growth occurs when adatoms impinge on the surface of the substrate. In this mode, the adatoms are more strongly attracted to the substrate than to each other and therefore the first few adatoms condense on the surface of the substrate to form an atomic monolayer. Subsequently, the next adatoms follow the same process on the first formed layer by layer growth takes place. Typically FM growth mode is favorable when lattice mismatch between films and substrate is less and the surface energy of the substrate ($\gamma_{substrate}$) is greater than or equal to the sum of the surface energy (γ_{film}) of the film and interface energy of the films and substrate ($\gamma_{interface}$), which can be expressed as

$$\gamma_{substrate} \geq \gamma_{film} + \gamma_{interface} \quad (1.2)$$

This mode is dominantly prevalent in the metal on metal system.

1.7.1.2 Volmer Weber (VW) growth mode

In the VW growth mode (or 3D) mode, island growth is preferred because of the stronger adatom-adatom interaction than that of adatom with the surface of the substrate. Thus, adatoms form clusters on the substrate and grow into individual islands. Typically, the VW growth mode is preferable when lattice mismatch is large and the surface energy of the substrate ($\gamma_{substrate}$) is less than or equal to sum of the surface energy (γ_{film}) of the film and interface energy of the films and substrate ($\gamma_{interface}$), which can be written as

$$\gamma_{substrate} \leq \gamma_{film} + \gamma_{interface} \quad (1.3)$$

This method of growth is evident in several metals on insulator system.

1.7.1.3 Stranski-Krastanov (SK) growth mode

The SK growth mode, also known as layer-plus-island growth mode, is favorable when the lattice mismatch is moderate. In the SK growth mode, initially films grow by the layer by layer mode, during which strain is accumulated with increasing thickness of the films. When the thickness reaches a critical value, the strain is released by the formation of small islands. As active species further impinge on it, the small island continues to grow until they are fully ripened. This kind of growth mode is usually seen in metal on semiconductor surface. The growth conditions can be visualized as

$$\textit{Initially}, \gamma_{\text{substrate}} \geq \gamma_{\text{film}} + \gamma_{\text{interface}} \quad (1.4)$$

$$\textit{Finally}, \gamma_{\text{substrate}} \leq \gamma_{\text{film}} + \gamma_{\text{interface}} \quad (1.5)$$

Growth of GaN on Sapphire

The growth of w-GaN on sapphire substrate is very interesting in this regard. Due to the large lattice mismatch between GaN and sapphire, direct growth of GaN on bare sapphire occurs in VW mode. However, low temperature (LT) buffer layer over sapphire drastically changes the surface morphology. Conventional way of LT nucleation layer growth and its recrystallization at high temperature, provides well separated nucleation sites, and thus stimulates the 3D growth mode at the early stages of nitride layer. Transition to 2D growth mode takes place when 3D islands merge. This finally leads to a smooth layer which grows in the 2D mode⁹⁴. King *et al.* studied the growth of GaN on AlN buffer layer over 6H-SiC substrate⁹⁵. According to their observation, at low temperatures $\approx 650 - 750$ °C the growth of GaN on AlN occurs via SK mode (2D \rightarrow 3D type mechanism) with the transition to 3D growth occurring after a film thickness of 10-15 Å. The mechanism changes to FM (layer-by-layer growth) mode above 800 °C. Similarly the growth of AlN on GaN occurred via the FM layer-by-layer mechanism in the 750-900 °C temperature range.

In this thesis work, we have taken advantage of above discussed phenomena to kinetically control the growth situations to obtain structurally and optically superior GaN nano-structures, and have studied their various properties in details. Further, impact of dopant concentration on different properties of the materials are also discussed in detail in the later part of the thesis.

Chapter 2

Literature Overview

This chapter provides the historical background on the studies of growth of pristine and Mg doped GaN nanostructures and their properties, in the literature. This chapter also includes some of the challenges and ambiguities related to the growth of GaN on various substrates. Issues related to efficient p-type doping of GaN are also discussed briefly.

2.1 Growth of GaN Nanostructures

Despite the great success in the fabrication of high crystalline quality GaN thin films during 1970-1980s, GaN based LEDs were not commercialized until 1993; partly due to their poor optical properties and inefficient p-type doping. This section summarizes the improvements made over the years to increase light emission from GaN and enhance p-doping in GaN.

Since the devices are majorly fabricated using thin film deposition techniques, it is important to find a suitable substrate on which the growth of thin films can take place. For growing GaN of high quality, the GaN substrates (homoepitaxial) are not only too expensive but it has not yet been possible to grow large size wafers. Therefore, majority of the thin film growths are carried out on a substrate with different lattice parameters. Such heteroepitaxial growth leads to a large strain at the interface which is released by the formation of dislocations in the overgrown thin films. These dislocations play a crucial role in determining the device performance, as they act as scattering centers for mobile

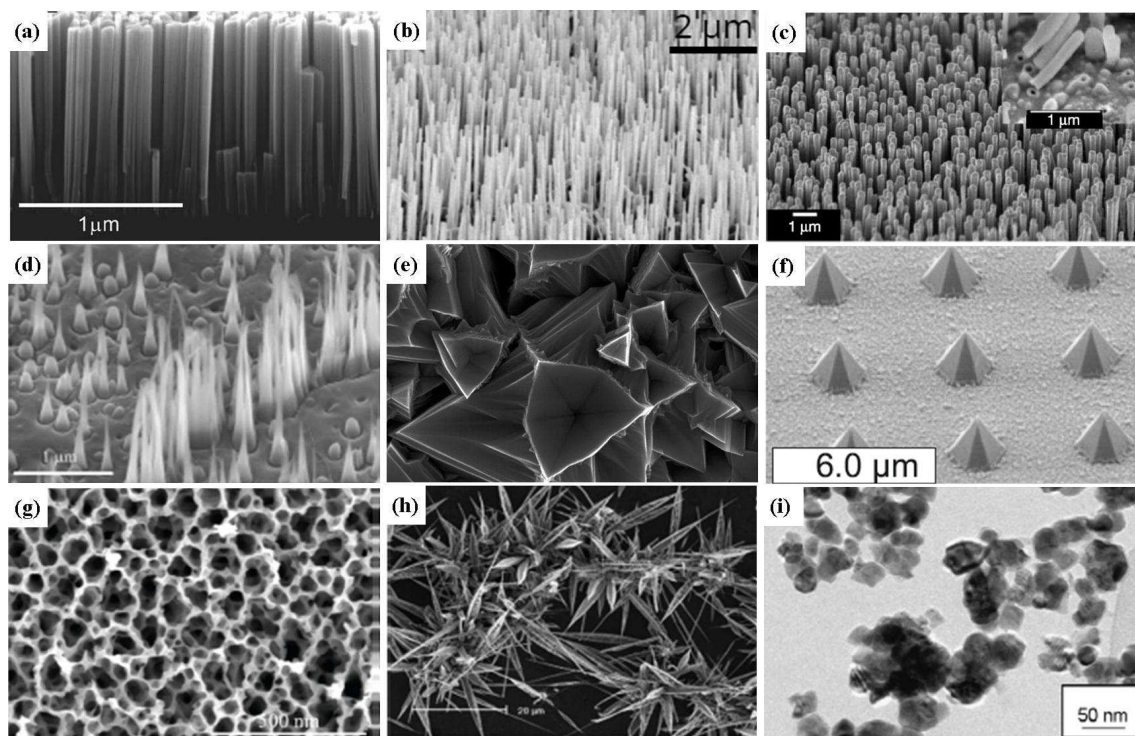


Figure 2.1: FESEM image of different morphologies of GaN reported in the literature. Fig. (a-i) shows morphologies of Nanorods⁹⁶, Nanowires⁹⁷, Nanotubes⁹⁸, Nanowhiskers⁹⁹, Nanoflowers¹⁰⁰, nano-pyramids¹⁰¹, Nanoporous¹⁰², Nano-leaves¹⁰³ and Nanoparticles¹⁰⁴ respectively. All images are reproduced with permission from appropriate publishing agencies.

charge carriers. Dislocations also act as non-radiative recombination centers, an unwanted physical phenomenon for optoelectronic device applications. A lot of effort has been made to improve the crystal quality by minimizing such dislocations (especially the threading dislocation density (TDD)). One of the earliest method used was to deposit a buffer layer prior to the desired thin film growth. It was assumed that by lowering TDD, light emission from GaN would increase, similar to the enhanced electrical properties of GaN. But of late¹⁰⁵, it was realized that GaN based LEDs were able to provide sufficient brightness even with dislocation densities of $\approx 10^{10} \text{ cm}^{-2}$. A theoretical study carried out by Karpov *et al.*¹⁰⁶ suggested that, to achieve an internal quantum efficiency of unity, dislocation density should be less than 10^7 cm^{-2} . This motivated researchers to explore wide varieties of growth techniques such as Epitaxial lateral overgrowth (ELOG)¹⁰⁷, pendo-epitaxy¹⁰⁸ and nanostructuring^{109,110}. Among these, nanostructuring showed a lot of promise, since the dislocations terminate at the side-walls and hence the dislocation density reduces significantly with the increase in film thickness. Since their contact area on the substrate is small, the lattice mismatch is accommodated and consequent defects are minimal. Taking advantages of such properties, exploration of GaN nanostructure based devices is being conducted extensively till date. Usually growth of nanostructures can be achieved by either by catalyst-assisted or the catalyst free method¹¹¹. The catalyst-assisted growth typically occurs via a vapor-liquid-solid (VLS) process where pure metal droplets are used initially as seed whereas, catalyst free growth does not require any such seed layer. GaN nanostructures with various shapes and sizes can be synthesized with various techniques. Some of the popular nanostructures and their characteristics are mentioned here and are shown in Fig. 2.1.

- Nanorod: Diameters range from 1-100 nm. Aspect ratio (length divided by width) is 3-5.
- Nanowire: Diameters range from 1-100 nm. Aspect ratio is greater than 1000.
- Nanotube: Nanometer-scale tube-like structure.
- Nanoparticles: 1-100 nanometers in size.
- Nano and Microporous: Presence of pore like structure in its microstructure, rendering a large surface to volume ratio of the order of $500 \text{ m}^2/\text{cm}^3$.

One of the major issues which has been very critical over the years is the low light extraction efficiencies (LEE) of GaN based LEDs (*By definition External Quantum Efficiency (EQE) of a LED is the product of Internal Quantum Efficiency (IQE) and LEE.*). The LEE from a high index material to a low index material can be estimated by the following equation

$$\eta_{ext} = \frac{1}{2} \int_0^{\theta_{SC}} T(\theta_{SC}) \sin(\theta_{SC}) d\theta_{SC} \quad (2.1)$$

where, $T(\theta_{SC})$ is the polarization-averaged Fresnel transmission at the incident angle θ_{SC} . The values of θ_{SC} for nitrides are $\approx 24.6^\circ$, thus, only about 4% of generated light can fall within the ‘escape cone’ (see Fig. 2.2) and come out from the material. Such low LEE is the consequence of the large mismatch between the refractive indices of GaN ($n = 2.5$ at 460 nm) and ambient ($n = 1$)¹¹². To overcome this problem, various techniques has been adopted such as chip shaping^{113,114}, contact geometry design¹¹⁵, photonic crystal^{116,117}, graded refractive index anti-reflective coatings¹¹⁸, micro and nano scale texturing^{109,110}, nano-porous structuring^{119–121}, self-assembled monolayer of microsphere arrays^{122,123} etc. By using chip shaping technique an enhancement of 10% in the EQE is achieved¹¹⁴ while a 100% increase in light emission was recorded by contact geometry design¹¹⁵ technique. Photonic-crystal based LED has a light extraction efficiency of 73%¹¹⁷. Graded refractive index anti-reflective coatings techniques shows an increse in LEE by 24.3%, where ITO is coated over InGaN based LED. Ishida *et al.* demonstrated, by using needle-shaped indium tin oxide p-contact on GaN based LEDs, enhancement of EQE is by 1.5 times¹⁰⁹ whereas, micro/nano patterning on p-GaN surface showed enhancement in LEE by 48%¹¹⁰. Further, Lee *et al.* demonstrated that by using various size of the silica sphere on GaN based LED, LEE increases 1.1-1.32 times compared to the conventional GaN based LEDs¹²². On the other hand Li *et al.* showed increased in the LEE by 1.8-1.9 times by using TiO₂ microsphere¹²³. Thus, for reduction of defect densities as well as for enhancement of LEE nanostructuring of material could be effectively used. The enhancement of LEE in GaN by employing nano-porous structure are reported as 46%¹²⁰ and 150%¹²¹. Hwang *et al.* showed that in case of GaP based LEDs, the LEE from the active layer of a LED with nanoporous structure is increased by about 30%-50% as compared to a non-porous layer¹²⁴. Lin *et al.*¹²⁵ observed from PL measurements (T= 300 K) that the light enhancement ratio, of an MQW active layer and a GaN layer, containing a porous structure on the top

surface, are 1.42 times and 7.4 times respectively, as compared to the standard sample without any porous structure. Such enhancement of LEE due to presence of porous structure opens up a new route for the realization of high brightness and efficient LEDs. The pores in the porous structure act as scattering centers for light. The mean free path for transport of light (l) in the porous structure is given by¹²⁴

$$l = \frac{1}{\rho\sigma_c} \quad (2.2)$$

where ρ denotes the density of scatterers (i.e. pore density) and σ_c denotes the scattering

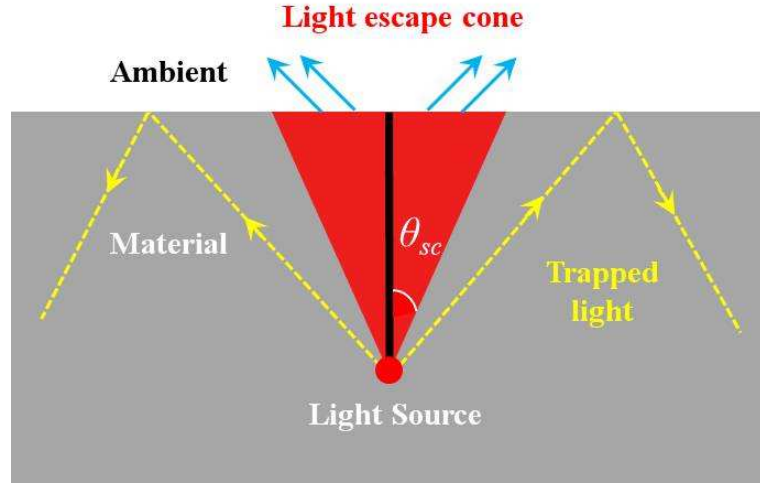


Figure 2.2: shows light extraction process from materials with high refractive index.

crosssection (i.e. pore size). Further, scattering crosssection (σ_c) maximizes when the pore sizes are comparable to the wavelength of scattered light due to multiple scattering of photons and consequently enhances the light extraction efficiency of the system. Adding to that several studies reveal that porous TiO_2 ¹²⁶, GaP ¹²⁷ as well as GaN ¹²⁸, show a reduction of the refractive index with increased porosity. The effective refractive index (n_{eff}) in the Bruggeman Effective Medium Approximation (EMA) is given by¹²⁹

$$f_v \left[\frac{(n_v^2 - n^2)}{(n_v^2 + n^2)} \right] + f_c \left[\frac{(n_c^2 - n^2)}{(n_c^2 + 2n^2)} \right] = 0 \quad (2.3)$$

where f_v , f_c , n_v , n_c and n represent fraction of voids, fraction of material, refractive index of vacuum, refractive index of bulk material and effective refractive index (n_{eff}) respectively. Thus, the presence of pores gives multiple advantages and can be used as an ideal photon extractor from high refractive index materials.

Most of the nanoporous films are formed by chemical etching¹³⁰ or ion bombardment methods,¹³¹ whose performance is limited by contamination, undesired interface and defect states, and degradation in crystallinity and composition. Kucheyev *et al.* observed the amorphization of GaN while irradiating by heavy ion (Au)¹³². Further, Jagadish *et al.*¹³³ demonstrated a strong surface disorderness in the film. Such disorderness of films degrades the film quality and device performance. Adding to that, such process involve multiple steps and require an additional experimental setup. GaN nanoporous films, grown epitaxially by varying growth parameteres, can overcome these or afore mentioned disadvantages. Recently, few groups^{134–136} including ours^{137,138} have demonstrated the formation of porous GaN in the form of nanowall network geometry by kinetically controlled growth, using molecular beam epitaxy (MBE) or chemical vapour deposition (CVD). However, in previous studies, the role of pore dimension on optical properties have not been discussed and the role of growth conditions on pore dimensions is not well understood. Although various groups have attempted to study the growth mechanism^{135,139}, appropriate mechanism which can explain the growth of nanowalls is not available yet. We have adressed both these issues in **chapter 4** of the thesis.

2.2 Unintentional n-type doping and high electrical conductivity in GaN

The residual carrier concentration ($n=10^{17}-10^{19} \text{ cm}^{-3}$) of GaN has been a major obstacle for the fabrication of efficient devices, especially in the fabrication of p-doped GaN. Since the optimization of GaN-based electronic and optoelectronic devices require control over the doping concentration, it is very much essential to understand it's origin. In the early days the composition of unintentionally doped films could not be studied rigorously due to limited capabilities of spectroscopic tools and hence, in the absence of suitable evidence for impurity species, the n-type conductivity was tentatively attributed to nitrogen vacancies¹⁴⁰. But by the early 1980s it was realized that significant impurity concentrations can be present in HVPE-grown GaN crystals, which led various researchers to consider the possibility that impurities may be the main source of the high n-type electrical conductivity^{141,142}. However, study conducted by Tingberg

et al. showed that, concentration of O and Si were contrary to the trend of the carrier concentration¹⁴³, which were believed to be the main culprit. Various techniques such as conductive atomic force microscopy¹⁴⁴, electro-chemical capacitance-voltage profiling, cathodoluminescence¹⁴⁵, temperature-dependent Hall effect measurements^{146,147}, and depth-profiling Hall effect measurements¹⁴⁸ were used to understand the origin of n-type conductivity in unintentionally doped GaN. Results of these measurements suggested that the oxygen concentration near GaN/sapphire substrate interface was high and hence high electrical conductivity was originating from near-interface region. The compositional and electrical measurements appeared to present a unified picture of unintentional doping in GaN/sapphire. Moreover, oxygen diffusion from the sapphire into the near interface region, resulted in a high local concentration of donors, leading to unintentional high electrical conductivity. In all these studies the source of oxygen was attributed to sapphire substrate. However, high dissociation energy¹⁴⁹ of Al-O bond in sapphire is counterintuitive to such arguments. Further study carried out by Speck *et al.*¹⁵⁰ showed that by increasing III/V ratio the carrier concentration was increased, which suggested intrinsic defects could also play a significant role in unintentional doping of GaN.

Theoretical studies of the various possible donors have also helped in understanding the relative roles of native point defects and impurities. The use of *first-principles* based calculations to estimate the formation energy of point defects in wide band gap semiconductors has been comprehensively reviewed by Van De Walle *et al.*¹⁵¹. According to their studies, nitrogen vacancies do behave as shallow donors in GaN. However, under n-type conditions their energy of formation is too high for them to form spontaneously during the epitaxial growth and hence, can not be the main source of unintentional doping in as grown GaN. The impurities which are most likely to be unintentionally incorporated during GaN growth are carbon and oxygen. Carbon is an amphoteric dopant in GaN, behaving as a donor when incorporated on a gallium site (C_{Ga}), and as an acceptor when incorporated on a nitrogen site (C_N). *First-principles* based calculations suggest that, the formation energy for C_{Ga} is much higher than that of C_N , so carbon is more likely to lead to unintentional p-type doping than the observed high levels of n-type conductivity. Oxygen on the other hand, when substituted into nitrogen site (O_N) acts as a shallow donor and has a relatively low formation energy, making it a likely reason for the observed

unintended n-type conductivity. However, at early stage the calculations have been carried out by semilocal approach (LDA/ GGA) which happens to under or overestimate the band gap and lattice parameters and hence leads to inaccuracy in the defect formation energy. Recently, calculations carried out by Yan *et al.*¹⁵², Buckeridge *et al.*¹⁵³ and Miceli *et al.*¹⁵⁴ suggest that the formation energy of the N-vacancy is indeed low. Further, not only the estimation for defect formation energy is crucial to draw a definitive conclusion, but also stabilization of the defect configuration(s) is important. It has been observed that Ga-vacancy is most stable at -3e charge state while N-vacancy are stable at 3+ and 1+ charge states. In addition one of the major issues which may mislead while calculating the formation energy is the interaction between image charge, since charge-charge interaction is long ranged. Typically, the common method is to use the one proposed by Makov and Payne¹⁵⁵. However, the approach of Makov and Payne failed in the limit of a completely delocalized defect charge, where the interaction between image charges is completely canceled because of the compensation due to the background charge. The method proposed by Freysoldt, Neugebauer, and Van de Walle¹⁵⁶ (FNV) is more suitable for the case of charged defects within a dielectric medium. The FNV scheme provides a rather general framework for calculating energy corrections for defects in supercells. The scheme applies to supercells and defect charge distributions of any shape.

Unintentional n-type doping and high conductivity is also observed in GaN grown with Molecular Beam Epitaxy (MBE)¹⁵⁷. As MBE uses ultra pure metal and gases as the sources, and the films are grown in Ultra High Vacuum (UHV) conditions, the cause of auto-doping in this case may be attributed to intrinsic point defects instead of carbon and oxygen impurities. Bhasker *et al.*^{157,158} has reported the high electrical conductivity in GaN nanowall network (NWN) grown on sapphire substrate and the surface electronic structure is proposed to be the origin of high conductivity of the material. Since the thin film material has very high surface to volume ratio, the defect concentrations on the surface is expected to be higher than the bulk, whose quantitative analysis need to be performed. Further, the effect of such defect on the electronic structure is not well understood, which will be discussed in **chapter 5** of the thesis.

2.3 Issues with p-doping in GaN

Early attempts for the fabrication of p-type GaN was made by Amano *et al.*¹⁴ by doping with zinc (Zn). However, despite external LEEBI treatment p-type conductivity in GaN was not observed. In late 1980s, Amano *et al.*^{15,159} further demonstrated the synthesis of p-GaN by doping with Mg and fabricated GaN based UV LEDs. However, to obtain p-type GaN, LEEBI treatment was compulsory till that time. In 1992, Nakamura *et al.*¹⁶ claimed that p-type GaN could be obtained by simple thermal annealing of as grown sample. Today, almost all LED manufacturing companies use the thermal annealing technique. The mechanism or activation of p-type conduction, which involves the desorption of hydrogen near Mg acceptors in MOCVD or MOVPE growth techniques, was first identified by Vechten *et al.*¹⁶⁰ and was further confirmed experimentally by Nakamura *et al.*¹⁶.

P-type doping in GaN still remains a critical issue for GaN-based electronic and optoelectronic devices, partly due to high n-type background doping of intrinsic GaN, origin of which have been discussed in the previous section. Adding to that, the activation energy of p-dopants (e.g. Mg, Be) is very high. Zhang *et al.* reported that the ionization energy of Mg in GaN is (≈ 200 meV)¹⁶¹. Although the estimated ionization energy of Be is smaller (≈ 135 - 170 meV)^{162,163} compared to Mg, Be always prefers to occupy interstitial sites and/or form the defect complex $\text{Be}_{\text{Ga}}\text{V}_{\text{N}}$, which acts as donors. Hence Mg is preferential over Be, but Mg doping is hindered by H-passivation. Castiglia *et al.*¹⁶⁴ studied this issue and showed that hydrogen incorporates proportionally with Mg and are likely to form Mg-H complex, but saturates at a Mg doping threshold of about 3×10^{19} atoms cm^{-3} . Higher Mg doping densities cannot be achieved due to this effect. In addition, postgrowth annealing treatments are not able to remove entirely hydrogen atoms¹⁶⁴. As a consequence, part of the Mg_{Ga} acceptors remains electrically inactive. Molecular beam epitaxy (MBE) has been proposed to be an alternative growth technique to overcome these doping limitations.

Because of very high activation energy of Mg in GaN, only about 1% of incorporated Mg gets ionized and contribute to the hole concentration. Thus, to get sufficient p-type conductivity with high hole concentration, a very large concentration of Mg incorporation in the host is required¹⁶⁵. Typical Mg dopant concentrations of $10^{17} - 10^{19} \text{cm}^{-3}$ have been

incorporated in planar GaN films^{166,167}. However, increased Mg concentration in thin films may not necessarily give higher hole concentration due to *self-compensation* effect, whose microscopic (or atomistic) origin is still controversial. Many reports^{164,168–171} suggest that the hole concentration starts to dropoff as soon as Mg concentration reach 10^{19} atoms / cm^3 . The decrease in the hole concentration above Mg incorporation density of 10^{19}cm^{-3} could arise from the deterioration of the crystal quality of the thin films. It is expected that, above the solubility limit, the excess of Mg would precipitate to form clusters of different phases, causing the degradation of the crystallinity of thin films. Such deterioration in the crystalline quality of samples may affect the carrier transport properties. However, the experimental measurements carried out by Kaufmann *et al.*¹⁷¹ suggest that hole mobility in GaN:Mg does not undergo any dramatic change over the doping range of $3 \times 10^{18} - 7 \times 10^{19} \text{ cm}^{-3}$. The experimental evidence mentioned above suggests that, neither the presence of hydrogen nor the deterioration of crystallinity can cause the dropoff in the hole concentration. Hence, the compensation mechanism based on either intrinsic or Mg-related point defects is generally invoked to explain the dropoff of hole concentration. In early studies, the key role in the self-compensation process has generally been assigned to the nitrogen vacancy (V_N)^{172,173}. Later, the $\text{Mg}_{\text{Ga}}V_N$ defect complex, a deep donor defect in GaN:Mg, is assigned for the self compensation effect^{174,175}. The existence of $\text{Mg}_{\text{Ga}} - V_N$ defect complex was further verified through positron annihilation spectroscopy. However, this defect complex turned out to occur only in moderate concentrations ($2 \times 10^{17} \text{ atoms cm}^{-3}$) and are unstable against annealing above $500 \text{ }^\circ\text{C}$ ^{174,175}. Moreover, Miceli *et al.* suggested that, Mg at interstitial site can be the primary region for self-compensation in heavily Mg doped GaN¹⁷⁶, which is well supported by the observation of Wahl *et al.*¹⁷⁷. However, our study suggests a new kind of defect complex possibly responsible for self-compensation effect, which will be discussed in the coming chapters.

Coming to the optical properties of GaN:Mg; commonly observed luminescence peaks are at $\approx 3.27 \text{ eV}$ due to donor acceptor pair (DAP) transition for moderately Mg incorporated (Mg concentrations less than $10^{19} \text{ atoms cm}^{-3}$) samples and a broad $\approx 2.7\text{-}2.9 \text{ eV}$ blue luminescence¹⁷⁸ for heavily Mg incorporated samples (Mg concentration higher than $10^{19} \text{ atoms cm}^{-3}$). Further, the BL can be greatly enhanced by thermal annealing

at temperatures 600-800 °C. Kaufmann *et al.*¹⁷⁹ has attributed this peak to transition from deep donor to shallow acceptor state, where deep donor state originates due to the formation of vacancy complex $\text{Mg}_{\text{Ga}}\text{V}_{\text{N}}$. However, Akasaki *et al.*¹⁸⁰ has assigned the transition to be occurring from the hydrogen-related deep donor to shallow Mg acceptor states. Such attribution is well supported by the fact of, a very large shift of the BL band with increasing excitation intensity¹⁸¹. However, it was observed that the BL band is greatly enhanced by thermal annealing, whereas the concentration of the $\text{Mg}_{\text{Ga}}\text{V}_{\text{N}}$ complexes significantly decreases after annealing at $T > 500$ °C^{174,175}. An alternative model claims that the BL band is caused by transitions of electrons from the conduction band to the Mg_{Ga} deep-acceptor (0.7 eV above VBM)¹⁸². Such a claim can not explain the large shift of the BL band maximum and the absence of BL in lightly doped samples. Thus, identification of the luminescence peak from atomistic prospective is still elusive.

As the GaN in nanowall network geometry shows excellent luminescence properties and its morphology plays a crucial role for the same, it is essential to know whether GaN NWN retains its morphology or changes it with dopant concentration. Further, there is no report regarding the study of doping in GaN NWN. Adding to that, experiments based on X-ray photoelectron spectroscopy (XPS) and secondary ion mass spectroscopy (SIMS) measurements of GaN flat films show that concentration of Mg incorporated on the surface is higher than in the bulk¹⁸³⁻¹⁸⁶, suggesting that GaN with higher surface area may enable higher incorporation of Mg. Since NWN with its porous structure has a very high surface to volume ratio, it can be a potential candidate for achieving higher incorporation of Mg by increasing the solubility limit of Mg in GaN. Effect and properties of Mg doping in GaN NWN is discussed in **chapter 6** in the thesis.

2.4 Growth of GaN on silicon substrate and p-doping of GaN nanostructure

The growth of GaN on silicon substrates attracts a lot of attention due to the potential integration of microelectronics and optoelectronics. Adding to that, GaN-on-silicon is a low-cost alternative to the growth on sapphire or SiC substrate. Since, Si based technology is mature, integrating III-Nitride to it gives extra advantages for various ap-

plications. However, there are major challenges that need to be addressed. One such challenge is the large mismatch of the in-plane thermal expansion coefficient between Si and GaN (see Table 1.2 of Chapter 1) which leads to cracks in the film while cooling down the sample after the growth¹⁸⁷. Further, the large difference in the lattice parameters of GaN (0.31892 nm) and Si (0.38403 nm, in (111) direction) yields a lattice mismatch (19%)¹⁸⁸ resulting in high initial dislocation density ($\approx 10^{11} \text{ cm}^{-2}$). Since Si is a non-polar substrate, inversion domain defects (anti-phase boundaries) will be produced due to the growth of polar GaN layer on it¹⁸⁹, which may lead to the formation of non-epitaxial nucleation layer and anti-phase domains, unless the surface of Si is carefully prepared. Surface nitridation of Si has been explored intensively^{190–193} to overcome such issues. The tendency to form a few nano-meter thick amorphous silicon nitride layer on Si surface, when exposed to reactive nitrogen sources, introduces a phase mixture. The substrate nitridation consequently degrades the substrate surface. III-V compound semiconductor nanostructures, including quantum dots, nanowires and nanorods are epitaxially grown on Si and have been extensively investigated widely throughout the literature^{194–197} due to the fact that the effective lateral stress relaxation of such nanoscale heterostructures can originate due to the presence of facet edges and sidewalls which can also minimize or eliminate the formation of dislocations and consequently leads to the fabrication of nearly defect-free III-V semiconductor nanostructures on Si^{198,199}. Additionally, semiconductor lasers, that use quantum dots or nanowires as gain regions, are expected to exhibit superior performance, due to the strong carrier confinement and the resulting near-discrete density of states.

The work on GaN and InGaN one-dimensional (1D) nano-materials was initiated in the late 1990s^{200–202}. In 2004, high-brightness and high-efficiency LEDs based on InGaN/GaN multiple quantum well (MQW) nanorod arrays (NRAs) grown by MO-HVPE were demonstrated by Kim *et al.*²⁰³. Compared to conventional planar LED heterostructures, the use of 1D nanorods offers several advantages such as reduced dislocation densities^{204,205}, lower polarization fields²⁰⁶, and enhanced light output efficiency²⁰⁷ partly due to the large surface-to-volume ratios. Adding to that, this also gives hope to reduce the cost of the LED fabrication with large-area Si substrates. Multi-color emission can also be obtained by varying nanorod diameters, composition and morphologies or by applying

external electrical field^{208–210}. In addition, Guo *et al.* demonstrated that, the defect-free nanowires significantly reduce the Auger recombination and droop effect²¹¹.

GaN-based nanorod LEDs can be fabricated by either top-down or bottom-up approaches. The fabrication of GaN-based^{206,212} nanorod LED using a top-down approaches involves dry etching which has its own detrimental consequences. Typically top-down etching causes sidewall damage and creates a large amount of defects resulting in large leakage currents that limit the light output power. Therefore, a passivation process should commonly be considered. Chiu *et al.*²¹² reported the fabrication of InGaN/GaN nanorod LEDs using inductively coupled plasma reactive-ion etching (ICP/RIE) via self-assembled Ni nanomasks followed by a photo-enhanced chemical (PEC) wet oxidation process. The strain relaxation effect was confirmed by electroluminescence (EL) spectra, where higher efficiency and a 10.5 nm blue shifted peak with respect to the as-grown LED sample were recorded²¹². Huang *et al.*²⁰⁶ fabricated the InGaN/GaN MQW light-emitting diodes with a self-organized nanorod structure with the help of lithography of surface patterned silica spheres followed by dry etching. Further, both the EL and Raman spectroscopy showed a strain relaxation of the nanostructures.

Bottom-up fabrication is the other alternative method for fabrication of nanorod based LEDs. Many kinds of growth methods are used for the growth of nitride nanorod arrays, including hydride vapor phase epitaxy (HVPE), molecular beam epitaxy (MBE)²⁰³ and MOCVD. Kim *et al.*²⁰³ reported, MO-HVPE grown high brightness and high-efficiency LEDs with dislocation-free InGaN/GaN MQW nanorod arrays. Due to the absence of dislocations and the large surface areas provided by the sidewalls of nanorods, both internal and extraction efficiencies were significantly enhanced. At 20 mA current, the MQW nanorod array LEDs emit about 4.3 times more light than conventional LEDs, even though overall active volume of the MQW nanorod array LEDs is much smaller than that of conventional LEDs. However this approach has few disadvantages, namely, the metal catalyst will inevitably incorporate into the nanowire which may be prohibitive for the device applications. In order to solve this problem, vertically aligned and faceted GaN nanorods with controlled diameter were grown without catalyst by Deb *et al.*²¹³ and Hersee *et al.*²¹⁴.

P-doping by Mg incorporation was found to strongly influence the morphology of

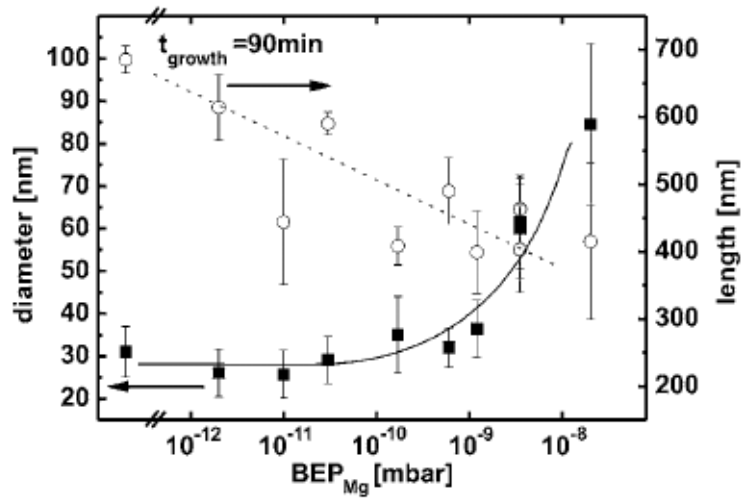


Figure 2.3: shows changes in GaN nanorod's diameter and length as a function of Mg dopant concentration²¹⁵. [Reprinted from J. Appl. Phys. 104, 034309 (2008), with the permission of AIP Publishing]

nanorods. A small amount of Mg increases the tendency of the rods to coalesce. However, it was claimed that the diameter of the rods remained constant and does not broaden or taper²¹⁶. Furtmayr *et al.*²¹⁵ studied the Mg doping effect on GaN nanorod by MBE growth, and showed that the increase of Mg flux caused an increase in the diameter and decrease of the height of the nanorods (see Fig. 2.3). They concluded that increase in GaN nanorod diameter is due to the enhancement of radial growth rather than larger nucleation site. Mg doping not only affects the rod morphology, but also the crystallinity of the nanostructure. In Arbiol *et al.*'s TEM studies on the Mg-doped GaN nanorods grown by MBE²¹⁷, triple-twin domains were observed and the density of such structure was found to increase with increasing Mg concentration. The local electronic properties of GaN could also be modified due to formation of such domains, which has also been identified by PL measurements²¹⁷. Further work of Zhang *et al.*²¹⁸ and Andrews *et al.*²¹⁹ suggests an increasing in the diameter of the nanowire and nanorod, respectively, with increase in Mg flux. However, Bae *et al.*²²⁰ reported that, higher Mg flow rates affected the equilibrium shapes of the top regions of the nanorods and caused height variations instead of promoting vertical growth. No clear understanding has been reported yet on the origin of such increase in radial growth of nanorod in MBE grown samples, which will be addressed in the **chapter 7** of the thesis.

Chapter 3

Experimental and Simulation Techniques

This chapter is dedicated to provide brief discussions on the different experimental techniques used to grow nanostructured thin films of doped and undoped GaN and characterize them. Further, this chapter also introduces different simulation techniques used in the study that enable us to draw appropriate conclusions at an atomistic level of understanding.

3.1 Crystal Growth: Molecular Beam Epitaxy

Molecular Beam Epitaxy (MBE) is an advanced ultra-high-vacuum technique (base pressure 10^{-13} Torr) to grow compound semiconductor materials with precise control of thickness, composition and morphology. MBE was invented by J. R. Arthur and Alfred Y. Cho in 1960s at Bell Telephone Laboratories. The word epitaxy refers to “an ordered manner”, *i.e.* orientation of the overgrown thin film that is structurally commensurate with the underlying crystalline substrate. The major difference between epitaxy and the other methods of crystal growth is the substrate, which is a single crystal, usually in the form of a thin, smooth, finally polished wafer. Various kinds of epitaxy exist, which differentiate from each other based upon the methods of generation of active species: the source could be a molecular beam, gas, liquid or even an amorphous solid layer. Because of the precise control of growth parameters, MBE has been successfully used to produce

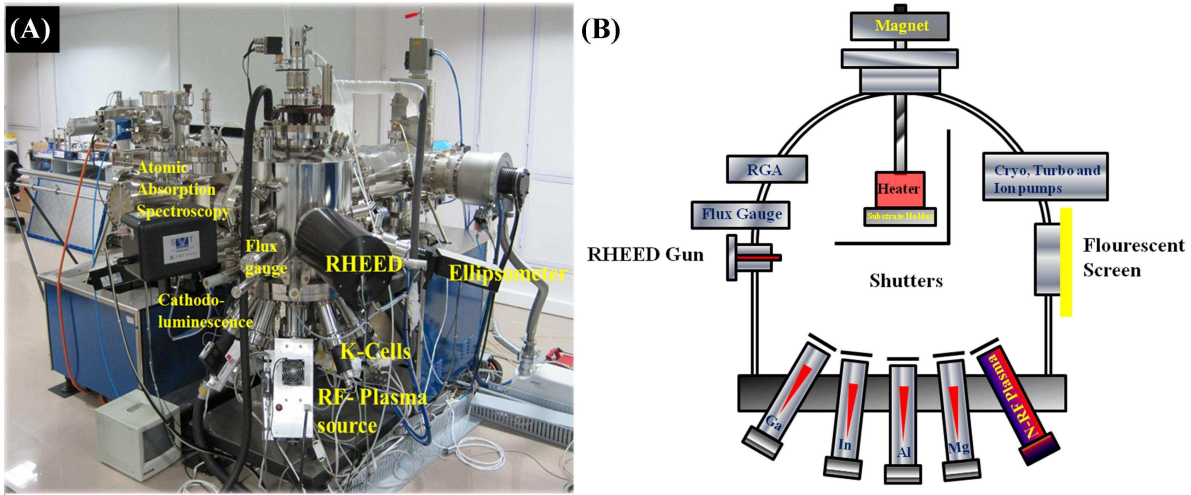


Figure 3.1: (A) shows photograph of MBE system used for growth of thin films. Figure (B) represent the schematic diagram of the growth chamber.

a large range of unique structures, including quantum well devices, superlattices, etc., as well as nanoscale devices.

In the process of MBE, beams of atoms or molecules in an ultra-high vacuum environment are incident upon the surface of the substrate which is at moderately elevated temperatures. This temperature provides sufficient thermal energy to the arriving atoms such that they migrate over the surface to reach suitable potential energy sites. In the UHV environment, the beam of atoms and molecules travel in nearly collision-free paths until arriving either at the substrate or else at the walls of the growth chamber. When a shutter is placed in the path of beam, that beam is effectively turned off almost instantly. These features make it possible to grow the films very slowly without any contamination and most importantly, to change the composition of the arriving atom stream very abruptly. In fact, the composition of the flux can be changed in times much shorter than that is needed to grow a single atom layer of the film. Very simplistically, MBE growth might be similar to spray painting the substrate crystal with layers of atoms, changing the composition or impurity level in each layer until a desired structure is obtained. In this sense MBE is nearly the ideal approach for material preparation since the composition can be tailored, layer-by-layer.

Figure 3.1 shows the nitride plasma assisted MBE (PA-MBE) (SVTA, USA) system used for the growth of thin films in this thesis work. To generate high vacuum ($\approx 10^{-11}$

Torr) in this system, various pumps such as diaphragm, turbo, cryo and ion pumps are used. During the growth, turbo and cryo pumps are used. The main chamber or the growth chamber's wall has a two layered structure with a gap in between through which liquid N_2 is supplied to cool down the system, which also acts as cryo pump to contain degassing. The growth manipulator, which can heat the substrate up to 1200 °C is cooled by chilled water (≈ 16 °C) supply. For a uniform coating all over the substrate, the sample holder is continuously rotated by the magnet assembly attached to a stepper-motor. The rotation speed (0-60 rpm) and steps size can be controlled by an electric switch panel. The transfer of the samples is a three step process. At the first step the samples are kept in a load lock chamber, which is equipped with a diaphragm and turbo pump. Once the pressure is reached to a certain value (typically 10^{-5} - 10^{-6} Torr), the samples are transferred to the preparation chamber through a gate valve. The preparation chamber is equipped with an ion pump and a sample heating/degassing facility up to 700 °C. Once the degassing is finished, the sample is finally transferred to the main chamber for the synthesis of desired crystal.

Active nitrogen radicals are supplied by a radio frequency inductively coupled plasma source. Group-III elements along with Mg dopants are supplied by effusion cells. Windows of the effusion cells are equipped with automated shutters, by controlling which a precise growth thickness at the substrate can be obtained. Evolution of growth can be monitored by *in-situ* reflection high energy electron diffraction (RHEED) set up. Substrates upto a 3" diameter can be mounted on the growth stage, with a growth uniformity of $< 0.1\%$ over the diameter of 2.8 inch. Flux rates are frequently calibrated by using Accu Flux atomic absorption system and a flux gauge, which are attached to the growth chamber. The operation of the MBE system can be carried out through the manual panel control as well as by an automated computer system.

3.1.1 Effusion Cells

Effusion cell or Knudsen cell is an effusion evaporator source for relatively low partial pressure elementary sources (such as Ga, Al, Mg). Effusion cells are preferable in MBE growth technique because of its excellent controllability of the temperature of the evaporating material and consequently its growth rate. The Knudsen effusion cell was first

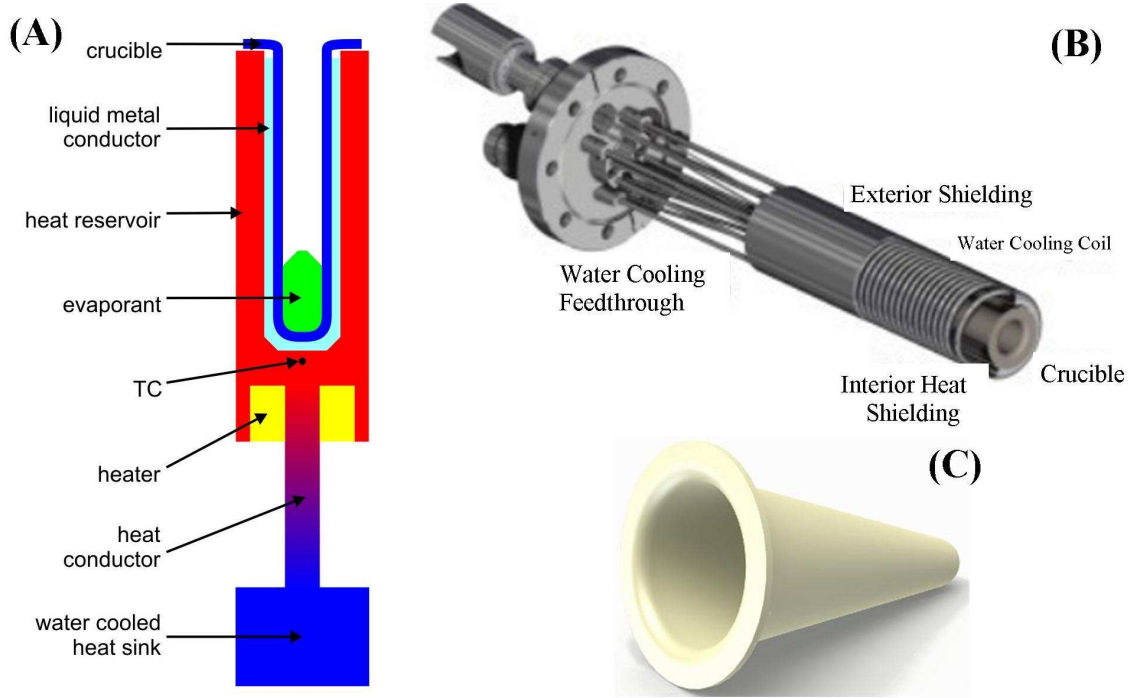


Figure 3.2: (A) schematic diagram of the Effusion cell. Figure (B) and (C) are the image of the Effusion cell and the crucible, respectively. (*source: www.mbe-komponenten.de*)

developed by Martin Knudsen. A typical Knudsen cell contains a crucible (made of pyrolytic boron nitride, quartz, tungsten or graphite), heating filaments (made of tantalum), water cooling system, heat shields, and a shutter (see Fig.3.2).

Working principle of Effusion Cell

The mass evaporation rate per unit area of a source is given by the Langmuir-Knudsen expressed as relation²²¹

$$\Gamma_e = N_A \alpha_e \frac{P^* - P}{\sqrt{2\pi M \bar{R} T}} \quad (3.1)$$

where N_A is the Avogadro's number, \bar{R} is the specific gas constant, α_e is the sticking co-efficient. M and P^* and T are the molecular mass, vapour pressure and absolute temperature at which evaporants are being evaporated, respectively. At maximum evaporation rate in vacuum where $P = 0$ and $\alpha_e = 1$, then eqn 3.1 is reduced to

$$\Gamma_e = 5.834 \times 10^{-2} \sqrt{\frac{M}{T}} P^* \quad (3.2)$$

At a vacuum of 10^{-2} Torr, Γ_e is of the order of 10^{-4} g cm $^{-2}$ s $^{-1}$. For a K-cell with very small aperture with area A_e in comparison to r , where r refers to distance from source to substrate, through which the evaporated atom spread into the growth chamber, then the source behaves like a point source, and thus mass deposition rate per unit area of the substrate R is given by

$$R = \frac{\Gamma_e A_e}{\pi r^2} \cos\theta \cos\phi = 1.856 \times 10^{-2} A_e \sqrt{\frac{M}{T}} P^* \frac{\cos\theta \cos\phi}{r^2} \quad (3.3)$$

where r is the distance between source and substrate. For a substrate of diameter D

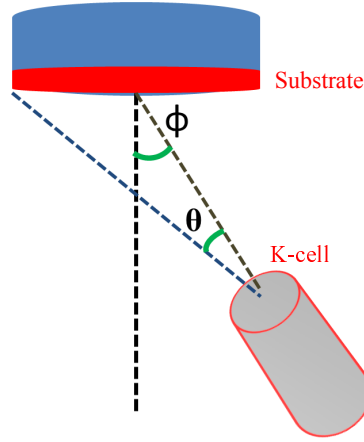


Figure 3.3: Representation of θ and ϕ

placed above the source, the mass deposition rate on the center of the substrate R_1 and on edge R_2 are proportional to :

$$R_1 \propto \frac{1}{r_1^2} \quad (3.4)$$

$$R_2 \propto \frac{1}{r_2^2} \cos^2\theta = \frac{r_1^2}{r_2^4} \quad (3.5)$$

Now we define the uniformity as

$$\sigma(\%) = \frac{R_1 - R_2}{R_1} (\%) \quad (3.6)$$

which implies

$$\sigma(\%) = 1 - \left[1 + \frac{D^2}{2r_1^2}\right] \approx \frac{D^2}{2r_1^2} \quad (3.7)$$

For example, a thickness uniformity of 1% on the surface with a diameter of 10 cm requires r_1 to be at least 70 cm. In practice double of this value is required. Such large

r values are needed for thickness uniformity of the deposited film and thus requires large chambers and pumps with high pumping speeds, which consequently make deposition rates low and wastage of large amount of the evaporants, therefore, the evaporant is collimated by using a tubular K-cell. The film deposition rate also depends on the distance between the source and the substrate (r) and the emission angle.

3.1.2 Nitrogen Plasma Source

For the synthesis of compound semiconductor such as GaN, we need both the Ga and N sources individually. In the case of MBE growth of GaN, we obtain Ga from effusion cell and active N from the plasma generated by a radio-frequency (RF) source. A plasma is an ionized gas containing freely and randomly moving electrons and ions. It is usually (nearly) electrically neutral, *i.e.*, the negatively charged particle density equals to the positively charged particle density within a fraction of percent²²². The RF range is of particular interest as, at the lower end all except the most massive ions in gas discharge plasmas are able to follow the instantaneous RF fields and at the higher end, all ions are inertially constrained, responding only to the time-averaged fields. Throughout the RF range, electrons are able to respond instantaneously to fields. Adding to that, RF-plasma source give rise to higher plasma density and a higher efficiency than DC plasma sources²²³.

Generation of plasma

There are various methods to generate plasma, such as

- Direct current
- Capacitively coupled
- Inductively coupled
- Helicon plasma

The system used for this thesis work generated plasma by the inductively coupled method.

In the capacitively coupled plasma sources, electromagnetic fields are applied directly to the electrodes, whereas for inductively coupled plasma source, the electromagnetic field is induced by an inductive coil²²⁴. The inductively coupled plasma discharges can reach

high antenna currents, high electric conductivity, and high electron density at relatively low values of electric field and voltage²²⁴ compared to capacitively coupled plasma. The inductive coil in inductively coupled plasma source can be considered as a transformer, where the coil represents the primary windings and the plasma is the secondary winding. Therefore, the coil can effectively increase the current going into the plasma discharge. It is this effective coupling between the inductive coil and the plasma that allows the inductively coupled plasma to achieve as much as 10 times higher electron density compared to that of the capacitively coupled plasma²²⁴. Further, an inductively coupled plasma source is electrodeless and does not have any issues relating to contamination of the electrode. In an inductive source, RF current and voltage are usually applied to a planar or cylindrical coil outside the discharge. The RF power is coupled to the plasma through a dielectric window or wall. Due to the time varying current applied to the coil, it generates an inductive magnetic field and electric field inside the discharge. The electric and magnetic fields can only penetrate into the plasma within a distance from the surface of the discharge what is known as the skin layer and the thickness is known as the skin depth. The skin depth δ is the inverse of the spatial decay constant α within a plasma for an electromagnetic wave normally incident on the boundary of a uniform density plasma²²⁵.

$$\alpha = \frac{1}{\delta} = -\frac{\omega}{c} \text{Im}K_p^{0.5} \quad (3.8)$$

In equation 3.8 ω is the applied RF frequency, $c = \sqrt{\frac{1}{\mu_o \epsilon_o}}$ the speed of light, and K_p is the relative plasma dielectric constant, expressed as

$$K_p = 1 - \frac{\omega_{pe}^2}{\omega(\omega - j\nu_m)} \approx -\frac{\omega_{pe}^2}{\omega^2(1 - j\nu_{en}/\omega)} \quad (3.9)$$

where ν_{en} is the electron-neutral collision frequency. For the collisionless regime,²²⁶ where $\nu_{en} \ll \omega$, and substituting the expression for electron plasma frequency, the skin depth is reduced to

$$\delta = \sqrt{\frac{m}{e^2 \mu_o n_s}} \quad (3.10)$$

The skin depth thickness is therefore inversely proportional to the square root of the electron number density. For example, if the density is $10^{16}/m^3$, the skin depth thickness is 5 cm, but if the density is one order of magnitude higher at $10^{17}/m^3$, the skin depth thickness is 1.7 cm.

The collisionless assumption made in deriving equation 3.10 is valid only for the low pressure regime in this experiment. For higher pressures, where the condition $v_{\text{en}} \ll \omega$ no longer holds, the collisional skin depth thickness is:

$$\delta_c = \delta \sqrt{\frac{2v_{\text{en}}}{\omega}} = \sqrt{\frac{2}{\omega \mu_0 \sigma_{\text{dc}}}} \quad (3.11)$$

where σ is the electron conductivity, which is proportional to the electron number density. For 250 mtorr and 13.56 MHz, the collisional skin depth is greater than the value of the collisionless skin depth by a factor of 2-3. In both collisionless or collisional regimes, power from the electric field can only be transferred to the plasma electrons within this skin depth layer near the plasma source. The plasma density, therefore, is concentrated in this layer. The layer thickness can be controlled by the frequency, but at the same time, is affected by the electron number density. Higher electron number density reduces the skin depth thickness²²⁷.

Lastly, it is important to note that even if an inductive mode is excited, there is always some capacitive coupling²²⁵. At high plasma densities, the skin depth thickness is small, and inductive coupling dominates. But at lower densities, the skin depth thickness can be large (for example, 5-10 cm) and power deposition through capacitive coupling can be significant.

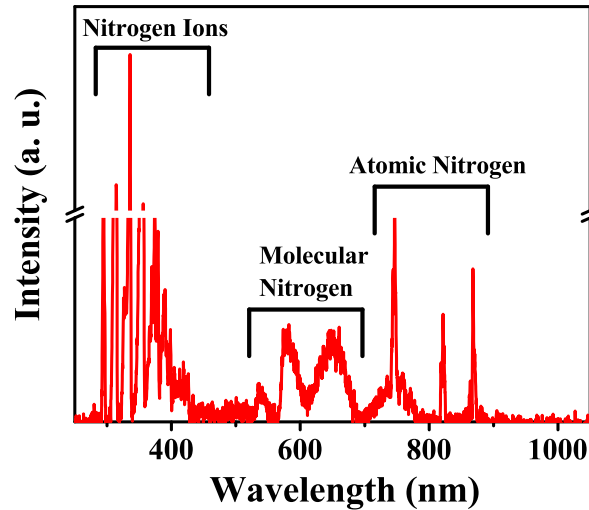


Figure 3.4: A typical spectra of nitrogen plasma used in the thesis work. The flow rate and forward plasma power was at 4.5 sccm and 375 W, respectively.

3.1.3 Residual Gas Analyser

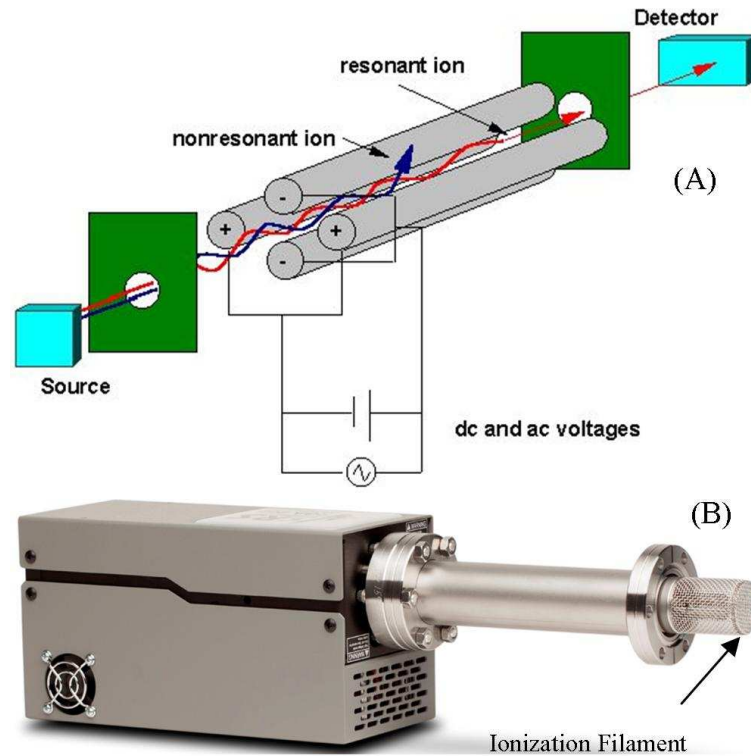


Figure 3.5: (A) shows schematic diagram of the RGA. (B) represents the image of the RGA.

A residual gas analyzer (RGA) is a small and rugged mass spectrometer, typically designed for process control and contamination monitoring in most of the vacuum systems. It uses the difference in mass-to-charge ratio (m/ze) of ionized atoms or molecules to single out them from each other. In our studies we have used a quadrupole mass spectrometer which consists a dual thoriated-iridium(ThO_2/Ir) filament as the source of electrons. An electron emitted from the beam knocks out an electron of the residual gas present in the chamber to create ions, that are directed into a quadrupole mass filter consisting of four parallel metal rods arranged as shown in Fig. 3.5(A). Two opposite rods experience an applied voltage of $V_{dc} + V\cos\omega t$ while other two rods experience an applied voltage of $-V_{dc} + V\cos\omega t$, where V_{dc} and $V\cos\omega t$ represents applied DC and AC voltage component. The trajectory of the ions moving between the four rods is influenced by applied voltage. Only ions of a certain mass-to-charge ratio will reach the detector for a given ratio of voltages; other ions have unstable trajectories and will collide with the rods. This permits

selection of an ion with a particular m/z or allows the mass spectrometer to scan for a range of m/z values by continuously varying the applied voltage. Our MBE system is equipped with Stanford Research System RGA, which can monitor gaseous species of upto 200 a.m.u.

3.2 Characterization Techniques

3.2.1 Reflection High Energy Electron Diffraction (RHEED)

Reflection high energy electron diffraction (RHEED) is a technique used to characterize the surface of crystalline materials. Its unique geometry gather information only from the surface of the samples; thus is a vital technique to study the evolution of the surface morphology during the epitaxial growth²²⁸. A RHEED system requires an electron source (gun) and a phosphor screen. The electron gun generates a beam of electrons which strike the sample at a very small angle relative to the sample surface. Incident electrons diffract from the surface of the sample, and a small fraction of the diffracted electrons interfere constructively at specific angles and form regular patterns on the detector. The electrons interfere according to the position of atoms on the sample surface, so the diffraction pattern at the detector is influenced by the sample surface.

Working principle of RHEED

In this technique, a beam of electron of energy nearly 10 keV is incident upon the surface of the materials with an extremely small angle of incidence (1-4°). Thus, the effective penetration depth is $\approx 0.5-1 \text{ nm}$ ²²⁸ and a very few layers of the surface contribute to RHEED pattern. The scattered electrons from the surface interfere constructively or destructively on the phosphor screen giving rise to specific diffraction pattern. The diffraction pattern can be further used to study the structural and morphological properties of the material surface. The Ewald sphere analysis is used to study the diffraction pattern. As the scattering of electron is occurring from just few atomic layer of the surface, unlike bulk which require a 3D analysis, a 2D analysis is sufficient (see Fig.3.6(A)) in RHEED. The Ewald's sphere is centered on the sample surface with a radius equal to the reciprocal of the wavelength of the incident electrons. The reciprocal lattice of the surface will be a

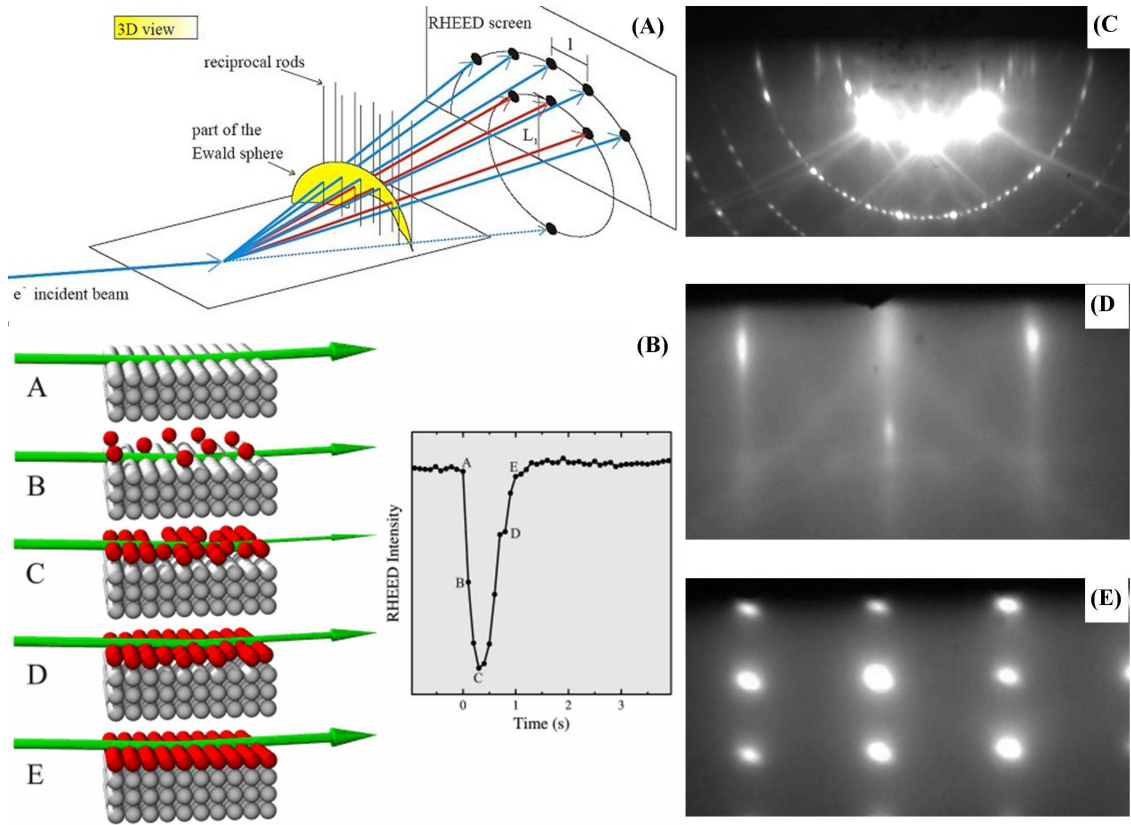


Figure 3.6: (A) shows schematic diagram of mechanism to form RHEED pattern. Figure (B) shows the RHEED oscillation with surface morphology evolution. Figure (C), (D) and (E) represent RHEED pattern of 7×7 reconstructed Si (111), clean surface of sapphire (0001) and 3D growth of GaN on Sapphire substrate (0001), respectively. (*source: <http://lippmaa.issp.u-tokyo.ac.jp/rheed/> and www.wmi.badw.de/methods/leed_rheed.htm*)

series of streaky lines (for example see Fig.3.6(D)) due to the absence of third direction in the diffraction condition,

Ewald Construction

Let \vec{k}_o be the incident wave vector of electron, which is given by

$$|\vec{k}_o| = \frac{2\pi}{\lambda} \quad (3.12)$$

where λ is the wavelength of incident electrons.

Diffraction conditions are satisfied where the rods of reciprocal lattice intersect the Ewald's sphere. Therefore, the magnitude of a vector \vec{k}_i from the origin of the Ewald's

sphere to the intersection of any reciprocal lattice rods is equal in magnitude to that of the incident beam

$$|\vec{k}_o| = |\vec{k}_i| \quad (3.13)$$

An arbitrary vector, \vec{G} , defines the reciprocal lattice vector between the ends of any two k vectors, such that

$$\vec{G} = \vec{k}_o - \vec{k}_i \quad (3.14)$$

It is obvious that, many of the reciprocal lattice rods meet the diffraction condition, however the RHEED system is designed in such a way that only the low orders of diffraction are projected on the detector. The RHEED pattern at the detector is a projection of the only \vec{k} vectors that are within the angular range that contains the detector. The size and position of the detector determines which of the diffracted electrons are in the angular range that reaches the detector, so the geometry of the RHEED pattern can be related back to the real geometry of the reciprocal lattice of the sample surface through the use of known trigonometric relations and the distance from the sample to detector.

The \vec{k} vectors are labeled such that they form the smallest angle with the sample surface and is called 0th order beam. The 0th order beam is also known as the “*specular beam*”. Each successive intersection of a rod and the sphere further from the sample surface is labeled as a higher order reflection. The center of the Ewald’s sphere is positioned in such a way that the specular beam forms the same angle with the substrate as the incident electron beam. The specular point has the highest intensity on a RHEED pattern and is labeled as the (00) point by convention. The other points on the RHEED pattern are indexed according to the reflection order they project. A streaky RHEED pattern indicate atomically smooth flat film (see Fig. 3.6(D)) where as spotty pattern indicate 3D nature of the film in nanoscale (see Fig. 3.6(E)), where some electrons are transmitted through the 3D rough surface and cause an interference pattern. The growth rate also can be determined from RHEED oscillation as each cycle of the oscillation represent one layer of growth (see Fig. 3.6(B)) .

The RHEED (STAIB instrument) system used in our work is connected to the main chamber of the MBE system. The energy of incident electrons are varied within the range of 0 -10 keV.

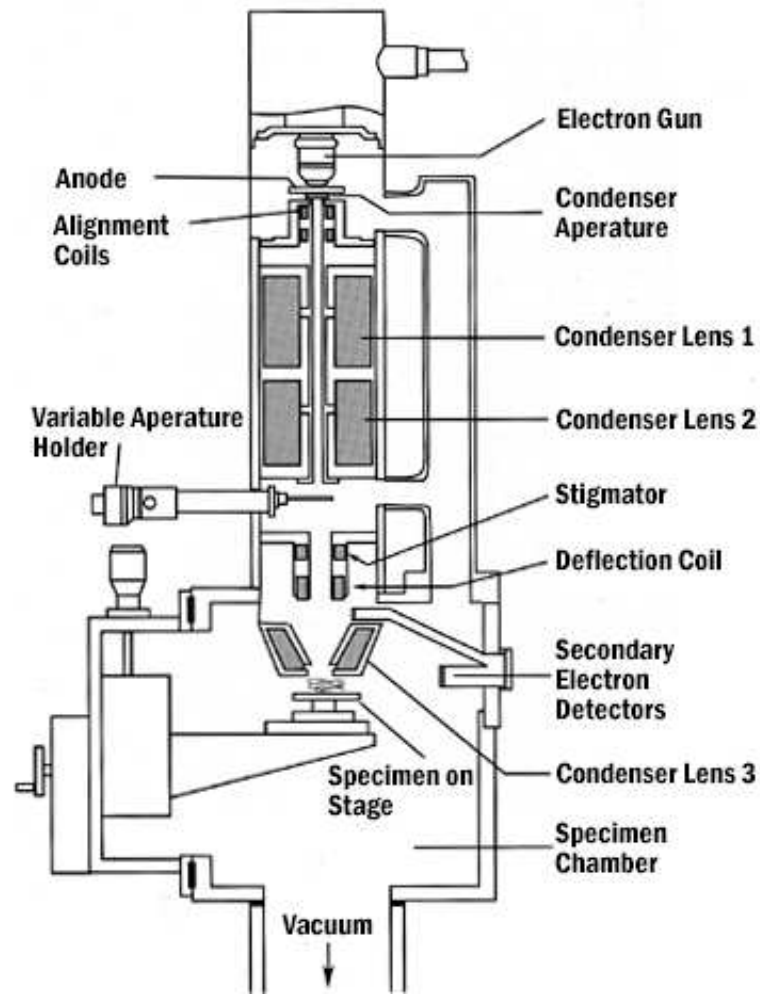


Figure 3.7: shows schematic of SEM.*

3.2.2 Field Emission Scanning Electron Microscopy (FESEM)

FESEM is a type of electron microscope used to visualize the topography of materials having resolution upto a few nanometers, by scanning the surface of the materials using a focused electron beam. The electron beam is generally scanned in a raster scan pattern, and the beam's position is combined with the detected signal of the secondary electrons generated by source electron and material interaction to produce a reconstructed image. A typical SEM system contains an electron source, condenser lenses for regulation of intensity and direction of electron beam on the specimen surface and a detector which detect the intensity, energy and the position of the secondary electrons (see Fig.3.7). Generally, the source electrons in the SEM are generated thermonically by heating a tungsten (W)

*<https://cmrf.research.uiowa.edu/scanning-electron-microscopy>

filament up to 2800 °C. Use of tungsten is preferable due to highest melting point and lowest vapour pressure among known metals²²⁹. Lanthanum hexaboride (LaB₆) is also another choice for the filament. Unlike the traditional SEM, the source of electron in FESEM is generated not by heating but by applying voltage across the electrodes of the emitters. In this case, the cathode is referred as “cold-cathode”. The magnitude of the applied voltage between cathode and anode is of the order of 0.5 to 30 kV. The image quality in FESEM is remarkably better than the one obtained by conventional SEM since the electron beam produced by the field emission (FE) source is about 1000 times smaller than in a standard microscope. In contrast to a conventional tungsten filament, a FE tip lasts theoretically for a lifetime, provided that the required vacuum level is maintained.

At any given moment, the specimen is bombarded with electrons over a very small area. Several things may happen to these electrons. They may be elastically reflected from the specimen, with no loss of energy. They may be absorbed by the specimen and give rise to secondary electrons of very low energy, along with X-rays. They may be absorbed and give rise to the emission of photons (an effect known as cathodoluminescence). All these effects can be used to produce an image of the material, showing different properties. Commonly, the image formation is performed using the information obtained from low-energy secondary electrons.

In this thesis work, all FESEM images are obtained using quanta-3D, FEI, Netherlands FESEM system, where a CL and FIB accessory systems are attached.

3.2.3 High Resolution X-ray Diffraction (HRXRD)

X-ray scattering techniques are non-destructive analytical techniques which reveal information about the crystal structure, chemical composition, and physical properties of materials and thin films. These techniques are based on observing the scattered intensity of an X-ray beam hitting a sample as a function of incident and scattered angle. X-ray diffraction (XRD) is a sub-set of X-ray scattering, where the scattering is elastic and the scattering object is crystalline²³⁰.

XRD involves probing of crystal with X-ray having wavelength (λ) of the order of its lattice spacing. The X-rays are scattered by the electron cloud surrounding the ions in the crystal, resulting in a constructive interference pattern between the scattered rays

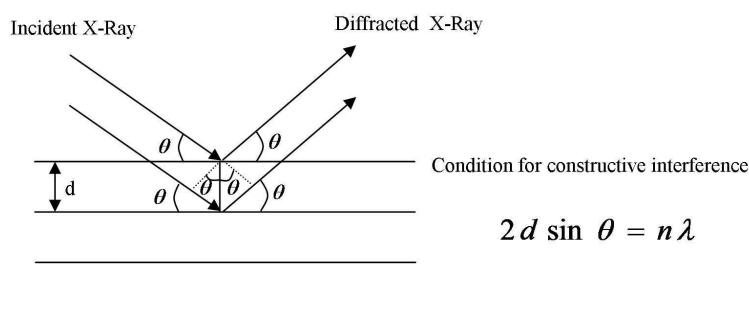


Figure 3.8: Schematic of mechanism of X-ray diffraction from a periodic crystal

with a path difference that is integral multiple of λ . The path difference is equivalent to $2d \sin \theta$, where d and θ are the interplanar spacing and angle of incidence, respectively as shown in Fig.3.8.

HR-XRD Setup

The XRD measurements of the samples studied in this thesis were carried out using Bruker D8 diffractometer, which consist of

- A X-ray tube source with a copper cathode, which generates the incident CuK_α X-ray beam ($\lambda = 1.540595(2) \text{ \AA}$)
- Four bounce Ge 220 monochromator to obtain a highly monochromatic parallel incident beam with a X-ray wavelength corresponding to CuK_α with a maximal resolution of 10^{-5} \AA
- A goniometer, where the sample is mounted, enables X, Y, Z translation as well as Eulerian tilt- χ and ω , azimuthal $-\phi$ rotations. Here χ is defined as the angle between sample surface and the plane of the interest (in the $0-90^\circ$ range), ϕ corresponds to azimuthal rotation around the surface normal of the sample (in the range $0-360^\circ$). The angle of incidence ω is the angle between X-ray source and normal to the surface, where as 2θ is the angle between diffracted X-ray source and the detector
- A scintillation point detector (Pathfinder): The scattered beam path can be directed through the three different optics: the automatic receiving slit or the Ge (220) \times 3 analyser.

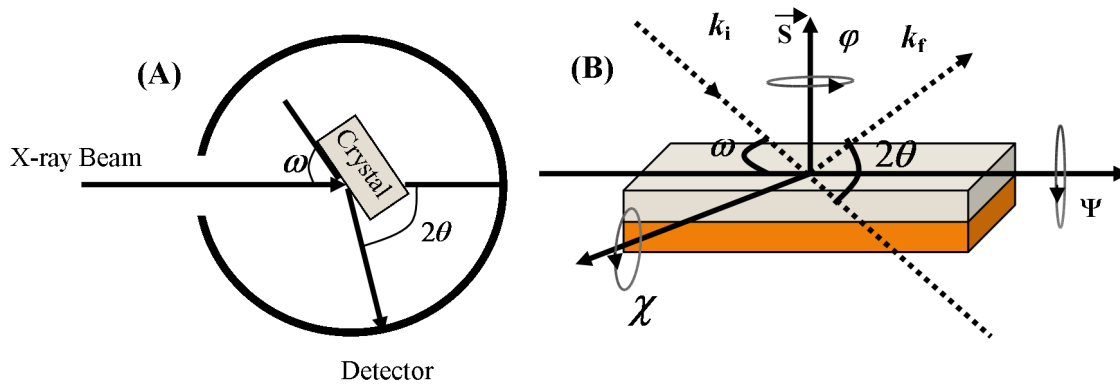


Figure 3.9: (A) shows schematic of HR-XRD diffractometer. (B) illustrates all the Euler angles, which are possible to access in a HRXRD set up.

Characterization of real crystals by HRXRD

By means of HRXRD, deviations from the ideal crystal structure are investigated. For this purpose, the position and the width of X-ray reflexes are measured by registering the scattered X-ray intensity while rotating the sample around an Euler angle or changing the detector position and thus varying the length and the direction of the scattering vector.

Different scan types, available on the high-resolution diffractometer employed in this study are listed here :

- $2\theta - \omega$ Scan : By executing a $2\theta - \omega$ scan, only the length of the scattering vector (\vec{S}) is varied by rotating the sample around the ω -axis and by simultaneously rotating the detector on the rocking cantilever with twice the angular velocity. The direction in which the scattering vector is pointing thereby remains unchanged. For symmetrical reflexes $\Omega = \theta$, and therefore the scan direction is along q_{\perp} . Particularly this scan along q_{\perp} is useful to check if there are other crystalline phases incorporated in the crystal. Moreover, the occurrence of forbidden reflexes hints at structural disorder in the examined crystal.
- ω -scan : For a ω -scan the sample is rotated around the ω -axis, which entails the variation of the scattering vector on a circular path around the origin. The plot of the scattered X-ray intensity as a function of ω is often called rocking curve.
- ϕ -scan : By performing a ϕ -scan, ω and θ are kept constant while the sample is rotated around the ϕ -axis.

3.2.4 Photoluminescence (PL) and Cathodoluminescence (CL)

Photoluminescence (PL) is the process of light emission from any material after the absorption of photons (electromagnetic radiation). It is one of the many forms of luminescence (light emission) and is initiated by photoexcitation (excitation by photons), hence the prefix “photo-”. In a typical PL experiment, a semiconductor is excited with a light-source that provides photons with an energy larger than the bandgap energy. The incoming light excites a polarization that can be described with the semiconductor Bloch equations²³¹. Once the photons are absorbed, electrons and holes are formed with finite momenta \vec{k} in the conduction and valence bands, respectively. The excitations then undergo energy and momentum relaxation towards the band gap minimum. Typical mechanisms are Coulomb scattering and the interaction with phonons. Finally, the electrons recombine with holes and results in the emission of photons.

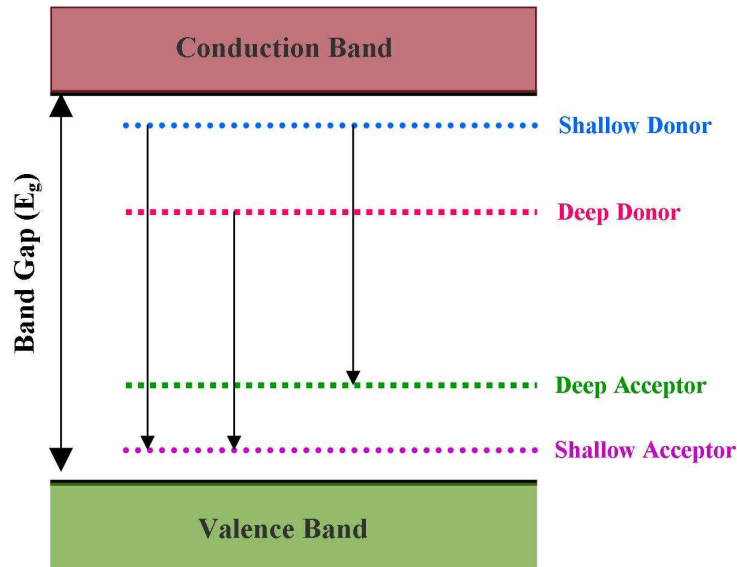


Figure 3.10: shows some basic luminescence recombination centers responsible for the observed PL and CL spectra.

Ideal, defect-free semiconductors are many-body systems where the interactions of charge carriers and lattice vibrations have to be considered in addition to the light-matter coupling. In general, the PL properties are also extremely sensitive to internal electric fields and to the dielectric environment (such as in photonic crystals) which impose further degrees of complexity. A precise microscopic description is provided by the semiconductor luminescence equations²³². We can also use PL to study crystal defects, such as atomic

vacancies and substitutions (see Fig. 3.10) which creates unique electronic states in electronic structure. This is of particular importance for materials having relatively higher band-gap such as diamond, Silicon Carbide (SiC) and GaN. Not only that we can identify the defect, but we can also tell if the crystal has internal stresses.

For the present work, Horiba Jobin Yvon *iHR320* PL system with Xenon lamp (450 W) as the source is used.

Unlike in PL, cathodoluminescence (CL) spectroscopy uses the high energetic electron beam (≈ 10 keV) as source. The advantages of CL over PL are higher quantum yield, better spatial resolution and depth dependent study.

3.2.5 Raman Spectroscopy

Raman spectroscopy (named after Sir C. V. Raman) is a spectroscopic technique used to observe vibrational, rotational, and other low-frequency modes in a system^{233,234}. It relies on inelastic scattering, or Raman scattering, of monochromatic light, usually from a laser in the visible, near infrared, or near ultraviolet range. The laser light interacts with molecular vibrations, phonons or other excitations in the system, resulting in the energy of the laser photons being shifted to lower or higher values around the incident energy. The shift in energy gives information about the vibrational modes in the system. The change in energy of the photon are often reported in wavenumbers, which have units of inverse length, as it is directly related to energy. In order to convert between spectral wavelength and wavenumbers of shift in the Raman spectrum, the following formula can be used:

$$\Delta\omega = \frac{1}{\lambda_0} - \frac{1}{\lambda_1} \quad (3.15)$$

where $\Delta\omega$ is the Raman shift expressed in wavenumber, λ_0 is the excitation wavelength, and λ_1 is the Raman spectrum wavelength. Most commonly, the unit chosen for expressing wavenumbers in Raman spectra is inverse centimeters (cm^{-1}).

Raman scattering is a standard optical characterization technique for studying various aspects of solids such as lattice properties, electronic properties, and magnetic properties. Raman scattering has many advantages when compared with other spectroscopic techniques: it is in principle non-destructive, contactless, and requires no special sample preparation technique such as thinning or polishing. Furthermore, when a standard Ra-

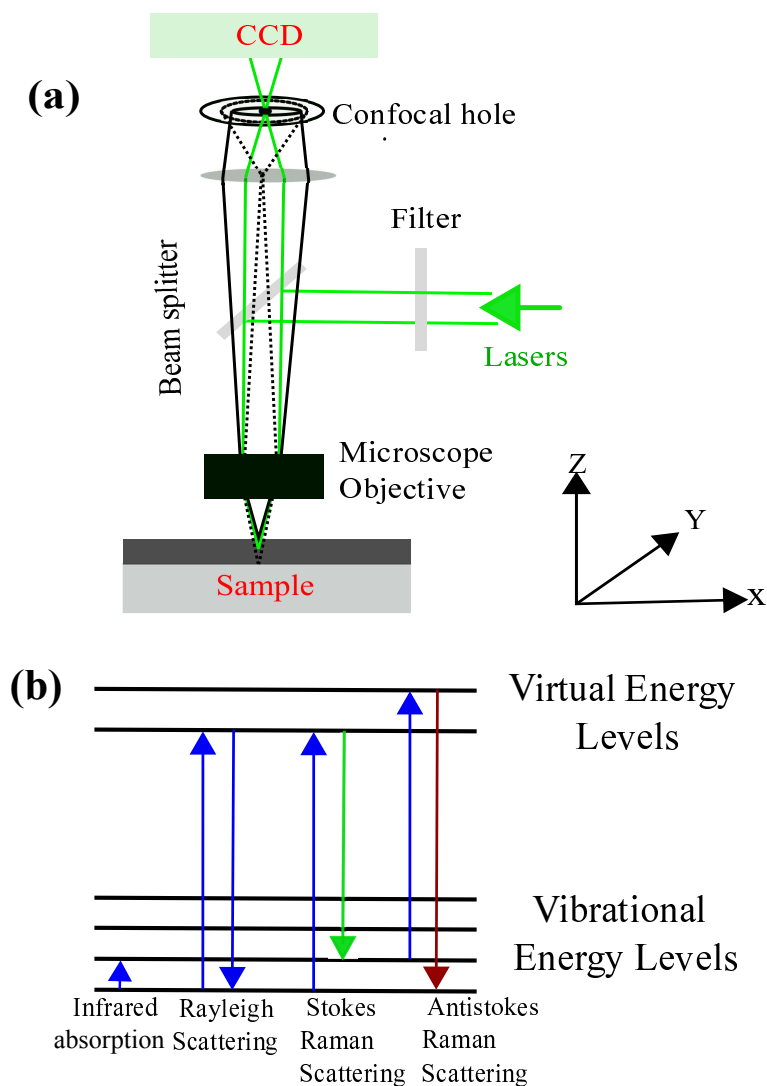


Figure 3.11: (A) shows the geometry of the measurements system. (B) shows transitional level for various vibrational modes.

man microscope is used with a visible laser for excitation, we can obtain lateral resolution of $\approx 1 \mu\text{m}$ or less, which is determined by the beam waist of the probe laser at the sample surface. Raman scattering occurs essentially as a result of modulation of the electronic polarizability induced by various elementary excitations in solids such as phonons and plasmons. In the case of Raman scattering by phonons, the scattering efficiency is higher in covalent crystals than in ionic crystals, because the valence electrons are less localized and larger fluctuation of the polarizability can be induced by lattice vibration. From this viewpoint, nitride semiconductors are suitable for Raman scattering studies, since the chemical bonding is a mixture of covalent and ionic bonding. Furthermore, nitride semi-

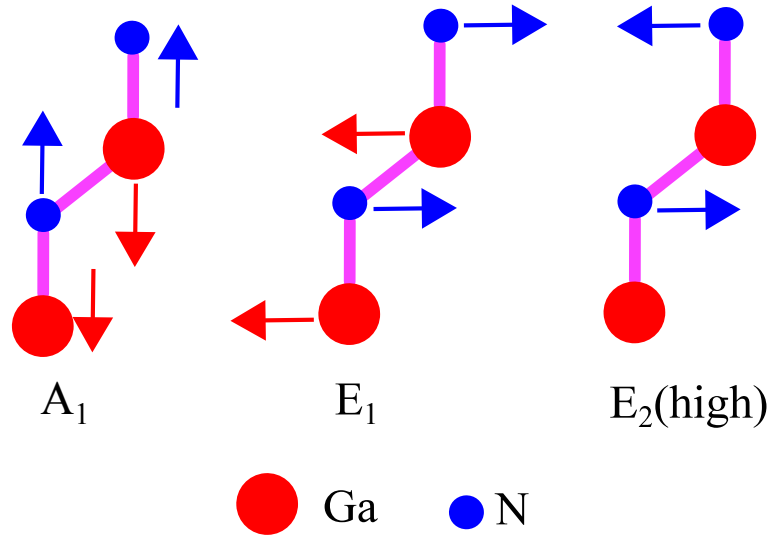


Figure 3.12: Different vibrational modes in III-Nitride.

conductors are generally robust and stand up well to laser irradiation, which is another advantage of Raman scattering studies.

3.2.5.1 Raman scattering in GaN

The first-order phonon Raman scattering is caused by phonons with wavevector $k \rightarrow 0$ (Γ -point) because of a momentum conservation rule in the light scattering process. In the hexagonal structure, group theory predicts eight sets of phonon normal modes at the Γ -point ($2A_1+2E_1+2B_1+2E_2$). Among them, one set of A_1 and E_1 modes are acoustic, while the remaining six modes ($A_1+E_1+2B_1+2E_2$) are optical²³⁴. The atomic displacement scheme of the optical modes is shown in Fig.3.12.

Residual strain in layered structure is a well known critical issue in fabricating optoelectronic devices. As a typical example, strain in a laser diode structure may change the electronic band structure in the optically active region and affect the laser gain²³⁵. There are several causes behind the lattice strain: first, lattice mismatch and difference in thermal expansion coefficient between hetero-epitaxial layers or between a deposited layer and its underlying substrate may cause in-plane uniaxial or biaxial strain; second, lattice structure may be distorted in the neighbourhood of native defects or incorporated impurities. These point defects will induce a three dimensional strain such as hydrostatic stress if the defects are uniformly distributed. Generally, hydrostatic strain and uniaxial or biaxial strain may coexist in hetero-epitaxial layers. Biaxial strain in the c-plane of the

hexagonal GaN layer is most easily probed by observing the $E_2(\text{high})$ phonon mode by means of Raman scattering^{236,237}; this is because of the fact that the frequency is sensitive to biaxial strain in the c-plane as expected from the atomic displacement scheme and, furthermore, this mode conveniently gives the strongest signal in the spectra.

If impurity atoms replace host-lattice atoms that are heavier than the host, atomic oscillation can be induced in a limited range around the impurities, which is the so-called local vibrational mode (LVM). Its frequency appears in the energy gap between the acoustic and optical branches of phonons, or above the optical branch. If the impurity is lighter, the LVM frequency becomes higher and the vibration is more localized²³⁴. Another typical foreign signal derives from defects known as the defect mode. Point defects such as vacancies can cause a defect mode with a sharp peak similar to the LVM. On the other hand, heavily disordered systems such as ion-implanted or low-temperature-grown crystals can exhibit a different type of defect mode called the disorder-activated Raman scattering (DARS) mode. DARS occurs as a result of phonon confinement to small (typically less than 100 nm) defect-free regions. This confinement relaxes the Raman selection rules, allowing phonons with non-zero wave vectors to contribute to first order Raman scattering. The DARS reflects, therefore, the phonon density of states of the host lattice, and usually appears with broad spectral features.

3.2.6 X-ray photoelectron spectroscopy (XPS)

X-ray photoelectron spectroscopy (XPS) also known as Electron Spectroscopy for Chemical Analysis (ESCA) is a surface-sensitive quantitative spectroscopic technique that measures the elemental composition at the parts per thousand range, empirical chemical formula, chemical state and electronic state of the elements that exist within the surface of a material. XPS spectra are obtained by irradiating a material with a beam of X-rays while simultaneously measuring the kinetic energy and number of electrons that escape from the top 0 to 10 nm of the material being analyzed. Conventional XPS requires ultra-high vacuum ($< 10^{-9}$ Torr) conditions, although a current area of development is ambient pressure XPS, in which samples are analyzed at pressures of a few tens of Torr.

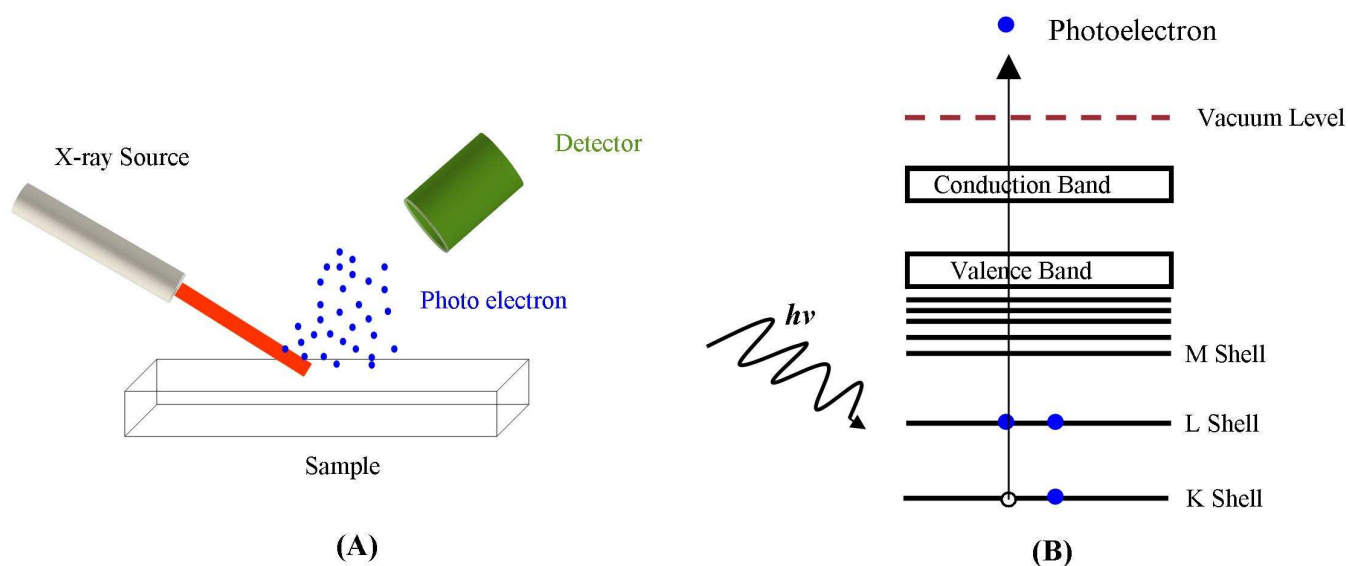


Figure 3.13: Schematic and the mechanism of XPS

Working principle

X-ray photoelectron spectroscopy (XPS) is based on the photoelectric effect. Each atom has core electrons with their characteristic binding energies that is conceptually but not strictly, equal to the ionization energy of that electron. When an X-ray beam falls on the sample surface, the energy of the X-ray photon is absorbed completely by the core electron of an atom. If the photon energy, $h\nu$, is large enough, the core electron will then escape from the atom and consequently from the surface. The emitted electron with the kinetic energy of E_k is referred to as the photoelectron. The binding energy of the core electron is given by the Einstein relationship

$$h\nu = E_b + E_k + \phi \quad (3.16)$$

or

$$E_b = h\nu - E_k - \phi \quad (3.17)$$

where $h\nu$ is the X-ray photon energy (for Al K_{α} , $h\nu=1486.7$ eV); E_k is the kinetic energy of photoelectron, which can be measured by the energy analyzer; and ϕ is combination of work function induced by the analyzer and material, about 4-5 eV. Since the work function, ϕ , can be compensated artificially, it is eliminated, giving the binding energy as

follows:

$$E_b = h\nu - E_k \quad (3.18)$$

Since each element has a unique set of core level kinetic energies, this can be used to identify elements from XPS spectrum²³⁸. Chemical shifts in peak position due to charge transfer in different elements provides valuable information on the valence state(s) or oxidation state(s) of the elements. The spectra around the fermi level also give useful information of the occupied states in the valence band. The width ΔE of the XPS peak is defined as a full width at half maximum (FWHM) of the peak after background subtraction. The width of the core level peak is a combination of various contribution:

$$\Delta E = [\Delta E_n^2 + \Delta E_p^2 + \Delta E_a^2]^{1/2} \quad (3.19)$$

where ΔE_n is natural width of core level, ΔE_p is natural width of photon source radiation, ΔE_a is analyser resolution. Additionally the peak can be broadened by sample inhomogeneity or by differential charging. The shape of a core-level photoelectron peak depend on a peak type as well as on the insulator or metallic nature of the sample, and several overlapping component due to co-existence of the different chemical states of the same element. The shape of a peak corresponding to a single chemical component can be determined separately for every chemical compound. The peak shape is deconvoluted to Gaussian-Lorentzian Function (also known as Voight) profile by the Doniach-Sunji scheme²³⁹. The stoichiometry of the sample surface can be estimated from the area ratio of the XPS peak using the general formula

$$I = n f \sigma \theta y \lambda A T \quad (3.20)$$

where n is the atomic concentration, f is the X-ray flux, σ is the photoelectronic cross-section for the atomic orbital of interest, θ is the angular efficiency factor for the instrumental arrangement, y is the efficiency in the photoelectric process for formation of photoelectron of the normal photoelectron energy, λ is the mean free path of the photoelectron in the sample, A is the area of the sample from which photoelectrons are detected, T is the detection efficiency for electrons emitted from the samples. The stoichiometry ratio of two elements A and B can be determined from the peak areas:

$$\frac{n_A}{n_B} = \frac{(I_A / \sigma y \lambda T)_A}{(I_B / \sigma y \lambda T)_B} = \frac{I_A / S_A}{I_B / S_B} \quad (3.21)$$

where S_A and S_B are the atomic sensitivity factor for the elements for the respective electron transition. Thus, if the surface has n number of elements than a generalized expression for determination of the atomic fraction of any constituents in a sample can be written as:

$$X_e = \frac{I_e/S_e}{\sum_{i=1}^n I_i/S_i} \times 100\% \quad (3.22)$$

where the summation represents over all the constituent of the surface.

XPS and, more in general, all electron spectroscopies are highly surface sensitive, due to the strong interaction of electrons with matter. The latter entails that electrons travelling in a solid exhibit a very short inelastic mean free path (λ_e). This quantity describes the average distance that an electron can travel through the material without suffering energy losses by inelastic scattering; it therefore provides an indication of the electron escape depth. For electrons with kinetic energy in the range between 10 and 1000 eV, λ_e can vary between 5 and 30 Å depending on the material and thus amounts only to a few atomic layers. As a result, in a typical photoemission experiment only electrons originating from a narrow region at the solid-vacuum interface can reach the detector without losing energy, thus contributing to the main lines of the measured spectrum. For this reason, PES and XPS are widely employed to probe the electronic structure and composition of solid surfaces and thin films.

For the present studies, Omicron XPS system is used for identification, quantification and analysis of the chemical state and electronic structure of the thin films. XPS spectral deconvolution is achieved in XPSPeak4.1 open source software, where Shirley type background subtraction has been employed before the deconvolution process. The shape of the peak (height, width, Gaussian/Lorentian, etc.) are automatically varied until the best fit to experimental spectrum is achieved, considering realistic physical aspects like peak position and FWHM.

3.2.7 Transmission Electron Microscopy (TEM)

Transmission electron microscopy (TEM) is a microscopy technique in which a beam of electrons is transmitted through an ultra-thin specimen, interacting with the atoms

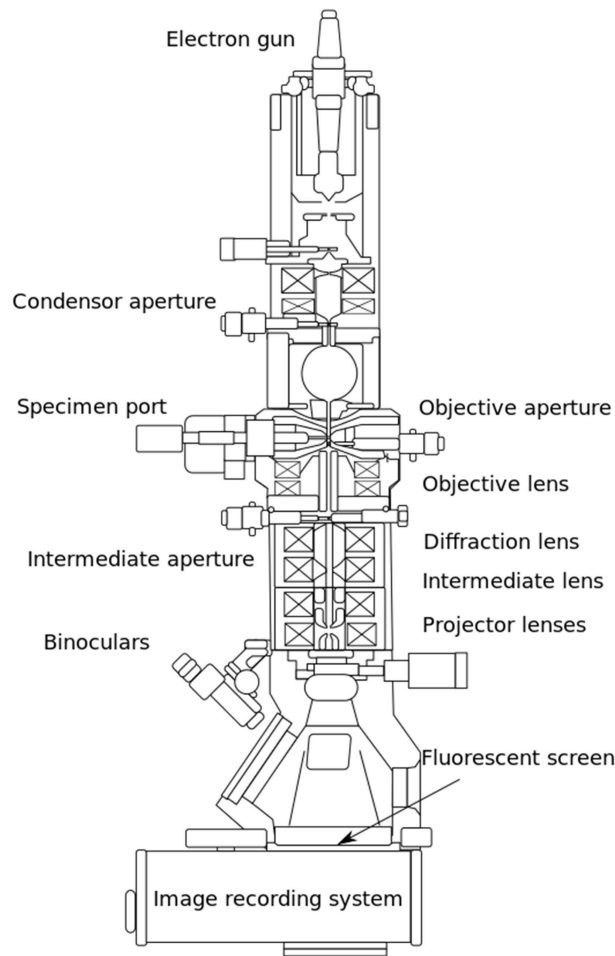


Figure 3.14: Schematic of a typical TEM. (*source: <http://www.diamond.ac.uk>*)

within it. An image is reconstructed from the interaction of the electrons transmitted through the specimen; the image is magnified and focused onto an imaging device, such as a fluorescent screen, on a layer of photographic film, or to be detected by a sensor such as a charge-coupled device (CCD).

In a conventional TEM (see Fig.3.14), a thin specimen is irradiated with an electron beam of uniform current density. Typically, electrons are emitted from the electron gun (source) to illuminate the specimen through a two or three stage condenser lens system. Objective lens provides the formation of either image or diffraction pattern of the specimen. The electron intensity distribution behind the specimen is magnified with a three or four stage lens system and is viewed on a fluorescent screen. The image can be recorded by direct exposure of a photographic emulsion or an image plate or digitally by a CCD camera.

The acceleration voltage is kept routinely at 120 to 200 kV. Medium-voltage instruments work at 200-500 kV to provide a better transmission and resolution, and in high voltage electron microscopy (HVEM) the acceleration voltage is in the range 500 kV to 3 MV. Acceleration voltage determines the velocity, wavelength and hence the resolution (ability to distinguish the neighbouring microstructural features) of the microscope.

Depending on the aim of the investigation and configuration of the microscope, transmission electron microscopy can be categorized as :

- Conventional Transmission Electron Microscopy
- High Resolution Electron Microscopy
- Analytical Electron Microscopy
- Energy-Filtering Electron Microscopy
- High Voltage Electron Microscopy
- Dedicated Scanning Transmission Electron Microscopy

Electron Diffraction

Electrons of 0.072 Å wavelength with 100 kV excitation energy, are transmitted through $\approx 0.1 \mu\text{m}$ thin foil specimen and are diffracted by the electron cloud in the specimen according to Bragg's law, $n\lambda = 2d\sin\theta$, forming a diffraction pattern (consisting of transmitted and diffracted beam spots) on the display screen of the microscope. The real diffraction phenomena is due to complex interactions of charged electrons with the periodic potential field of the lattice. However, Bragg's Law or Laue conditions are sufficient approximations for useful practical applications. A diffraction pattern is, in the simplest sense, a Fourier transform of the periodic crystal lattice, giving us information on the periodicities in the lattice, and hence the atomic positions²⁴⁰. Reciprocal lattice is a concept, used together with Ewald sphere construction, for geometrical interpretation of the Bragg law or Laue conditions that describe the diffraction conditions. According to this, diffraction pattern is the planar section of the reciprocal lattice perpendicular to beam direction, which is also the zone of planes appearing as spots in the pattern. Electron diffraction patterns produced in TEM can be of three different types:

- Ring Pattern

- Selected Area Diffraction Pattern
- Convergent-Beam Electron Diffraction Pattern

Imaging in TEM

The image of the specimen in conventional microscopy is formed selectively allowing only the transmitted beam (Bright Field Imaging) or one of the diffracted beams (Dark Field Imaging) down to the microscope column by means of an aperture. The origin of the image contrast is the variation of intensities of transmitted and diffracted beams due to the differences in diffraction conditions depending on the microstructural features on the electron path.

Other techniques that can be measured in a TEM are:

- Absorption contrast
- Lattice Imaging
- Weak Beam Imaging
- 3D Imaging
- $2\frac{1}{2}$ D Imaging

Spectroscopy in TEM

Electron energy loss spectroscopy (EELS) is a family of techniques that measure the change in kinetic energy of electrons after they interact with the specimen. This technique is used to determine the atomic structure, electronic structure and chemical properties of a specimen, including the type and quantity of atoms present, chemical state of atoms and the collective interactions of atoms with their neighbors. As electrons pass through a specimen, they interact with atoms of the solid. Many of the electrons pass through the thin sample without losing energy (elastic scattering). A fraction will undergo inelastic scattering and lose energy as they interact with the specimen. This leaves the sample in an excited state. The material can de-excite by giving up energy typically in the form of visible photons, X-rays or Auger electrons. As the incident electron interacts with the sample, it changes both its energy and momentum. We can detect this scattered incident

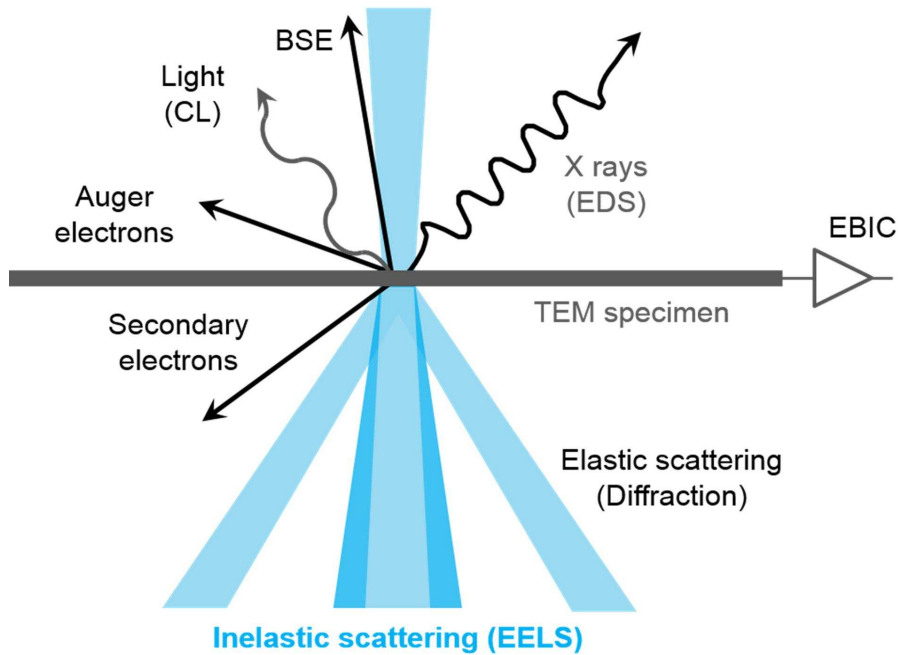


Figure 3.15: Schematic of different electron scattering processes during TEM

electron in the spectrometer as it gives rise to the electron energy loss signal. The sample electron (or collective excitation) carries away this additional energy and momentum. Core-loss excitations occur when tightly bound core electrons are promoted to a higher energy state by the incident electron. The core electron can only be promoted to an energy that is an empty state in the material. These empty states can be bound states in the material above the Fermi level (so called anti-bonding orbitals in the molecular orbital picture). The states can also be free electron states above the vacuum level. It is the sudden turn-on of the scattering at the Fermi energy and the probing of empty states which makes the EELS signal sensitive to both the atom type and its electronic state. We can visualize the initial spectral features in the core-loss excitations when we align the Fermi level with the zero-loss peak (ZLP) of the spectrum. The edges can now be seen as the point where the electrons lose enough energy to promote the core level atomic electrons to the Fermi level. This analogy fails to reproduce the scattering above the Fermi level, but is helpful to visualize the core level edge by the sudden increase in intensity. A typical energy loss spectrum includes several regions. The first peak, the most intense for a very thin specimen, occurs at 0 eV loss (equal to the primary beam energy) and is therefore called the zero-loss peak (ZLP). It represents electrons

that did not undergo inelastic scattering, but may have been scattered elastically or with an energy loss too small to measure. The width of the zero-loss peak mainly reflects the energy distribution of the electron source. It is typically 0.2-2.0 eV but may be as narrow as 10 meV or lower in a monochromated electron source²⁴¹. In this thesis work we have used an aberration corrected high resolution transmission electron microscopy (HRTEM, FEI TITAN operated at 300kV) for obtaining images with atomic resolution, electron diffraction and EELS of samples.

3.2.8 X-ray Absorption Near Edge Spectroscopy (XANES)

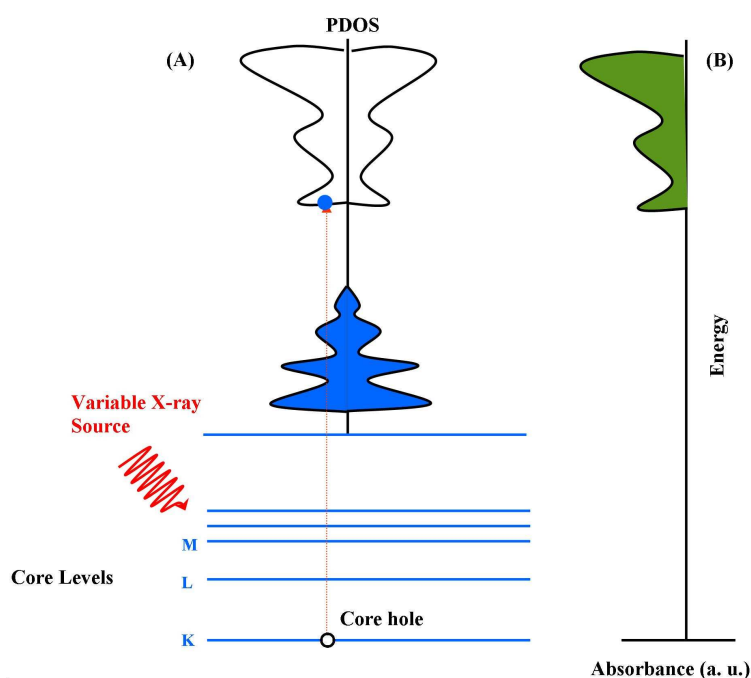


Figure 3.16: Schematic of X-Ray absorption process

X-ray absorption near edge spectroscopy (XANES), also known as near edge X-ray absorption fine structure (NEXAFS), is a type of absorption spectroscopy that indicates the features in the X-ray absorption spectra (XAS) of condensed matter, due to the photo-absorption cross section for electronic transitions from an atomic core level to final states in the energy region of 50-100 eV above the selected atomic core level ionization energy, where the wavelength of the photoelectron is larger than the interatomic distance between the absorbing atom and its first neighbour atoms.

The fundamental phenomenon underlying XANES is the absorption of an X-ray

photon by material with the formation of many body excited states characterized by a core hole in a selected atomic core level (see the Figure 3.16). In the single particle approximation theory, the system is separated into one electron in the core levels of the selected atomic species of the system and $N-1$ passive (screening) electrons. In this approximation the final state is described by a core hole in the atomic core level and an excited photoelectron. The final state has a very short life time because of the short life-time of the core hole and the short mean free path of the excited photoelectron with kinetic energy in the range around 20-50 eV. The core hole is filled either via an Auger process or by capture of an electron from another shell followed by emission of a photon. The difference between XANES and traditional photoemission experiments is that in photoemission, the initial photoelectron itself is measured, while in XANES the fluorescent photon or Auger electron or an inelastically scattered photoelectron may also be measured which is significant; in photoemission, the final state of the emitted electron captured in the detector must be an extended free-electron state. By contrast, in XANES, the final state of the photoelectron may be a bound state such as an exciton, since the photoelectron itself need not be detected. The effect of measuring fluorescent photons, Auger electrons, and directly emitted electrons is to sum over all possible final states of the photoelectrons, therefore XANES measures the total joint density of states of the initial core level with all final states, consistent with conservation rules. The distinction is critical because in spectroscopy final states are more susceptible to many-body effects than initial states, meaning that XANES spectra are more easily calculable than photoemission spectra.

Synchrotron radiation that can have tunable energy and high intensity, has a natural polarization that can be utilized to great advantage in XANES studies. The commonly studied molecular adsorbates have σ and π bonds that may have a particular orientation on a surface. The angle dependence of the X-ray absorption tracks the orientation of resonant bonds due to dipole selection rules²⁴². For our study we used BL-01 SXAS synchrotron beam line facility at Raja Ramanna Centre for Advance Technology (RRCAT), Indore, India.

3.2.9 Secondary Ion Mass Spectrometry (SIMS)

Secondary ion mass spectrometry (SIMS) is a technique used to analyze the composition of solid surfaces and thin films by sputtering the surface of the specimen with a focused beam of primary ions and collecting and analyzing ejected secondary ions. The mass/charge ratios of these secondary ions are measured with a mass spectrometer to determine the elemental, isotopic, or molecular composition of the surface to a depth of 1 to 2 nm. Due to the large variation in ionization probabilities among different materials, SIMS is generally considered to be a qualitative technique, although quantification is possible with the use of standards. SIMS is the most sensitive surface analysis technique, with elemental detection limits ranging from parts per million to parts per billion.

Instrumentation

A secondary ion mass spectrometer consists of (1) a primary ion gun generating the primary ion beam, (2) a primary ion column, accelerating and focusing the beam onto the sample (and in some devices an option to separate the primary ion species by Wien filter or to pulse the beam), (3) high vacuum sample chamber holding the sample and the secondary ion extraction lens, (4) a mass analyser separating the ions according to their mass to charge ratio, and (5) a detector. SIMS requires a high vacuum with pressures below 10^{-6} Torr. This is needed to ensure that secondary ions do not collide with background gases on their way to the detector. (i.e. the mean free path of gas molecules within the detector must be large compared to the size of the instrument), and it also prevents surface contamination by adsorption of background gas particles during measurement. Three types of ion guns are generally employed. In one, ions of gaseous elements are usually generated with duoplasmatrons or by electron ionization, for instance noble gases ($^{40}\text{Ar}^+$, Xe^+), Oxygen (^{16}O , $^{16}\text{O}^{2+}$, $^{16}\text{O}^{2-}$), or even ionized molecules such as SF_5^+ . Depending on the SIMS type; there are three basic analyzers available: sector, quadrupole, and time-of-flight. Detection limits for most trace elements are between 10^{12} and 10^{16} atoms per cubic centimetre²⁴³ depending on the type of instrumentation and the primary ion beam used and also on the analytical area, and other factors.

3.3 Simulation Techniques

Theory and simulation of materials plays a major role in understanding the basic properties of the materials. In this section a brief discussion on the techniques used in this thesis is given.

3.3.1 Finite Difference Time Domain (FDTD) method

Finite-difference time-domain or Yee's method is a numerical analysis technique used for modeling computational electrodynamics (finding approximate solutions to the associated system of differential equations). The FDTD approach is based on a direct numerical solution of the time-dependent Maxwell's curl equation. The FDTD method belongs in the general class of grid-based differential numerical modeling methods. In this method the time-dependent Maxwell's equations are discretized using central-difference approximations to the space and time partial derivatives. The electric field vector (\vec{E}) components in a volume of space are solved at a given instant in time; then the magnetic field vector components in the same spatial volume are solved at the next instant in time; and the process is repeated over and over again until the desired transient or steady state electromagnetic field behavior is fully evolved²⁴⁴.

Mathematical Foundation

Electromagnetic waves generated by a pulse is given by Maxwell's curl equations. Maxwell's curl equations in free space are

$$\frac{\partial \mathbf{E}}{\partial t} = \frac{1}{\epsilon_0} \nabla \times \mathbf{H} \quad (3.23)$$

$$\frac{\partial \mathbf{H}}{\partial t} = -\frac{1}{\mu_0} \nabla \times \mathbf{E} \quad (3.24)$$

where \mathbf{E} and \mathbf{H} are three dimensional electric field and magnetic field vectors respectively. For simplicity let's assume electromagnetic (EM) wave travels along z direction (assuming one dimensional problem) *i.e.* electric field oscillates in the xz -plane. Then $E_y = E_z = H_y = 0$ because of the transverse characteristic of EM wave and hence $\mathbf{E} = (E_x, 0, 0)$. As it is well known that \mathbf{E} and \mathbf{H} travels perpendicular to each other, then

$$\mathbf{E} \cdot \mathbf{H} = (E_x, 0, 0) \cdot (H_x, H_y, 0) = E_x H_x = 0 \quad (3.25)$$

since E_x is non zero, H_x must be zero here. Now equation 3.23 and 3.24 reduces to

$$\frac{\partial E_x}{\partial t} = -\frac{1}{\epsilon_0} \frac{\partial H_y}{\partial z} \quad (3.26)$$

$$\frac{\partial H_y}{\partial t} = -\frac{1}{\mu_0} \frac{\partial E_x}{\partial z} \quad (3.27)$$

Equations 3.26 and 3.27 corresponds to transverse plane-polarized waves travelling in z -direction. In a dielectric medium with a dielectric constant of ϵ_r , Equations 3.26 and 3.27 take the forms

$$\frac{\partial E_x}{\partial t} = -\frac{1}{\epsilon_r \epsilon_0} \frac{\partial H_y}{\partial z} \quad (3.28)$$

$$\frac{\partial H_y}{\partial t} = -\frac{1}{\mu_0} \frac{\partial E_x}{\partial z} \quad (3.29)$$

3.3.2 Density Functional Theory (DFT)

Density functional theory (DFT) is a computational technique which uses quantum mechanical method to investigate the ground state electronic structure of many-body systems such as atoms, molecules, and/or the condensed phases of a material. DFT is primarily based on two theorem proposed by Hohenberg and Kohn²⁴⁵. Hohenberg and Kohn showed that “a special role can be assigned to the density of particles in the ground state of a quantum many-body system; the density can be considered as a “basic variable,” *i.e.* all properties of the system can be considered to be unique functionals of the ground state density”²⁴⁶. The Hamiltonian of a system of interacting particles is given as

$$\hat{H} = [\hat{T} + \hat{V} + \hat{U}] = \left[\sum_i^N \left(-\frac{\hbar^2}{2m_i} \nabla_i^2 \right) + \sum_i^N V_{ext}(r_i) + \sum_{i<j}^N U(r_i, r_j) \right] \quad (3.30)$$

where, for the N -electron system, \hat{H} is the Hamiltonian, E is the total energy, \hat{T} is the kinetic energy, V_{ext} is the potential energy from the external field due to positively charged nuclei, and \hat{U} is the electron-electron interaction energy. There are many methods for solving the many-body Schrödinger equation based on the expansion of the wavefunction in Slater determinants. The simplest one is the Hartree-Fock method, more sophisticated approaches are usually categorized as post Hartree-Fock methods. However, the problem with these methods is the huge computational effort, which makes it virtually impossible to apply them efficiently to larger and/or more complex systems. Here DFT provides an

appealing and much more versatile alternative as it provides a way to systematically map the many-body problem, with \hat{U} , onto a single-body problem without \hat{U} . In DFT the key variable is the electron density $n(r)$, which for a normalized Ψ is given by

$$n(r) = N \int d^3r_1 \dots \int d^3r_N \Psi^*(r_1, r_2, r_3, \dots, r_N) \Psi(r_1, r_2, r_3, \dots, r_N) \quad (3.31)$$

The two theorems of Hohenberg and Kohn are as follows:

- **Theorem 1** For any system of interacting particles in an external potential $V_{ext}(r)$, the potential $V_{ext}(r)$ is determined uniquely, except for a constant, by the ground state particle density $n_0(r)$.

$$V[n_0] = \int V(r) n_0(r) d^3r \quad V[n] = \int V(r) n(r) d^3r \quad (3.32)$$

- **Theorem 2** A universal functional for the energy $E[n]$ in terms of the density $n(r)$ can be defined, valid for any external potential $V_{ext}(r)$. For any particular $V_{ext}(r)$, the exact ground state energy of the system is the global minimum value of this functional, and the density $n(r)$ that minimizes the functional is the exact ground state density $n_0(r)$.

The total energy is given by:

$$E[n] = T[n] + U[n] + \int V(r) n(r) d^3r \quad (3.33)$$

with respect to $n(r)$, assuming with reliable expressions for $T[n]$ and $U[n]$. A successful minimization of the energy functional will yield the ground-state density n_0 and thus all other ground-state observables. At first, the energy functional without electron-electron interaction energy term can be written as

$$E_s[n] = \langle \Psi_s[n] | \hat{T} + V_s | \Psi_s[n] \rangle \quad (3.34)$$

where V_s is an external effective potential. So the Kohn - Sham equation of the non interacting system is expressed as

$$\left[-\frac{\hbar^2}{2m} \nabla^2 + V_s(r) \right] \phi_i r = \epsilon_i \phi_i r \quad (3.35)$$

which yields the orbitals ϕ_i that reproduce the density $n(r)$ of the original many-body system in the form

$$n(r) = n_s(r) = \sum_i^N |\phi_i(r)|^2 \quad (3.36)$$

Now the effective single particle potential can be written as

$$V_s(r) = V(r) + \int \frac{e^2 n_s(r')}{|r - r'|} d^3 r' + V_{XC}[n_s(r)] \quad (3.37)$$

where the $V_{XC}[n_s(r)]$ is called exchange-correlation potential which includes all many body interaction energy term. Since the Hartree term and $V_{XC}[n_s(r)]$ depend on $n(r)$, which depends on the ϕ_i , which in turn depends on V_s ; the problem of solving the Kohn-Sham equation can be done in a self-consistent (i.e., iterative) way. Usually one starts with an initial guess for $n(r)$, then calculates the corresponding V_s and solves the Kohn-Sham equations for the ϕ_i . From these, one calculates a new density and starts again. This iterative procedure is then repeated until convergence is reached.

3.3.2.1 Approximations (exchange-correlation functionals)

The major problem with DFT is that the exact functionals for exchange and correlation are not known, except for the free electron gas. However, various approximated functionals exist which can be use to calculate various physical quantities quite accurately.

Local Density Approximation (LDA)

In LDA, the functional depends only on the density at the coordinate where the functional is evaluated²⁴⁷⁻²⁴⁹:

$$E_{XC}^{LDA}[n] = \int \epsilon_{XC}(n)n(r)d^3r \quad (3.38)$$

With spin included in the LDA

$$E_{XC}^{LSDA}[(n_\uparrow, n_\downarrow)] = \int \epsilon_{XC}(n_\uparrow, n_\downarrow)n(r)d^3r \quad (3.39)$$

The LDA assumes that the density is the same everywhere. Because of this, the LDA has a tendency to over-estimate the exchange-correlation energy.

Generalized Gradient Approximation (GGA)

To correct the tendency of overestimation of exchange-correlation energy, GGA scheme have been proposed, where the XC functional contains not only the charge density but also the gradient of the charge density, and thus the name Generalized Gradient

Approximation^{250,251}.

$$E_{XC}^{GGA}[(n_{\uparrow}, n_{\downarrow})] = \int \epsilon_{XC}(n_{\uparrow}, n_{\downarrow}, \nabla_{n_{\uparrow}}, \nabla_{n_{\downarrow}})n(r)d^3r \quad (3.40)$$

Using GGA, very good results for molecular geometries and ground-state energies have been achieved. However, few parameters obtained from the GGA also vastly differ from experimental data. Thus, a new ‘hybrid’ type of functional is introduced, where a certain percentage of the Hartree-Fock exchange is used.

Hybrid Functional (e.g. HSE)

The HSE (Heyd-Scuseria-Ernzerhof) exchange-correlation functional uses an error function screened Coulomb potential to calculate the exchange portion of the energy in order to improve the accuracy of the computational results²⁵².

$$E_{XC}^{\omega PBEh} = aE_x^{HF,SR}(\omega) + (1-a)E_x^{PBE,SR}(\omega) + E_x^{PBE,LR}(\omega) + E_c^{PBE} \quad (3.41)$$

where a is the mixing parameter and ω is an adjustable parameter controlling the short-rangeness (SR) of the interaction.

3.3.3 Full Multi Scattering (FMS) Theory

To study the EELS and XANES results, simulation based on FMS is employed in this thesis. Since XAS measures the X-ray absorption co-efficient $\mu(\omega)$, which characterizes the decay of the intensity I of an X-ray beam passing through the material thickness d *i.e.*

$$I = I_0 e^{-\mu(\omega)d} \quad (3.42)$$

The contribution to $\mu(\omega)$ at a X-ray energy $\hbar\omega$ is proportional to the total absorption cross-section $\sigma(\omega)$. For any given material the cross-section can be calculated in terms of the many-body ground state $|0\rangle$ and excited N -particle state $|F\rangle$ of the system using Fermi’s golden rule,

$$\sigma(\omega) = 4\pi^2 e^2 \frac{c}{\omega} \sum_i^f |\langle f | \alpha \cdot \epsilon e^{ik \cdot r} | 0 \rangle|^2 \delta(\hbar\omega + \epsilon_f - \epsilon_i) \quad (3.43)$$

where α represents Dirac matrices, ϵ_i is the ground state energy, ϵ_f is the excited state energy ($e = \hbar = m = 1$). Calculations of both XAS and LDOS in a periodic system,

are efficiently carried out within a real-space multiple scattering (RSMS) Greens function formalism. For example total DOS $[\rho(E)]$ is given by the integral of the $\text{Im}(G)$ in real space,

$$\rho(E) = -\frac{2}{\pi} \text{Im} \int d^3r G(r', r, E) \quad (3.44)$$

where $G(r', r, E) = \langle r' | G(E + i\eta) | r \rangle$ and $\eta = 0^+$. Both the X-ray absorption and emission spectra can be calculated from the same one-particle Greens function. From Fermi's golden rule and the one-electron and dipole approximations, the X-ray absorption coefficient is given by

$$\mu(E) \propto -\frac{2}{\pi} \text{Im} |i\rangle \hat{\epsilon} \cdot r' G(r', r, E) \hat{\epsilon} \cdot r |i\rangle \quad (3.45)$$

The equation of crossection with full multiple scattering is given by

$$\sigma_{tot}(\omega) = -\frac{4\pi}{c\omega} \text{Im} \sigma_i \langle i | d_\epsilon^* G(\omega + \epsilon_i) d_\epsilon | i \rangle \theta(\omega + \epsilon_i - \epsilon_F) \quad (3.46)$$

where ϵ_F is the Fermi energy and $\theta = \frac{1}{1 + \exp((\omega + \epsilon_i - \epsilon_F)/kT)}$ and G is the Green function and is given by

$$G(r, r', E) = \langle r | G(E) | r' \rangle = \langle r | \frac{1}{E - H + i\eta} | r' \rangle = \sum_f^{\text{all}} \frac{\langle r | |f\rangle \langle f | |r' \rangle}{E - \epsilon_f + i\eta} \quad (3.47)$$

where $\eta = 0^+$. Details on the theory of full multiple scattering can be found elsewhere²⁵³⁻²⁵⁶. For the calculations of local density of states and X-ray absorption crossection, FEFF9.05 code²⁵⁷ was used for this thesis work.

Chapter 4

Growth and Characterization of GaN Nanowall Network

In this chapter, the study of the role of pore dimensions of GaN nanowall network (NWN) on band-edge emission is described. The films are grown by a PA-MBE system and their morphological, structural and optical properties are probed by complementary characterization tools. We propose a growth mechanism of GaN NWN by experimentally monitoring its morphological evolution and complementing it by first-principles DFT calculations. Finite Difference Time Domain (FDTD) simulation is performed to understand the role of total internal reflection and scattering on light extraction from the nanowall network.

4.1 Growth, Structural and Optical Properties of GaN NWN

4.1.1 Introduction

Modifying the surface topology and using at least one component of the LED as porous structure, the light output has seen to be enhanced by $\approx 46\%$ ¹²⁰ and yielded $\approx 150\%$ higher electro-luminescence (EL)¹²¹. The porous structure behaves as a highly scattering medium when the pore dimensions are comparable to the wavelength of scattered light. In this case, it causes multiple scattering of photons inside the pores that

consequently enhances light extraction efficiency (LEE) of the system. Studies on porous TiO_2 ¹²⁶, GaP ¹²⁷ as well as GaN ¹²⁸ have also shown not only a reduction of the refractive index with increased porosity, which minimizes total internal reflection dependent optical losses, but the different facets of the porous structure also give extra degrees of freedom for the photon to fall within the ‘escape cone’. Most of the nanoporous films are formed by top down approaches such as chemical etching¹³⁰ or ion bombardment¹³¹, whose performance is limited by contamination, undesired interface and defect states and degradation in crystallinity and composition. Spontaneous formation of porous nanostructures using controlled growth have yielded high quality GaN films with geometries that enhance light extraction. Recently, a few groups^{134–136} including ours^{137,138}, have formed GaN nanowall network structures by kinetic growth control, using molecular beam epitaxy (MBE) or chemical vapour deposition (CVD).

Kesaria *et al.* provide a phase diagram of the formation of different morphologies of GaN nanostructures¹³⁷ obtained by varying the kinetics of growth. From this particular study it was noted that GaN NWN on sapphire (0001) substrate forms within a small narrow range of growth conditions. This study reports GaN growth at a substrate temperature of 680° and N_2 flow rate of 4.5 sccm. The Ga BEP was varied by changing the K-cell temperature and it was reported that at Ga BEP 2.3×10^{-7} Torr, the GaN NWN was formed. Further, another set of growth conditions was identified where a constant Ga flux at 3.85×10^{14} atoms $\text{cm}^{-2}\text{s}^{-1}$, N_2 flow at 2 and 8 sccm can also result in the formation of NWN^{137,258}. A detailed PL study was published by Thakur *et al.* on various samples of GaN NWN and proposed that the superior structural quality of the NWN is responsible for the observed high PL intensity in comparison to commercial flat GaN epitaxial layer²⁵⁹. However, in this study the role of morphology on PL yield was not discussed. This part of this chapter dedicates the growth of various samples with different porosity (or morphology) and study their impact on PL yield.

4.1.2 Experimental Details

The GaN films are grown under nitrogen rich conditions by using radio frequency plasma assisted molecular beam epitaxy system operating at a base pressure of 3×10^{-11} Torr. The films A2, A3 and A4 are grown over bare c-plane of sapphire ($\alpha - \text{Al}_2\text{O}_3$).

The $\alpha - \text{Al}_2\text{O}_3$ wafer substrates were degassed prior to growth at 500 °C for 30 min in the preparation chamber and then in the growth chamber at 800 °C for 10 min. The temperature of Gallium (Ga) effusion cell is maintained at 980, 1000 and 1030 °C to vary the Ga flux rate, resulting in GaN films with different morphology labelled A2, A3, and A4. A constant nitrogen flow rate of 8.0 sccm, plasma forward power of 375 W, substrate temperature of 630 °C and growth duration of 4 hrs were maintained for all the films. The sample A1 is a flat GaN epitaxial layer of 2 μm thickness that is used commercially for LED production and is chosen here for comparative study. Surface structural evolution was monitored *in-situ* by reflection high energy electron diffraction (RHEED) and the morphology was determined *ex-situ* by field emission scanning electron microscope (FESEM). Bulk structural quality of the films is determined by high-resolution X-ray diffractometer with a Cu K_α X-ray source (wavelength of 1.5406 Å) and a high resolution TEM. Optical emission of the films were characterized by photo-luminescence spectroscopy using a Xenon lamp source with 325 nm excitation and an integrating sphere for obtaining the total PL intensity.

4.1.3 Results and Discussion

4.1.3.1 Correlation between Morphology and PL yield

Fig.4.1 is panel of the FESEM images showing the plan view of the different surface morphologies of the four samples formed here with their respective RHEED pattern as top-right insets. Sample A1 has a smooth and flat surface, whereas A2 shows a rougher surface with small pores. A3 comprises of inverse pyramidal shapes with pores and sample A4 is composed of quasi 3D walls defined as the nanowall network (NWN). The roughness of the samples is defined by the mean pore sizes (maximum diameter across any void shown by red circles) and are estimated to be 45 ± 13 , 170 ± 31 , 215 ± 43 nm for A2, A3 and A4, respectively. The pore density is $\approx 10^9 - 10^{10} \text{ cm}^{-2}$, with the pores aligned along the c- direction. Respective insets in Fig.4.1 shows RHEED pattern recorded along $(11\bar{2}0)$ direction, with the characteristic streaky pattern for the flat A1 sample, while the pattern is spotty for A2, A3 and A4 due to transmission through the rough single crystalline wurtzite surfaces.

To study the impact of pore dimensions on PL yield, spectra of the near band edge

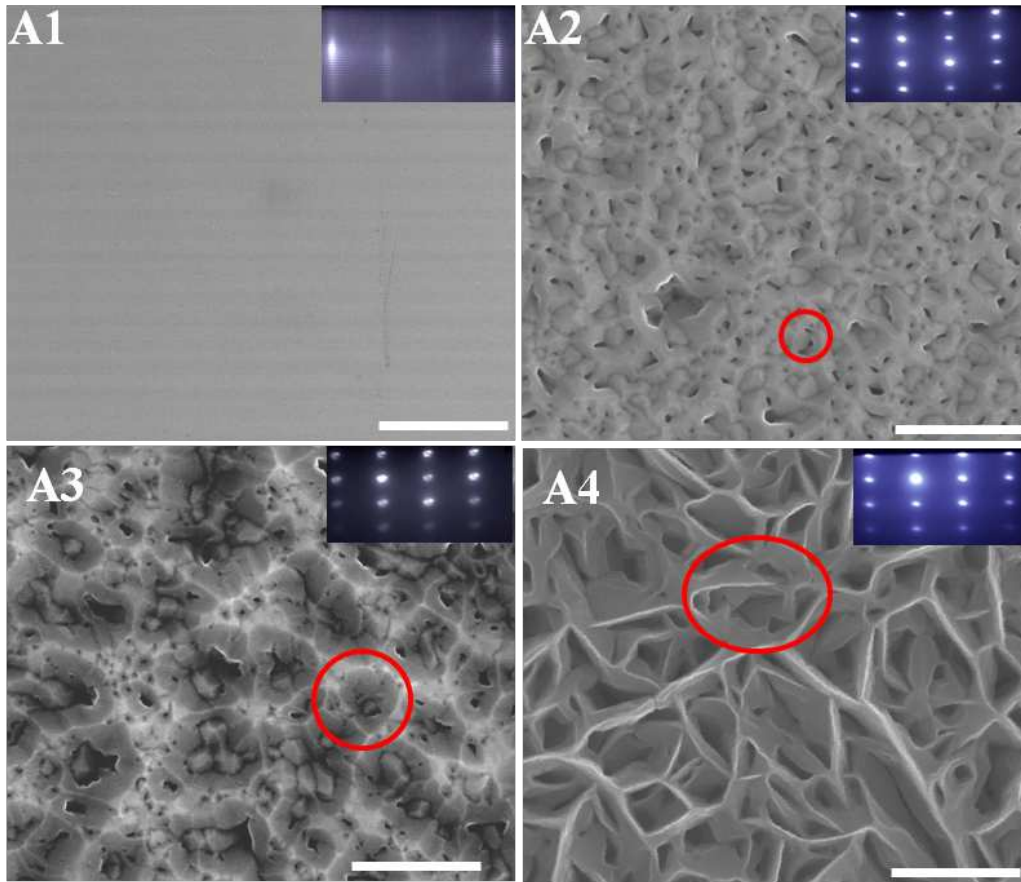


Figure 4.1: shows FESEM plan view images and corresponding RHEED pattern (top-right inset) of GaN epilayer (A1) and porous GaN NWN(A2, A3, A4) respectively. The area marked red are considered as respective pore sizes of the samples. The scale bar is 500 nm for all the images.

emission (NBE) around 3.4 eV were recorded for all the samples under similar conditions as shown in Fig.4.2. Sample A1 shows a small band edge emission and a strong yellow luminescence (YL) defect peak,^{138,260} centered at 2.2 eV (see Fig.4.3). In all the grown porous samples (A2, A3 and A4), YL is nearly absent, which indicates low defect density of the porous or NWN samples. The NBE positions of all the samples are listed in Table 4.1. We find for the samples A2 and A3, NBE is red shifted while for sample A4, it is same as compared to sample A1. Further, in the PL intensities aspect, we find least intensity for A1 and intense for the NWN (A4) in this study and we infer that the PL intensity increases with increase in pore dimensions. The intensity (area under the NBE curve) ratio between A1, A2, A3 and A4 is 1:4:12:140, showing that the GaN NWN has the highest

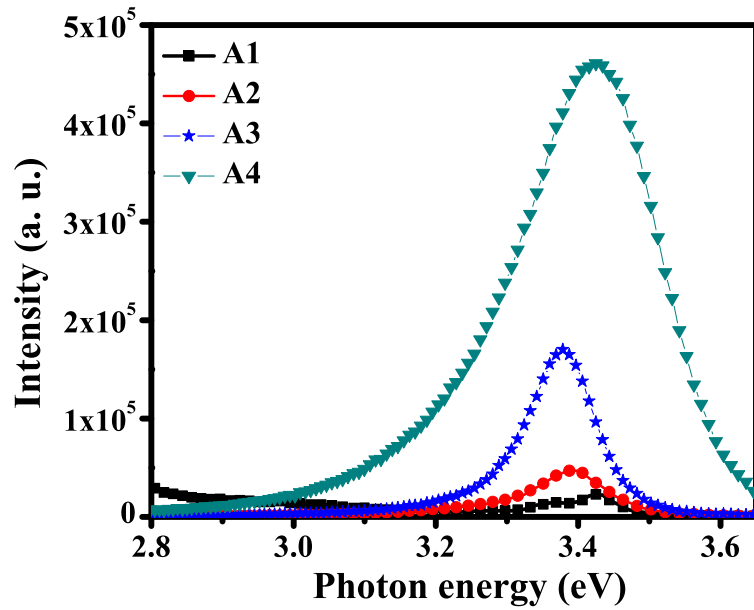


Figure 4.2: shows the band edge emission of PL spectra (in linear scale) of the four samples (A1-A4).

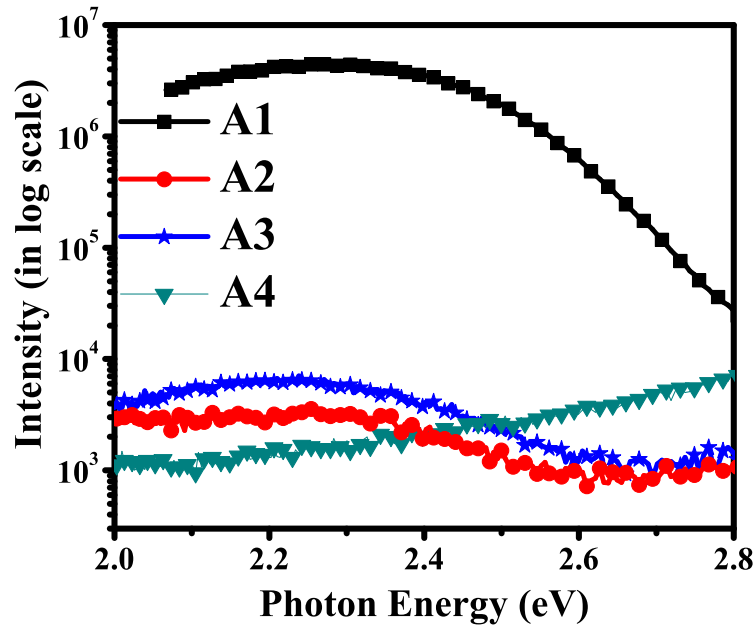


Figure 4.3: shows the yellow luminescence part of PL spectra of the four samples (A1-A4).

emission. The Full Width at Half Maximum (FWHM) values of the PL spectra of all the films tabulated in Table 4.1 show that, rougher samples (A2, A3, and A4) show higher FWHM compared to smooth film A1 (≈ 0.06 eV). We attribute such a broadening of PL spectra to the varying thickness of wall of NWN and presence of a large density of band

tail states¹⁵⁷. The red shift in NBE of A2 and A3 is due to lower strain as compared to A1. Although HR-XRD shows lowest strain in A4 (discussed later), the NBE position is equal to that of A1 (see Table 4.1), which is can be due to the quantum confinement of electrons at the nanowall apex region that are ≈ 10 nm wide¹⁵⁷.

Table 4.1: Results of XRD and PL measurements

Sample Name	Average pore size (in nm)	NBE position (in eV)	FWHM of NBE (in eV)	2θ of (0002) peak (in Degree)	FWHM of (0002) (in Degree)
A1	-	3.43	0.06	34.47	0.06
A2	45 ± 13	3.39	0.13	34.56	1.08
A3	170 ± 31	3.38	0.12	34.57	1.11
A4	215 ± 43	3.43	0.23	34.57	0.83

4.1.3.2 Structural quality of the films and its impact on PL yield

HR-XRD Analysis

In order to investigate the crystallinity and orientation of the samples, HR-XRD studies were carried out on these samples. The 2θ values for (0002) planes and FWHM of rocking curves obtained are listed in Table 4.1. The epitaxial orientation of NWN with respect to Al_2O_3 is seen to be $GaN(0001) \parallel Al_2O_3(0001)$, showing that the grown films are c-oriented. The 2θ values, obtained by $2\theta - \omega$ scan are listed in Table 4.1 and suggest that samples with rougher morphology are more strain relaxed than the smooth film, as validated by Raman spectroscopy in our another study²⁶¹. Table 4.1 and Fig. 4.5 shows the large width of the XRD rocking curve for the grown films in comparison to the epilayer which at first instance suggests that the crystal quality of GaN epilayer (A1) is better than that of A2, A3 and A4. However, if the crystalline quality was bad in these films, it contradicts our observation of the absence of YL and enhanced NBE for A2, A3 and A4 (see Fig.4.2 and 4.3).

To understand the cause of wide FWHM of the rocking curves for the (0002) reflection in Fig.4.5, inspite of lower strain, we considered other causes of XRD peak broadening,

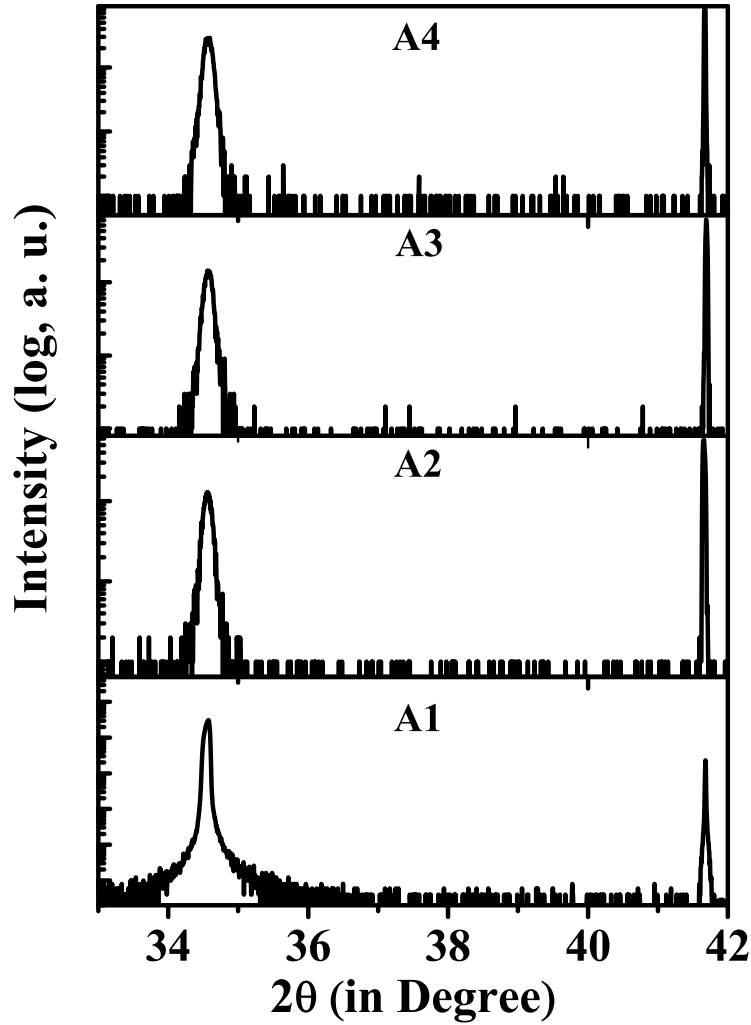


Figure 4.4: shows HRXRD $2\theta - \omega$ scans of all samples.

such as crystallite sizes and mosaicity of the films. Zhang *et. al*²⁶² attributed the broadening of XRD peaks in ZnO nano-walls to their small width (Scherrer broadening). Thus, here to estimate the contribution from Scherrer broadening in these samples we model the role of variable sizes of nanowall on XRD broadening in 2D. The Figure 4.6 (a) represents the small part of nanowall. As shown in figure, first, we divide the nanowall in to many different dimensions as observed in TEM micro-graph (see Fig.4.7). Then, we calculate the broadening of the (0002) XRD peak due to the size of individual crystallites using the Scherrer Formula,

$$D = (0.94\lambda)/\beta\cos\theta \quad (4.1)$$

here $\lambda = 1.54 \text{ \AA}$ and $\theta = 34.47^\circ$ *i.e.* 2θ value of (0002) peak of GaN epilayer and β is

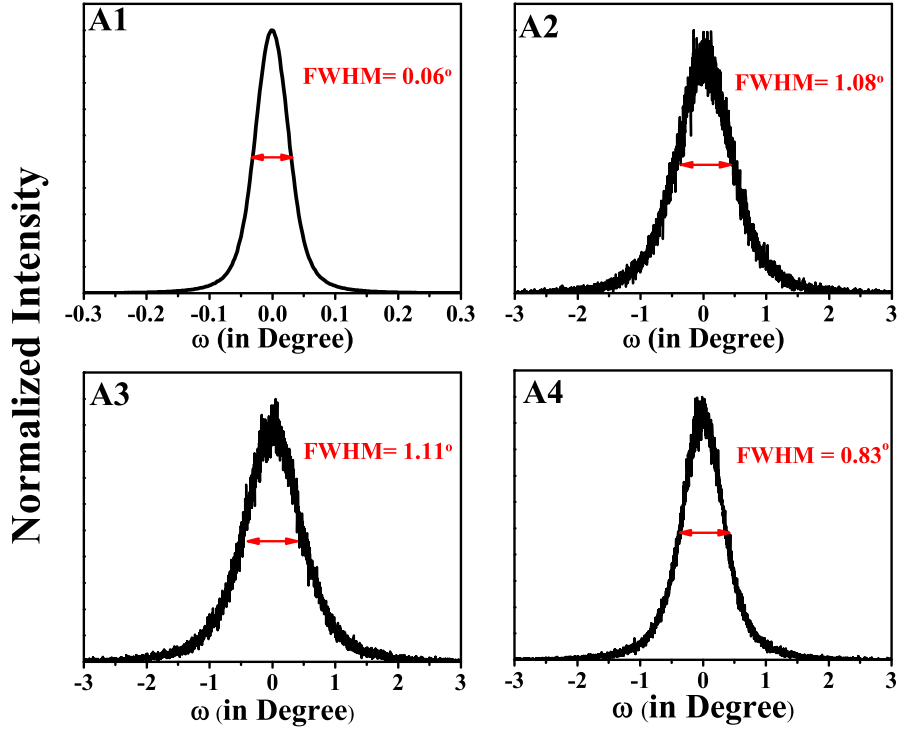


Figure 4.5: shows the HRXRD rocking curves of (0002) plane for samples A1, A2, A3, and A4 respectively

the broadening factor.

Since individual scattered intensity of the crystallite size is related to number of atoms present in the crystallite, the contribution of each crystallite to the final XRD pattern is given by (assuming the XRD peak shape have Gaussian Distribution)

$$Y_{final} = \sum Y_i \quad (4.2)$$

where,

$$Y_i = Y_o + \frac{A_i}{\beta_i \sqrt{\frac{\pi}{2}}} \exp \left[\frac{-2(x_i - x_c)}{\beta_i} \right]^2 \quad (4.3)$$

here, Y_o is a constant quantity, A_i represents the volume fraction (= 1 for crystallite size of 150 nm), β_i is the broadening of the XRD pattern of the respective crystallite size (obtained from equation 4.1), x_i represent ω values and x_c is the peak position of 2θ of XRD pattern. Figure 4.6 (b) shows the simulated XRD broadening (both FWHM and intensity) of individual crystallite and sum of all the individual crystallites. In the present case, even-though the wall dimensions are in nanometer range (≈ 10 nm at tip and ≈ 150 nm at bottom), our estimation of Scherrer broadening (β) is only $\approx 0.1^\circ$ and thus

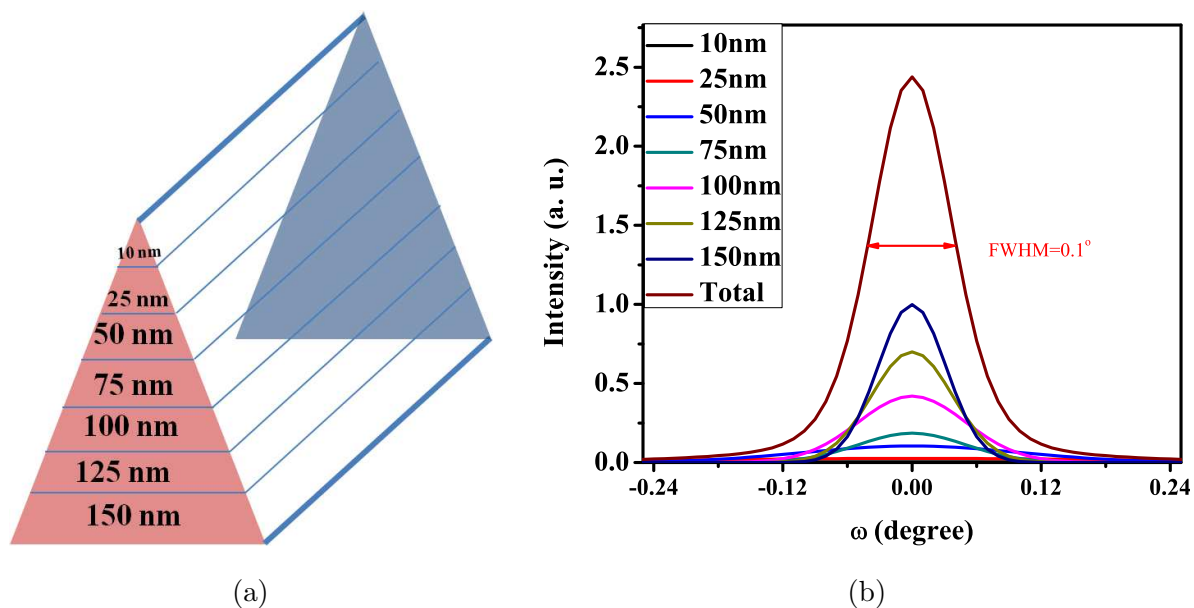


Figure 4.6: (a) shows schematic of the model used for the simulation. Size of NWN is varying from 10 nm to 150 nm. Fig. (b) shows simulated XRD broadenings of (0002) peak for different crystallite sizes and resultant broadening for all the crystallites.

could not account for the observed width in XRD peaks.

HR-TEM Analysis

To study the other sources of XRD broadening such as mosaicity and interfacial properties of the GaN NWN on Al_2O_3 , sample A4 is characterized using HR-TEM and the results are shown in Fig.4.7. Fig.4.7 (A) shows cross-sectional two beam bright field TEM micrograph of GaN/ Al_2O_3 interface of the sample A4 with $\vec{g} = (0002)$ along $[11\bar{2}0]$. The invisibility criterion $\vec{g} \cdot \vec{b} = 0$, for dislocation for $\vec{g} = (0002)$, is used to reveal screw dislocations in this configuration. Inspection of the images shows that the upper part (tip) of the nanowalls don't have any screw dislocations, while they exist in the lower region. Thus, in this morphology the dislocation propagation is terminated at the bottom region of the nanowalls, rendering high structural quality in most part of the nanowalls. Fig.4.7 (B) shows the cross-sectional HR-TEM image of the interface of GaN and Al_2O_3 taken along $[11\bar{2}0]$ zone axis where an atomically sharp interface and growth of a good quality crystalline film can be seen. The inter-planar spacing measured for the substrate and over-layer, matches with the values of 0.43 nm for sapphire (0003) and 0.52 nm for GaN

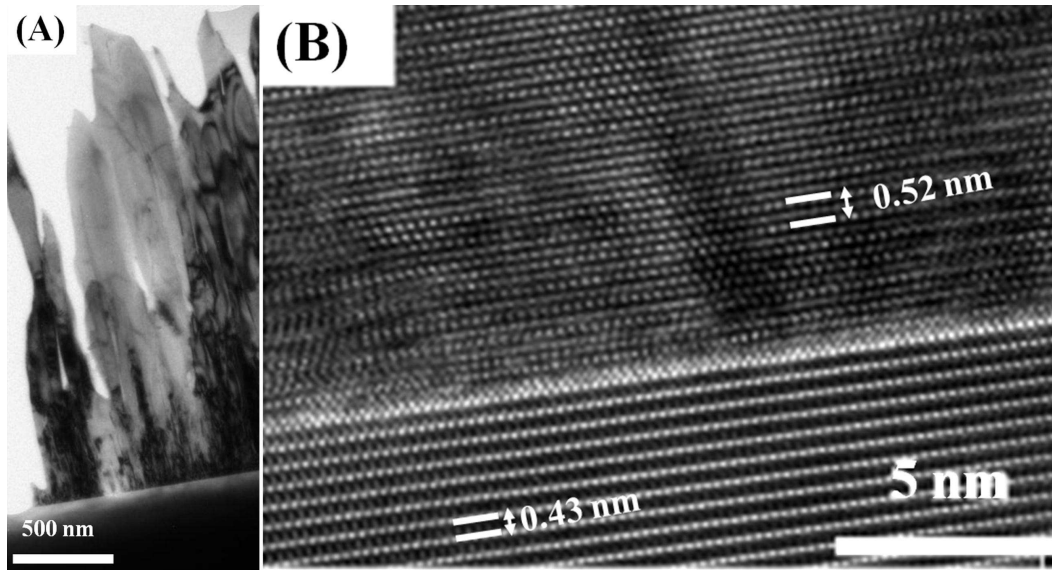


Figure 4.7: (A) shows the two beam bright field HRTEM image of the GaN NWN with $\mathbf{g} = (0002)$ at $[11\bar{2}0]$ zone axis. Figure (B) shows the interface of $Al_2O_3(0001)$ and GaN with the zone axis as $[11\bar{2}0]$.

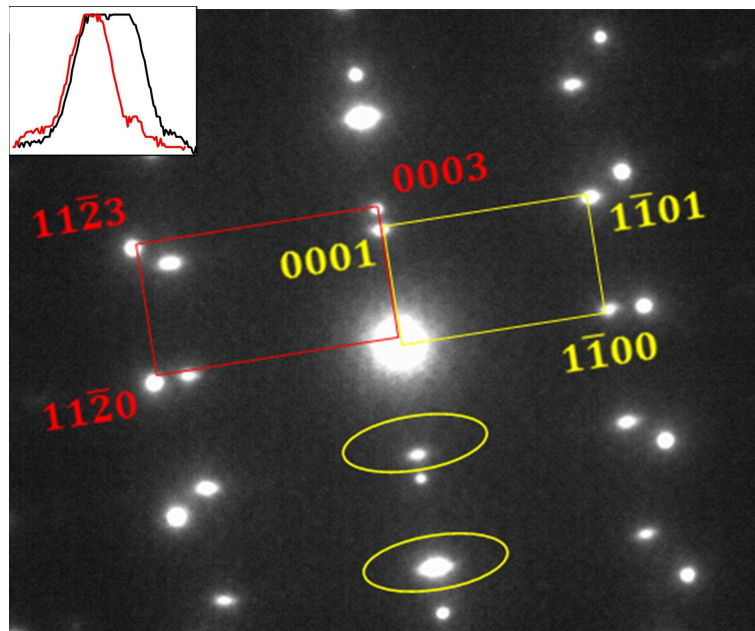


Figure 4.8: shows the SAED pattern of the interface of $Al_2O_3(0001)$ and GaN, with zone axis as $[11\bar{2}0]$. Inset shows line scan of single diffraction pattern along the elongated direction and perpendicular to the same.

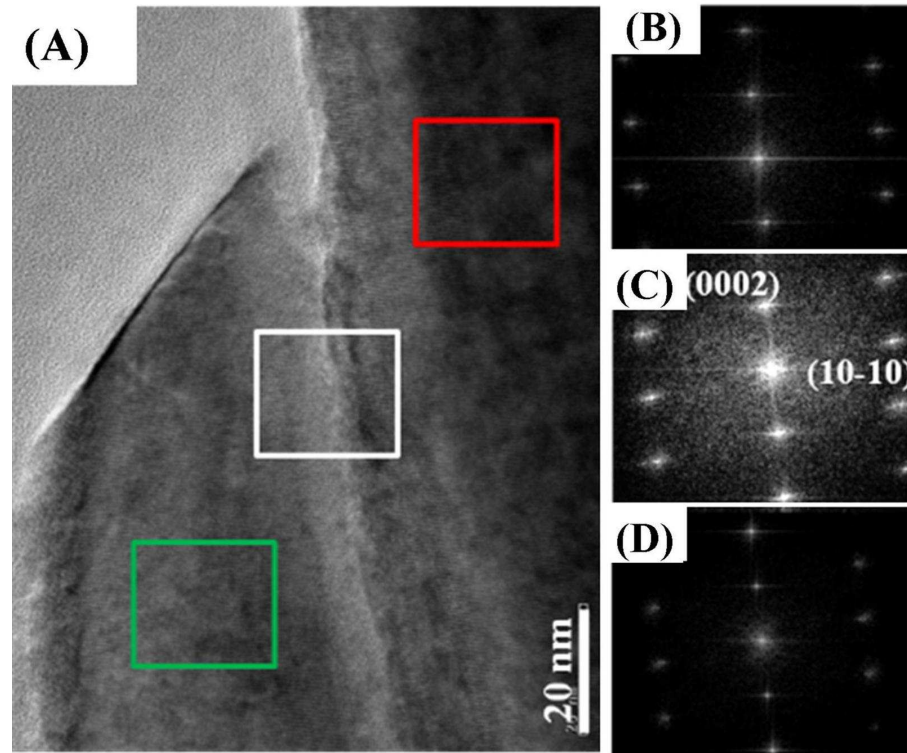


Figure 4.9: Figure (A) shows HRTEM image of two proximal nanowalls. The respective FFT pattern of the regions marked by red, white and green squares in Fig.4.9 (A), are shown in Fig. 4.9 (B), (C) and (D).

(0001) planes respectively. Figure 4.8 is the Selected Area Electron Diffraction (SAED) pattern obtained along the $[11\bar{2}0]$ zone axis from the interface. Both images (Fig. 4.7(B) and 4.8) confirm the high crystalline quality of the wurtzite phase of GaN NWN and its interfacial integrity. The TEM data also confirms the epitaxial relation *i.e.* (0001) GaN \parallel (0001) Al_2O_3 and $(10\bar{1}0)$ GaN \parallel $(11\bar{2}0)$ Al_2O_3 as previously determined by HRXRD.

Inspection of the SAED pattern (see Fig.4.8) shows that the (0002) spots are slightly elongated along the $[10\bar{1}0]$ direction, which indicates the presence of mosaicity in the film. Line scans (shown as left-top inset of Fig.4.8) of an individual diffraction spots (inset of Fig. 4.7(B)) clearly reflects their elongation along the $[10\bar{1}0]$ direction. To further validate the alignment between proximal walls, we consider Fig.4.9(A) which shows a region of the overlap between two proximal Nanowalls. We have performed fast fourier transformation (FFT) of the image in different regions marked in Fig.4.9(A) and are shown as (B), (C) and (D), *i.e.* Fig.4.9 (B) and (D) represent FFT of the two individual nanowalls and (C) shows the FFT of the region where the two walls overlap. Elongation of the (0002) spots

are seen in Fig. 4.9(C) along the $[10\bar{1}0]$ direction while isotropic sharp spots are observed in case of (B) and (D). This confirms that the nanowalls are slightly tilted with respect to each other by $\approx \pm(0.6^\circ)$ and consequently introduces mosaicity to the structure, which causes the broadening of FWHM in the XRD rocking curves in Fig.4.5.

Role of carrier density

To study the role of unintentional doping level to the high PL intensity, we have carried out Hall measurements for the samples A1, A2 and A3. The carrier concentration of sample A4 is obtained by the method discussed by Dhar *et al.*¹⁵⁷. We find that the carrier density of A1 is of the order of 10^{17} cm^{-3} , whereas sample A2, A3 and A4 are of the order of 10^{19} cm^{-3} . Thus, the enhanced band edge emission of sample A4 in comparison to A2 and A3 cannot be ascribed to unintentional doping levels.

Although, samples A2 and A3 both have equal broadening in their XRD rocking curves, the PL intensity of A3 is 4 times higher than that of A2. The observation of rocking curve and PL emission suggests that higher PL intensity does not depend upon the broadening of XRD rocking curve. Further, the PL enhancement from A1 to A4 can also be understood on the basis of Mie scattering theory²⁶³, where the increasing pore sizes act as scattering centers for light¹²⁴. Since the average pore size in NWN (A4) is 215 nm, and is comparable to the wavelength of band edge emission from GaN (364 nm), it makes the pore configuration a highly scattering material with multiple reflections, resulting high light extraction. The increased surface area in the NWN also enhances absorption and renders high PL emission due to the uniquely rough 3D morphology.

4.1.3.3 FDTD Simulations

To provide a description of the effect of pore sizes on light extraction from the GaN porous film, we have performed a complementary Finite Difference Time Domain (FDTD) simulation for simplified geometries of our four samples on a 2D grid as shown in Fig.4.10. The GaN epilayer sample A1 is modelled as a rectangular slab of thickness $1.2 \mu\text{m}$ and the GaN NWN samples A2 to A4 as isosceles triangles of height $1.2 \mu\text{m}$ with varying bases, displaying pore sizes between their tips (Model of A1 and A4 can be seen in left panel in Fig.4.10) which are placed on a sapphire substrate. The pore sizes for samples A2 to A4 were set to 45 nm, 170 nm and 215 nm, respectively. Refractive indices used are 2.6573 for

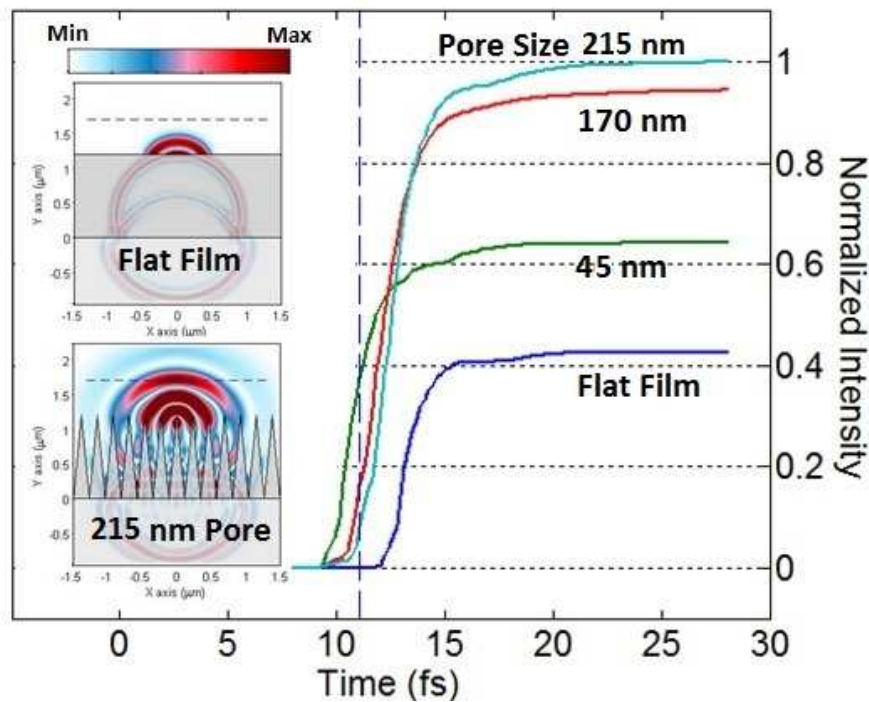


Figure 4.10: shows the time evolution of emitted light intensity obtained by FDTD simulation. The model of field pattern for flat film and Nanowall network (215 nm pore size) are shown in the left panel at 11 fs. The right panel shows the cumulative intensity as a function of time for the films.

GaN and 1.7936 for sapphire. Absorbing boundaries were used on all four sides of the grid. The simple 2D model uses constant refractive indices and does not include dispersion or polarization effect. We have used a single pulse excitation as a point source of light of 364 nm. The source is located at around 300 nm above the base and modeled as a Gaussian pulse in time domain having 1 femto-second (fs) pulse width with an offset of 3 fs from the beginning of the simulation. The grid is $3\mu\text{m}$ long along x - axis with 533 grid points and $3.2\mu\text{m}$ along y -axis with 569 grid points. The smallest length element along each axis is set to 5.6285 nm. The smallest time step (accounting the Courant stability condition) is set to 9.3874×10^{-18} s. Size of the perfectly matched layer (PMLs) is 20 grid points. We have collected the cumulative intensity on a horizontal detector placed at $y = 1.7\mu\text{m}$ spanning more than $2\mu\text{m}$ x - axis and the simulation is run for 28.2 fs. The time evolution of the detected intensity is plotted after normalization with the maximum detected values (right panel in Fig.4.10). The detected cumulative intensity for each sample saturates at

a value when most of the light that could reach the detector has already passed through it. The sample A4 with pore size 215 nm showed the highest emission which is 2.35 times of that of sample A1. This 2-D model qualitatively demonstrates that for isotropic light emission directed upwards when roughness or porosity reduces the total internal reflection and enhances light extraction. The detection onset of the nanostructural films is less than 10 fs, while that of the flat epilayer is larger due to the efficient escape of light from the dielectric.

4.1.4 Summary

In summary, single crystalline stress-free rough surfaces of varying porosity are grown epitaxially on c-sapphire in a PA-MBE system by changing the V/III flux ratio. A comparative study is carried out between a GaN epilayer and grown rough samples using FE-SEM, HR-XRD, room temperature PL and HR-TEM. The band edge intensity is found to strongly increase with the average pore dimensions of the films. The nanowall with largest pore size (≈ 215 nm) shows a two orders of magnitude enhancement of integrated PL intensity compared to that of the GaN flat film. We have performed FDTD simulation that qualitatively demonstrates the role of pore dimensions on light extraction from porous film by the reduction of total internal reflection. Study of SAED and FFT pattern of HR-TEM images reveals that the mosaicity observed by HRXRD in the films is due to misorientation between the nanowall, explaining the broadening of the HR-XRD rocking curves in spite of good structural quality of the films. The enhancement in PL intensity is attributed to the higher light extraction from larger pore sized films due to reduced total internal reflection, high crystalline quality of the faceted nanowalls structure of GaN NWN and higher surface area. The higher PL emission of GaN NWN a strong candidate for use in the fabrication of high brightness LEDs and Laser Diodes.

4.2 Growth Mechanism of GaN NWN

4.2.1 Introduction

The dynamics of shape transitions plays a critical role in the evolution of surface morphology and uniformity of hetero-epitaxial thin film and nanostructure growth²⁶⁴⁻²⁶⁸. Critical to success of such nanostructure, especially while it is forming spontaneously, is the flexibility of the structure. However, lack of understanding on the role of attachment kinetics of adatoms and thermodynamic factors to the self assembly and the shape transitions is the major obstacle in achieving control over the growth of such structures. Therefore, investigations of the growth process of nanostructures enable us to gain high control over the self-assembly. Further, the evolution of a structure from the early stages to the finally attained morphology is a very interesting and complex phenomena as many physical parameters compete with each other during that period²⁶⁹⁻²⁷¹.

We have shown earlier that by controlling V/III ratio, spontaneous formation of porous nanostructures can be achieved by using PA-MBE system,^{258,258,272-274} as also followed by a few other groups^{135,275-277}. In growth of GaN NWN, understanding the growth mechanism is crucial to control the shape and size of the pores, to enhance light extraction efficiency²⁷³. Poppitz *et al.*¹³⁵ carried out a thickness dependent study of porous GaN on 6H-SiC, where they found that the islands get laterally elongated to form a network like structure. Further, Wu *et al.*¹³⁹ demonstrated a similar pathway for the growth of ZnO nanowall on sapphire substrate by Metal-Organic Chemical Vapour Deposition (MOCVD). Both of these reports show step-wise evolution of the morphology, but no clear mechanism is proposed in either case. Here, we monitor the shape transition of the NWN that occurs during the initial stage of the growth as it plays a crucial role in determining the final morphology of thin films and nanostructures²⁶⁴⁻²⁶⁸. In this part of the thesis, we elucidate on the growth mechanism of GaN NWN on sapphire substrate by experimentally monitoring the evolution of surface morphology at intermediate stages of growth, complementing it by using *first-principles* Density Functional Theory (DFT) simulations. We find that the shape transition for this unique nanostructure of GaN from initial 3D island is driven by Structure Dependent Attachment Kinetics (SDAK) induced instability also known as *Edge Sharpening Instability (ESI)*, which was previously used to

Table 4.2: Growth parameters

Sample Name	Ga-K cell temp ($^{\circ}\text{C}$)	N_2 flow rate (sccm)	Duration (minute)
A	1030	4.5	10
B	1030	4.5	20
C	1030	4.5	40
D	1030	4.5	60
E	1030	4.5	80

understand the growth of snow crystals by Libbrecht *et al*^{278–280}. We have undertaken this complementary study of experiment and calculations to correlate such instability induced growth mechanism of thin films and/or nanostructures of the grown GaN samples.

4.2.2 Methods

4.2.2.1 Experimental Details

The GaN films were grown under nitrogen rich conditions by using radio frequency Plasma Assisted Molecular Beam Epitaxy system over (0001) plane of sapphire ($\alpha - \text{Al}_2\text{O}_3$) with base pressure of $\approx 3 \times 10^{-11}$ Torr. The detailed procedure of substrate preparation are discussed earlier in this chapter. Substrate temperature of 630 $^{\circ}\text{C}$ and plasma forward power of 375W were maintained for all the samples grown for this work. The other growth parameters are listed in Table 4.2. The film structure was monitored *in-situ* by reflection high energy electron diffraction (RHEED) with an acceleration voltage of 7 kV, the morphology was determined *ex-situ* by field emission scanning electron microscope (FESEM) with an acceleration voltage of 20 kV and atomic force microscopy (AFM) in contact mode.

4.2.2.2 Simulation Details

Adsorption energy of Ga ad-atom on (20 $\bar{2}$ 1) surface is estimated by total energy calculation using *first-principles* Density Functional Theory (DFT), as implemented in the SIESTA code²⁸¹. Generalized Gradient Approximation (GGA) proposed by Perdew

*et al.*²⁸² is used for the exchange and correlation function. We use the norm-conserving pseudopotentials of Troullier and Martins, with valence electron configurations of Gallium, Nitrogen, and Hydrogen as $3d^{10} 4s^2 4p^1$, $2s^2 2p^3$ and $1s^1$, respectively. A double zeta basis set with polarization functions is used for all atoms. Hartree and exchange correlation energies are evaluated on a uniform real-space grid of points with a defined maximum kinetic energy of 200 Ry. Brillouin Zone of w-GaN is sampled on a Γ -centered $5 \times 5 \times 3$ mesh of k-points in the unit cell of reciprocal space²⁸³. Positions of all the atoms are allowed to relax by the conjugate gradient technique to optimize energy until forces on each atom is less than $0.04 \text{ eV}/\text{\AA}$. The optimized lattice parameters of the unit cell are $a = 3.25 \text{ \AA}$ and $c = 5.23 \text{ \AA}$. We construct a replica of the edge of the pyramid embedded with $(20\bar{2}1)$ surface, makes an angle 75° with c-plane. A vacuum of 15 \AA is added along all three axes to minimize the interaction of image configuration. The bottom layer and surface atoms, except the ones at $(20\bar{2}1)$ facets, were passivated with Hydrogen (see Fig. 4.13(c)). For the construction of the wedge structure, a total of 135 atoms (including H) are used. The adsorption energy of Ga on different sites of $(20\bar{2}1)$ surface is estimated by the equation

$$E_{\text{ads}}(\text{Ga}) = E_{\text{tot}}(\text{adatom} + \text{wedge}) - E_{\text{tot}}(\text{wedge}) - \mu_{\text{Ga}} \quad (4.4)$$

where $E_{\text{tot}}(\text{adatom} + \text{wedge})$ is the total energy of the combined system with Ga ad-atoms and the wedge shape, $E_{\text{tot}}(\text{wedge})$, is the total energy of the pristine wedge and μ_{Ga} is $\frac{1}{8}th$ the total energy of α -Ga. The potential energy surface (PES) is constructed by placing Ga ad-atoms at various sites and allowing them to relax along the perpendicular to the $(20\bar{2}1)$ surface.

4.2.3 Results

To study the initial nucleation and evolution of surface morphology, we carry out growth of GaN NWN for durations of 10, 20, 40, 60 and 80 minutes. The corresponding FESEM images of the resulting morphology are shown in Fig.4.11. A careful visualization of the FESEM image of sample B shows most of the larger islands have tetrahedron (3 faced pyramids) shape (see inside the white circle of Fig.4.11 (a)) while smaller islands have random shapes. Along with these large tetrahedron shaped islands, we also observe a

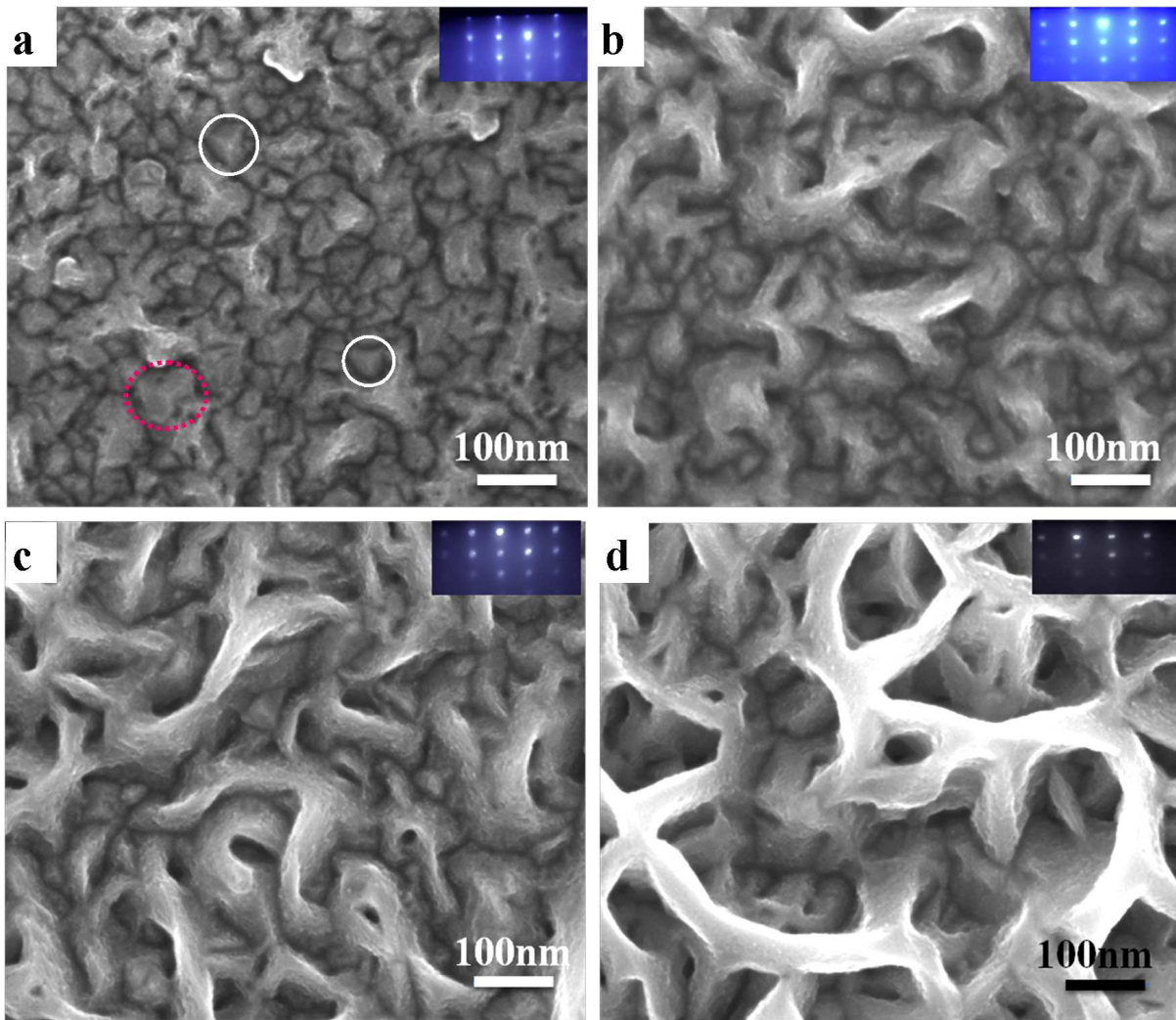


Figure 4.11: (a), (b), (c), (d) show top view FESEM images of sample B, C, D and E, respectively. Top-right inset shows RHEED pattern of respective samples taken along $[11\bar{2}0]$ direction.

few Y-shaped structures (see inside red circle of Fig.4.11 (a)). Sample C, grown for higher duration (40 min) shows mostly Y-shaped structures with a few tetrahedron islands. Further, the length of tails of Y-shaped structure for sample B are $\approx 45\text{-}55$ nm while for sample C they are longer ($\approx 55\text{-}75$ nm). Such increase in length of the tail of the Y-shaped structure with increased growth durations suggests that enhanced growth of the edges is responsible for the Y-shaped morphology. However, not all Y-shaped islands are connected to each other in both samples B and C. For samples grown for higher duration (samples D and E), we observe the Y-shaped structures connect with each other to form wall like features. To further look at earlier stages of island formation, we grow a film for

10 minutes under identical growth conditions. Fig.4.12 (a) and (b) shows the AFM image of samples A and B, respectively. At this early stage of growth (10 mins), we observe the formation of mostly oval shaped 3D islands with a large density ($\approx 3.24 \times 10^{10} \text{ cm}^{-2}$, see Fig.4.12 (a)). The island size distribution is plotted in Fig.4.12(c) where we find that the island sizes have a relatively uniform distribution with mean area $\approx 1900 \text{ nm}^2$ with a standard deviation of 550 nm^2 . However, with increase in the deposition time to 20 minutes, size of most islands increases while that of a few ($\approx 1.05 \times 10^{10} \text{ cm}^{-2}$) remains unchanged (see Fig.4.12(c)), resulting in a broad distribution of island sizes ($\approx 1200\text{-}8000 \text{ nm}^2$). Height profile obtained from AFM images suggest that the height of oval shaped islands (sample A) are around $10 \pm 2 \text{ nm}$ while for sample B, we note that height of bigger and smaller islands are 30 ± 4 and $12 \pm 2 \text{ nm}$ respectively. This AFM analysis suggest that there are two kinds of islands have formed at the initial stages of growth: for first kind neither size nor height changes significantly while for other kind both size and height increases with growth time. It is very clear from SEM and AFM images, that the in-plane growth along the edges of the tetrahedron is dominant, resulting in the formation of the Y-shaped structure. To understand such edge enhanced growth mechanism, it is necessary to understand the dynamics of adatoms on the side facets of the tetrahedron. From line-scan analysis of selected larger islands (see Fig.4.12 (d)) we find that the side walls of the tetrahedron, observed in sample B, make an angle of $75 \pm 2^\circ$ with c-plane, and is identified as $(20\bar{2}1)$ surface of GaN.

Thus, to study the surface diffusion of Ga adatoms on the side surface of the tetrahedron, we construct a wedge shaped structure (schematic shown in Fig.4.13(c)), where the edge is the intersection of $\{20\bar{2}1\}$ planes and is shown in Fig.4.13. We note that on the nitrogen terminated $(20\bar{2}1)$ surface, the atomic arrangements are in following ways:

- Two type of nitrogen atom are present depending upon number of dangling bond(s) associated with them. In one case number of dangling bonds is two while in other it is only one.
- At the edge of the structure the number of dangling bond of nitrogen atoms are two and three, and varies alternatively along the edge.

In the relaxed structure of the wedge, we find the Nitrogen (N) having two dangling bonds at surface forms dimers, whereas at the edge a trimer is formed (see blue arrows

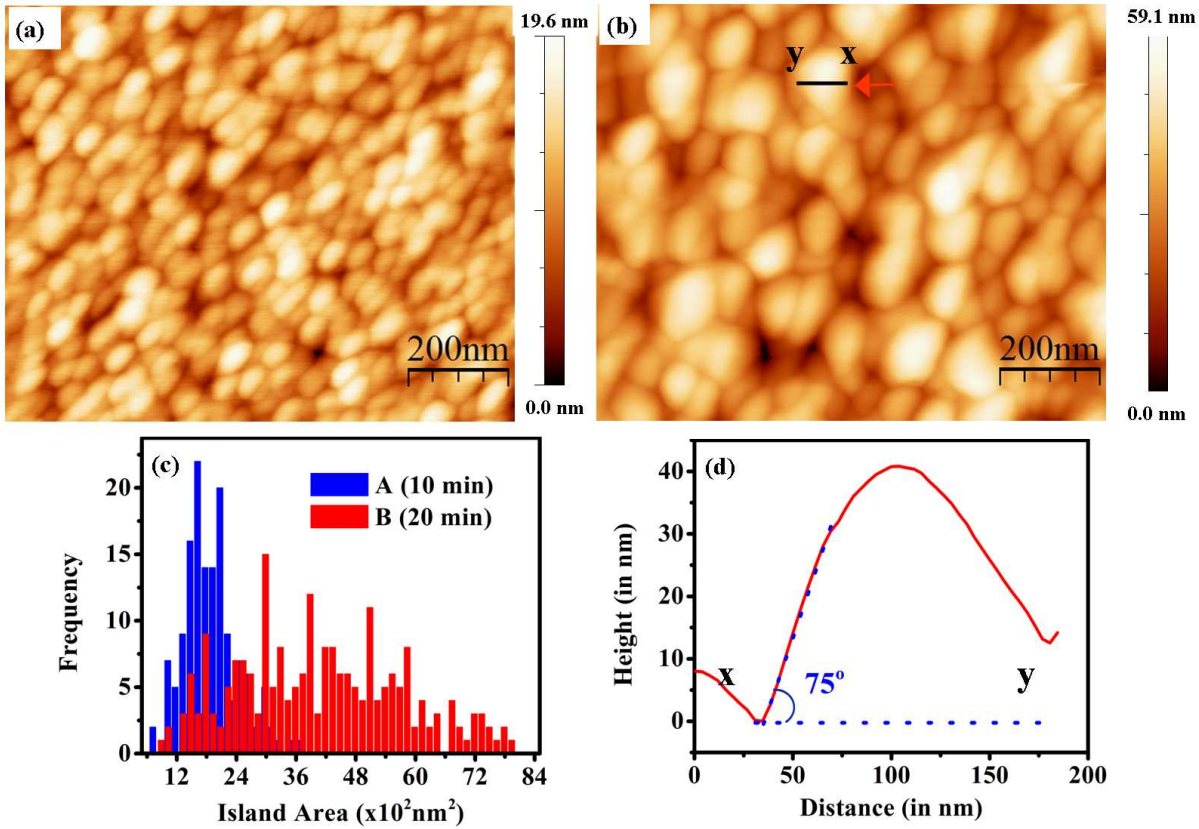


Figure 4.12: (a) and (b) show AFM image recorded in contact mode of samples A and B, respectively. Fig. (c) shows size distribution (area) of islands of sample A (blue bars) and B (red bars). Fig.(d) shows line scan pattern of the island (x,y) shown by a red arrow.

in Fig.4.13(b)) due to Stirling's instability²⁸⁴. We estimate the adsorption energy of Ga ad-atoms at various positions of the relaxed structure; on the surface and at the edge (see Fig.4.14(c)). We find that the most favorable sites for Ga adatom are the hollow sites (see Fig.4.14(c)). The adsorption energy of Ga adatom at the hollow site of O1-O2-A1 triangle is -1.75 eV where the width of the wedge (w) is 6.35 Å whereas, for the hollow site of O2-O3-A2 triangle the adsorption energy is -2.37 eV, while the width w is 3.14 Å. We estimate the adsorption energy at various equivalent points on the surface such as at O1, O2 and O3, H1, H2 and H3, as well as at A1 and A2 (see Fig.4.14 (b) and (c)) and find that the adsorption energy reduces with reduction in the width of the wedge ' w '. However, interestingly, nearby the N-N dimers and N-N-N trimers, the adsorption energy is substantially high due to the strong bonding character of N atoms. Further, to look at the diffusion barrier of the Ga adatom on the $(20\bar{2}1)$ facets, we estimate the adsorption

energy at very close distances (0.4 Å) along the $[11\bar{2}0]$ direction (see Fig. 4.14 (d)). It is very clear that, adatoms have to overcome a barrier potential of nearly 0.36 eV to cross from hollow site of O1-O2-A1 triangle to hollow site of O2-O3-A2 triangle, whereas for reverse diffusion the barrier potential is 0.98 eV.

4.2.4 Discussion

The nucleation mechanism of GaN on sapphire has been studied widely in the literature^{285–287}. Degave *et al.*²⁸⁶ show that growth of GaN on bare surface of sapphire results in the formation of 3D islands from the early stages of the growth, consistent with our observation of the morphology of sample A. It is well known that, in highly lattice mismatched systems (e.g. GaN on c-sapphire (16%)) the growth mode is governed by the interface and surface energies only²⁶⁹. In such systems the strain relaxation of grown island occurs in two different relaxation regimes. At the early stage of growth the elastic relaxation is preferable where the nuclei evolves by aiming to minimize total free

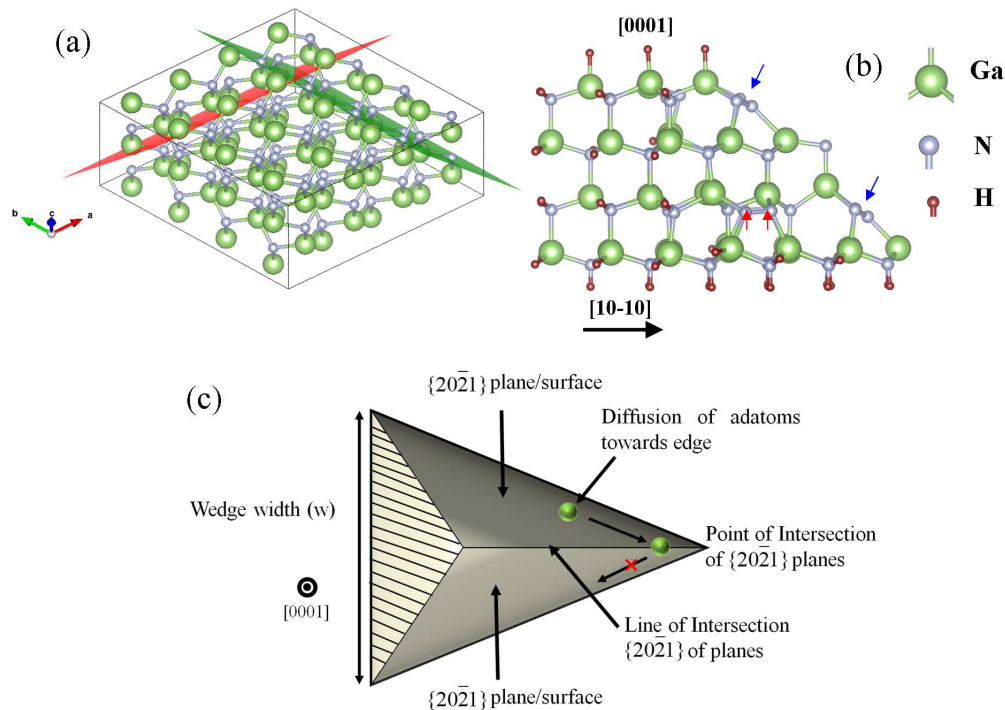


Figure 4.13: (a) shows the construction of the wedge shaped structure. Both red and green surfaces represents $\{20\bar{2}1\}$ planes. Fig.(b) shows relaxed atomic structures of the wedge shape. Fig.(c) shows schematic of the wedge structure.

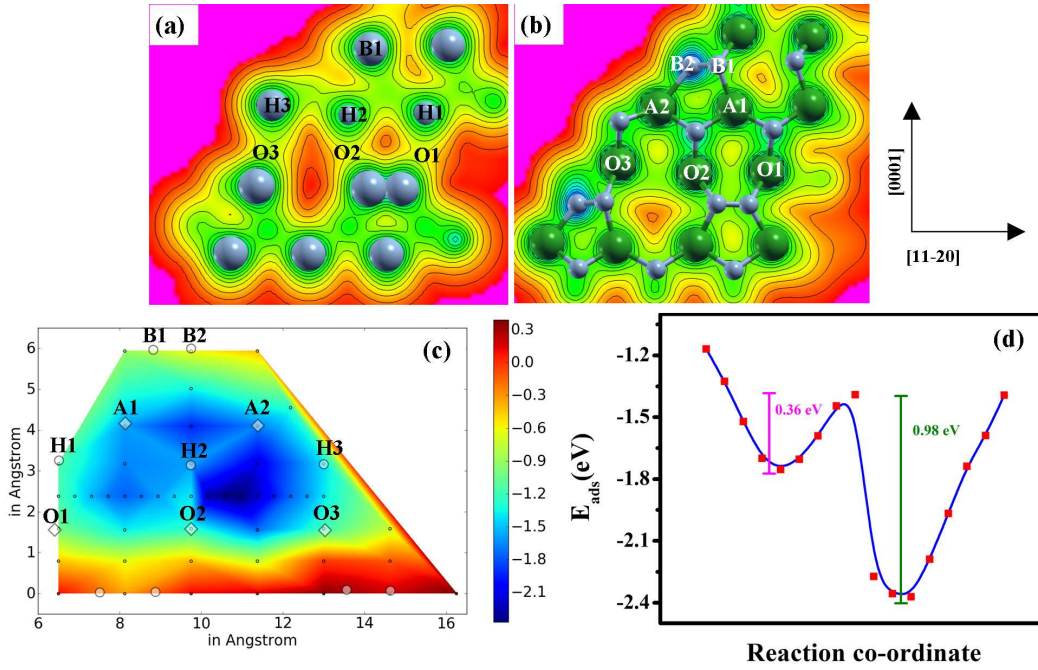


Figure 4.14: (a) and (b) show surface electron charge density plots of 1st and 2nd atomic layers of the $(20\bar{1})$ surface constitutes the side surfaces of the tetrahedron shaped island. Fig.(c) shows contour plot of the estimated adsorption energy of Ga ad-atom at various sites on the surface. Fig.(d) depicts the adsorption energy as a function of spatial coordinates along $[11\bar{2}0]$.

energy per unit volume by relieving the lattice mismatch induced strain ($\Delta E_{\text{elastic}} < 0$) and accordingly by reducing their stored elastic strain energy and/or the nuclei attain the lower energy state by changing its shape (such as formation of crystal facets), surface area ($\Delta A > 0$)²⁸⁸, while with increase in film thickness the plastic relaxation occurs by formation of misfit dislocations²⁸⁹.

Further, as observed experimentally the wider distribution of island sizes in sample B may be due to the fact that the growth of the islands with dislocation is energetically preferable than coherent islands, since the strain energy per unit volume is minimum in the former while later leads to increase in strain energy^{290,291}. Thus, we believe that only the islands with dislocation(s) grows both in c as well as in-plane direction, while coherent islands do not grow significantly. Such phenomena results into wider distribution in island size and height. Observation of wider distribution in island size also indicate that the plastic relaxation mechanism took place within 20 minutes growth of the samples.

The appearance of pyramidal shaped islands is possible due to the difference in adatoms attachment and/or site exchange rates between atomic steps induced by Ga adlayers on GaN (0001)²⁹². The shape transition of such pyramidal islands is mainly governed by the interplay between stored elastic strain energy, total interface and surface energies of all facets composing of all the surfaces of the pyramid. Shchukin *et al.*²⁶⁹ pointed out that, edges of the two surfaces could also play a crucial role in the final shape transition, as at this point the discontinuity of the surface stress occurs. Further, Libbrecht *et al.*²⁷⁹ suggested that, when diffusion related growth is coupled with structure dependent attachment kinetics (SDAK) of ad-atoms the edge enhanced growth can be dominant. Typically, SDAK instability is the consequence of decrease in the nucleation barrier on a faceted surface when the width of the facets decreases, consistent with our *first-principles* calculations. It is relatively easy for Ga ad-atoms to diffuse from thicker part of the wedge (where w is higher) to relatively thinner part (where w is lower *i.e.* towards the point of intersection of $\{20\bar{2}1\}$ planes) but the diffusion of ad-atoms from edges of the wedge to the thicker part is energetically not preferable (see Fig.4.13(c)) as it has to overcome a large potential barrier of 0.98 eV. Thus, it is evident that a large amount of flow of ad-atoms towards the edges (*i.e.* intersection region of the $\{20\bar{2}1\}$ planes) of the pyramid is responsible for edge enhanced growth. This anisotropic growth further sharpens the edge, enhancing the edge growth rate. This positive feedback results in a growth instability promoting formation of sharp edges. This process continues to lengthen the edges of the tetrahedron until it meets with other similar growing edge of another proximal island to form a junction. Once such junctions are formed, the in-plane growth of the edge stops due to unavailability of thin edges for attachment of the adatoms and the dominant growth will now be along perpendicular direction to the surface of the substrate. Based on the FESEM images and results from *first-principles* calculations we present a 2D schematics on the morphological evolution and the shape transition of NWN from 3D islands in Fig.4.15.

At the initial stage of growth we observe oval shaped islands shown with green objects in Fig.4.15. As with increase in growth time we note a wider distribution of size of islands, we portray this situation with a combination of small green objects and larger triangular shaped objects (white colored). In stage III of the growth model we

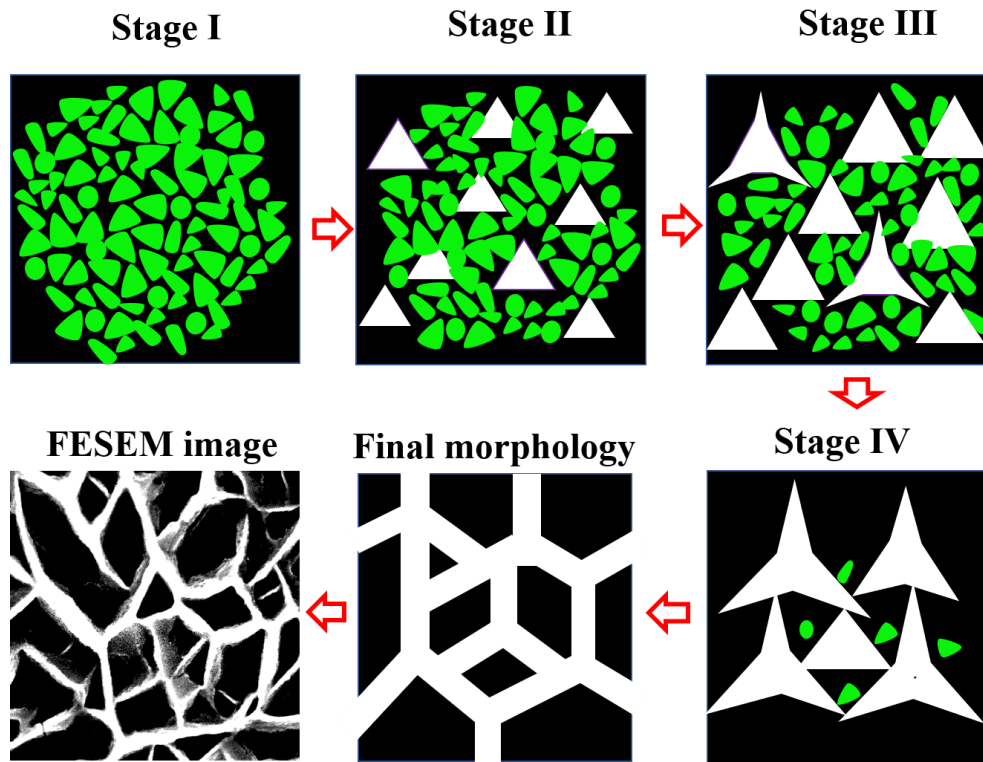


Figure 4.15: show schematic of the shape transition and evolution of surface morphology of GaN NWN. The final model is a false colored (B/W) plan view FESEM image of a NWN grown for 4 hours.

show the appearance of Y shaped structure, whose origin has been discussed in the earlier part of this section. Continuous growth of Y shaped structures along the direction of the edges is depicted in the stage IV of the sketch. When the growing edges meet each other or some other islands, the edge enhanced growth stops. Further, with increase in the growth time, the side facets of the Y-shaped structure change from $(20\bar{2}1)$ to $(10\bar{1}0)$ surface²⁹³ due to low surface free energy of the later²⁹⁴. The predicted final structure is shown as final morphology in Fig.4.15 along with a FESEM image of fully grown NWN. It can be clearly seen that the predicted final surface morphology lookalike with the experimentally observed morphology. The final surface morphology observed with higher growth time^{258,272,274,293} is also consistent with the morphology (hollow columnar) proposed by Libbrecht *et al.*²⁷⁹.

As discussed earlier, the adsorption energy of Ga adatoms nearby the N-N dimers and N-N-N trimers (including at edge) is substantially high, due to the strong bonding character of N atoms. Despite adding an adatom nearby to the dimers they maintain their

stability. Such surface and/or edge reconstruction of N atoms are commonly observed in different semipolar surfaces of III-V semiconductors, but their desorption as N₂ molecule is energetically favorable^{284,295}. Thus, the possibility of the presence of dimers and trimers in the grown crystals is negligible.

4.2.5 Summary

In summary, we have carried out growth of GaN NWN for various durations to monitor the evolution of the surface morphology. At the initial stages we observe the formation of tetrahedron shaped 3D island. With increase in growth time, we observe a wider distribution of islands sizes due to co-existence of coherent and islands with dislocation(s). From *first-principles* simulations we find that the thinner edges of such tetrahedron are more favorable for attachment of adatoms than their thicker counterparts, resulting in edge driven growth. We find an anisotropy in the diffusion barrier for adatoms on (20 $\bar{2}$ 1) surface depending upon width of the facets, that leads to the formation of the nanowall network. We infer that the evolution from 3D island to NWN morphology is a clear example of SDAK instabilities induced shape transition in thin film growth.

Chapter 5

Energetics, stability and electronic structure of vacancy defect in bulk and at $(10\bar{1}0)$ surface of GaN

Electrical characterization of NWN samples reveal a characteristics of high electrical conductivity and is partly due to presence of high densities of carriers (electrons). The atomistic origin of this auto-doping is controversial throughout the literature; especially for MBE grown samples. In this work, we shed light on the role of vacancies to the auto-doping of GaN by using first-principles DFT calculations. Here, we simulate the atomic and electronic structure and estimate formation energies and stability of Ga and N vacancies in bulk as well as at $(10\bar{1}0)$ surface of GaN. A brief discussion on Electron Energy Loss Spectroscopy (EELS) study of GaN NWN is also presented.

5.1 Introduction

Ab – initio calculations have been very effectively used^{296–299} in understanding the electronic properties of pristine *w*-GaN as well as *w*-GaN with defects. Numerous attempts have been made to manipulate magnetism in GaN by incorporating magnetic impurities^{61,300,301} for spintronic applications. Several authors proposed that the cation vacancies in *w*-GaN lead to ferromagnetism^{302,303} while, anion vacancies in *w*-GaN showed paramagnetic behavior³⁰⁴. This is linked with the fact that the cation vacancy acts as

acceptor whereas, anion vacancy acts as donor¹⁵¹. While atomic and electronic structure of Ga vacancies in GaN have been studied extensively, the structure and associated properties of N vacancies remain elusive^{297–299,305–308}.

Overcoming the unintentional n-type doping of GaN has been a great challenge for the semiconductor industry and the origin of such auto-doping is controversial. Van de Walle and Neugebauer¹⁵¹ eliminated the N-vacancies as a possible cause of auto-doping, arguing that its formation energy is too high and suggested that oxygen and/or carbon impurity may explain the observed high conductivity in films grown with Metal Organic Chemical Vapor Deposition (MOCVD), where organometallic precursors are used and could be one of the sources of the mentioned impurities. However, unintentional n-type doping and high conductivity are also observed in GaN grown with Molecular Beam Epitaxy (MBE)¹⁵⁷. As MBE uses pure metal and ultrapure gas as the sources, and the films are grown in Ultra High Vacuum (UHV) conditions, the cause of auto-doping in this case may be attributed to point defects instead of carbon and oxygen impurities. Calculations carried out by Boguslawski *et al.*³⁰⁷ showed that N vacancy introduces a shallow donor state which might be the origin of auto-doping.

There is a lot of variation in the reported estimates of formation energy of N-vacancies in bulk *w*-GaN under N rich conditions based on *ab – initio* calculations, which range from 1.1 to 5.08 eV^{297–299,305–308}. Secondly, the properties related to vacancies at the (10 $\bar{1}$ 0) surface³⁰⁹ have not been studied in depth. Point defects can form more easily in lower dimensional structures, for example at the surface of thin films and nanowires, due to the fact that the surface itself is a planar defect having atoms with lower coordination numbers and dangling bonds.

In the work of Bhasker *et al.*^{157,158,310}, high electrical conductivity was observed for the GaN NWN grown on sapphire (0001) substrate (see Fig.5.1) and the surface electronic structure was proposed to be the origin of its high conductivity. Microscopic imaging of the structure shows that the side wall surface of GaN NWN is (10 $\bar{1}$ 0) surface (see Fig.5.2). To investigate the role of (10 $\bar{1}$ 0) surface in yielding a high conductivity of the material, we simulated the atomic structure and electronic properties of (10 $\bar{1}$ 0) surface of *w*-GaN with point defects such as Ga and N vacancies by using *ab-initio* Density Functional Theory (DFT). For completeness and a consistent comparison, we also obtained atomic structure

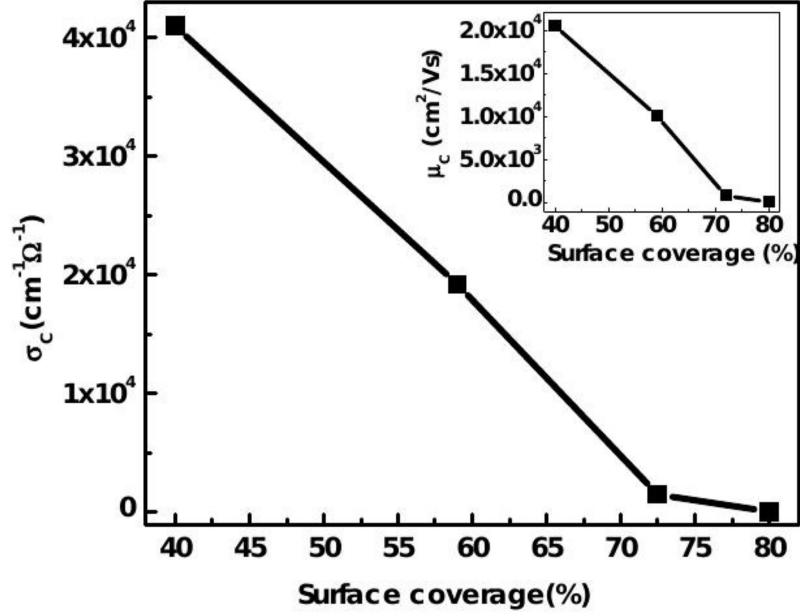


Figure 5.1: Corrected conductivity as a function of the surface coverage. Inset shows the room temperature mobility as a function of the surface coverage. Data was reproduced from the work of Bhasker *et al.*³¹⁰ [Reprinted from AIP Conf. Proc. 1583, 252 (2014), with the permission of AIP Publishing].

and electronic properties of Ga and N vacancies in bulk *w*-GaN.

5.2 HR-TEM and HR-EELS study of NWN

We probe the electronic structure of the NWN by HRTEM and EELS and they are shown in Fig.5.2(D) and (E). We have obtained both the Valence EELS and core-loss EELS of the $(10\bar{1}0)$ surface, where the beam direction is along $[11\bar{2}0]$. Fig.5.2(D) shows the energy loss function and the imaginary part of the dielectric function ($\text{Im } \epsilon(\omega)$), obtained from Kramers-Kronig analysis. We have recorded a transition at 2.2 eV along with an early rise of dielectric profile (from ≈ 3.0 eV) in comparison to typical band gap of GaN (3.4 eV at RT). Observation of 2.2 eV peak in low loss EELS spectra (see Fig. 5.2) indicate the presence of deep and localized states in the gap. The rise of the dielectric profile before the energy of band to band transitions elucidates that a large density of shallow donor or acceptor states are also present in the electronic structure of NWN.

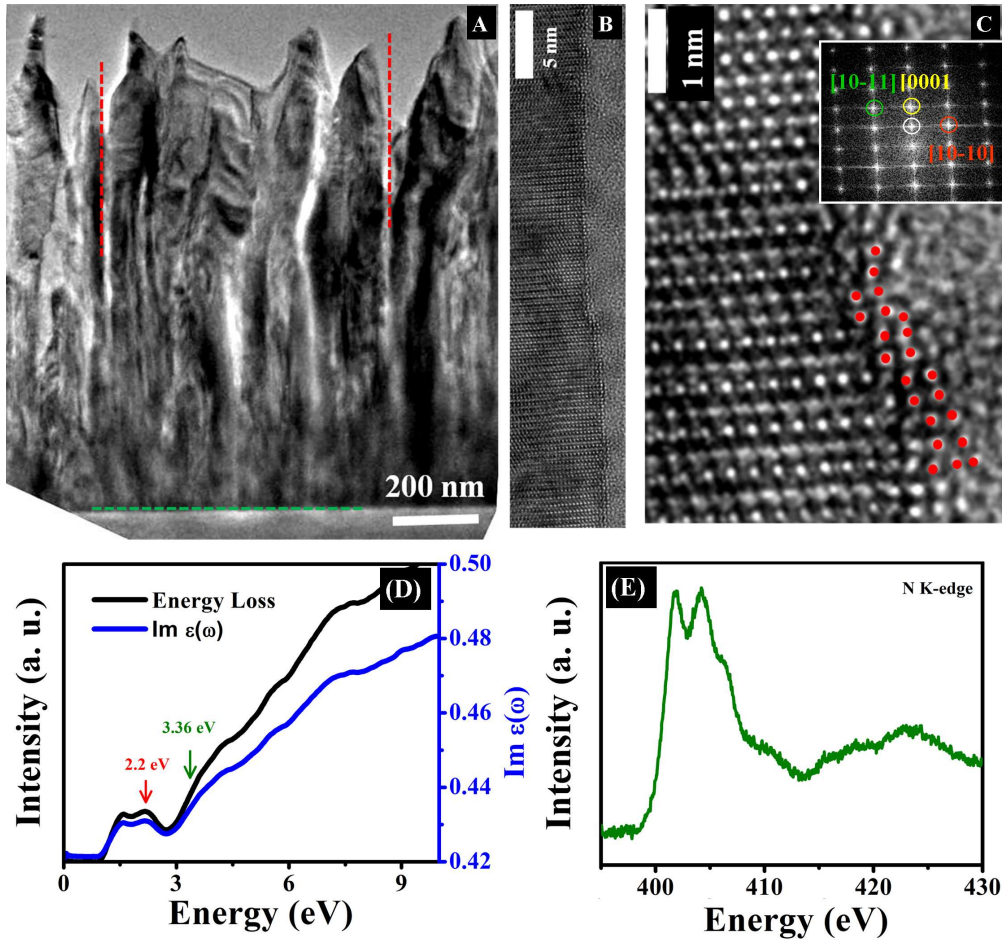


Figure 5.2: Transmission Electron Microscopy (TEM) image of GaN NWN (A). (B) represent the High Resolution -TEM image of the side wall surface which is $(10\bar{1}0)$ surface. The formation of atomic steps can be seen in (C).

5.3 Computational Details

Our calculations are based on density functional theory as implemented in “Spanish Initiative of Electronic System with Thousands of Atoms” (SIESTA) code³¹¹. Local Density Approximated (LDA) functional parametrized by Ceperley and Alder³¹² was used for treating exchange and correlation energy. Norm-conserving pseudopotentials generated by the scheme of Troullier and Martin³¹³ in the Kleinman - Bylander³¹⁴ form were used for ionic cores of Ga and N with valence electronic configuration $3d^{10}4s^24p^1$ and $2s^22p^3$ respectively. Interaction between core and valence electrons was included as nonlinear core correction (NLCC)³¹⁵. Valence electron wave functions were expanded by using a combination of single zeta (SZ) and double zeta orbitals with polarization function

(DZP). Hartree potential and charge density were computed on a uniformly spaced grid with a resolution corresponding to kinetic energy cutoff of 200 Ry. Brillouin zone of w -GaN was sampled by a Γ - centered $5 \times 5 \times 3$ mesh of k-points in the unit cell of reciprocal space³¹⁶. Positions of all the atoms were allowed to relax to minimize energy using the conjugate gradient technique until forces on each atom were less than 0.02 eV/Å. For Ga vacancy in bulk GaN, we used a $4 \times 4 \times 2$ super-cell (128 atoms), which amount to a vacancy concentration of 1.56%. To study the N-vacancies in bulk GaN, we used three different supercell such as $2 \times 2 \times 2$, $3 \times 3 \times 2$ and $4 \times 4 \times 2$, which induces vacancy concentrations of 6.25%, 2.76% and 1.56%, respectively. In simulation of stoichiometric (10 $\bar{1}$ 0) surface of GaN, we used a symmetric slab of 32 atoms. A vacuum space of ~ 12 Å was used to keep the interaction between the periodic images of the slab weak. We used a 2×2 periodic-cell in the plane of the slab to simulate surface vacancies (Ga and N). Formation energy of defects in bulk as well as at surfaces was calculated using the Zhang-Northrup scheme³¹⁷, given by

$$E_f = E_{tot}(V_{N \text{ or } Ga}) - E_{tot}(pristine) + \sum n_i \mu_{i(N \text{ or } Ga)} + q(E_F + E_{VBM} - \Delta V_{0/b}) + E_q^{corr} \quad (5.1)$$

where $E_{tot}(V_{N \text{ or } Ga})$ and $E_{tot}(pristine)$ are the total energies of the super-cell containing the N or Ga vacancy and the reference pristine supercell respectively. n_i and μ_i represent the number of vacancies and chemical potential of i^{th} species respectively. In this work, we have calculated the defect formation energy under both Ga rich and N rich conditions. Under N rich conditions μ_N is the energy of N- atom (obtained from the total energy $E_{tot}(N_2)$ of N_2 molecule, *i.e.* $\mu_N = \frac{1}{2}E_{tot}(N_2)$), and the chemical potential of Ga is calculated using the assumption of thermodynamic equilibrium, *i.e.* $\mu_{Ga} + \mu_N = E_{GaN}[bulk]$; where $E_{GaN}[bulk]$ is the total energy of one formula unit of bulk w -GaN. Similarly, for Ga rich conditions μ_{Ga} is the chemical potential of Ga atoms in bulk α -Ga (*i.e.* $\mu_{Ga} = \mu_{Ga}[bulk]$), and chemical potential of N atom (μ_N) is calculated from thermal equilibrium condition. Under Ga rich conditions, the defect formation energy of Ga and N vacancy are shifted by $-\Delta H_f$ and ΔH_f respectively, as compared to N rich condition, where ΔH_f is the formation enthalpy of w -GaN and is estimated by the formula, $\Delta H_f = E_{GaN}[bulk] - \mu_{Ga}[bulk] - \frac{1}{2}E_{tot}(N_2)$. The estimated value of $\Delta H_f[GaN]$ is -1.9 eV, which is in good agreement with earlier calculations based on LDA^{297,298}. E_F , E_{VBM} stand for fermi energy and bulk valence band maximum of the pristine GaN re-

spectively. $\Delta V_{0/b}$ is used for aligning the electrostatic potentials of bulk and the neutral defective supercells and can be obtained by comparing the electrostatic potentials in the bulk-like region far from the neutral defect and in the pristine bulk calculation. We have used the electrostatic correction term E_q^{corr} for charged defect in the supercell by using the correction method proposed by Van De Walle *et al.*¹⁵⁶ as implemented in CoFFEE code³¹⁸. We have used the static dielectric constant (ϵ_s) of GaN as 9.06 obtained from the literature where similar methodology was adopted³¹⁹ in the estimation of E_q^{corr} .

The thermodynamic transition level (q_1/q_2) between two charge states of defects is estimated by the relation

$$(q_1/q_2) = \frac{E_f(q_1; E_F = 0) - E_f(q_2; E_F = 0)}{q_2 - q_1} \quad (5.2)$$

where $E_f(q; E_F = 0)$ is the formation energy of the defect in the charge state q when the Fermi energy is at the VBM.

Surface energy (σ) is calculated using the relation

$$\sigma = \frac{1}{2A}(E_{slab} - n \times E_{GaN}[bulk]) \quad (5.3)$$

where E_{slab} is the total energy of slab, “ n ” is the number of formula units of GaN in the slab and A is the area of surface unit cell in slab. In simulations of vacancies at the surface, corresponding atoms were removed from the two surfaces of the slab.

5.4 Results and Discussion

5.4.1 Atomic and Electronic structure of bulk w -GaN

5.4.1.1 Pristine bulk w -GaN

The equilibrium lattice parameters (a and c), internal parameter (u) and the band gap (E_g) of bulk w -GaN, estimated by different methods including experimental values are listed in Table 5.1. Our estimates of lattice parameters agree well with earlier calculations and are within a deviation of $\approx 0.4-0.5\%$ from the experimental values³²⁰. Our estimates of the band gap of bulk w -GaN is 2.06 eV at Γ point (see Fig.5.3(A)) is in good agreement with earlier calculations^{321,322} based on plane wave (PW) basis, but is much lower than

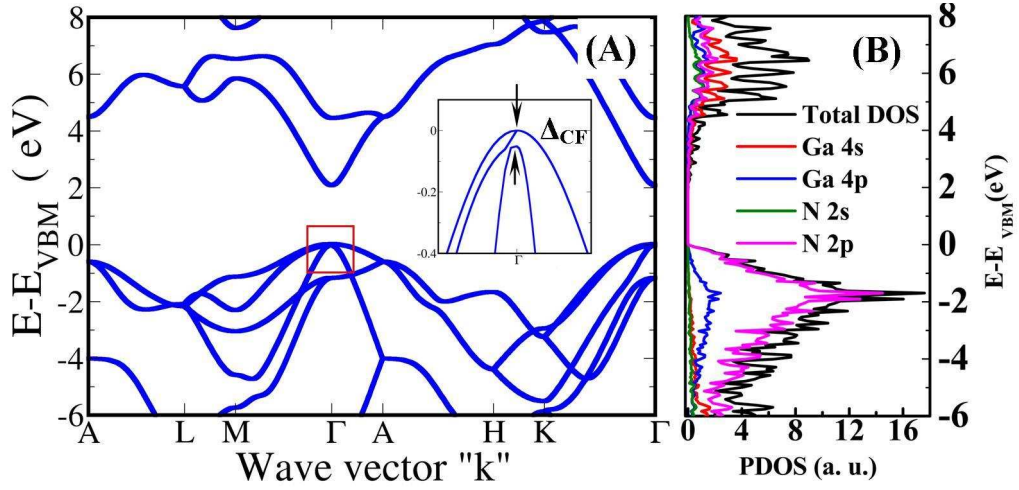


Figure 5.3: Electronic structure of bulk *w*-GaN (A) and total DOS and PDOS are plotted in (B) obtained with SIESTA.

the experimentally observed value of 3.4 eV at RT. Such underestimation of band gap is typical of DFT-LDA calculations^{322–325}.

Projected density of states (PDOS) (Fig.5.3(B)) shows that the valence band is primarily composed of 2p orbitals of N along with a small contribution from 4p orbitals of Ga while the conduction band is composed of 4s and 4p orbitals of Ga and a weak contribution from 2s and 2p orbitals of N. Our estimates of the crystal field splitting (Δ_{CF}) (in absence of spin-orbit coupling) at Γ point is ≈ 50 meV, which is abit smaller than the earlier theoretical estimates of 72 meV by Suzuki *et al.*³²⁶ and larger than 42 meV estimated by Wei *et al.*³²³, where both calculations were carried out by using LDA. The experimental estimates of Δ_{CF} reported in different works spanned from 10 to 25 meV^{327–330}. The theoretical estimated values of Δ_{CF} have been higher than the experimental values. The effective mass of electron near Γ point (conduction band) is estimated using $\frac{1}{m^*} = \frac{1}{\hbar^2} \left(\frac{\partial^2 E}{\partial k^2} \right)$, and our results are $0.16m_e$ ($m_{\parallel}^*, \Gamma - A$) and $0.18m_e$ ($m_{\perp}^*, M - \Gamma$), in good agreement with earlier calculated values ranging from $0.18m_e$ to $0.22m_e$ ^{326–331}, and with the experimental values of $0.18 - 0.29m_e$ ³³². Favorable comparison of our results with published results (see TABLE 5.1) establishes the credibility in the numerical parameters used in our work here.

Table 5.1: Optimized lattice parameters (a and c in Å), internal parameter (u) and band gap (E_g in eV) of bulk w -GaN

	SIESTA LDA Ref-1 ³³³	SIESTA GGA Ref-2 ³³⁴	VASP LDA Ref-3 ³²¹	VASP LDA Ref-4 ³²²	Expt. Ref-5 ³²⁰	Present LDA
a	3.23	3.28	3.155	3.160	3.189	3.173
c	5.19	5.31	5.145	5.150	5.186	5.163
u	-	0.378	0.3764	0.3765	0.377	0.3768
E_g	2.37	1.44	2.12	2.10	3.4	2.06

5.4.2 Atomic and Electronic structure of Ga vacancies in bulk w -GaN

Due to a neutral cation (Ga) vacancies with concentration of 1.56%, four neighbouring N atoms move away from their positions causing a contraction of their bonds with other Ga neighbors by ≈ 1.9 -2.3 %. This agrees qualitatively but is smaller than earlier estimates of the change in bond-lengths of ≈ 3.5 -3.7% reported by Neugebauer and Van de Walle, using a PW pseudopotential based calculation with LDA approximation²⁹⁹ and by Carter and Stampfl³³⁴ using GGA approximation with SIESTA code (2.9-3.7 %). We find that Ga vacancies in charged state of -1, -2, and -3, the contraction in bond length varies from 2.5-2.6%, 3.3-3.4 % to 4.1-4.3%, respectively. Our estimate of the formation energy of neutral Ga vacancy obtained under N (Ga) rich conditions is 6.90 (8.80) eV, which is in good agreement with earlier calculations (see Table 5.3). The formation energy of a Ga vacancy obtained under N (Ga) rich conditions at p-type growth condition with $-1|e|$, $-2|e|$ and $-3|e|$ charge state is 7.17(9.07), 8.29 (10.19) and 10.18 (12.08) eV respectively. From the defect formation energy versus Fermi energy plot (see Fig.5.6 (a)), we find the thermodynamic transition levels (0/-), (-/2-) and (2-/3-) of V_{Ga} are present at 0.27, 1.11 and 1.89 eV, above the VBM. Our estimate to the correction term ($E_q^{corr} + q\Delta V_{0/b}$) is 0.12, 0.65, 1.56 eV for the defects with -1, -2 and $-3|e|$ charge state respectively. We find that neutral Ga vacancy is more stable under p-type growth conditions while $-3|e|$ charged state is more stable under n-type growth conditions. The thermodynamic transition levels

determined here agree qualitatively with the calculation where finite size corrections are adopted³³⁵. In the electronic structure of GaN with Ga vacancy concentration of 1.56% (see Fig.5.4(A)), we identify the defect bands (denoted as D) by visualizing the spatial distribution of wave functions at high symmetry k points such as Γ , A and M. Calculated electronic structure supports that the neutral Ga vacancies in bulk GaN are triple acceptors and the associated states are spin polarized. The three states are located 0.59, 0.63 and 0.63 eV above the valence band maximum (VBM) at Γ -point.

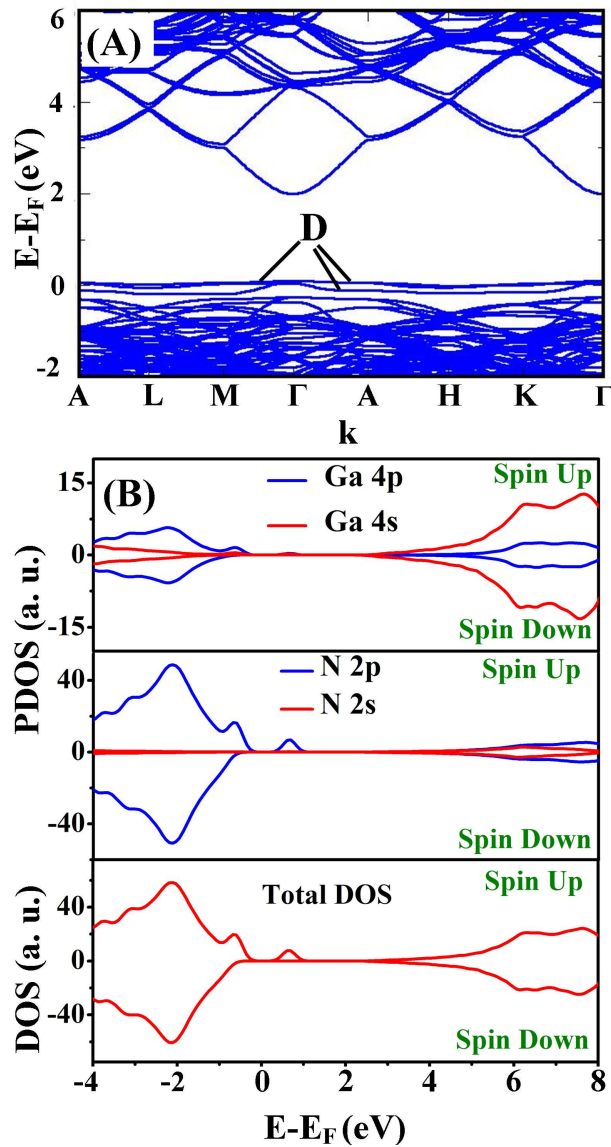


Figure 5.4: Electronic structure of bulk *w*-GaN with Ga vacancy concentration of 1.56% (A). Total DOS and PDOS are plotted in (B).

As is evident in the spin dependent DOS and PDOS of GaN with vacancy concentra-

tion of 1.56% (see Fig.5.4 (B)), acceptor states have the 2p orbital (N) character, and arise from those N atoms which co-ordinate with the Ga vacancy, displaying a local magnetic moment of $\approx 3.0 \mu_B$, consistent with earlier report³⁰². The estimated spin polarization energy ($E_{spin\ un-polarized} - E_{spin\ polarized}$) is ≈ 0.2 eV, suggesting that the magnetic state may be realized well above the room temperature. However, in the work of Dev *et al.*³⁰² the coupling between spins of the neutral Ga vacancies in bulk GaN is found to be Anti-Ferro Magnetic (AFM) in nature. As the neutral Ga vacancies in bulk *w*-GaN act as p-type dopants having weakly dispersed bands with a width ($\approx 0.4 - 0.7$ eV) and thus the observed higher conductivity of GaN is unlikely to arise from neutral Ga vacancies.

5.4.3 Atomic and Electronic structure of N vacancies in bulk *w*-GaN

To simulate N vacancies at varying concentrations in bulk *w*-GaN we use three supercells, *i.e.* $2 \times 2 \times 2$ (32 atoms), $3 \times 3 \times 2$ (72 atoms) and $4 \times 4 \times 2$ (128 atoms), and removed one N atom that causes vacancy concentrations of 6.25%, 2.76% and 1.56%, respectively. As stated earlier, reports of defect structure and formation energy of N vacancies in N-rich conditions exhibit a wide spread^{297-299,305-308}, partly due to two different relaxation processes proposed by different groups. Van de Walle *et al.*³³⁶ reported, using plane wave DFT (LDA) (32 atom supercell *i.e.* vacancy concentration of 6.25%), that the neighbouring Ga atoms move away from the N-vacancy site and found that the subsequent contraction of Ga-N bonds near the vacancy is $\approx 4\%$. This is consistent with the calculations of Gulan *et al.*³³⁷, where the contraction of Ga-N bond length is by $\approx 3.7-3.9\%$ (96 atom supercell) based on a GGA approximation of DFT and atomic orbital basis for the expansion of Kohn-Sham states. Further, Carter *et al.*³³⁴ reported a similar trend by using the GGA calculations with SIESTA code, but their estimates of bond length contraction is much weaker ($\approx 0.2-0.3\%$ (96 atom supercell)) compared to the results discussed earlier. They concluded that such low values of outward relaxation may arise from the inclusion of Ga 3d electrons in the valence. Contrast to these results, Gorczyca *et al.*²⁹⁸ reported inward relaxation of Ga atoms towards the N vacancy in 32 atoms supercell of bulk cubic phase of GaN (*c*-GaN) using the LMTO method (LDA) and an elongation of Ga-N bond by $\approx 2\%$. Another report by Chao *et al.*³³⁸ based on

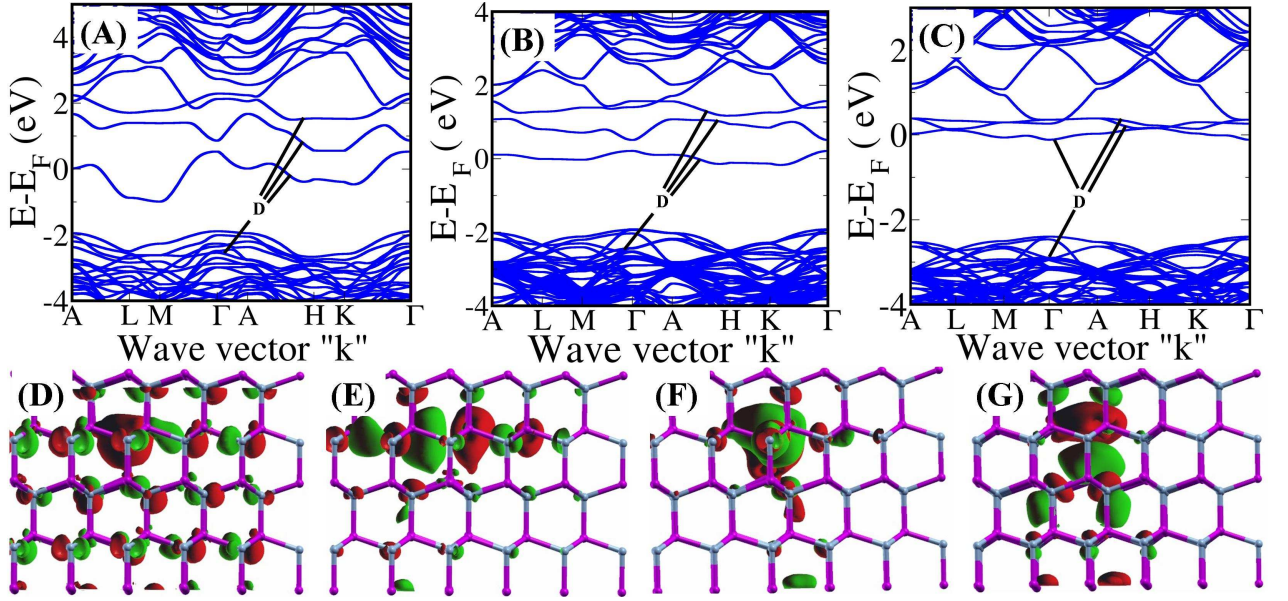


Figure 5.5: (A), (B) and (C) shows electronic structure of N vacancies in bulk *w*-GaN with vacancy concentrations of 6.25%, 2.76%, and 1.56% respectively. All identified defect bands are designated as D. The wave function of defect bands that lie below the VBM and the CBM are visualized and charge distribution of the bands are shown in (D), (E), (F) and (G) for the vacancy concentration of 1.56% respectively, with an isosurface value of $5.0 \times 10^{-2} e/\text{\AA}^3$.

calculation with a plane wave basis code with GGA also showed an inward relaxation of Ga atom causing the elongation of Ga-N bonds by ≈ 1.9 -3.4 % using a 16 atom super-cell.

To present a clear picture of ionic relaxation due to N-vacancies in *w*-GaN, we have considered three different concentrations of N-vacancies : 6.25%, 2.76%, and 1.56%. The structural changes due to ionic relaxation in these configurations are similar, and the Ga atoms that co-ordinate with a N vacancy move towards the vacancy site causing elongation of their bonds with N neighbours. The extent of elongation of bond-length varies with N-vacancy concentration. In the case of vacancy concentration of 6.25%, 2.76%, and 1.56%, the Ga-N bond stretches by ≈ 1.23 -2.5%, 0.8-3.6 % and 0.6-0.7% respectively, similar to the theoretical predictions of Gorczyca *et al.*²⁹⁸ and Chao *et al.*³³⁸. A recent work based on HSE methodology which is computationally much more expensive also predicts a similar trend³³⁹. Such type of ionic relaxation has also been seen in the case of N vacancies in Indium Nitride (InN)³⁴⁰. For N vacancies in charged states such as $+1|e|$,

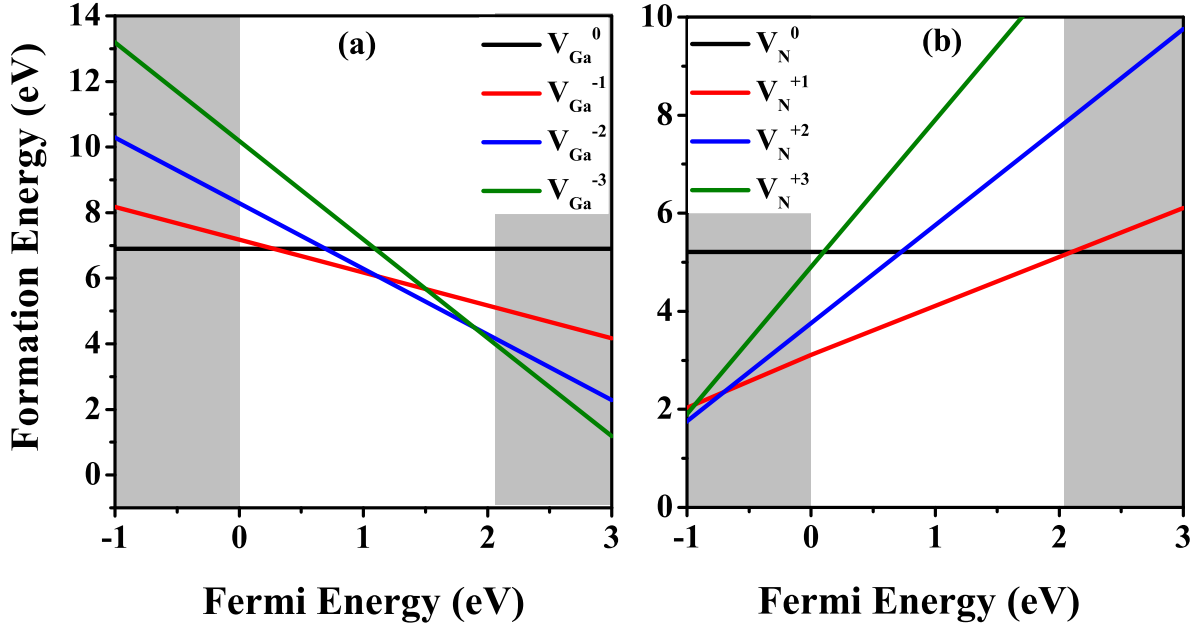


Figure 5.6: Defect Formation energy of Ga vacancy (a) and N vacancy (b) versus Fermi level in bulk. The white region indicate the LDA calculated band gap.

$+2|e|$ and $+3|e|$, the nearest neighbour Ga atoms displace away from the N-vacancy site causing reduction in Ga-N bond length to 0.10-0.35% .

Formation energy of a N vacancy estimated as a function of concentration is ≈ 4.73 , 4.75 and 5.21 for $2 \times 2 \times 2$, $3 \times 3 \times 2$ and $4 \times 4 \times 2$ supercell respectively, under N-rich conditions. The estimated formation energies of V_N in p-type condition with charge state of $+1|e|$, $+2|e|$ and $+3|e|$ are 3.10, 3.75 and 4.90 eV respectively. The thermodynamic transition levels of V_N such as $(+/0)$, $(2+/3+)$, $(3+/+)$ are lie 2.10 eV above the VBM (*i.e.* inside the conduction band), 0.7 and 0.9 eV below the VBM respectively. Our estimation of the correction term ($E_q^{corr} + q\Delta V_{0/b}$) is 0.17, 0.74 and 1.70 eV for defects with $+1|e|$, $+2|e|$ and $+3|e|$ charged states respectively. We find that V_N in $+1|e|$ charge state is most stable throughout the band gap region within DFT-LDA (see Fig.5.6 (b)).

N vacancy in the bulk w -GaN is a triple donor and introduces four defect states in the electronic structure. Out of these defect states, as shown by Van de Walle *et al.*²⁹⁹; one fully occupied state lies below the conduction band and three other defect states lie inside the conduction band manifold. However, the work of Carter *et al.*³³⁴, where an outward ionic relaxation are noted, revealed the presence of three singlet states near the

CBM, two of which are below the CBM by 0.1 and 0.9 eV respectively and third one is above the CBM by 0.3 eV. In addition, there is a state about 0.5 eV below the VBM. To find the energies of defect states as a function of concentration of N vacancy in GaN, we examined their electronic structure and DOS (see Fig.5.5). At all concentrations of N-vacancies considered here; one fully occupied state is present below the VBM and the other three states are present near the conduction band minimum (CBM). We have visualized the bands at different high symmetry k points and identified the defect bands shown in Fig.5.5(D),(E),(F) and (G) for the N-vacancy concentration of 1.56%. The energy level of fully occupied band lies below the bulk VBM by 0.6 eV for defect concentration of 6.25 % while for 2.76% and 1.56% this defect band lies 0.5 eV below the VBM. The other three states lie in the gap below the CBM.

Further, to analyse the magnetic properties of N-vacancies in bulk *w*-GaN, we have obtained spin-polarized DOS within the LDA. At all the defect concentrations studied here, we do not find any net magnetic moment. Our results are consistent with the results of Xiong *et al*³⁴¹, while they differ from the other works^{304,305} that reported a net magnetic moment of $1.0\mu_B$ per N-vacancy. To further-check our results, we performed “fixed-spin” calculation with a fixed net magnetic moment of $1.0\mu_B$, and found out the N-vacancies with vanishing magnetic moment is energetically lower than with a net magnetic moment of $1.0\mu_B$ by 0.23 eV, at N-vacancy concentration of 6.25%. Although, N-vacancy is a triple donor, the presence of a fully occupied state below the VBM makes it effectively a semiconductor with one electron per single N-vacancy for conduction. Higher defect formation energy and the presence of a fully occupied state just below the VBM indicate that the cause of auto-doping is not the N vacancies in bulk *w*-GaN. Secondly, very weak dispersion and band widths of the defect bands indicates that N vacancy states are localized and may not contribute to the observed high electrical conductivity in GaN NWN.

5.4.4 Atomic and Electronic structure of Pristine ($10\bar{1}0$) surface

($10\bar{1}0$) - surface of *w*-GaN has two configurations of surface termination, of which the one with a single dangling bond per atom is energetically more stable than the other one with two dangling bonds at the surface³⁴⁴. This prompted the use of former in the

Table 5.2: Calculated change in bond lengths (Δb) w.r.t. bulk, vertical separation between surface Ga and N atoms (Δz), buckling angle (ω_b), surface energy (σ) and band gap (E_g) of $(10\bar{1}0)$ surface of w -GaN.

	Present calculation	PWPP	VASP	VASP	PWPP
	LDA	LDA	LDA	GGA	LDA
		Ref-1 ³⁴²	Ref-2 ³²²	Ref-3 ³²²	Ref-4 ³⁴³
Δb (in %)	6	6	7.23	7.51	6
Δz (in Å)	0.44	0.22	-	-	0.36
ω_b (in °)	14.03	7	7.5	8.183	11.5
σ (in meV/Å ²)	168	118	123	97.70	-
E_g (in eV)	1.86	-	1.815	1.534	-

present calculations, where a slab geometry is used to model the pristine non-polar $(10\bar{1}0)$ surface of GaN. In the relaxed $(10\bar{1}0)$ surface of w -GaN (shown in Fig.5.7(B)), Ga atoms at the surface of the slab move inwards into the bulk, whereas N atoms move outward into the vacuum, causing a vertical separation of ≈ 0.4 Å along $\langle 10\bar{1}0 \rangle$ between Ga and N atoms and buckling of surface Ga-N bond by 14.2° , which is slightly over-estimated than $7 - 11^\circ$ obtained in calculations based on PW basis^{322,343}. Upon structural relaxation at the surface, bond length of Ga-N at $(10\bar{1}0)$ surface reduces to 1.83 Å *i.e.* contracted by $\approx 6\%$ *w.r.t* that in bulk. This agrees well with earlier works^{322,342,342,343,345,345}, where it was suggested that the structural relaxation of $(10\bar{1}0)$ surface involves re-hybridization of surface Ga and N atoms resulting in sp^2 and sp^3 hybridization respectively³⁴², which is also evident in our analysis. Our estimates of the surface energy (σ) of $(10\bar{1}0)$ surface is 168 meV/Å² which is a slight overestimation in comparison to other published reports (see Table 5.2).

From the surface electronic structure (shown in Fig.5.7(C) and (D)), a fundamental direct band gap obtained for the $(10\bar{1}0)$ surface slab is 1.86 eV, which is 0.2 eV lower than the calculated bulk band gap. This is because of the two surface states that arise within the band gap of bulk w -GaN. The occupied surface N state (S_N), which mainly originates from the $2p$ orbital of the N atoms, from 1^{st} surface layer and 2^{nd} sub-surface layer, with a small contribution from atoms in the 1^{st} sub-surface layer. In the electronic structure it

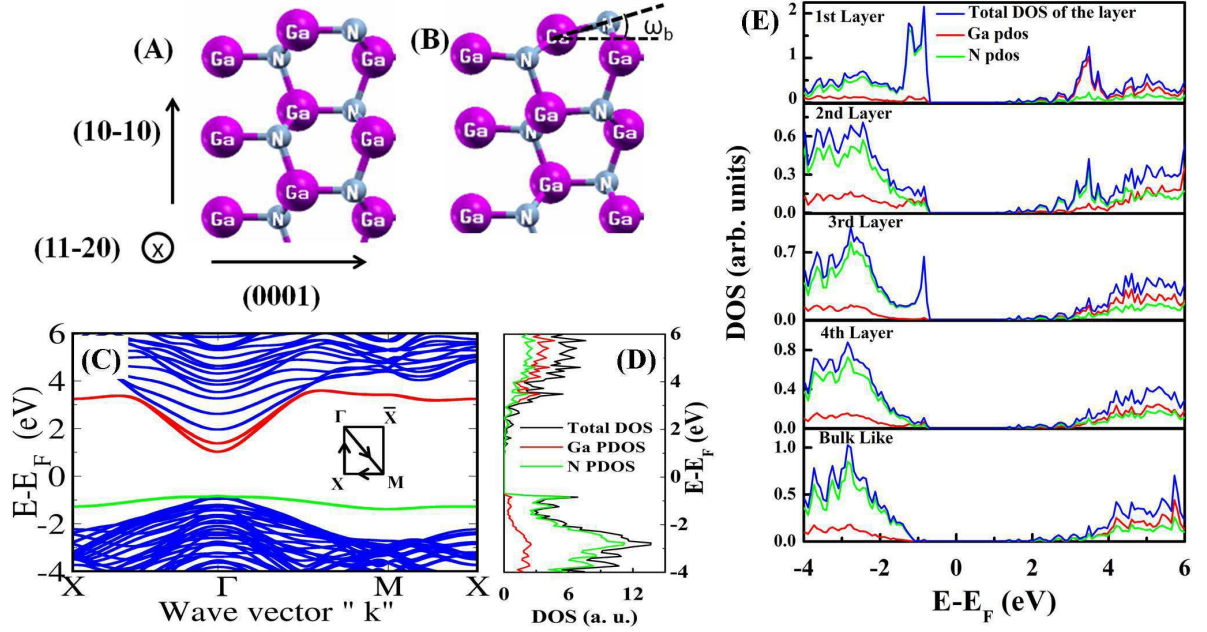


Figure 5.7: (A) and (B) shows ideal and relaxed slab for $(10\bar{1}0)$ surface respectively. (C) shows surface band structure of 1×1 slab of $(10\bar{1}0)$ surface. The band colored in red denotes the surface Ga state and in green represent surface N state. DOS along with PDOS of N (green) and Ga (red) atoms are shown in (D). Layer resolved total DOS (in black lines) of the slab with the projected DOS of N (in green) and Ga (red) atoms are shown in (E).

appears near to valence band and has a weaker dispersion with a band width of 0.44 eV reflecting its confinement to surface. Unoccupied Ga surface state (S_{Ga}) originates mainly from 4s orbitals of the Ga atoms and from 1st layer with a weaker contribution from 2nd layer of the slab. Unlike S_N , S_{Ga} has a higher dispersion with a band width of 2.2 eV and appears near to the conduction band in the electronic structure. Layer resolved DOS (see Fig.5.7(E)) clearly shows the origin of surface states, where a significant difference can be seen between DOS of the bulk-like layers and the first layer of the slab. From the spin polarized DOS it is seen that the dangling bonds at $(10\bar{1}0)$ surface do not necessarily show spontaneous spin polarization. The pristine $(10\bar{1}0)$ surface is insulating in nature, and our estimate of the effective mass of electrons in Ga derived surface states is $\approx 0.2m_e$ similar to that of bulk. Thus, high electrical conductivity may not arise from the conduction through these surface states either.

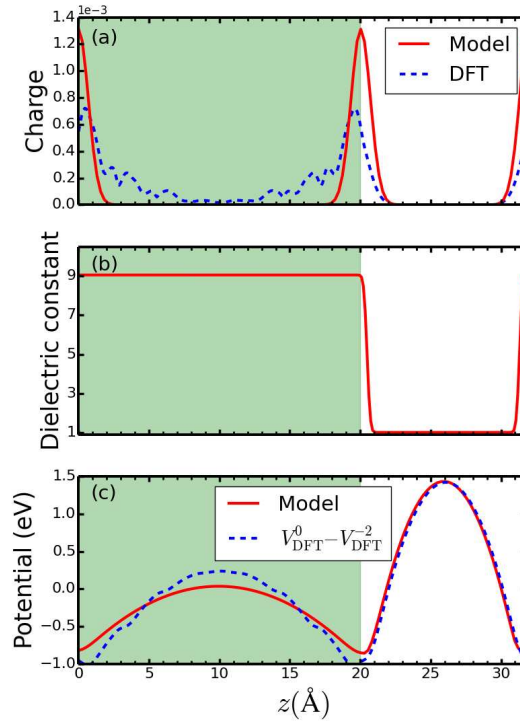
Methodology used in the estimation of E_q^{corr} for slab calculations

Figure 5.8: (a) shows charge density profile of defect state obtained from DFT calculation (dashed line) and model profile used for estimation of E_{corr} . (b) shows dielectric profile used for same. (c) shows the Hartree potential obtained from DFT calculation (dashed line) and with model charge distribution (solid line)

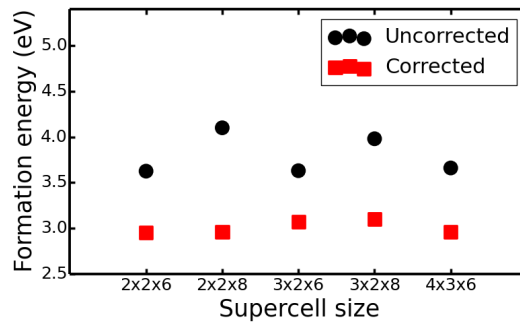


Figure 5.9: shows formation energy of gallium vacancy with -1 charge state with various supercell sizes. Note that for these calculation ionic relaxation were not performed.

Before we discuss effects of Ga and N vacancies on structural and electronic properties of $(10\bar{1}0)$ surface of GaN, we provide a brief discussion on the methodology and reliability

of the estimation of E_q^{corr} term of Eqn. 5.1. The correction term is computed using the CoFFEE code³¹⁸ by solving the Poisson equation for a model system. Figure 5.8(a) shows a plot of the planar averaged defect wavefunction. It can be seen that the defect states are localized at the surface, around the site of the defect. To obtain the electrostatic corrections, they are modelled using a Gaussian distribution as shown in Fig. 5.8(a). A model dielectric profile of the slab is constructed as shown in Fig. 5.8(b) to mimic the total charge density of the slab. The value of the dielectric constant inside the material is taken as 9.06 and outside the material as 1. Figure 5.8(c) shows the DFT difference potential, $V_{DFT}^0 - V_{DFT}^{-2}$, and the model potential. They match well far from the defect, which indicates that the chosen model charge and dielectric profile are appropriate for this system. For the estimation of E_{iso} , we extrapolate the value of the model electrostatic energy (E_{per}) to infinitely large supercell. The electrostatic correction is then given by $E_{iso} - E_{per}$. In Fig.5.9, we show the uncorrected and corrected formation energy of V_{Ga} on the surface of the slab with -1 charge state, with varied supercell sizes and different vacuum dimensions. The thickness of the GaN slab is kept fixed in these calculations. The corrected formation energies are found to be the same (upto 0.1 eV) irrespective of the supercell size or the vacuum dimension.

5.4.5 Atomic and Electronic structure of Ga-vacancies at $(10\bar{1}0)$ surface

In the simulations of Ga vacancies at the $(10\bar{1}0)$ surface, we used a 2×2 in-plane super-cell (128 atoms) and introduced a vacancy at Ga site on both surfaces of the slab amounting to a surface Ga vacancy concentration of 25% (surface Ga:N=0.75). Upon structural relaxation of the $(10\bar{1}0)$ surface with Ga vacancies at the surface, we find that the neighboring N atoms move away from vacancy site causing contraction of Ga-N bonds ($\approx 1.5 - 2\%$) in the neighborhood of vacancies compared to the ideal Ga-N bonds at $(10\bar{1}0)$ surface. A similar structural relaxation process (contraction in Ga-N bonds by $\approx 2.3-3.5\%$ ³⁴⁶ and $\approx 2.9-3.7\%$ ³³⁴) is reported in the case of Ga vacancies at $(10\bar{1}0)$ side wall surface of GaN NWs. We find that the contraction in Ga-N bonds varies from 1.5-1.7%, 2.0-4.81% to 3.4-6.5% with the surface Ga vacancies in charged states of $-1|e|$, $-2|e|$ and $-3|e|$ respectively. Our estimate of the formation energy of a Ga vacancy at

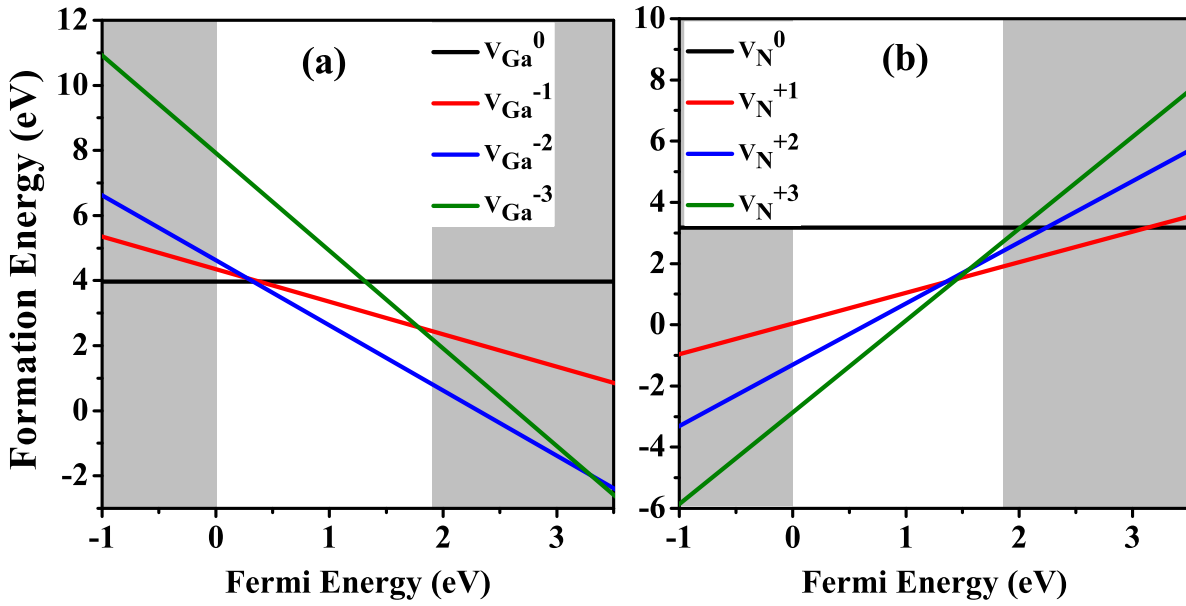


Figure 5.10: Defect Formation energy of Ga vacancy (a) and N vacancy (b) versus Fermi level on surface of the slab. The white region indicate the LDA calculated band gap.

($10\bar{1}0$) surface under N-rich conditions is 3.97 eV, which is 2.93 eV less in comparison to the bulk and is a consequence of lower coordination of atoms on the surface. Our estimate of the formation energy of surface Ga vacancies in charged states of $-1|e|$, $-2|e|$ and $-3|e|$ are 4.35, 4.62 and 7.92 eV respectively. Formation energy versus Fermi energy plot (see Fig.5.10 (a)) shows neutral Ga vacancies are more stable under p-type growth conditions while Ga vacancies in $-2|e|$ charged state is more stable under n-type conditions with a thermodynamic transition level ($0/2^-$) at 0.32 eV above N atoms derived surface state (or surface VBM).

In the electronic structure of ($10\bar{1}0$) surface with 25% Ga vacancy concentration (see Fig.5.11), three vacancy-related states (designated as D) are evident near the valence band just above the N atoms derived surface states. Thus, neutral Ga vacancies at ($10\bar{1}0$) surface act as a p-type dopant and has a low band width suggesting that the Ga-vacancies are not the source of the high electrical conductivity observed in GaN NWN. Furthermore, PDOS analysis (Fig.5.11(B)) shows that these hole-states originate from 2s/2p orbitals of the N atoms that co-ordinate with the Ga vacancy and are spin polarized.

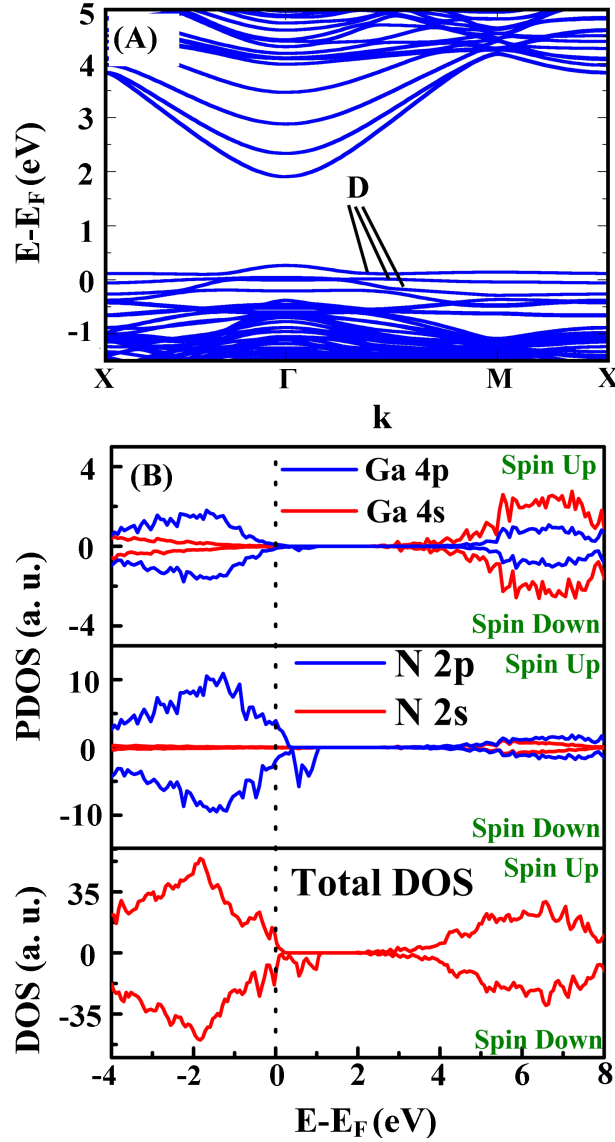


Figure 5.11: Spin un-polarized electronic structure (A) and spin polarized DOS and PDOS (B) of $(10\bar{1}0)$ surface slab of *w*-GaN with surface Ga vacancy concentration of 25%.

Due to symmetry breaking at the surface, the three N atoms contribute asymmetrically to the net magnetic moment with individual magnetic moments of 1.462, 0.427 and 0.427 μ_B respectively. Estimated spin polarization energy of 1.1 eV is relatively higher than that for bulk GaN. Thus, magnetization due to Ga vacancies at the surface is more stable than that in the bulk *w*-GaN. From Fig.5.10 (a) it is clear that formation energy of the V_{Ga} is too high to form in abundance which can contribute significantly to the free carrier concentration. Secondly, the obtained carrier type that is responsible for electrical conductivity in the GaN NWN is electron, thus we reiterate Ga vacancies are

not responsible for the high electrical conductivity observed in the GaN NWN.

5.4.6 Atomic and Electronic structure of N-vacancies at $(10\bar{1}0)$ surface

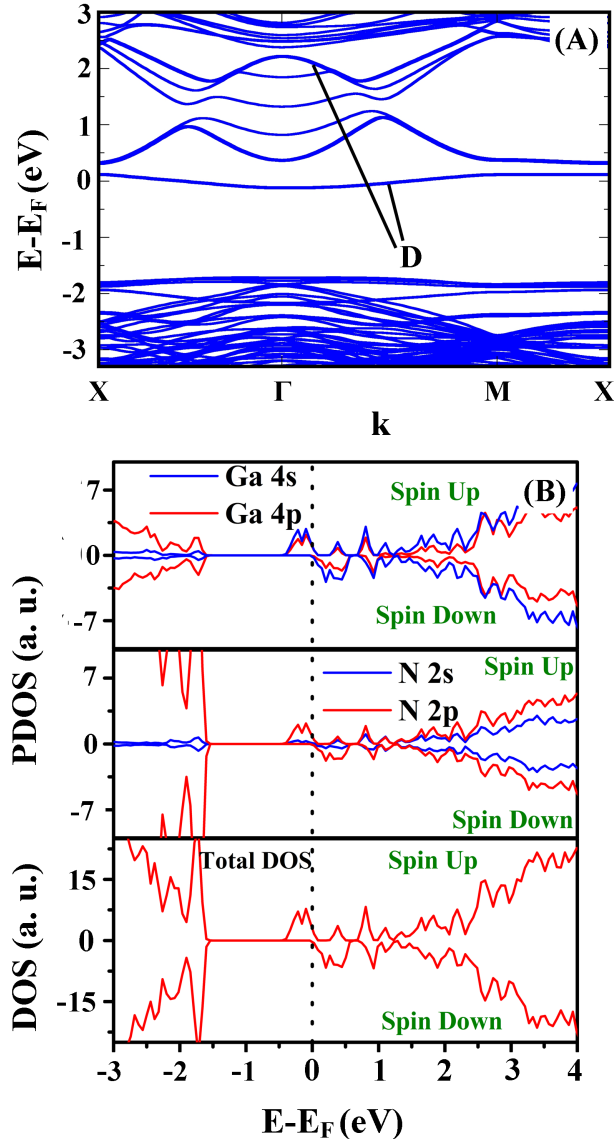


Figure 5.12: Spin un-polarized electronic structure (A) and spin polarized DOS and PDOS (B) of the $(10\bar{1}0)$ surface of GaN with 25 % of N vacancies.

To simulate N-vacancies at the $(10\bar{1}0)$ surface, we introduced a vacancy at N site on each surface of the 2×2 in-plane super-cell of slab amounting to a surface N vacancy concentration of 25% (surface Ga:N=1.33). We find upon structural relaxation of $(10\bar{1}0)$

surface with N vacancies at surface, the Ga atoms surrounding a N vacancy are found to move inwards the vacancy, resulting an elongation of Ga-N bonds by 2.6 - 6 % in comparison to the bond length at the pristine $(10\bar{1}0)$ surface. Because of the N vacancies on $(10\bar{1}0)$ surface, the basal plane Ga atom of vacancy site get displaced towards the vacuum, while remaining surface Ga atoms move inwards to bulk. Similar structural changes have been reported by Carter *et al.*³³⁴ in case of neutral N vacancies at the $(10\bar{1}0)$ side wall surface of a GaN NWs. Further, in $+1|e|$, $+2|e|$ and $+3|e|$ charged states of surface N vacancies, the stretching of Ga-N bonds varies from 0.64-1.56%, 0.67-1.12% to 0.48-0.51% respectively as compared to the ideal $(10\bar{1}0)$ truncated surface. Our estimate of the formation energy of a N vacancy at $(10\bar{1}0)$ surface of *w*-GaN is 3.17 eV, which is 2.04 eV less than for bulk *w*-GaN. Table 5.3 shows the comparison of formation energies of vacancies obtained in this work with those presented in the literature. The estimated defect formation energy of a surface N vacancy in charges states $+1|e|$, $+2|e|$ and $+3|e|$ are 0.04, -1.31 and -2.86 eV respectively. Formation energy versus Fermi energy plot (see Fig.5.10) reveals that N-vacancies in $+3|e|$ charged state is most stable under p-type growth conditions while $+1|e|$ charged state is more stable under n-type conditions with a thermodynamic transition level (3+ / +) 1.45 eV above surface VBM. It is clear that formation energy of the N-vacancy, both in bulk and at $(10\bar{1}0)$ surface, is significantly less than that of Ga vacancy suggesting the concentration of N-vacancies will dominate over that of Ga vacancies during the crystal growth. We can infer from Fig.5.10 (b) that N-vacancy can form spontaneously up to a Fermi level ≈ 1.0 eV above surface VBM. We further note that the Fermi level pins at 0.35 ± 0.02 eV below the surface CBM.

Electronic structure of the $(10\bar{1}0)$ surface with a N-vacancy (see Fig.5.12) at the surface reveals that they also act as n-type dopant and donate only one electron per vacancy for conduction. Because of the N vacancy at $(10\bar{1}0)$ surface, a half-occupied band appears in the fundamental band gap about 0.33 eV below the CBM at the Γ point, while leaving the remaining defect bands to overlap with the conduction and valence bands. We find that the band width of the band near the Fermi level is ≈ 0.25 eV, and is spin polarized. In contrast to N-vacancies in the bulk *w*-GaN, asymmetry in spin polarized DOS (see Fig.5.12(B)) can be seen near the Fermi level. From the spin polarized DOS, we find that the origin of this state is in 4s/4p orbitals of Ga atoms that co-ordinate with the

surface N vacancy and 2p orbitals of nearby N atoms. A net magnetic moment of $\approx 1.0 \mu_B$ per surface N vacancy is estimated. The Ga atom in the basal plane which is having 2 dangling bonds (db) due to the surface N vacancy contributes $0.415 \mu_B$ each, whereas the other two Ga atoms present in the 1st subsurface (with 1db) contribute $0.1 \mu_B$ to the total magnetic moment. Rest of the magnetic moment arises from the neighboring Ga and N atoms. A spin polarization energy of 0.11 eV is estimated, which is relatively lower than that of surface Ga vacancy. Thus, relative stability of the magnetization surface N-vacancies is weaker than that of surface Ga vacancies.

Further, a closer look at the HR-TEM image of NWN (see Fig.5.2 (A) and (B)) reveals that the side wall surface makes an angle of $\approx 90^\circ$ with (0001)-plane, with tapered surface at the top of the film due to formation of atomic steps (see red dots in Fig.5.2(C)). FFT pattern of HR-TEM image (see Inset Fig 5.2 (C)) confirms that the sidewalls consist of (10 $\bar{1}$ 0) surfaces of GaN. To simulate such atomic scale steps in the structure, we removed two N-atoms from each of the surfaces of the slab, which gives rise to a surface N-vacancy concentration of 50%. As the slab is periodic and extends in the XY plane, removal of two N-atoms from the surface is equivalent to removing a line of atoms creating a step. We considered two distinct configurations in the simulation of these atomic step structure (A and B) as shown in Fig. 5.13 (A) and (B). The separations between two N vacancies are 3.173 Å and 6.06 Å in A and B respectively. Total energies of the A and B structures reveal that configuration A is more stable than configuration B by 0.25 eV per (2x2) surface unit cell *i.e.* proximal vacancies are more stable and promote the clustering of vacancies.

Ionic relaxation for configuration A shows that all the surface Ga atoms present at the surface move along the (0001) direction and into the bulk region, by 0.45 Å from their ideal positions. The remaining N atoms get displaced towards vacuum. Such a displacement of Ga atoms leads to the formation of Ga metallic clusters which include Ga atoms of the first sub surface that are near the vacancy sites. The separation between surface Ga atoms and 1st subsurface Ga atoms near the N vacancies is ≈ 2.5 Å, which is very close to the Ga-Ga bond length in bulk α -Ga (2.534-2.818 Å)³⁵². Ionic relaxation of configuration B shows an unusual relaxation pattern and the simulated STM image obtained with constant current mode is shown in Fig.5.13 (D). From the STM image we

Table 5.3: Vacancy formation energy for Ga and N vacancy in bulk w -GaN and at $(10\bar{1}0)$ surface of w -GaN under both Ga and N rich conditions. All the values are given in electron volt (eV) unit.

Conf.	charge state	present calculation		ref-1 ³⁴⁸		ref-2 ³⁴⁹	ref-3 ³⁵⁰	ref-4 ³⁵¹
		Ga-rich	N-rich	Ga-rich	N-rich	Ga-rich	Ga-rich	Ga-rich
V_{Ga}^{Bulk}	0	8.80	6.90	7.02	6.58	8.40	8.84	9.06
	-1	9.07	7.17	8.90	8.46	8.83	9.23	9.31
	-2	10.19	8.29	10.56	9.60	9.60	9.98	9.95
	-3	12.08	10.18	14.14	13.70	10.67	11.14	11.05
V_N^{Bulk}	0	3.31	5.21	2.59	3.03	3.16	-	-
	+1	1.20	3.10	-0.58	-0.14	0.82	-	0.10
	+2	1.85	3.75	-	-	0.95	-	-
	+3	3.00	4.90	-1.95	-1.51	0.89	-	-1.08
V_{Ga}^{Surf}	0	5.87	3.97	-	-	-	-	-
	-1	6.25	4.35	-	-	-	-	-
	-2	7.34	4.62	-	-	-	-	-
	-3	9.82	7.92	-	-	-	-	-
V_N^{Surf}	0	1.27	3.17	-	-	-	-	-
	+1	-1.86	0.04	-	-	-	-	-
	+2	-3.21	-1.31	-	-	-	-	-
	+3	-4.76	-2.86	-	-	-	-	-

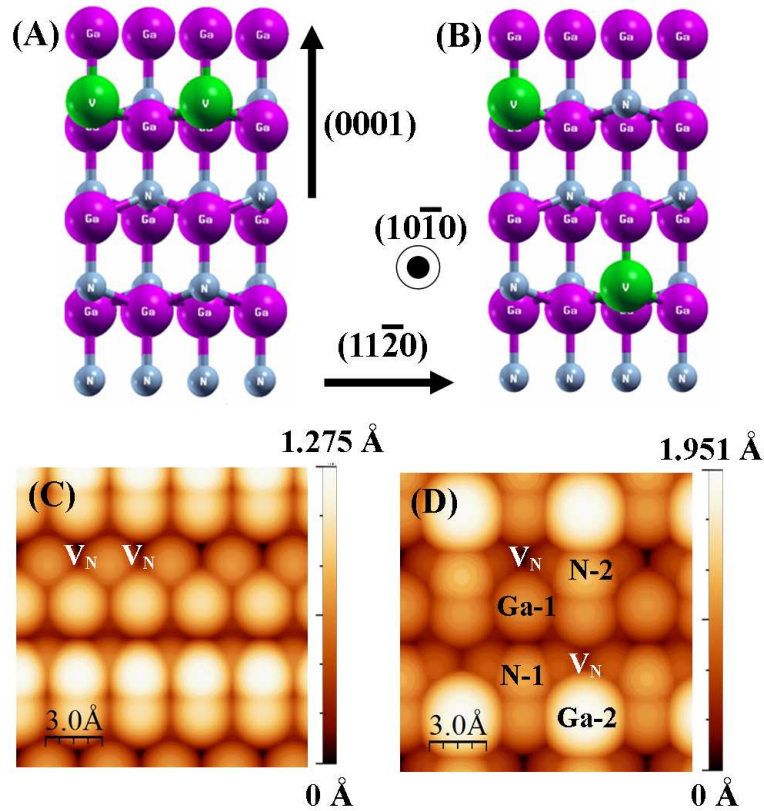


Figure 5.13: (A) and (B) shows the ideal atomic structure of vacancy configurations A and B respectively (Green spheres represent vacancy positions). (C) and (D) represent contour map representation of simulated STM image of surface configuration A and B respectively, computed with WSxM software³⁴⁷ with constant current mode. The scales represent the height of the surface atoms from the 1st subsurface layer.

can infer that the basal plane Ga atom (Ga-1) moves towards the bulk *i.e.* along $[10\bar{1}0]$ and along $[0001]$ direction, leading to the formation of Ga dimers in the subsurface. On the other hand, Ga atom (Ga-2) (brightest one in Fig.5.13(D)) move outwards to the vacuum. Out of two surface N atoms (N-1 and N-2 in Fig.5.13(D)), N-1 is displaced towards the bulk by 0.03 \AA while N-2 moves towards the vacuum by 0.085 \AA , relative to the pristine $(10\bar{1}0)$ surface.

The surface electronic structure of A and B configurations is shown in Fig.5.14 (A) and (C). In the electronic structure of configuration A, the Fermi level is in the conduction band indicating the metallic nature of the surface. The band designated as (i) in Fig.5.14 (A) has a higher dispersion width of 1.71 eV with a minimum at X and a maximum at Γ point in comparison to the defect bands in N-vacancies in the bulk and at the $(10\bar{1}0)$

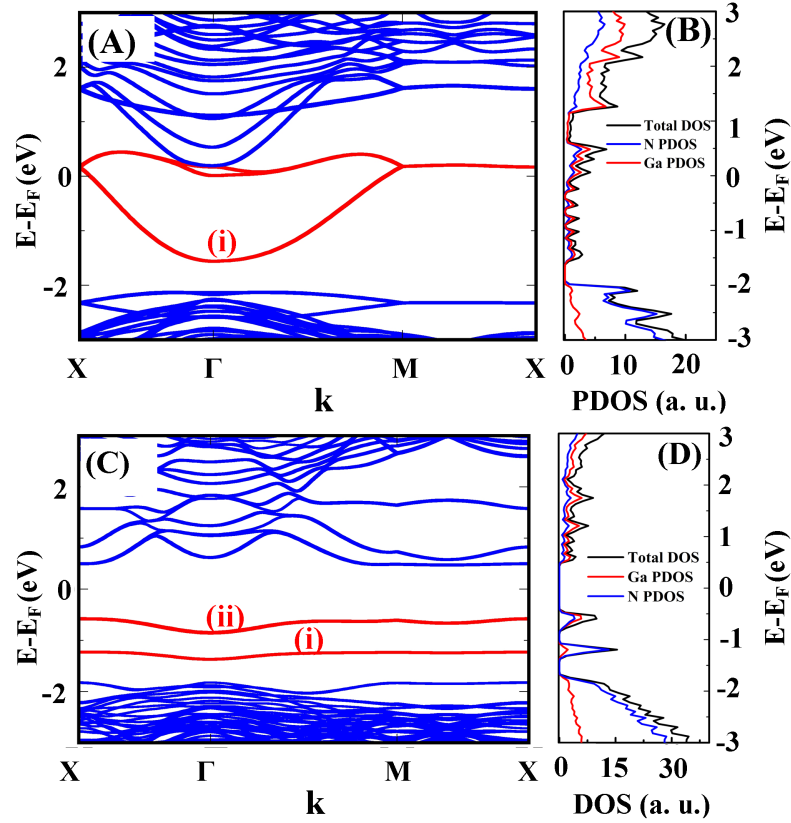


Figure 5.14: (A) and (C) represent the surface electronic structure of configuration A and B respectively. Band colored in red are identified as defect bands. (B) and (D) represent DOS and PDOS of configuration A and B respectively.

surface having N vacancy concentration of 25%. PDOS analysis shows that the states (designated as (i) in Fig.5.14 (A) and colored red), arise from 4s/4p orbitals of Ga atoms with a weak additional contribution from 2p orbitals of nearby N atoms. Our estimate of electronic effective mass corresponding to band (i) is $0.5m_e$ (X- Γ).

Since the relaxed geometry of configuration B is different, its electronic structure exhibits a different trend in comparison with configuration A. The band denoted as (i) in Fig.5.14 (C) is largely composed of N 2p orbitals of surface N atom N-1, while the same corresponding to N-2 appears near VBM. The band marked with (ii) in Fig.5.14 (C) is largely composed of 4s orbitals with a small contribution from 4p orbitals of surface Ga atom (Ga-1) and 2p orbital of surface N atom (N-1). Band corresponding to remaining surface Ga atoms appears near the CBM.

From the above calculations, we note that formation energy of N-vacancies is com-

paratively less than Ga vacancies, thus the concentration of N vacancies is higher than Ga vacancies during crystal growth. However, the formation energy of N-vacancies in the bulk GaN is substantially high to form in abundance. Our calculations suggest that the N-vacancies at the surface can form spontaneously under p-type growth conditions indicating a large density of such defects at surface. Further, the formation of steps by removing N atoms from the surface of $(10\bar{1}0)$ slab shows metallic character, thus we propose that the electrical conductivity observed in the work of Bhasker *et al.*^{157,158} is probably due to the formation of atomic steps and a large number of nitrogen vacancies on the side wall surface of GaN NWN, giving rise to larger density of free electrons for conduction.

Observation of 2.2 eV peak in low loss EELS spectra (see Fig. 5.2) indicate the presence of deep and localized states in the gap which is quite consistent with the deep and localized character of N-vacancies in the bulk and slab calculations. The rise of the dielectric profile before the energy of band to band transitions elucidates that a large density of shallow donor states are also present. Such experimental results are quite consistent with the electronic structure of N vacancy (both in bulk and slab) where unoccupied shallow states are being formed. The reduction in the electrical conductivity of GaN NWN after chemical etching also suggests that the higher conductivity can be attributed to the localized nature of the defect state at the surface. X-ray Photoelectron Spectroscopy (XPS) study on a similar structure²⁷⁴ reveals the formation of Ga rich and n-type surface of the GaN NWN due to N-vacancies, consistent with the Fermi level pinning of $(10\bar{1}0)$ surface close to surface CBM, which supports our proposed mechanism.

5.5 Summary

In summary, we have calculated atomic and electronic structure, formation energy, stability and magnetic ground state of native point defects in bulk *w*-GaN and at $(10\bar{1}0)$ surface using first-principles DFT- based calculations. Ga vacancies, whose formation energy is significantly higher than N-vacancies under both Ga and N-rich condition, act as p-type dopants and induce magnetism in GaN. N vacancy in GaN acts as n-type dopants (1 e/vacancy for conduction) and does not give rise to magnetic moment in the bulk, but a net magnetic moment $1.0\mu_B/\text{vacancy}$ arises at the N-vacancy at $(10\bar{1}0)$ surface.

We find that in bulk configuration, Ga vacancies in neutral state is more stable under p-type growth conditions while under n-type growth conditions it is more stable in $-3|e|$ charged state. At $(10\bar{1}0)$ surface, Ga vacancies in neutral state is more stable under p-type growth conditions while Ga vacancies in $-2|e|$ charged state is more stable. Further, in the bulk configuration, N vacancies in $-1|e|$ charged state is most stable throughout the LDA estimated band gap region. At $(10\bar{1}0)$ surface, N vacancies in $+3|e|$ charged state is more stable under p-type growth conditions while N vacancies in $+1|e|$ charged states is most stable under n-type growth conditions. Most importantly, N-vacancies at the surface form spontaneously under p-type growth conditions giving rise to native n-type character of $(10\bar{1}0)$ surface. Experimental evidence on the presence of N-vacancies was found by EELS measurements. Formation of an atomic step due of N-vacancies on $(10\bar{1}0)$ surface is found to give a metallic electronic structure with the clustering of vacancies and Ga-Ga metallic bond formation near the vacancies, which we attribute to be responsible for the observed high electrical conductivity in $(10\bar{1}0)$ faceted GaN NWN.

Chapter 6

Magnesium doping in GaN Nanowall Network

This chapter is dedicated to the growth and characterization of Mg incorporated GaN nanowall network (NWN) by plasma assisted molecular beam epitaxy (PA-MBE) system. Various characterization tools are used to study the structural, optical and electronic properties. An alternative, to overcome various difficulties with p-doping GaN is proposed. A detailed study to understand the luminescence center of blue luminescence (2.7-2.95 eV) peak in PL spectra is also carried out.

6.1 Issues related to Mg doping in GaN

6.1.1 Introduction

It is well known that n-type GaN can be obtained much easily and even unintentionally as compared to p-type. Magnesium (Mg) is the most successfully used dopant to make p-type GaN. Mg substitutes Ga in the GaN lattice resulting in an acceptor state in its electronic structure. However, the higher ionization energy (≈ 200 meV) of Mg¹⁶¹, and a high unintentional n-doping of intrinsic GaN, makes it difficult to obtain p-doped GaN. Thus, a very high concentration of Mg ($> 10^{20} \text{cm}^{-3}$) is required¹⁶⁵ for obtaining significant and useful p- doping. Typical Mg dopant concentrations of $10^{17} - 10^{19} \text{cm}^{-3}$ have been incorporated in planar GaN films^{166,167} while higher Mg incorporation is seen to induce defects such as N-vacancy, Mg- interstitials, and $\text{Mg}_{\text{Ga}}\text{V}_{\text{N}}$ like clusters. In ad-

dition, there can be polarity inversion in the film that can also lead to the degradation of its crystal structure, which results in poor optical properties. Moreover, these defects and complexes may result in self-compensation in p-GaN^{176,353}. Experiments based on X-ray photoelectron spectroscopy (XPS) and Secondary ion mass spectroscopy (SIMS) measurements of GaN flat film show that concentration of Mg incorporated on the surface is higher than in the bulk¹⁸³⁻¹⁸⁶, suggesting that GaN with higher surface area may enable higher incorporation of Mg. Since NWN with its porous structure has a very high surface to volume ratio we envisage it to be a potential candidate for achieving higher incorporation of Mg. In this part of the chapter, a study of the effect of incorporation of the different quantities of Mg on morphology, crystal structure and optical properties of the GaN NWN has been carried out.

6.1.2 Experimental Details

The GaN NWN films are grown on bare c-plane of sapphire (α -Al₂O₃) under nitrogen rich conditions by using radio frequency plasma assisted molecular beam epitaxy system, operating at a base pressure of 3×10^{-11} Torr. The detailed procedure of substrate preparation can be found in experimental section of chapter 4. The temperature of Gallium (Ga) effusion cell is kept at 1030 °C. A constant nitrogen flow rate of 8 sccm (standard cubic centimeter per minute), substrate temperature of 630 °C, plasma forward power of 375 W and growth duration of 4 hours were maintained for all the films. Mg flux was varied by controlling Mg K-cell temperature from 300 °C to 360 °C in steps of 20 °C. The flux of Mg and Ga were obtained from the beam equivalent pressure (BEP) and are tabulated in Table 6.1.

Surface structural evolution was monitored *in-situ* by reflection high energy electron diffraction (RHEED) and the morphology was determined *ex-situ* by a field emission scanning electron microscope (FESEM). Structural quality of the films is determined by a high-resolution X-ray diffractometer with a Cu K _{α} X-ray source of wavelength of 1.5406 Å. Optical properties of the films were studied by photo-luminescence spectroscopy using a Xenon lamp source with 325 nm excitation, Raman spectroscopy with Ar laser of wavelength 514 nm is performed in the back scattering geometry. Quantification of Mg incorporated in the film is done by *ex-situ* X-ray Photoelectron Spectroscopy (XPS)

Table 6.1: Details of Mg flux rate

Sample Name	Mg-k cell temp ($^{\circ}\text{C}$)	BEP (Torr)	Flux (atoms $\text{cm}^{-2}\text{s}^{-1}$)	Mg:Ga
A	-	-	-	0
B	300	2.9×10^{-10}	8.6×10^{10}	0.0017
C	320	7.1×10^{-9}	2.0×10^{12}	0.0393
D	340	1.1×10^{-8}	3.1×10^{12}	0.0622
E	360	2.0×10^{-8}	5.6×10^{12}	0.1102

with Al- K_{α} (1486.7 eV) source, with a relative composition detection better than 0.1%. Before performing XPS measurements, GaN NWN films were sputter cleaned by optimized low energy (0.5 keV, 2 μA) Ar^{+} ions, to remove physisorbed adventitious carbon and oxygen, without affecting the crystalline quality and composition of the film. The depth dependence of Mg distribution has been studied by secondary ion mass spectroscopy (SIMS) using O^{+2} ion beam of 3 keV with a spot size of 100 μm , rastered over a 5 mm \times 5 mm area.

6.1.3 Results and Discussion

In chapter 4 we have shown that the unique topography of GaN NWN structure results in superior optical properties³⁵⁴. In the present study we have controlled Mg incorporation in NWN while the Mg : Ga ratio was changed in the range of $0.0017 < \text{Mg} : \text{Ga} < 0.1102$. The surface morphology of the grown films, obtained by FE-SEM imaging, have similar morphology independent of the amount of Mg incorporation (see Fig.6.1). The average pore dimension of all the films are in the range of 200 ± 20 nm.

PL and Raman spectroscopy techniques have been extensively employed in the past to study the effect of Mg incorporation on the optical properties of GaN^{178,234,355,356}. In the literature, commonly observed luminescence peaks of Mg doped GaN appears at ≈ 3.27 eV due to DAP transition for moderately Mg incorporated (Mg concentrations less than 10^{19} atoms cm^{-3}) samples and a broad ≈ 2.7 -2.9 eV blue luminescence¹⁷⁸ for heavily Mg incorporated samples (Mg concentration higher than 10^{19} atoms cm^{-3}). Fig.6.2 shows

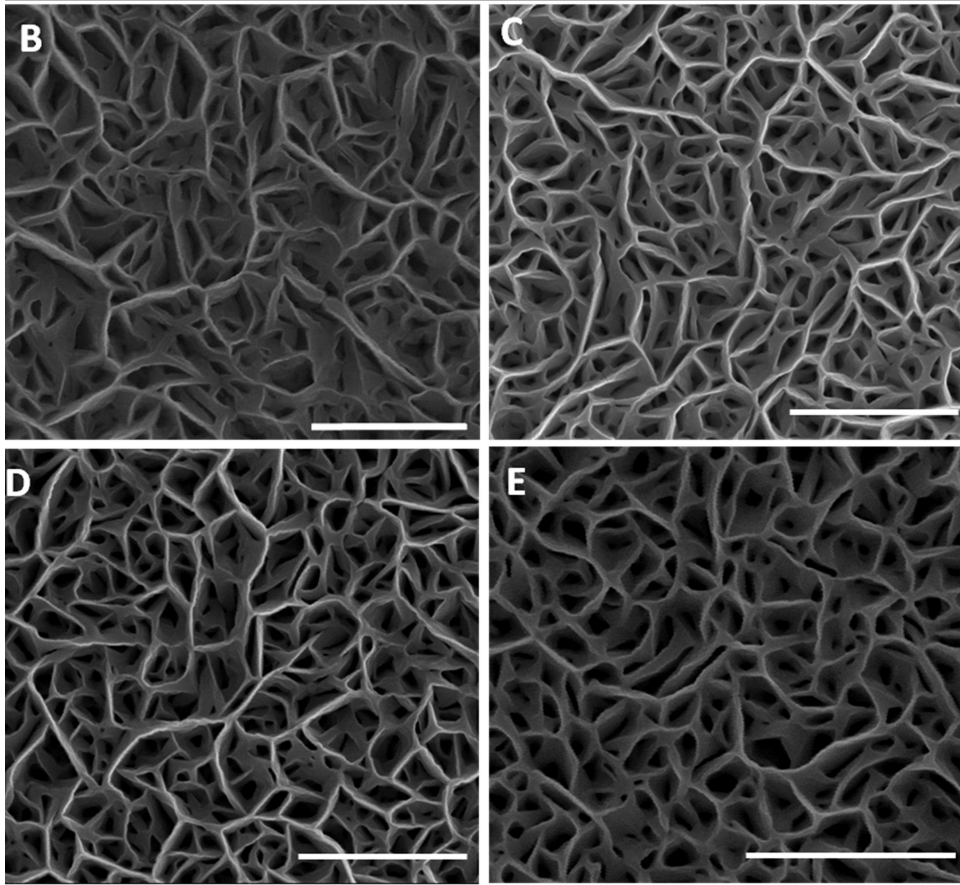


Figure 6.1: FESEM image of different Mg incorporated GaN NWN. The labels on the SEM images represent the sample name. The scale bar is 500 nm for all samples. SEM image of sample A is shown in previous chapter.

PL spectra of samples with different concentration of Mg incorporation (see Table 6.1). The PL intensities of samples B, C, D and E are shown relative to that of pristine GaN NWN (sample A). We have observed significant changes in the luminescence spectra of Mg incorporated films in comparison to pristine NWN. The near band edge (NBE) is dominant in sample A, B and C and its intensity increases with increasing Mg:Ga flux. However, in samples D and E, a broad blue luminescence is the dominant emission. Thus, we believe, samples B and C are moderately doped whereas samples D and E are heavily Mg doped GaN NWN. We have recorded 2 and 3.25 times increase of PL intensity for sample B and C, respectively, as compared to sample A. An increase in PL intensity at lower Mg incorporation has been previously attributed to the screening of polarization induced field by Mg³⁵⁷, which enables efficient overlapping of $e-h$ wave-function, resulting in a higher recombination probability. However, for samples D and E which are grown at

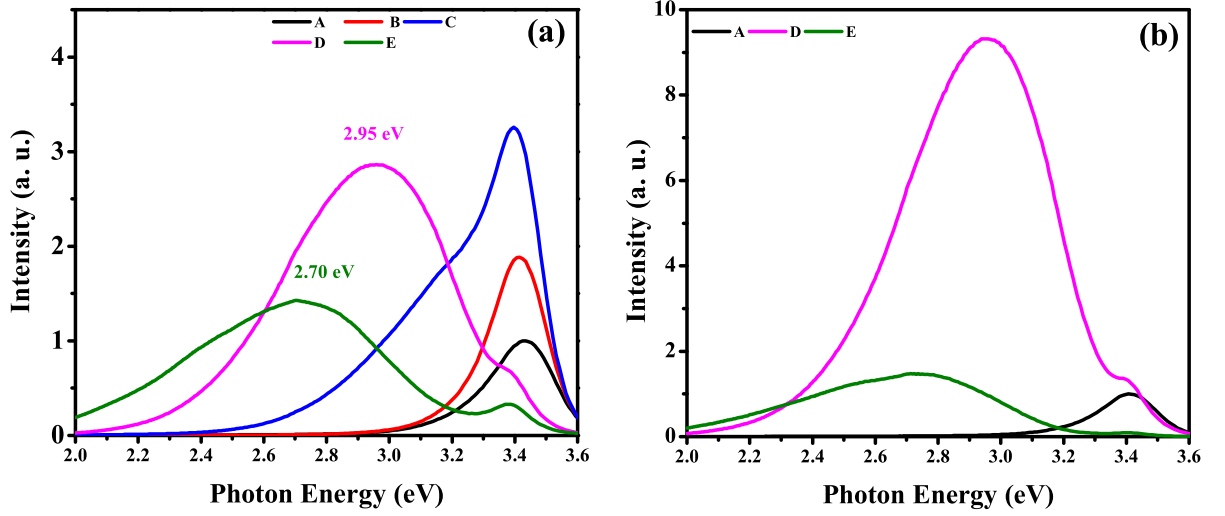


Figure 6.2: (a) shows room temperature photoluminescence (RT-PL) spectra of the undoped and Mg incorporated GaN NWN samples. (b) shows the PL spectra of sample D and E after annealing at 800 °C in presence of N₂ for 20 minutes. (Note that the PL spectra shown for sample A in Fig.(B) is obtain without annealing the sample.)

higher Mg flux, the NBE intensity gets significantly quenched while the intensity of broad blue luminescence peaks increases. It is noted that in sample C, unlike in samples A and B, a shoulder peak appears at ≈ 3.2 eV. The peak in this vicinity is usually attributed to donor-acceptor pair (DAP) luminescence originating either from the transition from shallow donor to a shallow acceptor level or due to Mg-H complex³⁵⁸. It is widely observed experimentally³⁵⁹ and estimated theoretically¹⁸² that the Mg in GaN creates a shallow transient state with a transition energy of 0.15-0.26 eV above VBM. In the present case, the difference between NBE and the corresponding peak falls within the range of the above mentioned values. Since the films were grown using N₂ plasma MBE, the formation of Mg-H complex is less probable, and thus we attribute this shoulder peak to DAP transition.

In cases of samples with higher Mg flux (D and E); we have observed reduced intensity in NBE emission from the Mg incorporated GaN NWN. In the case of sample D, the peak at 2.95 eV is dominant and a reduced NBE appears at 3.4 eV. For sample E, the NBE emission has further diminished and a broad peak at 2.7 eV becomes dominant. The origin of such blue luminescence peaks is highly debated³⁵⁹ while some recent experimental^{356,360} and Density Functional Theory (DFT)^{152,361} studies yield some understanding. Usually the 2.9 eV peak appears in heavily Mg doped GaN and is regarded as the signature

of Mg doped GaN³⁵⁶. In the literature, Kaufmann *et al.*¹⁷⁹ has attributed this peak to transition from deep donor to shallow acceptor state, where deep donor state is due to the formation of vacancy complex $Mg_{Ga}V_N$, whereas Akasaki *et al.*¹⁸⁰ has reported the origin to be the hydrogen-related deep donor to Mg acceptor states. Some reports suggest the blue luminescence (2.7-2.95 eV) is due to the transition from CBM to the deep acceptor, which appears due to hole localization¹⁸². It has been proposed theoretically that^{152,182}, the relaxation pattern (local strain behaviour) of neutral and charged Mg_{Ga} configuration is different from each other, which results in the creation of a deep acceptor state, 0.54 eV above the Mg_{Ga} related shallow acceptor state, which lies 260 meV above the bulk VBM. The appearance of this peak confirms the incorporation of Mg in GaN. It can be clearly seen from the PL spectra (see Fig.6.2) that the blue luminescence peak is intense and broad. The cause of broadening in such luminescence peaks can be understood from the configuration co-ordinate diagram shown by in Reshchikov *et al.*¹⁷⁸ and Van de Walle *et al.*,¹⁸² who have estimated that the energy difference between the blue luminescence and the zero phonon line is around 0.54 eV, which can also result in the broadening of blue luminescence in PL spectra. However, the microscopic origin of this BL peak is not clear yet, which we will discuss in detailed at next part of this chapter. Furthermore, the peaks observed at 3.43, 3.42, 3.41, 3.40 and 3.39 eV are attributed as NBE for undoped GaN and Mg incorporated GaN by using Mg flux of 8.6×10^{10} , 2.0×10^{12} , 3.1×10^{12} and 5.6×10^{12} atoms $cm^{-2}s^{-1}$, respectively. The results suggest that Mg incorporation in GaN yields a red-shift in NBE which is consistent with earlier reports³⁶².

To study the impact of thermal treatment on blue luminescence of Mg incorporated GaN, we have annealed sample D and E at 800 °C for 20 minutes in the presence of N_2 . The PL spectra (see Fig.6.2(b)) of annealed samples show a large increase in the intensity of 2.95 eV peak (for sample D) whereas the intensity of 2.7 eV peak (for sample E) did not change significantly, which indicates that the origin of these luminescence peaks are different. The increase in the intensity of blue luminescence is due to increased activation of incorporated Mg atoms as acceptors caused by high temperature annealing, which results in more acceptor recombination centers responsible for the DAP transition³⁶³. It is speculated that a complex of substitutional Mg and a nitrogen vacancy ($Mg_{Ga}V_N$) is responsible for the deep donor state³⁶³. However, the blue luminescence (2.95) is enhanced

by thermal annealing whereas the concentration of the $(\text{Mg}_{\text{Ga}}\text{V}_{\text{N}})$ complexes significantly decreases after annealing at $T > 500^\circ\text{C}$ ³⁶⁴, which suggests that its origin is not from the $\text{Mg}_{\text{Ga}}\text{V}_{\text{N}}$ complex. With increase in Mg flux, different defect complexes of substitutional Mg and interstitial Mg may become responsible for 2.7 eV peak, which is recently found to be compensating donors in Mg doped GaN¹⁷⁶. The appearance of blue luminescence in Mg incorporated GaN also suggests that the Mg concentration³⁶³ in GaN is higher than 10^{20} atoms cm^{-3} in case of samples D and E.

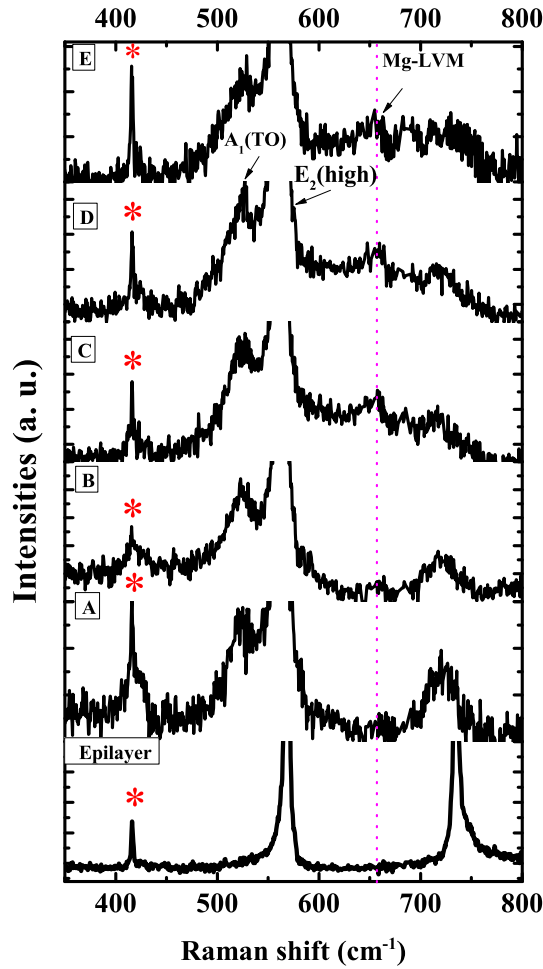


Figure 6.3: shows Raman spectra of the samples studied here. “*” represents phonon mode from Sapphire. The appearance of Mg related LVM can be seen with the increase in Mg:Ga flux. The dotted line is drawn at 657 cm^{-1} to ease the visualisation.

To study the impact of Mg incorporation on the local strain in the grown films, the local vibrational modes (LVM) are monitored by Raman spectroscopy and are shown in Fig.6.3. The LVM of Mg doped GaN^{234,355} appears at $\approx 657\text{ cm}^{-1}$. As Mg replaces

Ga, a compressive strain is introduced which shifts the $E_2(\text{high})$ mode towards higher energies. The $E_2(\text{high})$ mode, being a non-polar mode, is suitable for the study of in-plane strain²³⁴. To observe morphology induced changes, we have also plotted the Raman spectra from a flat 3 μm thick GaN epilayer on c-sapphire. Along with the allowed modes, two geometrically forbidden modes such as $E_1(\text{TO})$ and $A_1(\text{TO})$ are also observed in all the GaN NWN samples, due to scattering off the sidewalls of the porous structure^{261,365}. We have clearly observed (see Fig.6.3) the presence of LVM at 657 cm^{-1} , which is due to the Mg-N stretching mode. The LVM peak is absent for both GaN epilayer and undoped NWN, but increases with higher Mg flux. The variation of position and FWHM of $E_2(\text{high})$ mode with Mg flux as well as the Mg:Ga ratio for all the studied samples are shown in Fig.6.6. As it can be seen, the position of $E_2(\text{high})$ mode for sample B shifts towards higher energy as expected, but for other samples this mode shifts towards lower energy. As Mg in GaN usually induces compressive strain because of its higher ionic radius, the E_2 (high) mode shifts towards the high-frequency. However, if defect complexes or different charged states, other than Mg_{Ga}^0 (such as Mg_{Ga}^-) are formed, then the phonon frequency shifts towards the lower energy, due to the developed tensile strain in the structure³⁵⁵. The FWHM of E_2 (high) mode shows a large change from the highest value of 8.5 cm^{-1} in GaN NWN to 7.6, 5.6, 7.2, and 7.9 cm^{-1} for samples B, C, D and E, respectively, due to the generation of different defects³⁵⁵ in the films, with Mg incorporation.

Strain is introduced in the system not only with Mg replacing Ga in the lattice, but also due to the formation of point and extended defects and impurity complexes, which can also modify the lattice parameter^{355,366}. To study the impact of Mg incorporation on the crystal structure of the NWN, HR-XRD study has been carried out. We have recorded both $2\theta - \omega$ and ω -scans (rocking curve (RC)) of (0002) and (10 $\bar{1}$ 1) reflexes, which provide information about stress and crystal quality of the samples, respectively. We have compared the acquired results with those of an undoped GaN NWN. We have reported earlier that²⁶¹, undoped GaN NWN possesses very low strain as compared to a flat epitaxial thin film. For Mg-incorporated GaN NWN we observe a complex strain behaviour. The estimated a (c) lattice parameter from HR-XRD for samples A, B, C, D and E are 3.1714 (5.1915), 3.1983 (5.1926), 3.2004 (5.1913), 3.2017 (5.1909) and 3.1801

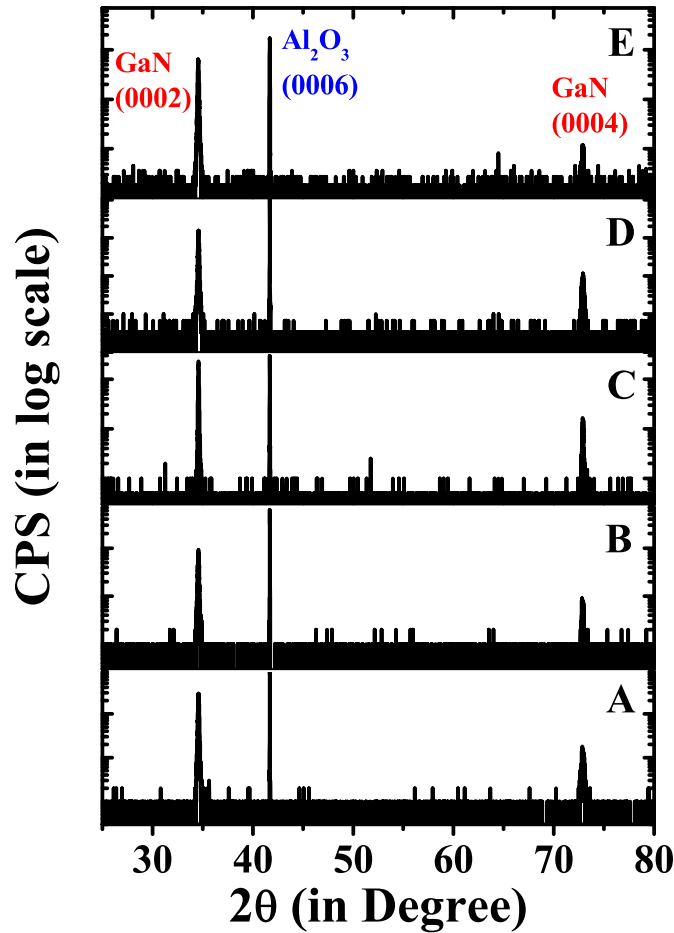


Figure 6.4: $2\theta - \omega$ scan of (0002) plane of all samples under consideration.

(5.1956)Å, respectively. The FWHM of the RC of (0002) and (10 $\bar{1}$ 1) reflexes for the samples are shown in Fig.6.6 (D), The FWHM of RC of (0002) displays an “U” type behavior with increasing Mg:Ga flux, whereas for (10 $\bar{1}$ 1), the values reduce as Mg incorporation increases. The broadening of XRD peaks in the NWN is mainly due to the mosaicity that arises due to the misalignment of the nanowalls as discussed in chapter 4. Thus, these observations suggest that Mg incorporation reduces mosaicity in films.

We have performed XPS measurement on samples A, C, D and E to study the variation in electronic structure and also to find the composition of Mg in sample E. Fig.6.7 (a), (c), (e) and (g) represent Ga-3d core levels and Fig.6.7 (b), (d), (f) and (h) represent N-1s core level spectra of samples A, C, D and E, respectively. All the core level peaks are deconvoluted and shown in the same figure to identify different constituent peaks. For sample A (undoped GaN), Ga 3d peak is found to be consist of a single peak, centered at 20.38 eV, originating due to Ga-N bonding. The deconvoluted N-1s core-

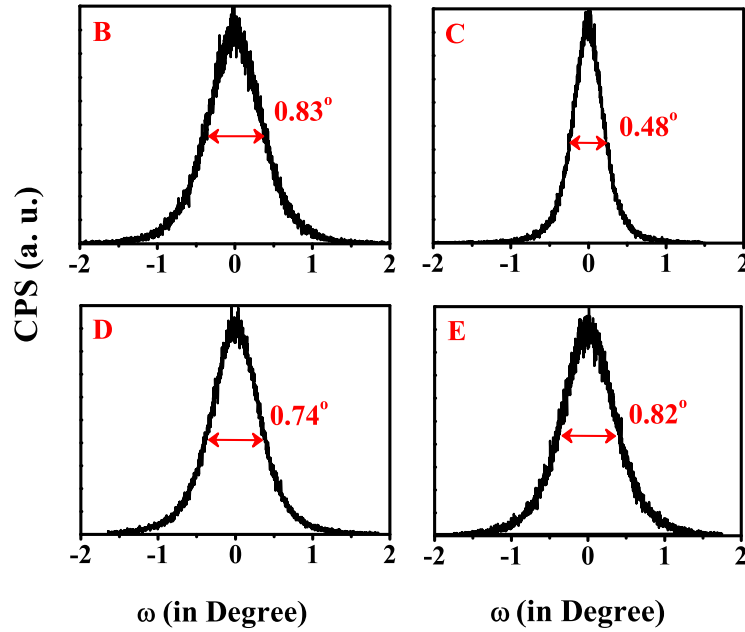


Figure 6.5: Rocking curve of (0002) plane of samples B, C, D and E.

level shows three different peaks centered at 397.89, 395.65 and 393.25 eV, respectively (see Table 6.2). The peak centered at 397.89 eV is assigned to the binding energy of N due to bonding with Ga, whereas the other two peaks are identified as Ga Auger LMM transitions¹⁸⁴.

For sample with Mg doping, we have observed that Ga-3d and N-1s core levels are broad and red-shifted, as compared to the undoped sample A. The deconvolution of Ga-3d peak (see Fig.6.7(b)) for sample C shows red shift in binding energy (BE), while deconvolution of N-1s peak shows red shift in BE as well as appearance of a new peak centered around 391 eV. The deconvolution of Ga-3d peak (see Fig.6.7(e)) for sample E indicates the presence of the two peaks centered at 20.38 and 19.05 eV, respectively. The peak centered at lower binding energy is due to the change in local chemical and structural properties around Ga atoms as a result of Mg incorporation. The deconvoluted N-1s core levels (see Fig.6.7(h)) show four different peaks, of which the peak corresponding to N-Ga bonding is red shifted by 0.76 eV, compared to the undoped sample (sample A). The origin of other two peaks centered at 395.65 and 393.25 eV are Ga Auger LMM transition, as already discussed. For sample E, the high red shift of $E_2(\text{high})$ mode and its broadening, as observed in the Raman study, is correlated to the defect complex formation within the film^{234,355}. Now, We have observed the appearance of a small peak centered at 391

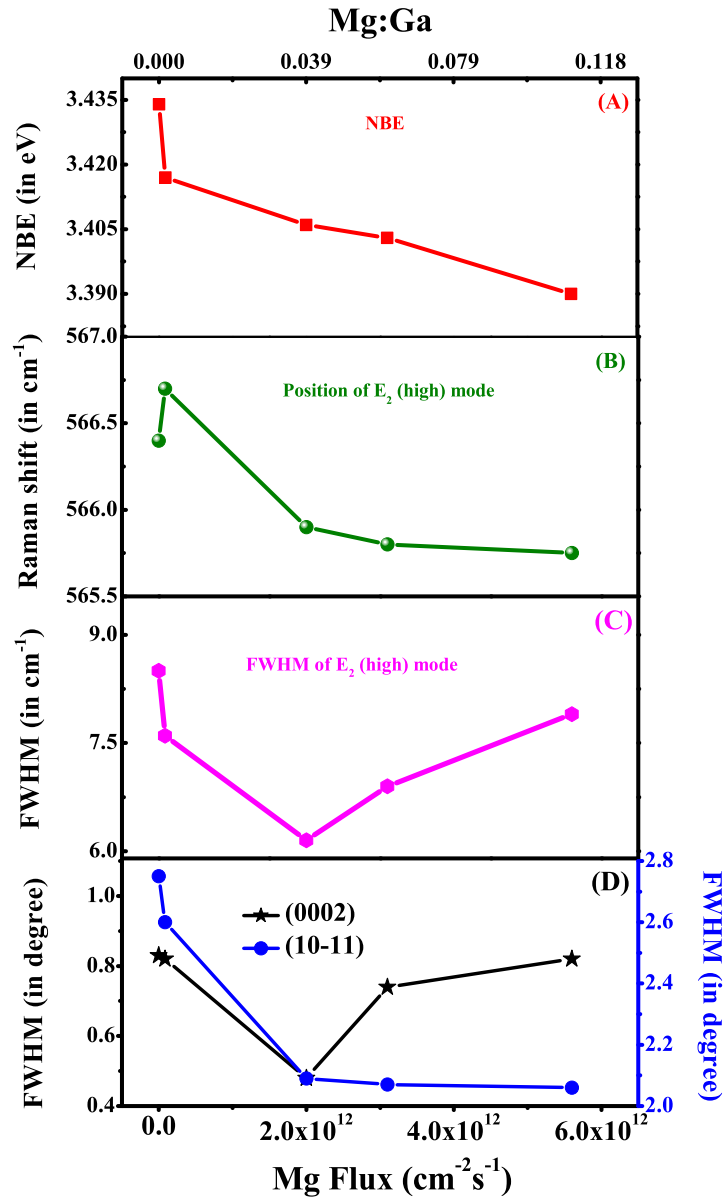


Figure 6.6: (A), (B), (C), (D) represent NBE, position of Raman E_2 (high) mode, FWHM of Raman E_2 (high) mode and FWHM of XRD rocking curve of (0002) and $(10\bar{1}1)$ reflex as a function of Mg flux (or Mg: Ga).

eV in N-1s core level for E (and also in case of C and D), which we believe is due to the defect complex formation during epitaxial growth.

From the Table 6.2, it is clear that, the binding energy of Ga-3d and N-1s core-levels of samples with increased Mg:Ga ratio, are red shifted (compared to A), which suggests a continuous downward shift of Fermi level towards VBM with increase in Mg concentration³⁶⁷. In order to study the position of the Fermi level in comparison to VBM,

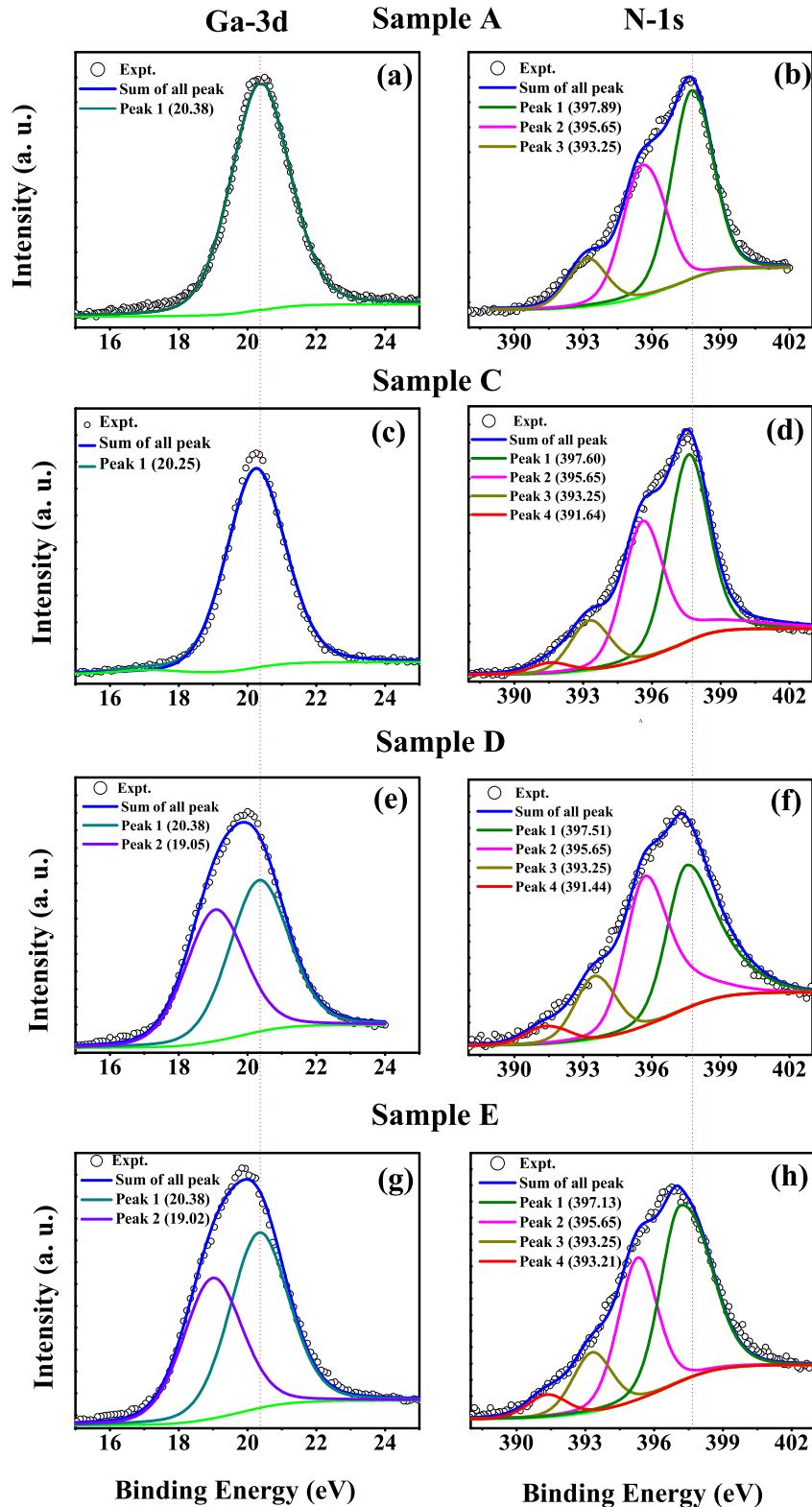


Figure 6.7: (a), (c), (e) and (g) show Ga-3d core level spectra and Figure (b), (d), (f) and (h) shows N-1s core level of samples A, C, D and E, respectively.

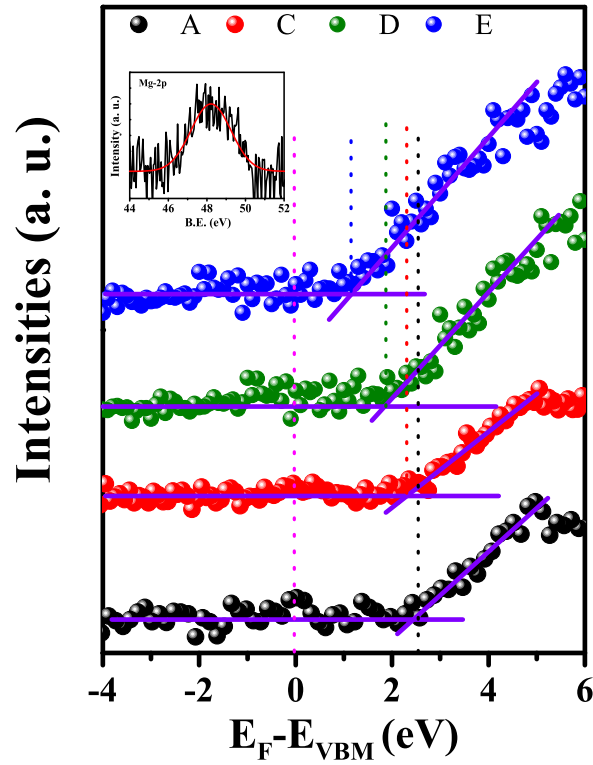


Figure 6.8: shows XPS Valence band spectra of samples A, C, D and E. Inset shows Mg-2p core level spectra of sample E.

Table 6.2: Details of XPS data analysis

Mg:Ga	Ga 3d-peak position (in eV)	FWHM of Ga-3d peak (in eV)	N 1s-peak position (in eV)	$E_{\text{Fermi}} - E_{\text{VBM}}$ (in eV)
0.0000 (A)	20.38	2.03	397.89	2.45
0.0017 (B)	-	-	-	-
0.0393 (C)	20.25	2.03	397.60	2.20
0.0622 (D)	19.90	2.57	397.51	1.84
0.1102 (E)	19.85	2.64	397.13	1.09

we have analyzed the valence band spectra of samples A, C, D and E, and the results are tabulated in Tab.6.2. Fig.6.8 shows Valence Band spectra of samples A and E. We have noted that with increasing Mg concentration, the difference between Fermi level and VBM ($E_{\text{F}} - E_{\text{VBM}}$) reduces. The difference ($E_{\text{F}} - E_{\text{VBM}}$) for undoped sample (A) is 2.45

eV which indicates n-type character, while for samples C, D, E the values are 2.20, 1.82 and 1.09 eV, respectively. This indicates a transition from n to p-type of GaN NWN, due to the increase in Mg dopant concentration. As the RT band gap of GaN NWN is ≈ 3.4 eV, $(E_F - E_{VBM})$ should be ≤ 1.7 eV to have a p-character, and thus, we conclude that the transition from n-type to p-type occurs when Mg:Ga is higher than 0.0622 (see Fig.6.9).

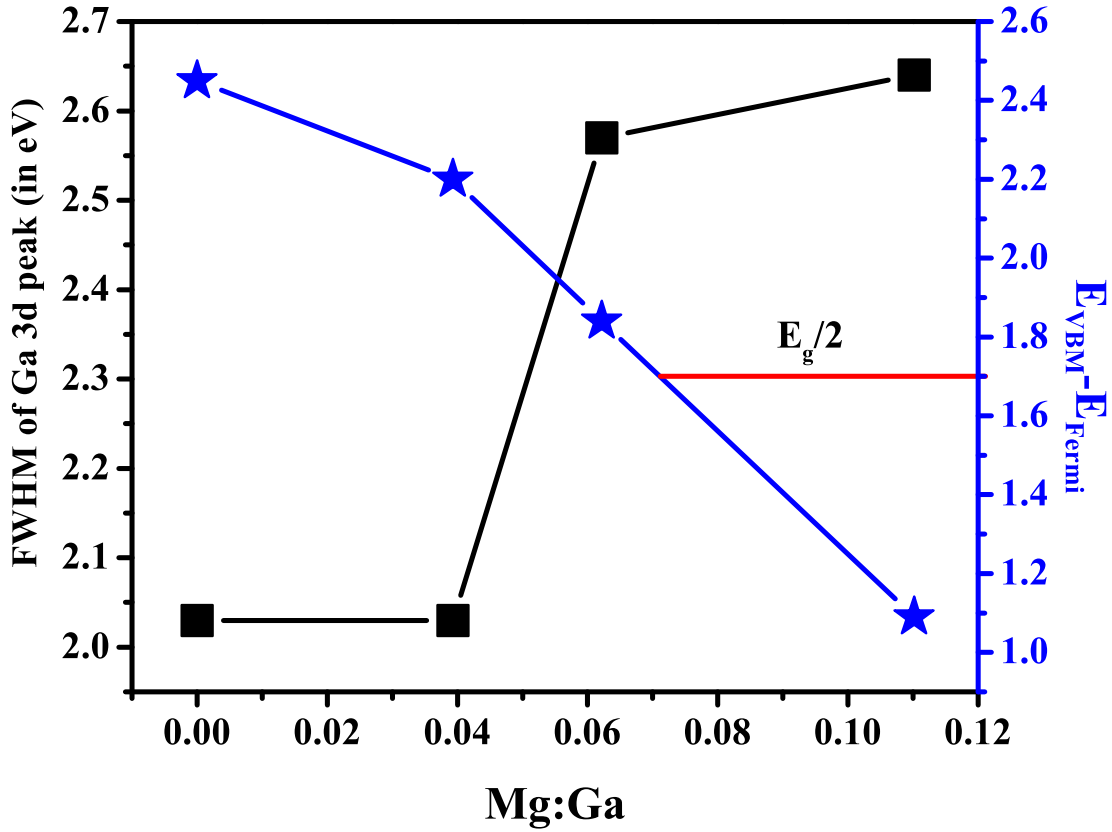


Figure 6.9: shows broadening of Ga 3d core level and $E_{Fermi} - E_{VBM}$ as a function of Mg:Ga.

We have further estimated the amount of Mg incorporation in sample E by the following relation

$$C_{Mg}(\%) = \frac{I_{Mg}/ASF_{Mg}}{\sum I_i/ASF_i} \times 100 \quad (6.1)$$

where, C_{Mg} , I_{Mg} , ASF_{Mg} represent the fraction of Mg, intensity of Mg-2p peak and its atomic sensitivity factor, while I_i and ASF_i are intensity and atomic sensitivity factors of the other constituent elements (i), respectively. We have used atomic sensitivity factors for Ga-2p_{3/2}, N-1s and Mg-2p as 3.720, 0.477 and 0.120, respectively. The estimated

value of Mg incorporation in the sample E is $\approx 3.3\%$, which corresponds to a Mg atomic concentration of $\approx 9 \times 10^{20} \text{ cm}^{-3}$, which is quite consistent with our predictions from PL measurements. Further, to understand the elemental distribution profile, we have carried

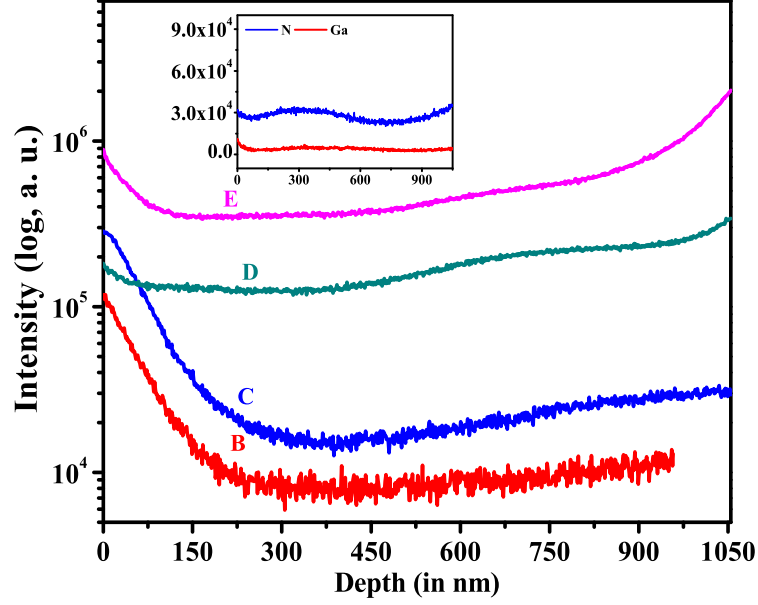


Figure 6.10: shows the depth profile of Mg as a function of depth. Inset of the figure shows depth profile of Ga and N of the sample D.

out SIMS measurements on all samples as shown in Fig.6.10. As discussed earlier, Mg is observed to segregate on the surface in Mg doped flat GaN thin films^{183–186}. Our results (see Fig.6.10) show that Mg segregates at the surface of the NWN and also at GaN/ Al_2O_3 interface for samples D and E. For heavily Mg incorporated sample E, Mg accumulates more at the interface. However, depth profile of Mg in samples B and C shows that Mg segregation occurs only at the surface and decreases monotonically towards the interface. To further verify that this profile is not due to the unique geometry of the NWN, we have recorded N and Ga depth profiles of all the samples and it was found that the depth profile remains almost constant along the depth. As a typical case, the N and Ga depth profile of sample D is presented as inset of Fig.6.10. The profile shows a fairly constant Ga and N distribution along the depth of the samples.

It has been proposed theoretically that, Mg incorporation is easier in Ga-polar surface than in N-polar surface³⁶⁸ and also such doping can change the polarity of the film

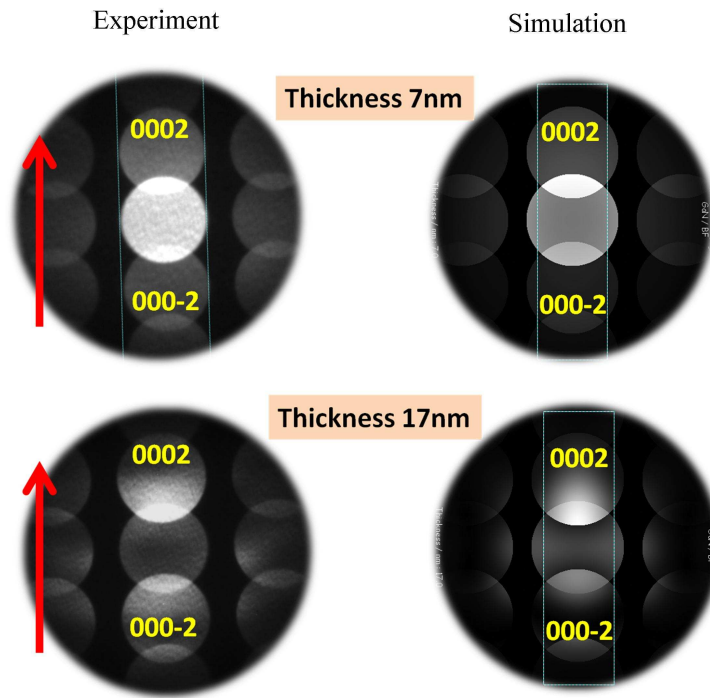


Figure 6.11: represents Convergent Beam Electron Diffraction (CBED) pattern of un-doped GaN NWN. CBED patterns as obtained for GaN in zone-axis $[10\bar{1}0]$ which is marked as experimental patterns along with its corresponding growth direction (marked red). The patterns have been compared with simulated patterns obtained using JEMS Software for different thickness. The compared patterns show that the GaN nanowall network is Ga-polar.

from Ga-polar to N-polar^{368,369}. Convergence Beam Electron Diffraction (CBED) measurements (see Fig.6.11) on the un-doped GaN NWN confirm that these pristine GaN NWN is Ga-polar in nature. Thus, at the initial stage of growth Mg incorporation is higher but as the growth continues change in polarity of the crystal occurs and inturn causes lower incorporation of Mg. We have observed that the Mg concentration in the films towards the interface is 1.6 and 1.9 times higher as compared to the surface for the samples D and E, respectively. Furthermore, a close inspection of the SIMS spectra of samples B and C shows a change in signal by an order, from the surface to bulk region, while for samples D and E the changes are small (≈ 2 times). This confirms that the concentration of Mg in the bulk is of the same order with surface Mg concentration in sample D and E.

The optical signature of GaN NWN:Mg indicates that the Mg atoms occupy Ga sites

in GaN NWN, which results in DAP transition, centered at 3.2 eV for lower incorporation of Mg. On the other hand, for higher Mg incorporation, the luminescence spectra is observed to be dominated by blue luminescence, whose origin is still widely debated in the literature. Raman study along with HR-XRD analysis of the grown samples suggests that, upon moderate incorporation of Mg in GaN NWN structure, the mosaicity of the film gets reduced. A detail XPS study reveals that, with the increase in the Mg concentration, Ga-3d and N-1s core levels get red shifted and broadened. The broadening of Ga-3d is attributed to the de-localized nature of hole, generated by Mg incorporation. The difference between Fermi-level and Valence Band edge consistently decreases with the increase in Mg concentration. Further, SIMS data analysis shows that the concentration of Mg in the bulk of films is of the same order as that on the surface. Thus, the entire material has uniform Mg incorporation which opens up a new route to obtain efficient p-GaN with high amount of Mg incorporation.

6.1.4 Summary

In summary, we have studied the structural, optical, electronic and dopant distribution in Mg-incorporated GaN NWNs. We have found 3.2 times enhancement in NBE for samples with low Mg flux ($\text{Mg:Ga} < 0.04$), while higher Mg flux ($\text{Mg:Ga} > 0.06$) appreciably reduces NBE and increases blue luminescence. Thermal annealing in presence of N_2 increases the intensity of blue luminescence (2.95 eV), however does not affect the 2.7 eV peak. We have observed that with increasing Mg:Ga flux the $E_2(\text{high})$ vibrational mode shifts towards lower frequency, indicating a change in local strain from compressive to tensile type. XPS reveals that more than 10^{20} cm^{-3} Mg atoms can be incorporated in the sample due to its unique morphology with very high surface to volume ratio, while retaining its NBE. XPS Valence band spectra shows the transition from n-type to p-type with increased Mg. Higher light extraction capability along-with higher incorporation of Mg, in the NWN morphology suggests that these GaN films with unique morphology can be used to fabricate p-type GaN in GaN/InGaN based quantum well structures for LEDs and LDs, with enhanced efficiency.

6.2 Origin of Blue luminescence in Mg doped GaN

6.2.1 Introduction

Incorporation of Mg in GaN results in characteristic luminescence peaks in Photoluminescence (PL) and Cathodo-luminescence (CL) spectra depending on the dopant concentration. A small amount of Mg doping ($< 10^{19} \text{ cm}^{-3}$) in GaN results in luminescence peaks at 3.270 and 3.466 eV (at $T=2\text{K}$)³⁵⁹. At higher Mg dopant concentration ($> 10^{19} \text{ cm}^{-3}$) in GaN thin films, a dominant PL peak appears in the range of 2.70 - 2.95 eV, emitting blue luminescence (BL), the origin of which has been debated in the literature in the past decade^{358,370-375}. Details on the nature of BL and the issues related to its origin is discussed in the first part of this chapter (see section 6.1). Recent DFT-based calculations suggest that the emergence of BL is due to different ionization energies of nitrogen vacancies (V_N) (at 2.95 eV)³⁶¹ and hole localization at neighboring N atoms (at 2.70 eV)¹⁸². This however, fails to explain the absence of BL from the samples with lower Mg-concentration. Moreover, no direct experimental evidence has been reported yet corroborating these mechanism.

X-ray absorption near edge spectroscopy (XANES) is an effective probe to determine the element or site specific properties such as oxidation state of an atom, local geometry and the electronic structure³⁷⁶. Here, we have discussed the growth of undoped and Mg doped GaN thin films and their characterization with PL and XANES spectroscopies. We have analyzed the experimentally acquired XANES spectra by and then co-related them with results of *first-principles* simulations of various defect complexes to decipher the characteristic features. Further, we have used the electronic structure of relevant defect complexes obtained from DFT-based simulations to identify luminescence centres in Mg doped GaN.

6.2.2 Experimental Details

The growth parameters are already discussed in first part (see section 6.1) of this chapter. Here, we have presented analysis of three samples of GaN films here: one pristine (A) and two doped (namely B and C), where the sample C is grown with higher Mg flux (Mg:Ga = 0.1102) than that used for B (Mg:Ga = 0.0393). Optical properties of these

films are studied with PL spectroscopy with excitation wavelength of 325 nm. XANES spectra of these samples are recorded in total electronic yield (TEY) mode at SXAS beam line (BL-01) of the Indus-2 Synchrotron Source at Raja Ramanna Centre for Advanced Technology (RRCAT), Indore, India, in an ultrahigh vacuum (UHV) chamber with a base pressure of 10^{-10} Torr. Optical system of the beamline contains toroidal mirror to focus the beam on the sample surface (vertically as well as horizontally), with slit width in front of the monochromator and sample are 1 mm and 0.1 mm, respectively. The energy resolution in the acquired spectra is better than 0.2 eV. The details of the experimental setup for XANES measurements are given elsewhere³⁷⁷. A typical data reduction procedure (background removal and normalization) of the XANES spectra is performed using the Athena software package³⁷⁸.

6.2.3 Simulation Details

In the simulation of XANES spectra, we have carried out *first-principles* DFT calculations, using a combination of many codes. Firstly, we have used the SIESTA code³¹¹ to obtain the lattice parameters and the optimized co-ordinates of atoms of defect configurations, where a Local Density Approximation (LDA) of Ceperley and Alder³¹² with Perdew and Zunger²⁴⁸ parametrization of the exchange and correlation energy functional is used. Integrations over Brillouin Zone of *w*-GaN are sampled on a Γ -centered $5 \times 5 \times 3$ uniform mesh of k-points in the unit cell of reciprocal space³¹⁶. Positions of all atoms are allowed to relax using a conjugate gradient algorithm to minimum energy until the forces on each atom is less than 0.04 eV/Å. Optimized lattice parameters of the unit cell are ‘*a*’ = 3.173 Å and ‘*c*’ = 5.163 Å, which are in good agreement with the experiment³⁷⁹ (‘*a*’ = 3.186 Å and ‘*c*’ = 5.189 Å). In simulation of GaN with defect(s), we have considered a $4 \times 4 \times 2$ supercell (128 atoms). We have used the relaxed atomic co-ordinates obtained from SIESTA to construct clusters for the calculations of *ab-initio* XANES spectra by FEFF9.05 code²⁵⁷, where the Hedin-Lundqvist exchange potential with an imaginary part of 0.2 eV is used. We have included a core hole, treated according to final state rule, in simulation of K-edges. The atomic potential is calculated by a 128 atoms cluster with a radius of 8 Å, while the full multiple scattering XANES spectra are determined by increasing the radius to 12.5 Å around the absorber. Electronic structure

of the relevant defect configurations is determined from calculations based on HSE06²⁵² hybrid functional as implemented in VASP code³⁸⁰. The optimized lattice parameters and relaxed atomic co-ordinates obtained from SIESTA are used to construct atomic structure for VASP calculations. *First-principles* DFT calculations were carried out using a plane-wave projector augmented wave (PAW) method as implemented in the VASP code, where a Local Density Approximation (LDA) of Ceperley and Alder is used for the exchange and correlation energy functional. The reference valence electronic configurations of Ga, N and Mg were considered as $3d^{10}4s^24p^1$, $2s^22p^3$ and $3s^23p^0$, respectively. We have used an energy cutoff of 500 eV to truncate plane wave basis. Electronic energy spectrum at Γ point was calculated by using Heyd-Scuseria- Ernzerhof (HSE) hybrid functional, where the mixing parameter for the Hartree-Fock exchange potential is set at 25%. The screening parameter in HSE calculations is fixed at 0.2.

Formation energy of defects (for neutral state) in the bulk was calculated using Zhang-Northrup scheme, given by

$$E_f = E_{tot}(defect) - E_{tot}(pristine) + \sum n_i \mu_i \quad (6.2)$$

where $E_{tot}(defect)$ and $E_{tot}(pristine)$ are the total energies of super-cells containing a defect and the reference pristine structure, respectively. n_i and μ_i represent the number of atom added or removed (if atom(s) are added it will take +ve sign whereas if atom(s) are removed it will take -ve sign) and chemical potential of i^{th} species, respectively. In this work, we have calculated the defect formation energy under N rich conditions. Under N rich conditions μ_N is the energy of N- atom (obtained from the total energy $E_{tot}(N_2)$ of N_2 molecule, *i.e.* $\mu_N = \frac{1}{2}E_{tot}(N_2)$). The chemical potential of Ga is calculated using the assumption of thermodynamic equilibrium, *i.e.* $\mu_{Ga} + \mu_N = E_{GaN}[bulk]$; where $E_{GaN}[bulk]$ is the total energy of one formula unit of bulk w -GaN. We have used chemical potential of Mg (μ_{Mg}) as the energy of single Mg atom in the hcp phase ($\mu_{Mg} = \frac{1}{2}E_{tot}(Mg_{hcp})$), noting that the primitive unit cell of hcp structure contains two atoms.

6.2.4 Experimental Results

Details of the structural properties of the films studied here were discussed thoroughly in earlier part of this chapter³⁸¹. Since GaN in NWN geometry does not show any

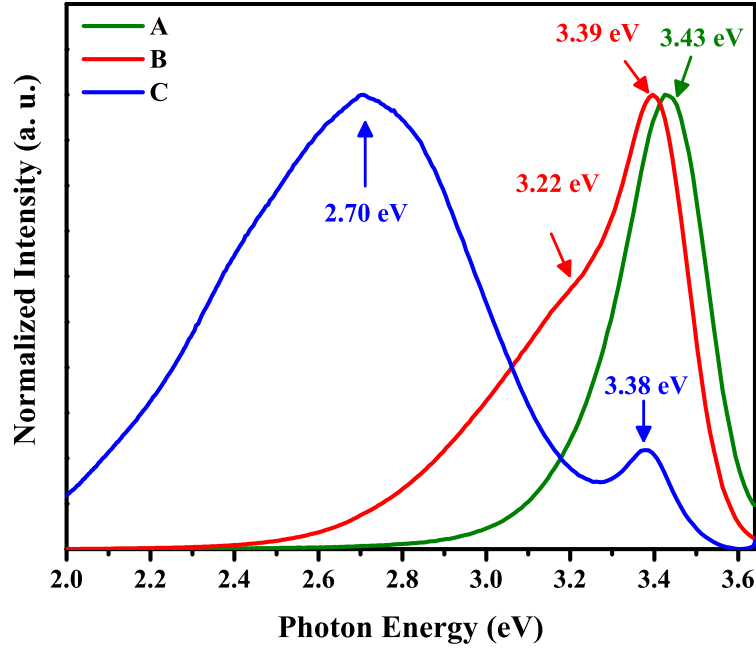


Figure 6.12: Normalized room temperature Photoluminescence (PL) spectra of samples A, B and C.

other luminescence peak(s) except near band edge (NBE) (\approx at 3.4 eV)^{273,381} making it the preferred choice for this particular study. In the photoluminescence spectra obtained at RT (see Fig. 6.12), it is seen that the sample A has only one dominant luminescence peak centered at 3.43 eV, assigned to NBE emission of GaN, whereas sample B exhibits two distinct peaks, centered at 3.39 and 3.22 eV, respectively. While the peak centered at 3.39 eV is assigned to NBE of GaN, the peak centered at 3.22 eV is assigned to electron-Acceptor (e-A) or donor acceptor pair (DAP) transition in Mg-doped GaN³⁵⁹. PL spectra of sample C shows two distinct luminescence features, and they are identified as the NBE at 3.38 eV and the intense BL peak centered at 2.70 eV, respectively.

To understand the origin of different luminescence peaks as observed in the PL spectra of samples, it is useful to study the electronic structure of all samples. To understand this, we have probed the N K-edge and Ga L_{2,3}-edge of the three samples using XANES (see Fig. 6.13(a) and (d)). For N K-edge, five distinct features (P1-P5) are seen clearly, which are consistent with earlier observations³⁸². We have considered the absorption edge as the location of the first significant peak in the first derivative of absorbance ($\mu(E)$) with respect to energy (*i.e.* $d\mu(E)/dE$)³⁸³ (see Fig. 6.13(b)). For each peak observed in Fig. 6.13(a) the corresponding maxima (P1'-P5') and minima (P1''-P5'') are shown in Fig.

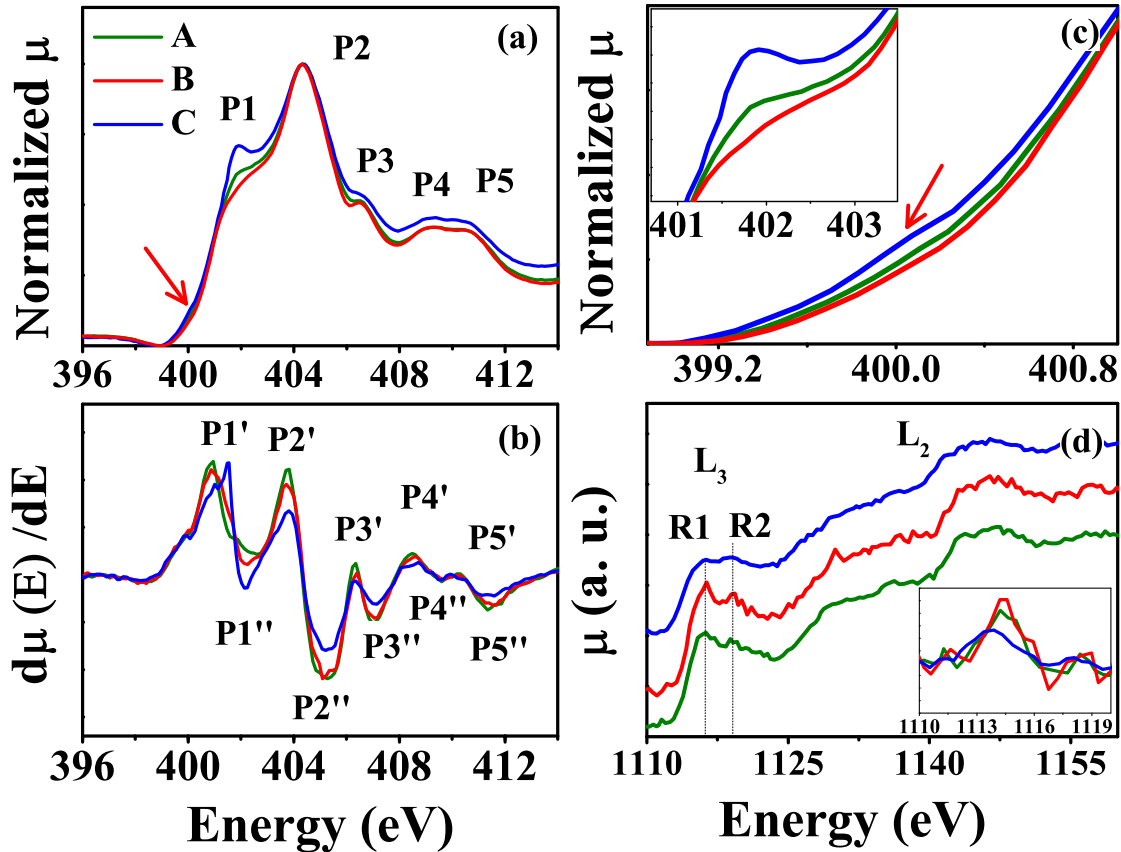


Figure 6.13: XANES spectra of normalized N K edges (a) and Ga L_{2,3} edges (d) and their first derivatives at (b) and inset of (d), respectively. Figure (c) shows the enlarged version of the lower energy side of the absorption profile. Inset of Fig. (c) shows enlarged version of the feature P1.

6.13(b). It is seen that the N K-edges (P1') of A and B do not show any significant changes in their absorption threshold, whereas that of sample C shows a shift of ≈ 0.7 eV towards higher energy relative to that of A, suggesting a small increase in the oxidation state of N atoms in sample C. Along with a change in the absorption edge, we have also observed a clear distortion of the peak P1. The peak intensity of P1 of sample C is higher and more pronounced than that of samples A and B (see inset of Fig. 6.13(c)). This increase in the peak intensity of P1 with higher Mg incorporation is consistent with a previous report³⁸⁴. Increase in the intensity of the feature P1 may arise from the localized states that form due to higher Mg incorporation in the film. We have further observed a small absorption feature at 400.16 eV (see arrow in Fig. 6.13(a) and Fig. 6.13(c)) in case of sample C.

Recorded L_{2,3} edge spectra of Ga atoms are presented in Fig. 6.13(d), with the first

derivative of L_3 edge in the inset. Similar to N K-edge, we have not observed any changes in the absorption threshold of samples A and B. However, we have observed a small red shift (≈ 0.80 eV) in that of sample C, indicating reduction in the oxidation states of Ga atoms in sample C. The two distinct features R1 and R2 are seen clearly in all three samples. For samples A and B, the intensity of R1 is higher than that of R2, whereas for the sample C, intensity of R2 is higher than that of R1, with a flat absorption profile near the L_3 edge.

6.2.5 Theoretical Analysis and Discussion

6.2.5.1 X-ray Absorption Near Edge Structure

To uncover the origin of observed changes and features in experimental XANES spectra as a function of Mg doping concentration, we have obtained *ab-initio* XANES spectra. We have focused on three possible mechanisms, which are widely speculated to be the origins of the BL in the literature: (i) nitrogen vacancy complexes, (ii) the configuration with hole localization and (iii) Mg interstitial defect complex (see Fig.6.14). Before studying the relevance of vacancy complexes to XANES spectra, we have benchmarked the simulation parameters with careful analysis of the pristine GaN. Fig.6.15 (a) and (b) show theoretical XANES spectra of N K-edge and Ga L_3 edge respectively, along with the experimentally observed spectra from a flat GaN epitaxial layer. Clearly, there is a good agreement between our theory and experiment (see Fig. 6.15), as well as with results reported earlier³⁸⁵.

We have observed that the N K-edge absorption edge is primarily dominated by the unoccupied N-2p orbitals, whereas Ga L_3 edge has a strong ‘s+d’ hybridized orbital character. Further, we have found that the feature R1 has a strong ‘s+d’ hybridized character whereas R2 and R3 are predominantly of ‘d’ character. The calculated local density of states (LDOS) projected on s, p, and d orbitals of N and Ga atoms reveal narrow energy sub-bands (marked with “*”) are in agreement with the energies of the characteristic features seen in the XANES spectra. The simulated N K and Ga L_3 edges in XANES spectra of the substitutional Mg at Ga site (Mg_{Ga}) are shown in Fig. 6.16(a) and (b) respectively. We have found that the peak P1 obtained from the simulation of configuration with (Mg_{Ga}) defect is not very prominent, and has a lower intensity relative

to the pristine GaN. This reduction in intensity of P1 is consistent with the behavior shown by sample B, and thus we infer that no other defect complexes are present notably in sample B and the luminescence peak centered at 3.22 eV is due to recombination of electron-Acceptor pair (e-A). Mulliken population analysis from results of SIESTA calculations suggest a small increase in the oxidation states of 1st nearest neighbor (NN) ($\approx 0.05|e|$) N atoms as well as in the oxidation state of 1st NN Ga atoms ($\approx 0.015|e|$), that co-ordinate the site of Mg substituent in Mg-doped GaN relative to that of undoped GaN. Despite this small increase in oxidation state of atoms seen in our simulations, we do not observe a significant change in the absorption edge of sample B due to significantly lower incorporation of Mg in the host. Further, we have simulated several defect configurations such as (i) complexes of Mg_{Ga} with a single N vacancy ($\text{Mg}_{\text{Ga}}\text{V}_{\text{N}}$), with two N vacancies ($\text{Mg}_{\text{Ga}} - 2\text{V}_{\text{N}}$), with Mg at interstitial site ($\text{Mg}_{\text{Ga}} + \text{Mg}_{\text{i}}$) (ii) complex of Mg at interstitial site with a nitrogen vacancy ($\text{Mg}_{\text{i}} - \text{V}_{\text{N}}$), (iii) Mg at Nitrogen site (antisites) (Mg_{N}), and (iv) Mg at interstitial site (Mg_{i}). The characteristic signatures of these configurations

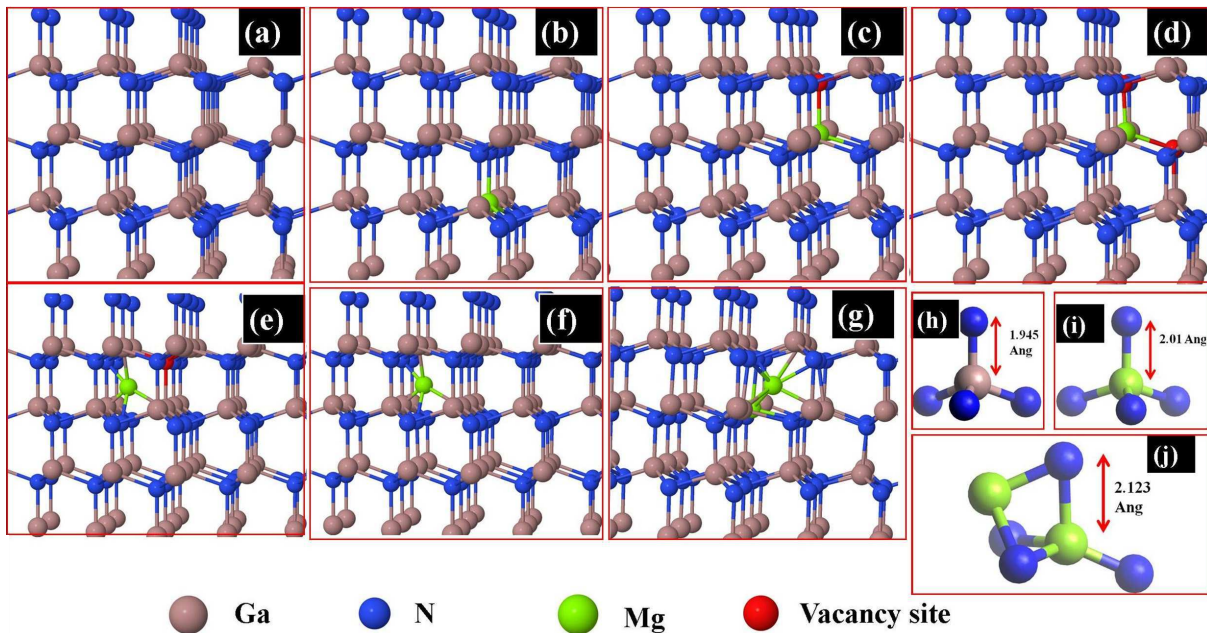


Figure 6.14: Ball and stick model of different configurations used in DFT and multiple scattering theory calculations as Pristine w-GaN (a), Mg_{Ga} (b), $\text{Mg}_{\text{Ga}} - \text{V}_{\text{N}}$ (c), $\text{Mg}_{\text{Ga}} - 2\text{V}_{\text{N}}$ (d), $\text{Mg}_{\text{i}}\text{V}_{\text{N}}$ (e), Mg_{i} (f), $\text{Mg}_{\text{Ga}} + \text{Mg}_{\text{i}}$ (g). Figure (h) and (i) shows tetrahedral structure of pristine Ga-N and Mg-N in Mg doped GaN, respectively. Figure (j) shows the relaxed structure of the $\text{Mg}_{\text{Ga}} + \text{Mg}_{\text{i}}$ defect complex.

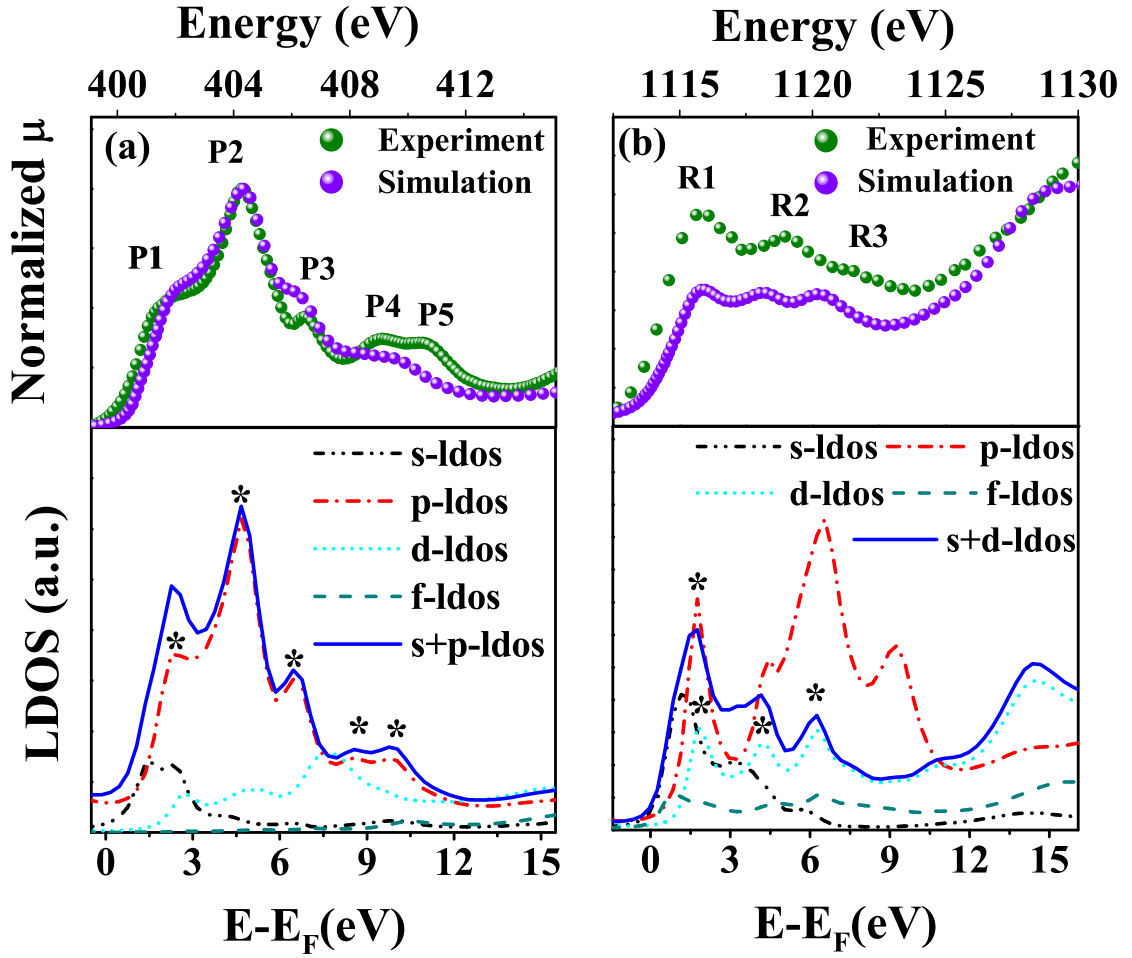


Figure 6.15: XANES spectra of N K-edge (a) and Ga L₃-edge (b) obtained from experiment (for commercial GaN) and simulation based on full potential multiple scattering methods. LDOS of individual orbital is shown at the bottom with their respective absorption edges.

in the XANES spectra are shown in Fig. 6.16(a) and (b). In the configurations of $\text{Mg}_{\text{Ga}}\text{V}_{\text{N}}$, we have considered N-vacancies in the axial and basal planes of the w -GaN, as the four Ga-N bond lengths are not same for GaN_4 tetrahedra. We have found that former configuration is energetically more preferable and does not show any significant change in the characteristics of XANES spectra with respect to pristine GaN. Thus, the increase in the peak P1 of sample C cannot be attributed to the formation of a $\text{Mg}_{\text{Ga}}\text{V}_{\text{N}}$ complex.

A comparison between the experimental and simulated results for XANES spectra clearly suggests that the possible causes for the enhanced intensity of P1 feature in N K-

edge of the sample C can be due to formation of the $\text{Mg}_{\text{Ga}} - 2\text{V}_{\text{N}}$, $\text{Mg}_{\text{i}} - \text{V}_{\text{N}}$, $\text{Mg}_{\text{Ga}} + \text{Mg}_{\text{i}}$ or Mg_{i} . Mulliken charges of N atoms near these defect complexes, due to the formation of defect complexes, are listed in Table 6.3 along with their formation energies. Clearly the oxidation states of N (Ga) atoms increase (decrease) slightly in these defect configurations. Thus, a clear conclusion on determination of dominant defect(s) could not be reached from the Mulliken population analysis alone. Further, our estimates of the formation energies of these defect complexes obtained using Zhang-Northrup scheme³¹⁷ (see Table 6.3) reveal that the defect configuration $\text{Mg}_{\text{Ga}} + \text{Mg}_{\text{i}}$ has the lowest formation energy, and is probably the most preferable defect complex that should form in Mg-doped GaN. Recently, Miceli *et al.*¹⁵⁴ and Reshchikov *et al.*³⁸⁶ predicted from Hybrid functional based DFT calculations that Mg interstitial is the energetically preferable defect in Mg-doped GaN, which was neglected earlier due to over-estimation of its formation energy with a semilocal functional^{387,388}, which is consistently evident in the results of our calculations

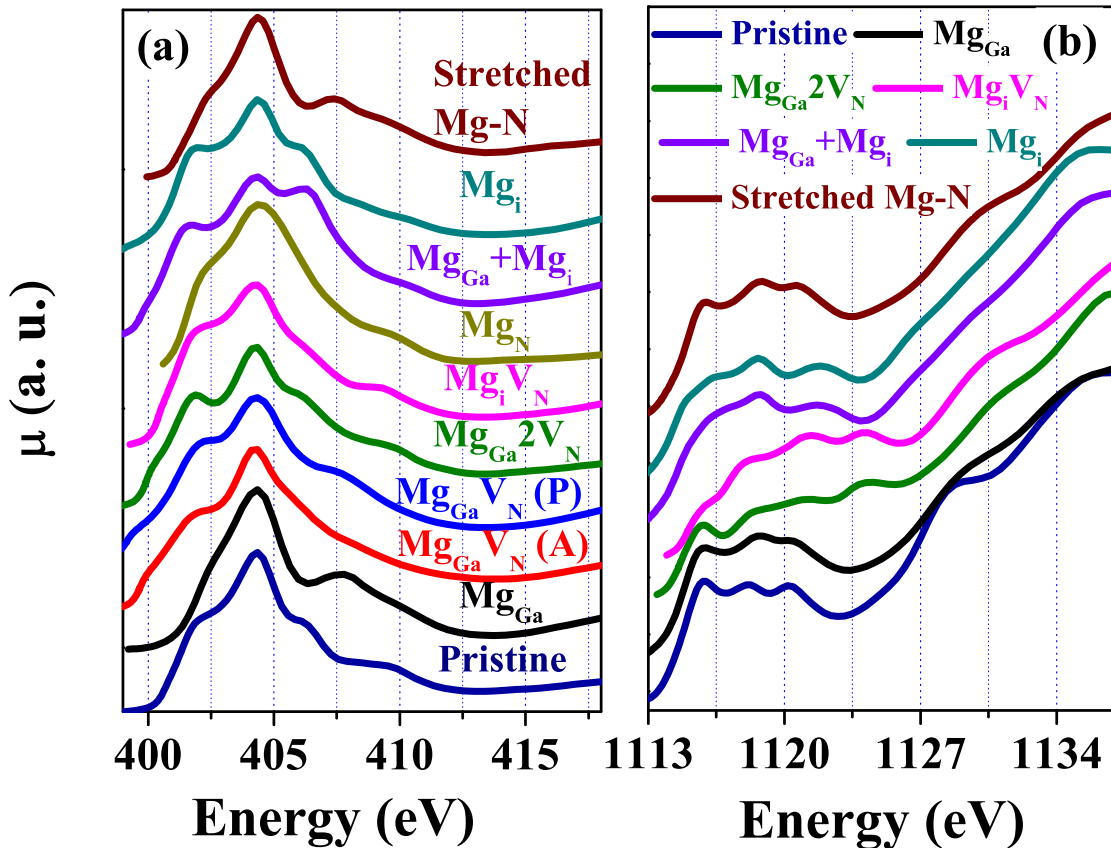


Figure 6.16: Simulated XANES spectra N K-edge (a) and Ga L₃- edge (b) for various defect configurations.

Table 6.3: Neutral Defect Formation Energy of different defect complexes under N-rich condition. The Mulliken charges of 1st nearest neighbor (NN) of the defect complex with reference to pristine GaN. The -ve (+ve) sign in Mulliken charge indicates increase (decrease) in the oxidation state.

Defect complex	Formation Energy (in eV)	Mulliken charge in $ e $	
		NN N	NN Ga
Mg_{Ga}	1.20	-0.050	-0.016
$Mg_{Ga}V_N$	0.51	-0.015	+0.152
$Mg_{Ga}2V_N$	4.91	-0.046	+0.181
Mg_iV_N	8.47	-0.056	+0.242
Mg_N	9.78	-0.064	+0.074
$Mg_{Ga} + Mg_i$	-0.17	-0.061	+0.055
Mg_i	4.80	-0.015	+0.068

here (see Tab.6.3). Simulated L_3 edge spectra of the configurations $Mg_{Ga}+Mg_i$ and Mg_i show (see Fig. 6.16(b)) that the peak R2 has a higher intensity than R1, as observed experimentally only for sample C.

Thus, we propose that the observed increase in intensity of P1 of sample C is due to the increase in the unoccupied donor states, originating from the formation of defect complex $Mg_{Ga}+Mg_i$ and/or Mg_i . Further, the shift in the absorption threshold of N-K edges of sample C in comparison to sample A is due to reduction in the Mulliken charges (oxidation states) of N atoms of the MgN_4 tetrahedra. We have found that the relaxed atomic structure of GaN, containing the $Mg_{Ga}+Mg_i$ defect complex, shows elongation of axial Mg-N bond by 14%, while in basal plane one Mg-N bond by 2.5% another other two Mg-N bond stretches by 5.4% relative to the Ga-N bonds of pristine GaN.

To connect with the prediction of Van de Walle *et al.*,¹⁸² we have simulated the XANES spectra of N K and Ga L_3 edges by stretching the Mg-N bond to a value 15% higher than the Ga-N bond, while allowing other atoms to relax and are shown in Fig. 6.16 as stretched Mg-N. We have not seen any significant change in the N K-edge w.r.t. pristine GaN in that case. Thus, the distortion of peak P1 in Fig.6.13 (a) can not be attributed to longer Mg-N bond. A careful observation of the simulated N K-edge spectra

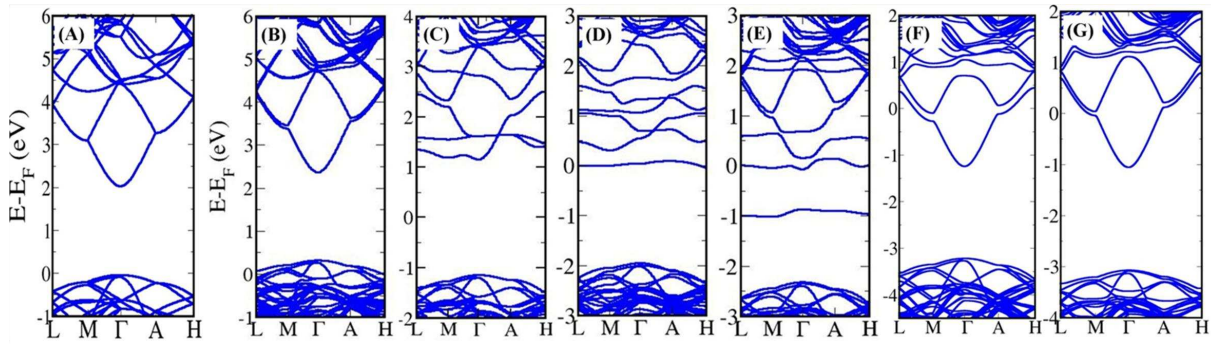


Figure 6.17: Electronic structure of different defect configurations obtained from SIESTA. Pristine w-GaN (A), Mg_{Ga} (B), $\text{Mg}_{\text{Ga}} - \text{V}_{\text{N}}$ (C), $\text{Mg}_{\text{Ga}} - 2\text{V}_{\text{N}}$ (D), $\text{Mg}_{\text{i}}\text{V}_{\text{N}}$ (E), Mg_{i} (F), $\text{Mg}_{\text{Ga}} + \text{Mg}_{\text{i}}$ (G). The Fermi level is set at 0 eV.

in Fig. 6.16(a) reveals an absorption edge (at ≈ 400 eV) for all the N-vacancy related complexes, and thus we have attributed this feature at ≈ 400.16 eV in the XANES spectra (see Fig.6.13(c)) to unoccupied states associated with N-vacancies.

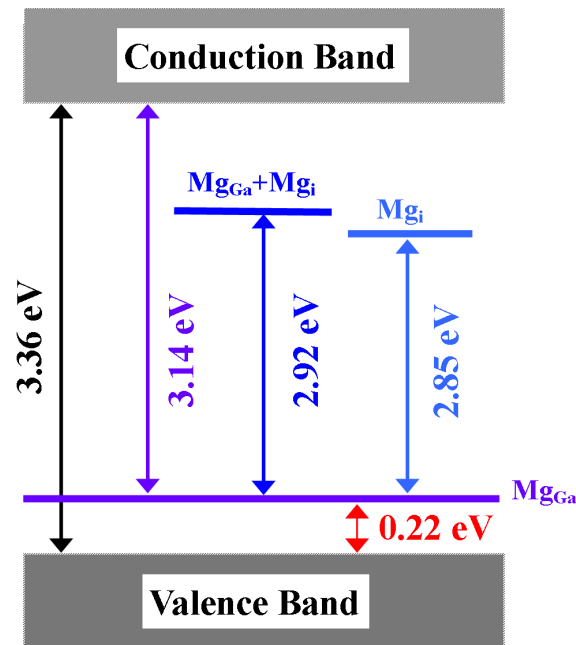


Figure 6.18: A schematic of electronic structure of heavily Mg doped GaN obtained with hybrid HSE06 functional based calculations (at Γ point).

6.2.5.2 Electronic Energy Levels

As DFT-LDA calculations typically underestimate the band gap (band gap of GaN calculated with SIESTA is 2.06 eV, much lower than its experimental value of 3.51 eV (see Fig.6.18)), we have used hybrid HSE06 functional based calculations to determine energy levels of the defect states in the electronic structure using VASP code. In these simulations with a $4 \times 4 \times 2$ supercell, we have used only Γ -point in sampling the Brillouin Zone integrations. Our estimate of the band gap of pristine GaN is 3.36 eV, reasonably close to the experimentally observed band gap of 3.51 eV at T=2K and 3.43 eV observed at RT in this study. For the configuration Mg_{Ga} , we have found a shallow acceptor state (≈ 0.22 eV above the VBM), which has a predominant N-2p orbital character. Configurations with $(\text{Mg}_{\text{Ga}}+\text{Mg}_i)$ and Mg_i exhibit deep donor states in the electronic gap \approx at 3.14 and 3.07 eV above VBM. Thus, the transition from the deep donor states to the shallow acceptor state occurs at $(3.14 - 0.22) \approx 2.92$ eV, very close to the emission peak of BL (in this case 2.7 eV) observed in sample C (see Fig.6.18).

Although in the past, a similar mechanism (transition between deep donor to shallow acceptor) on the origin of BL has been proposed, its atomistic origin was not clear^{358,389}. Lyons *et al.*¹⁸² has claimed an alternative mechanism where BL is a result of transitions of electrons from the conduction band to the deep and localized Mg_{Ga} acceptor level. However, it fails to explain large shifts in the BL peak position with increase in excitation intensity and absence of the same in lightly doped samples. In addition, work of Buckeridge *et al.*³⁶¹ has suggested that the BL may be due to the formation of isolated N-vacancy where authors have used a hybrid quantum mechanical (QM) and molecular mechanical (MM) embedded cluster method. In contradiction to this, few reports have claimed that isolated N vacancy gives rise to yellow luminescence (2.18 eV)¹⁵² and/or green luminescence (2.35 eV) in Mg doped GaN³⁸⁶. Also, some issues related to the accuracy in calculations of Buckeridge *et al.*³⁶¹ have been reported by other groups^{390,391}. Recently, Wahl *et al.*³⁹² have studied the site occupancy of Mg in GaN by implanting radioactive Mg in GaN, and found a notable amount of Mg in interstitial sites, while the majority of them occupy the substitutional Ga sites. As mentioned earlier, some reports^{154,386} have suggested that the formation energy of Mg occupying an interstitial site is less in p-type GaN. Thus, Mg prefers to be at the interstitial sites in the films during

the epitaxial growth process.

As the epitaxial growth temperature of GaN is reasonably high (630 °C in the present work), mobility of Mg adatom is also high during growth. When Mg at interstitial site diffuses close to a Ga vacancy site in the process, it takes up the same and becomes substitutional Mg at Ga site in GaN³⁹². In the films grown under low Mg flux, occurrence of Mg_{Ga} is expected to be dominant, resulting in the formation of a shallow acceptor state in the electronic gap, and associated 3.22 eV peak in the luminescence spectra. In contrast, during the epitaxial growth with higher Mg flux, the number of available Ga vacancy sites are not abundant enough for diffusing Mg_i to get converted to Mg_{Ga}. Instead, Mg_i adatoms will pair up with other suitable defects due to their relatively low formation energy and form defect complexes such as Mg_{Ga}+Mg_i, which create a deep donor state in the electronic gap. Our work shows that these are responsible for the BL emission arising from the deep donor to shallow acceptor state transitions. Further, the mechanism proposed in this study on the origin of BL clearly explains the large shift of peak position of BL with increase in the excitation intensity and absence of BL in lightly doped samples. Based on our analysis, we propose that the synthesis of p-type GaN under lower Ga flux (Ga poor condition) will be more efficient than under Ga rich conditions.

6.2.6 Summary

In summary, we have uncovered the origin of observed BL in Mg doped GaN through a combination of experiments and theoretical analysis of Mg incorporated at different concentration GaN thin films. With clear evidence in PL and XANES of heavily Mg incorporated GaN films, we have shown that the observed BL originates from defect complexes formed of interstitial Mg (Mg_i) and substitutional Mg (Mg_{Ga}). The BL is found to be associated with a transition from the deep donor state in electronic gap to shallow acceptor state. Our experiments have revealed a slightly higher oxidation state of N and lower oxidation state of Ga in heavily Mg incorporated GaN as compared to those in pristine GaN, which is supported by our *first-principles* calculations.

Chapter 7

Magnesium doping in GaN Nanorods grown over Si (111) substrate

In this chapter we discuss the growth and characterization of GaN Nanorods (NRs) formed on Si (111) surface. First part of this chapter is dedicated to the investigation of the enhanced radial growth of NRs upon Mg incorporation, where both electron microscopies and first-principles based calculations are used. The second part contains the study of structural, optical and electronic properties of the samples by X-ray diffraction and various spectroscopic techniques.

7.1 Enhanced Radial Growth

7.1.1 Introduction

P-doping with the incorporation of Mg was found to strongly influence the morphology of nanorods. In a previous report, it was claimed that a small amount of Mg increases the tendency of the rods to coalesce, while keeping their diameter constant, without broadening or tapering²¹⁶ of the rods. Furtmayr *et al.*²¹⁵, also studied the Mg doping effect on MBE growth of GaN NRs and showed that the increase of Mg flux causes an increase in the diameter and a decrease of the height of the nanorods. They further concluded that, the increase in GaN nanorod diameter is due to the enhancement of radial growth, instead of larger nucleation sites. Further work of Zhang *et al.*³⁹³ and Andrews *et al.*²¹⁹ reported that with increase in Mg flow rate the diameter of the nanowire and

nanorod increases. However, Bae *et al.*²²⁰ reported that, higher Mg flow rates affects the equilibrium shapes of the nanorod top regions and caused height variations instead of promoting vertical growth. However, no clear evidence has been reported yet on the origin of such increase in the radial growth of nanorods in MBE grown samples. In the present work we address this and provide novel insights to the growth mechanism of Mg doped GaN NRs on Si.

7.1.2 Methods

7.1.2.1 Experimental Details



Figure 7.1: RHEED pattern of 7×7 reconstructed surface of Si(111).

The GaN NRs were grown directly on Si (111) substrate under nitrogen rich conditions by using a radio frequency plasma assisted molecular beam epitaxy system operating at a base pressure of 3×10^{-11} Torr. Prior to the growth, Si (111) substrate was ultrasonically cleaned in acetone for 10 minutes. Degassing of the substrate at 600 °C for 60 minutes in the preparation chamber followed by degassing at 800 °C for 30 minute and at 825 °C for 5 minutes in the growth chamber were carried out to get a clean Si (7×7) reconstruction (see Fig.7.1). Before the growth, Si (7×7) reconstructed surface was exposed to metallic Gallium (Ga) for 10 second. The temperature of the Ga effusion cell was maintained at 1060 °C. A constant nitrogen flow rate of 4.5 sccm (standard cubic centimeter per minute), plasma forward power of 375 W, substrate temperature of 630 °C and a growth duration of 4 hours were maintained for the growth of all the samples. Mg flux was varied by adjusting the Mg K-cell temperature (see Table 7.1). The fluxes of the Mg and Ga were obtained from the beam equivalent pressure (BEP) and are tabulated in Table 7.1. Surface structural evolution was monitored *in-situ* by reflection high energy

electron diffraction (RHEED) and the morphology was determined *ex-situ* using a field emission scanning electron microscope. Structure of the NRs at atomic scale was studied by high resolution transmission electron microscopy.

Table 7.1: Details of Mg flux rate

Sample Name	Mg K-cell temp (°C)	BEP (Torr)	Flux (atoms cm ⁻² s ⁻¹)	Mg:Ga
A	-	-	-	0
B	340	4.5×10^{-9}	1.29×10^{12}	0.00818
C	350	6.2×10^{-9}	1.77×10^{12}	0.01127
D	360	8.9×10^{-9}	2.52×10^{12}	0.01618

7.1.2.2 Simulation Details

Ab-initio Density Functional Theory (DFT) simulations were carried to estimate the surface energy and diffusion barrier of adatoms on side wall surfaces of GaN NRs. A Generalized Gradient Approximation (GGA) of Perdew *et al.*²⁸² was used for the exchange and correlation energy functional. Integrations over Brillouin Zone of bulk w-GaN were sampled on a Γ -centered $5 \times 5 \times 3$ uniform mesh of k-points in the unit cell of reciprocal space³¹⁶. The lattice parameters and atomic co-ordinates were optimized by using conjugate gradient algorithm to minimize the energy until the forces on each atom were less than 0.04 eV/Å. Optimized lattice parameters of the unit cell of GaN are $a = 3.25$ Å and $c = 5.23$ Å. The surfaces (both undoped and doped) were constructed within the slab model, where 12 atomic layers in the $[10\bar{1}0]$ direction were considered. With this model, four layers of atoms in the middle were kept fixed at their bulk atomic positions to mimic the bulk configuration. We have used a vacuum of 16 Å perpendicular to $(10\bar{1}0)$ surface to keep the interaction between image configurations weak. In case of surface cells, a single k-point was used for the long cell direction, while for other directions, k-points were chosen to match the k-point density of the respective directions used in the bulk calculations. We have estimated surface energy of doped $(10\bar{1}0)$ surface by using the following formula:

$$E_{\text{surf}}(\text{Ga}_x\text{Mg}_{1-x}\text{N}) = \frac{1}{2A} [E_{\text{slab}}(\text{Ga}_x\text{Mg}_{1-x}\text{N}) - E_{\text{bulk}}(\text{Ga}_x\text{Mg}_{1-x}\text{N})] \quad (7.1)$$

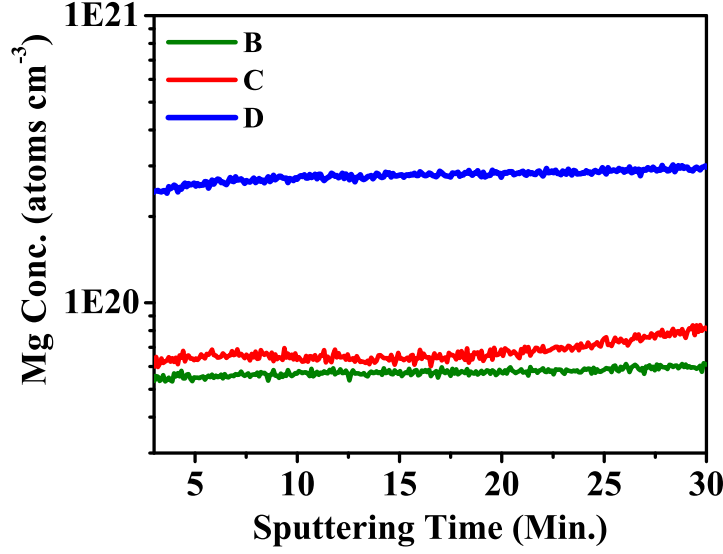


Figure 7.2: Depth profile of Magnesium by SIMS.

where A , E_{slab} , and E_{bulk} correspond to the surface area of the slab, the total energy of the slab, and the total energy of the bulk with same Mg concentration as slab. The diffusion barrier of the Ga adatom on undoped and doped surfaces were estimated from total energy calculations of respective configurations. The adsorption energy of Ga adatom was calculated using following formula:

$$E_{\text{ads}} = E_{\text{tot}}(\text{adatom} + \text{slab}) - E_{\text{tot}}(\text{slab}) - \mu_{\text{Ga}} \quad (7.2)$$

where $E_{\text{tot}}(\text{adatom} + \text{slab})$ and $E_{\text{tot}}(\text{slab})$ are total energy of slab with and without Ga adatom, respectively. μ_{Ga} is chemical potential of Ga adatom given by following formula:

$$\mu_{\text{Ga}} = \mu_{\text{GaN}} - \mu_{\text{N}} \quad (7.3)$$

where μ_{GaN} is chemical potential of GaN which is equivalent to total energy of one formula unit of bulk GaN and μ_{N} is chemical potential of N. Under nitrogen rich conditions μ_{N} is equal to total energy of one nitrogen atom ($\frac{1}{2}E_{\text{tot}}(\text{N}_2)$). Total energy of different configurations were estimated using SIESTA code²⁸¹.

7.1.3 Results and Discussion

7.1.3.1 Experimental Results

SIMS measurements were performed (see Fig.7.2) to confirm the presence and distribution of Mg in the prepared films. Acquired data is normalized with the sample with

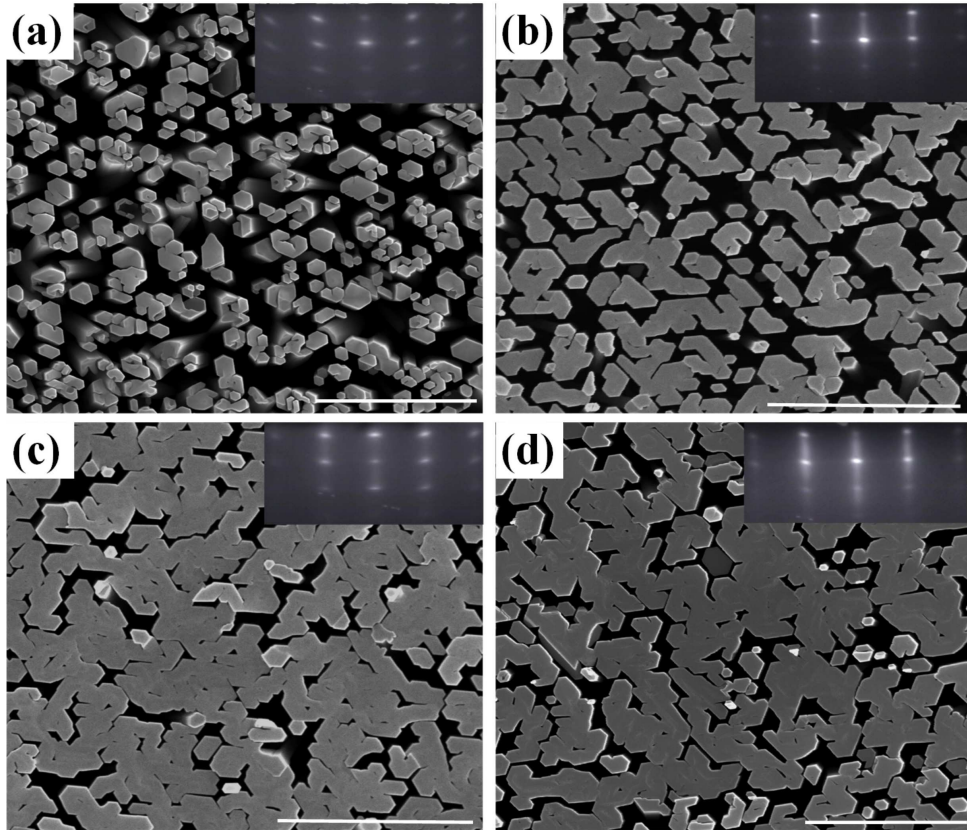


Figure 7.3: (a)-(d) Plan view FESEM images of samples A, B, C and D, respectively. The scale bar represent $2\mu\text{m}$ for all samples. Inset shows *in-situ* RHEED pattern taken along $\langle 11\bar{2}0 \rangle$ of respective samples.

a known Mg concentration to obtain the concentration in our samples. With increasing sputtering duration the Mg concentration is almost constant and therefore we infer that the Mg concentration is homogenous throughout the film. Also, the concentration increases with the increase in the Mg:Ga flux ratio.

Plan view FESEM images of samples A-D grown with different Mg flux-rates (see Table 7.1) are shown in Fig.7.3. We find that most of NRs are vertically aligned with the surface of substrate while few of them are slightly tilted for undoped sample. However, for doped samples (B, C and D), we observe well aligned NRs. It is widely observed that, the relative misorientation of GaN NWs or NRs grown on Si (111) are typically about 3° , both in-plane (twist) as well as out-of-plane (tilt)^{394–397}. The RHEED pattern shown as inset of the FESEM images confirm a typical wurtzite structure and spotty nature of it signifies 3D morphology. However, we also observe the elongation of RHEED pattern along $(10\bar{1}0)$ which may due to relative misorientation of NRs. The RHEED pattern of

doped samples (especially C and D) show an elongated spotty pattern with faint streaky lines which may be due to the electron scattering from the large flat c-plane tops of the NRs³⁹⁸.

To elucidate further we estimate surface coverage of sample A, B, C and D as $55\pm 2\%$, $65\pm 2\%$, $80\pm 2\%$ and $80\pm 2\%$ respectively from the SEM image (see Fig. 7.3). This suggests that by increasing Mg flux the surface coverage of the samples increases. Mg doping not only affects the diameters of the nanorods but also the length of the rod. As Ga and N supply is constant for all the samples, and only the Mg supply is varied with a very small fraction. So an increase in the diameter of nanorods should result in the decrease of the length²¹⁵, which is what we observe from our experimental results measured from cross-sectional FESEM images. The measured length of the NRs of samples A, B, C and D are 3.12 ± 0.05 , 2.94 ± 0.05 , 2.32 ± 0.05 and 2.29 ± 0.05 μm respectively. As for the reference, full cross-sectional FESEM images of samples A and D are shown in Fig.7.4 (a) and (b) respectively.

Further, to look at the interface of Si and GaN NRs, we carried out cross section FESEM imaging of samples (see Fig.7.4). At early stages of growth NRs are isolated but NRs tends to coalesce as growth proceeds. Interestingly, we find with increase in Mg flux, critical height (H_c) for coalescence of NRs is decreasing and is ≈ 900 nm, 280 nm, 250 nm, 210 nm for samples A, B, C and D respectively. Kaganer *et al.*³⁹⁹ suggest that coalescence of NRs or NWs is driven by the fact of gaining surface energy at the expense of elastic energy of bending and the H_c of coalescence is given by the relation:

$$H_c = 4 \left(\frac{E}{9\gamma\omega} \frac{I_1 I_2}{I_1 + I_2} l^2 \right)^{1/4} \quad (7.4)$$

where E is the Young modulus, γ the surface energy, ω the width of the contact area (for calculations it is equal to the radius of the thinner nanowire) and I_i indicates the geometrical moments of inertia of the cross-section of the corresponding nanowire ($i=1,2$). For a cylinder, $I = \pi R^4$ where R is the radius of the cylinder. l denotes separation between nanowires at the bottom. We estimate that a small change in the surface free energy (as shown in Fig.7.7(c)) of $(10\bar{1}0)$ with Mg incorporation may not have much impact on the reduction of critical height of coalescence of NRs. Moreover, comparatively thicker NRs need more energy to bend than their thinner counterparts, suggesting that the mechanism proposed by Kaganer *et al.*³⁹⁹ may not be appropriate for these cases. To

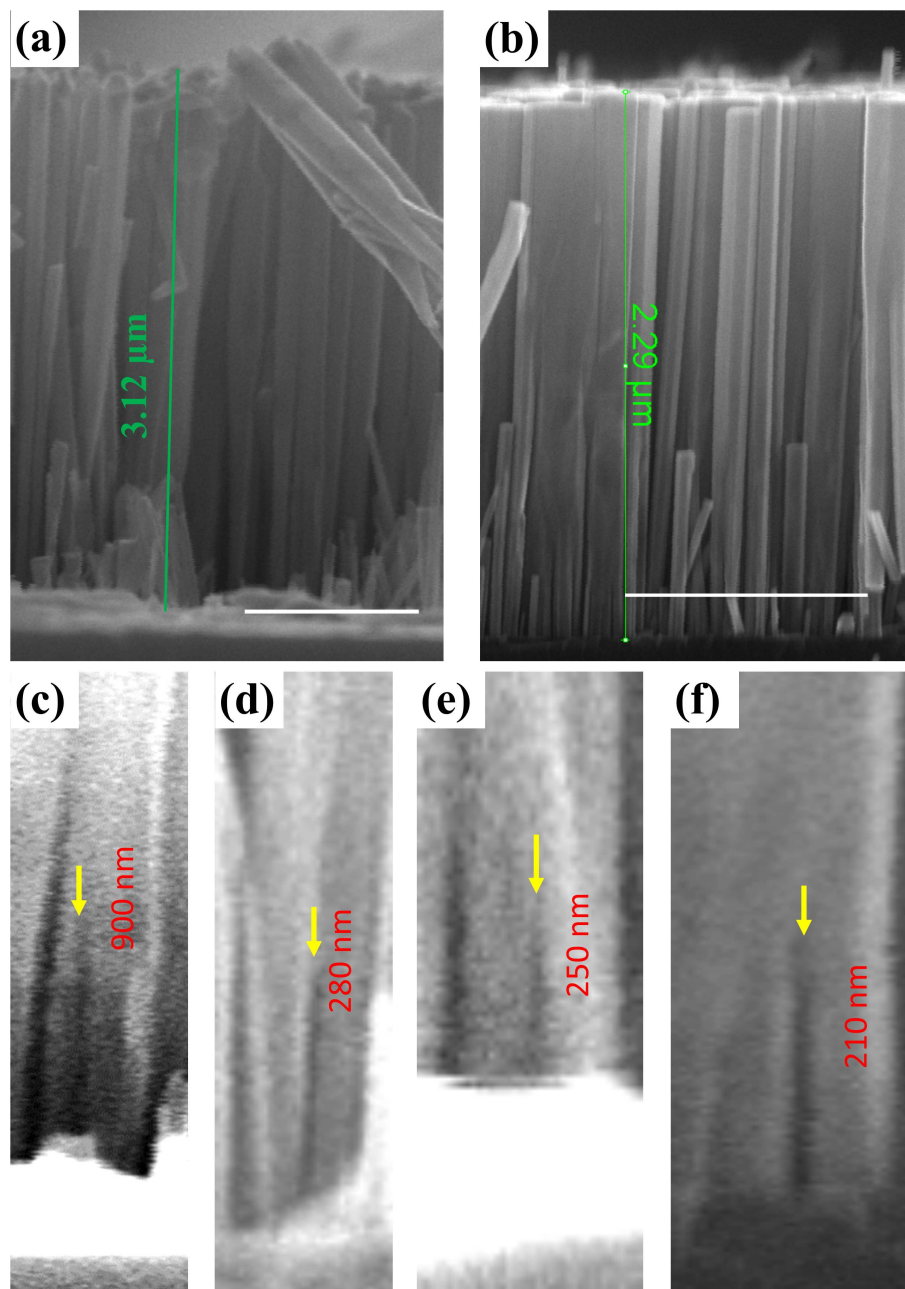


Figure 7.4: (a) and (b) show cross section FESEM images of samples A and D. (c), (d), (e) and (f) represent the cross section FESEM image nearby GaN/Si interface of samples A, B, C and D respectively. Scale bar in (a) and (b) represent $1\mu\text{m}$.

look at the atomistic origin of such behavior, we obtained HR-TEM image of samples B and are shown in Fig.7.5. In Fig.7.5 (a) the dimensions of two different NRs are shown at different heights, which enable us to infer that formation of tapered NRs is due to the formation of atomic steps (see red dots in Fig.7.5(b)) which is probably the consequence of the “shadowing effect” during growth. Figure 7.5 (a) also shows that high densities of

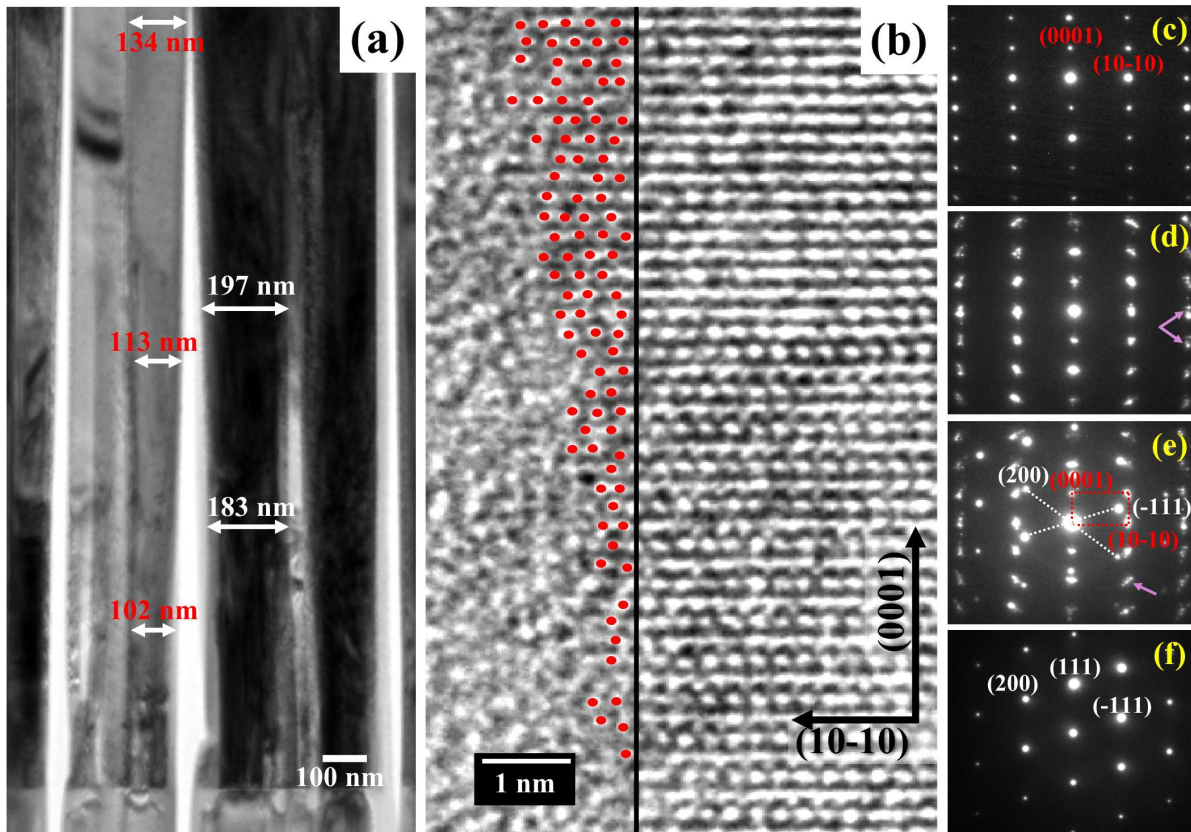


Figure 7.5: (a) shows bright-field TEM image of sample B. (b) shows HRTEM image of a single NRs. (c), (d), (e) and (f) represent SAED pattern recorded from top, just above GaN/Si interface, GaN/Si interface and substrate.

NRs are formed. Figure 7.5(c) shows SAED pattern at the top part of the NRs where a pattern which is perfectly single crystalline in nature was recorded. However, as we move towards the interface, we started observing other diffraction spots including the expected ones (see arrow marked spots in Fig.7.5 (d) and (e)). As these extra spots are lying on the same circle with the other expected spots, we conclude that the extra spots are due to mosaic nature of the NRs. From the SAED pattern of the interface we found that the epitaxial relations between GaN NRs and silicon substrate are $[0002]_{GaN} \parallel [111]_{Si}$ and $[\bar{1}\bar{2}10]_{GaN} \parallel [01\bar{1}]_{Si}$. Absence of any ring pattern in the SAED pattern obtained from the interface region further indicates that no amorphous region is formed at the GaN/Si interface.

The observation of high densities of NRs as well as the tapering effect are observed to be the main reasons for the coalescence of NRs in this particular case. Along with these factors, the reduction in the values of H_c with an increase in the Mg concentration

together suggest that the radial growth rate of sidewall surface of NRs is increasing with an increase in Mg incorporation. To find the atomistic origin of this enhanced radial growth of NRs we have carried out the *first-principles* calculations and the next section of the work is dedicated to same.

7.1.3.2 Estimation of Diffusion Barrier

It is estimated that for $(10\bar{1}0)$ (or ‘m’) plane of GaN, which forms the side wall surfaces of NRs, the diffusion barrier of Ga-adatom shows an anisotropic value. The diffusion barrier along $[11\bar{2}0]$ is merely 0.21 eV while along $[0001]$ direction it is 0.93 eV,⁴⁰⁰ which promotes radial growth of the NRs. To study the role of the presence of Mg atoms on the diffusion barrier of adatoms, we estimated that the total energy of various configurations where Ga adatoms were kept manually at various positions at the $(10\bar{1}0)$ surface as shown in Fig.7.7(a) and (b) wherein a 3×2 in-plane supercell was used. We have taken the similar path in both cases (see Fig.7.7) for the estimation of diffusion barrier of Ga adatoms along the $[11\bar{2}0]$ as discussed in work of Lymperakis *et al.*⁴⁰⁰ and Jindal *et al.*³⁴⁴. Before we discuss about the calculation regarding the estimation of diffusion barrier of Ga ad-atoms on both the undoped and doped surface, we provide a brief discussion on the atomic structure of both the surfaces. In the relaxed geometry of undoped $(10\bar{1}0)$ surface we observe that Ga atoms at the top layer of the slab moves inward into the bulk whereas N atoms moves outward into vacuum in comparison to the ideal $(10\bar{1}0)$ cleaved surface. This results in the vertical separation of ≈ 0.43 Å along $\langle 10\bar{1}0 \rangle$ and buckling of surface Ga-N bond by 13.45° . Because of a such relaxation, we find Ga-N bond reduced to 1.86 Å which is contracted by ≈ 6 % w.r.t. the same in the bulk. Such a behavior is quite consistent with the other reports in the literature^{345,401}. In case of relaxed surface of Mg doped $(10\bar{1}0)$ surface, the atomic relaxation of Ga, Mg and N is bit complex. While Ga atoms move inwards to the bulk, N atoms making bond only with Ga atoms move outward into the vacuum. The Mg atoms are displaced towards the bulk by 0.10 Å and the N atom that makes bond with Mg atoms moves inwards to the bulk by 0.03 Å. The Mg-N bond length at the $(10\bar{1}0)$ surface is ≈ 1.98 Å, while in bulk it is 2.05 Å, which suggests that the Mg-N bond length shrinks at the surface in comparison to bulk value by ≈ 3.4 %. We noted that the adsorption energy of the Ga adatom at doped surface is

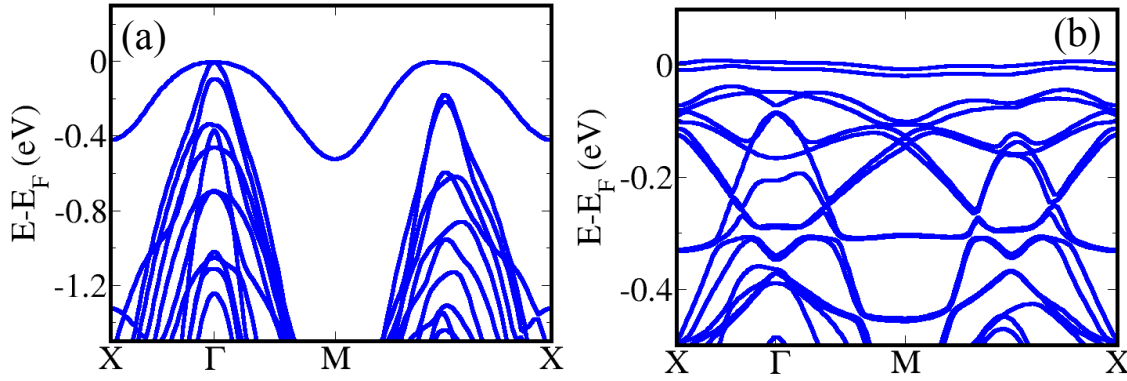


Figure 7.6: (a) and (b) are calculated band structures of undoped and Mg doped surface ($10\bar{1}1$) surface respectively. Please note that only valence band part is shown here. The in-plane supercell sizes used for the band structure calculations for undoped and doped surfaces are 1×1 and 3×2 respectively.

1.9 eV less than undoped surface.

We find the configuration attains minimum energy when Ga adatom takes “A” site (see yellow dot in Fig.7.7 (a)) where it make bond with two surface N atoms with a bond length of 2.30 Å (see Fig.7.7 (d)). Similarly, with Mg doped ($10\bar{1}0$) surface the minimum energy configuration is when Ga adatoms takes “A” site. We find that in this configuration the Ga-N bond lengths are 2.28 Å and 2.30 Å (see Fig.7.7 (e)). The physics and chemistry behind the reduction in the adsorption energy of Ga ad-atoms in Mg doped surface in comparison to undoped surface can be understood as follows: it is obvious that in the bonding of GaN, Ga atoms (cations) transfer $3|e|$ charges to the four nearest neighbouring N atoms (anions). In the undoped ($10\bar{1}0$) surface of GaN, the N derived surface states are completely filled^{402,403} while upon Mg doping, an unoccupied state (hole state) is present near the VBM *i.e.* Mg doped surface is electron deficient (see Fig.7.6). Thus, Ga adatoms can transfer charges more efficiently to Mg doped surface in comparison to undoped surface, by which the bonding of Ga adatom with the Mg doped surface is stronger in comparison to the undoped surface. Mulliken population analysis⁴⁰⁴ further validates our proposed mechanism and the estimated charge transfer from Ga adatom to the undoped and Mg doped slab are $\approx 0.56|e|$ and $\approx 0.59|e|$ respectively.

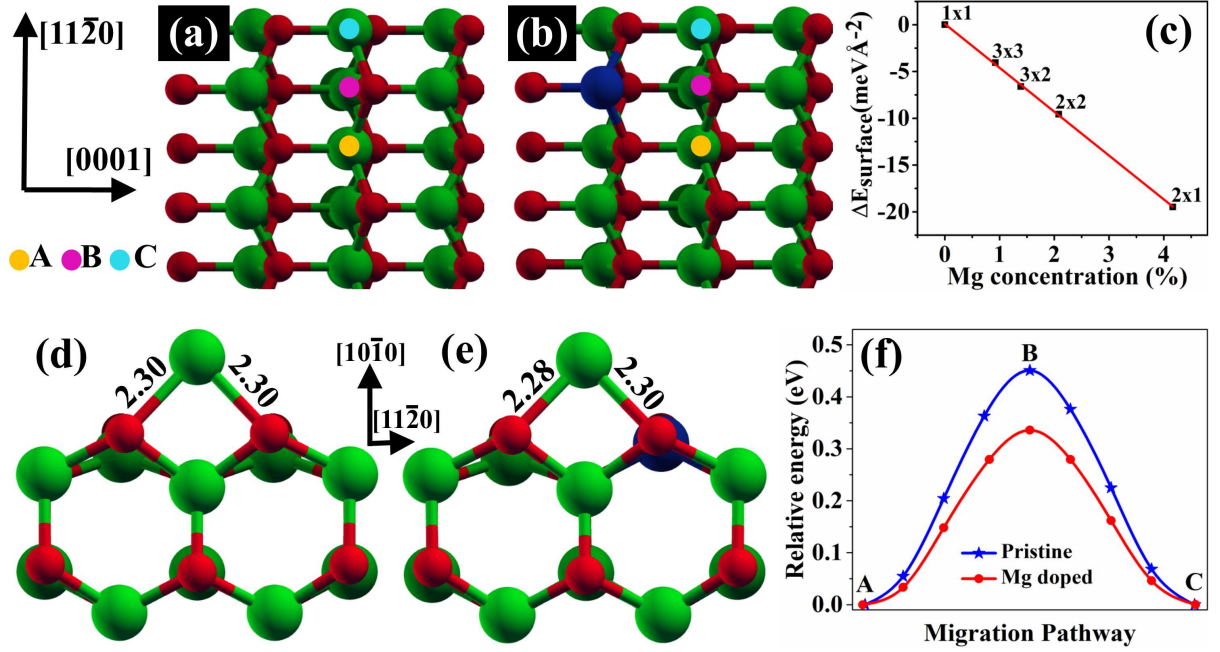


Figure 7.7: (a) and (b) show the undoped and Mg doped slab models used for calculations, respectively. (c) represent the estimated surface energy of the doped surface with different doping concentrations (the number mentioned nearby data points represent in-plane supercell dimension used for the particular calculation). (d) and (e) represent crosssectional view of relaxed atomic structure of Ga adatom at undoped and doped surface at most stable configurations of the respective cases. (f) represent the relative energy of different configurations where ad-atoms were kept at various position along the path A-B-C. The lowest energy configurations are the reference ones.

To estimate the diffusion barrier, we calculated the total energy of various the configurations where Ga adatom migrate from one minimum energy configuration (site “A”) to another (site “C”). At undoped surface, we estimated the diffusion barrier as ≈ 0.45 eV, while with Mg doped it reduced to 0.33 eV. Such a reduction in the diffusion barrier will increase the diffusion length (L_{diff}) of adatoms as L_{diff} is proportional to $\sim \sqrt{\Gamma\tau}$, where τ represent the average adatom life time. Γ is the diffusion coefficient which is proportional to $\sim exp(-E_{diff}/k_B T)$, where E_{diff} is the diffusion barrier, k_B and T are the Boltzmann constant and absolute temperature. By taking the growth temperature as 900 K, we find L_{diff} of Ga adatoms on Mg doped surface (with surface Mg concentration as 8.3%) is two times higher than the undoped $(10\bar{1}0)$ surface of GaN. Such an increase in the L_{diff} is due to the presence of Mg on surface which increases the probability of

incorporation of adsorbed Ga adatoms leading to the enhanced radial growth of NRs.

Work of Kaganer *et al.*³⁹⁹ suggests that, the nucleation of nanowires are random and homogeneous. After the nucleation, such nanowires attain a self equilibrated diameter beyond which nanowires grow only in the axial direction but not in the radial direction. We propose such a behavior of NRs growth is the reason for the pinning of surface coverage at $80\pm 2\%$ for higher Mg-doped samples.

7.1.4 Summary

In summary, we have synthesized and characterized Mg doped GaN NRs grown on Si (111) surface. We have observed that with an increase in the Mg concentration the surface coverage of the samples increases due to higher growth rate of the sidewall surface of NRs. From TEM analysis we have found that the NRs are tapered as a consequence of the formation of atomic steps on the side surfaces of NRs. From SAED analysis we have found that the NRs regions proximal to the interface possess more mosaicity while mosaicity decreases with the increase in nanorods thickness. From *first-principles* calculations we have shown that the reduction of the diffusion barrier for Ga ad-atom diffusion due to presence of Mg atoms, on the $[10\bar{1}0]$ surface, along the $[11\bar{2}0]$ is the reason for the enhanced radial growth rate of NRs.

7.2 Structural, Optical and Electronic properties

7.2.1 Experimental Details

The growth parameters employed in the study have already been discussed in the previous part of this work. The structural quality of the films was determined using a high-resolution X-ray diffractometer with a Cu K_α X-ray source with wavelength of 1.5406 Å. The optical properties of the films were studied by photo-luminescence spectroscopy (PL, Horiba Jobin Yvon) using a Xenon lamp source for excitation and Raman spectroscopy with an Ar laser of wavelength 514 nm was performed in the back scattering geometry. The electronic structure of the films were characterized by X-ray photoelectron spectroscopy (XPS) with Al- K_α (1486.7 eV) source.

7.2.2 Structural Properties

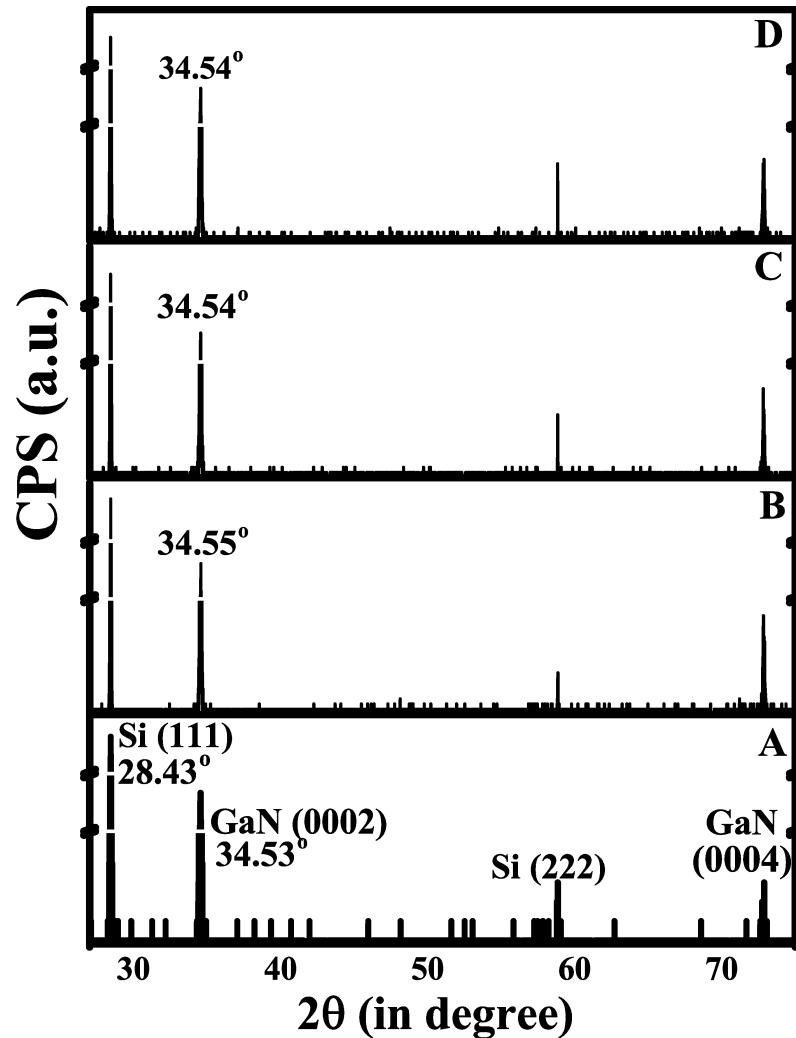


Figure 7.8: Symmetric 2θ - ω scan acquired by HRXRD of samples A-D, respectively.

To study the structural properties of Mg doped GaN NRs, we carried out HR-XRD measurements of the samples (see Fig 7.8). From the symmetric $2\theta - \omega$ scan, we find that the GaN (0002) reflex is present along with with Si (111), (222) and GaN (0004) reflexes (see Fig.7.8). Figure 7.8 suggests that all the GaN NRs samples (undoped and Mg-doped) possess single crystal, wurtzite structure with preferential growth direction along the c-axis (0001) with the epitaxial relation of $[111]_{Si} \parallel [0002]_{GaN}$. The intense GaN (0002) reflexes at 34.53° , 34.55° , 34.54° and 34.54° for samples A, B, C and D respectively suggest that with Mg incorporation, c lattice parameter of GaN has reduced. This is contrary to the typical behavior wherein the lattice parameters of GaN increase as ionic radius of Mg is larger than that of Ga³⁵⁵. However, if defect complexes are formed, this behavior

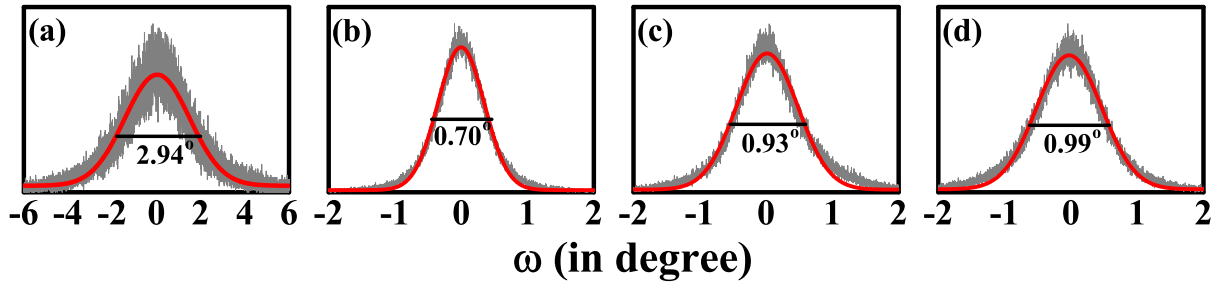


Figure 7.9: shows rocking curve of GaN (0002) reflex of samples A-D, respectively.

can be different³⁵⁵. Omega (ω) scan (or Rocking Curve) of all the samples shows (see Fig.7.9) that the FWHM of GaN (0002) reflex is less for Mg doped GaN NRs compared to undoped GaN NRs. To be specific, the recorded FWHM of GaN (0002) reflex obtained by ω -scan of undoped GaN NRs is 2.94° , which is much higher than doped samples B, C and D where the values are 0.70° , 0.93° and 0.99° respectively. As discussed previously, epitaxial growth of GaN on silicon surface possess mosaicity ($\approx 3^\circ$), which is the main reason for the increase in the FWHM of GaN (0002) reflex. The reduction in the FWHM of GaN (0002) reflex due to Mg incorporation suggests a reduction in the mosaicity of NRs. But with further increase in Mg incorporation the FWHM of GaN (0002) reflex increases possibly due to the formation of certain defects in the material, as discussed earlier in case of Mg doped GaN NWN.

7.2.3 Optical Properties

To study the optical properties of our samples PL, CL and Raman spectroscopy studies were carried out. Fig. 7.10 shows the PL spectra of all samples where it can be seen that, in case of undoped sample (A), the PL spectra primarily consists of two peaks, a dominant near band edge (NBE) emission at 3.4 eV and a broad yellow-luminescence (YL) peak centered at ≈ 2.2 eV. The origin of this YL peak has been debated over the years^{405–407}. Recent work based on Density Functional Theory (DFT)⁴⁰⁸ suggests that, Ga vacancies (V_{Ga}), which occurs predominantly in GaN thin films grown under N-rich condition is the microstructural origin of the YL. Similarly under Ga-rich condition, the N vacancy (V_N) formation energy is low and can also be responsible for YL. Another study⁴⁰⁹ suggests that an interstitial Ga (Ga_i) which creates a shallow donor state in the electronic structure whose formation energy becomes lower under p-type conditions

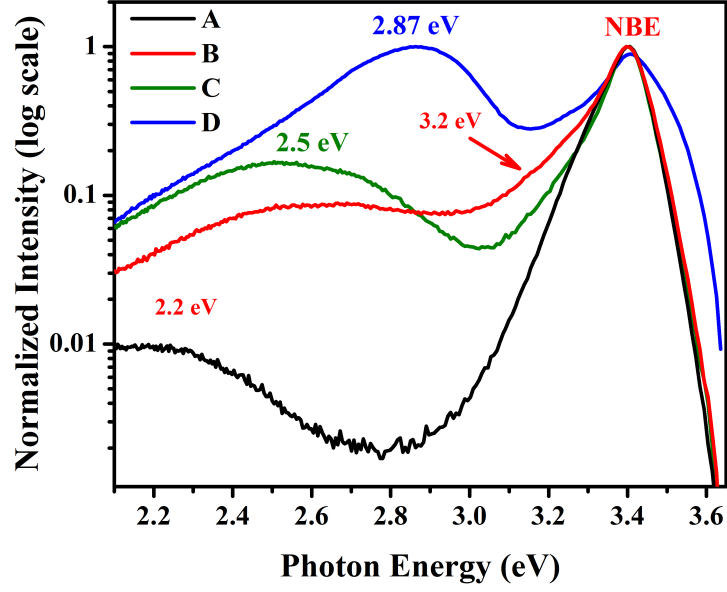


Figure 7.10: Room temperature photoluminescence (PL) spectra of undoped and Mg doped GaN NRs.

can also be another reason for the observed YL. The other mechanisms for YL are also proposed where it is the result of a transition from shallow donor (Si or O impurities) to deep acceptor (cation vacancy complex)⁴¹⁰ or shallow acceptor to deep donor⁴¹¹. For lightly doped samples B and C, we record a green luminescence (GL) peak centered at ≈ 2.5 eV and a small peak at ≈ 3.2 eV along with NBE. It is believed that the GL peak is a result of the blue shift of YL and has the same origin³⁸⁶. Reshchikov *et al.*³⁸⁶ has attributed this GL to internal transitions within the V_N donors where the atomic configuration of the donor changes from V_N^{2+} to V_N^+ . Referring to this report, we further attribute the YL peak to V_N as proposed by Van de Walle *et al.*³³⁵. We also attribute the peak centered at 3.2 eV to the DAP transition, which is due to a nominal incorporation of Mg in these samples (Mg concentrations of less than 10^{19} atoms per cm^3)¹⁷³. Highly Mg doped sample (D) shows a broad NBE peak and a broad 2.87 eV blue luminescence (BL) peak which is the signature of high Mg incorporation (here Mg concentration is 2.67×10^{20} atoms per cm^3)¹⁷³. Earlier reports suggest that BL band is due to optical transitions from a deep donor (350-430 meV) to a shallow Mg acceptor^{173,371} levels. However, recent DFT-based work suggests that the emergence of BL also due to different ionization energies of nitrogen vacancies (V_N)¹⁵³ and of hole localization at neighboring N atoms¹⁸². But all these claims do not explain the absence of BL from samples with lower Mg-concentration.

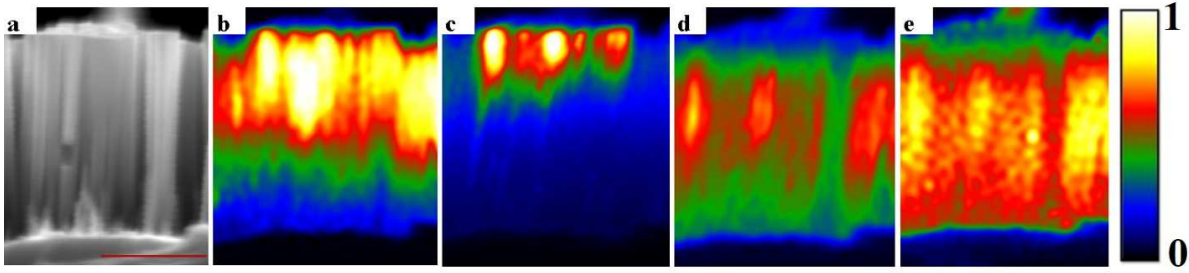


Figure 7.11: shows cross section FESEM (a), Panchromatic CL-mapping of whole spectra (1.77 - 4.13 eV) (b), monochromatic CL mapping of Band edge emission (3.35 eV) (c), (d) and (e) Mg related peak (2.93 eV and 2.70 eV, respectively).

Our recent study suggests (as discussed in **Chapter 6**) that Mg interstitial related defects complex ($Mg_{Ga}+Mg_i$) in high Mg incorporated GaN, gives rise to a deep donor state in the electronic band gap and may be responsible for the observed BL by deep donor-shallow acceptor pair (DAP) transition⁴¹². A typical PL spectra of heavily Mg-doped GaN shows only BL peak, whereas we find that for the grown GaN NRs display both NBE and BL.

To study the spatial distribution of the luminescence from the cross-section of sample D, we recorded the CL-map of each luminescence peak, which are shown in Fig. 7.11. We find NBE is mainly localized at the tip of the NRs and emission from bottom of the NRs is almost negligible. Similar behavior is also seen in undoped and other Mg-doped samples. Contrary to NBE, emission related to Mg impurity is quite uniform throughout the length of NRs. The low intense NBE emission from the bottom region of NRs is probably due to formation of misfit dislocations and/or point defects at the initial stage of growth because of large lattice mismatch between GaN and Si. The formation of atomic steps as seen from HR-TEM images, may also act as non-radiative recombination centers. With increase in the growth duration, these dislocations are pumped out of the material by sidewalls, thus increasing the band edge emission.

To study strain and stability of the grown NRs, we acquired Raman spectra of samples (see Fig. 7.12). The $E_2(\text{high})$ mode being non-polar in nature (meaning that its position is mainly influenced by strain) and can be used as a measure of the strain state of the material. The FWHM of this mode is an indicator of the defect incorporation in the film, since strain gradient or phonon-defect scattering can lead to the broadening of

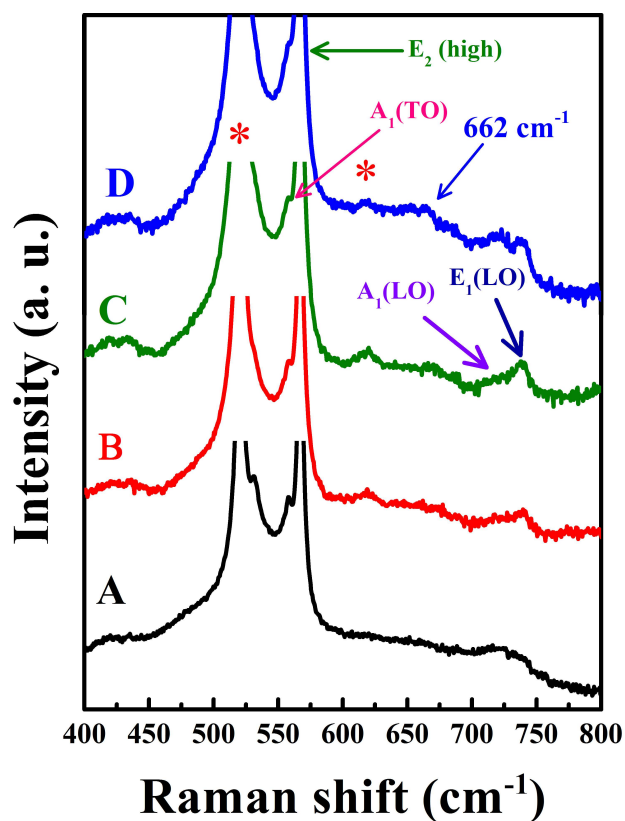


Figure 7.12: Raman spectra of undoped and Mg doped GaN Nanorods (NRs). “*” represents the phonon mode from silicon. The appearance of Mg related LVM can be observed at 662 cm^{-1} with increasing Mg:Ga ratio.

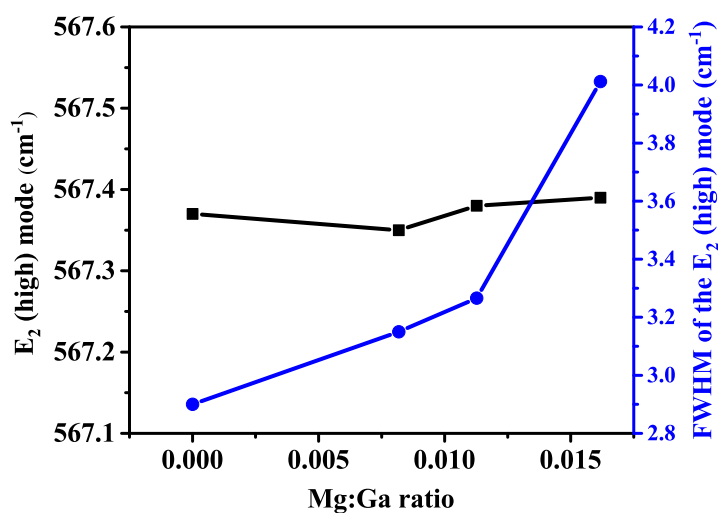


Figure 7.13: Variation of the position (squares) and FWHM (circles) of the strain sensitive E_2 (high) Raman mode with the Mg:Ga.

this mode. We find a small change in the position of $E_2(\text{high})$ peak (from 567.35 to 567.39 cm^{-1}) which suggests that a very small macroscopic strain is being generated in the NRs with Mg incorporation (see Fig. 7.13). We also find that with the increase in Mg-flux, FWHM of $E_2(\text{high})$ peak increases, which can be attributed to the generation of different defects in the samples depending on the concentration of Mg incorporation³⁵⁵ which possibly results in the different luminescence peak as seen in PL spectra (see Fig.7.10). Thus, we can attribute that, upon high Mg incorporation, the structure is still stable but different point defect complex(es) is (are) being generated. Along with the standard expected peaks from GaN, a LVM appears at 662 cm^{-1} , which has its origin in the formation of Mg-N bond⁴¹³.

7.2.4 Electronic Properties

7.2.4.1 XPS

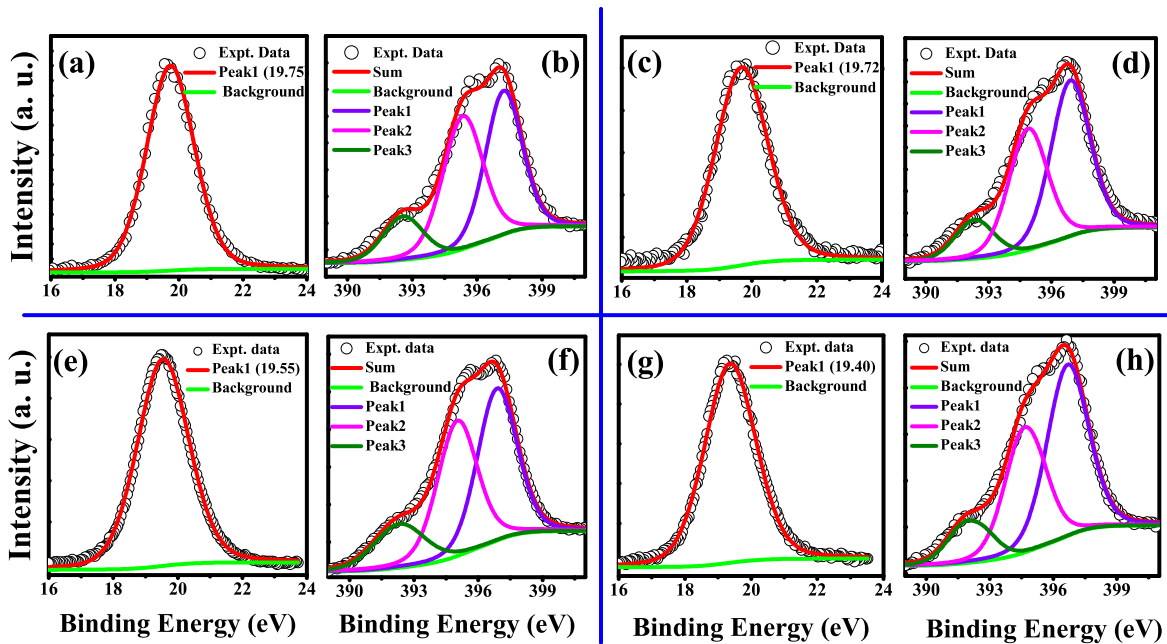


Figure 7.14: Ga-3d (a, c, e, g) and N-1s (b, d, f, h) spectra of the sample A, B, C and D, respectively.

To probe the electronic structure of these samples, we carried out XPS measurements. The deconvoluted spectra of Ga-3d and N-1s core level are shown in Fig.7.14. For Ga-3d core level spectra, we found only a single Voigt function (Gaussian: Lorentzian=0.8:0.2)

fitting appropriately, suggesting neither a metallic Ga-Ga nor the Ga-O bonding is present on the surface of samples. The deconvoluted N-1s core shows three peaks, one of them centered around 396-397 eV is assigned to the binding energy of N due to bonding with Ga, while the other two peaks are due to Ga LMM transitions. The energies and FWHM of Ga-3d and N-1s core levels of samples under consideration are listed in Table 7.2. From the Table it is clear that both Ga-3d and N-1s core level peaks are shifted to lower energy with increasing Mg incorporation. This is seen as a consequence of a continuous downshift of the Fermi level towards the VBM with increase presence of Mg. Further to quantify

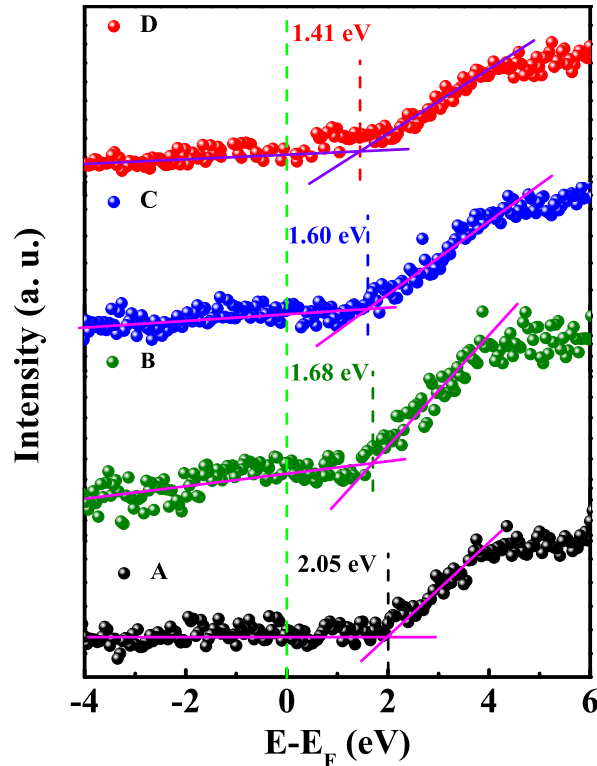


Figure 7.15: Valance band spectra of samples A, B, C and D.

the shift in the Fermi level with respect to the VBM, we have analysed the valence band spectra of these samples and shown in Fig.7.15. We find for the undoped sample, Fermi level is at 2.05 eV above VBM indicating native n-type character of pristine GaN NRs. With an increase in Mg incorporation the Fermi levels are observed at 1.68, 1.60 and 1.41 eV above the VBM for samples B, C and D respectively. This shows that the Fermi level is shifting towards the VBM, due to the increase of p type character with Mg incorporation.

Table 7.2: XPS Data

Mg:Ga	N-1s peak position (eV)	FWHM of N-1s peak (eV)	Ga-3d peak position (eV)	FWHM of Ga-3d peak (eV)	$E_{Fermi}-E_{VBM}$ (eV)
0.0000 (A)	397.28	2.00	19.75	1.77	2.05
0.0082 (B)	396.96	2.20	19.69	1.91	1.68
0.0113 (C)	396.93	2.17	19.57	1.88	1.60
0.0162 (D)	396.75	2.30	19.39	1.83	1.41

7.2.5 Summary

In summary, we have grown and characterized the Mg doped GaN NRs samples with various complementary characterization tools. We find that the mosaicity of the NRs reduces upon Mg incorporation, however with the increase in the Mg concentration, the crystal quality of the NRs slightly degrades. Further, optical properties of the NRs are found to be sensitive to Mg concentration probably due to the formation of different defect complexes with different Mg flow rate. XPS data clearly suggests that upon Mg incorporation, the core-level spectra get broader and also shift towards lower energy due to shift of Fermi levels towards the VBM. Thus the XPS results clearly suggest that p-type carriers are being generated.

Chapter 8

Conclusions

The aim behind the work of the thesis is to shed light on some of the important unanswered questions on growth and properties of Gallium Nitride nanostructures. All these issues have been studied and discussed thoroughly, by using complementary experimental and computational tools, in preceding chapters. This chapter summarizes all the work undertaken and attempts to draw conclusions from the inferences drawn from the observed results. This chapter also provides a brief outlook for the future direction for research as an outcome of the present work, lists the highlights of the work and also discussions on some limitations of the present study.

8.1 Summary and Conclusions

In the recent past, our group has been involved in studying the growth and properties of III-nitride thin films and nanostructures. Furthering that work, for this thesis, we have made an attempt to understand the growth and properties of GaN nanostructure, including effects to p-dope them, such as the ubiquitous nanowall network and nanorods. The nanowall network having demonstrated some unique and superior material properties in comparison to flat film, nanorod and nanowire configurations, desirous to be keenly understood so that it can be employed to fabricate devices. As already discussed in the previous work chapters, our approach has been a combination sophisticated experimental tools and *first-principles* theoretical calculations. The major issues that we have addressed in this thesis work are:

- The Growth mechanism underlying the formation of GaN nanowall network on the sapphire (0001) substrate
- Role of pore dimension in determining the photoluminescence intensity of GaN nanowall network
- Atomistic origin of the high electrical conductivity and high background carrier density observed in the GaN nanowall network
- Effect of Mg incorporation on morphological, structural, optical and electronic properties of GaN nanowall network on c-sapphire substrate
- Atomistic origin of the blue luminescence (2.7-2.95 eV) and self-compensation effect in heavily Magnesium doped GaN
- Effect of Mg incorporation on the morphology, structural, optical and electronic properties of GaN nanorods on silicon (111) substrate

In the study to understand the growth mechanism of GaN nanowall network, samples were grown for different durations and the evolution of the surface morphology was monitored at different stages. Our finding suggests that at a very early stage of the growth dome-shaped islands are formed, which increase in size with growth duration, and the shape changes forming $\{20\bar{2}1\}$ faceted tetrahedron shape islands. Further, at this stage we observed the formation of Y-shaped structures where the tail length of such Y-structures increases monotonically with the increase in growth time until it encounters other islands or another Y-shaped structure. *First-principles* DFT calculations were carried out to understand the Ga adatom diffusion dynamics on such faceted structures. Our finding suggests that the adsorption of Ga adatoms at the thinner part of the facets is energetically preferable in comparison to the thicker counterpart. The Ga adatoms have to overcome a barrier potential of nearly 0.36 eV to migrate from thicker faceted region to thinner ones, whereas for reverse diffusion the barrier potential is 0.98 eV. This shows why it is relatively easy for Ga ad-atoms to diffuse from thicker part of the wedge to thinner part (towards the edge) while the diffusion from edges of the wedge to the thicker part is energetically not favourable. It is evident that this causes a large amount of flow of ad-atoms towards the edges of the pyramidal islands, resulting in the edge enhanced

growth. Thus, we show that growth of GaN nanowall network is an excellent example of Structure-Dependent Attachment Kinetic (SDAK) instability induced thin film growth.

To understand the role of pore dimensions on the photoluminescence intensity of porous GaN in the form of nanowall network, we grew, by controlling the growth parameters, various samples of porous GaN with different pore sizes without the use of any catalyst (*i.e.* spontaneously formed) on sapphire (0001) substrate. The estimated average pore dimensions of the samples studied are $\approx 45, 170$ and 215 nm. The PL intensity (area under the Near Band Edge curve) ratio between a flat epitaxial layer and the homegrown films observed is 1:4:12:140, showing that GaN nanowall network has a very high emission with no defect level transitions in nanowall network. We also found that wider full width at half maximum of the high-resolution x-ray diffraction rocking curve for nanowall network sample in comparison to flat GaN epilayer is due to misalignment between individual nanowalls. Further, it was noted that the increase in the integrated PL intensity of GaN nanowall network is not solely depended upon the crystal quality of the films, but rather on the pore dimensions, which plays the dominant role. FDTD simulation reveals qualitatively that the geometry and porosity reduces the total internal reflection and enhances light extraction into the ambient.

Origin of high carrier (electron) density in as grown GaN is a topic of debate in the literature (especially for MBE grown samples). To understand the origin of this auto-doping is essential for controlling the native n-type character and for the synthesis of efficient p-doped GaN. We probe the presence of vacancy defects in bulk and also the role of vacancies at the $(10\bar{1}0)$ surface, the nanowalls are bound by this facet and relate these vacancies to the unintentional n-type doping of nanowall network using *first-principles* DFT calculations. The properties related to defects at the surface of GaN is very poorly understood in the literature due to the challenges in determining finite-size supercell correction, which is critical in the estimation of defect formation energy, for those with charge states. In this work, we overcome this issue by employing the methodology proposed by Freysoldt, Neugebauer, and Van de Walle (FNV) to estimate the finite-size supercell correction term. Estimated formation energy of neutral Ga vacancy obtained under N rich conditions is 6.90 eV, while in $-1, -2$ and -3 charge state the formation energies are calculated to be $7.17, 8.29$ and 10.18 eV, respectively. Estimated thermodynamic

transition levels (0/-), (-/2-) and (2-/3-) of V_{Ga} are at 0.27, 1.11 and 1.89 eV, respectively, above VBM. Further, the derived electronic structures suggest that neutral Ga vacancies in bulk GaN are triple acceptors and the associated states are spin-polarized. The highly debated role of N-vacancy in GaN was addressed by estimating the formation energy as a function of vacancy concentration. It was found that this formation energy varied in all the cases with values \approx 4.73, 4.75 and 5.21 eV for vacancy concentration of 6.25%, 2.76% and 1.56%, respectively. In addition, our estimate of the formation energy of V_N in the charged state of +1, +2 and +3 are 3.10, 3.75 and 4.90 eV, respectively at $E_F=0$. The thermodynamic transition levels of V_N such as (+/0), (2+/3+), (3+/+) are seen to be present 2.10 eV above VBM, 0.7 and 0.9 eV below VBM, respectively. We observe that spin-polarized DOS within the LDA does not give rise to any net magnetic moment due to N vacancies. We find that, although N-vacancy is a triple donor, the presence of fully occupied state below the VBM makes it effectively a semiconductor with one electron per single N-vacancy for conduction. From the surface electronic structure, the fundamental direct band gap obtained for the (10 $\bar{1}$ 0) surface slab is 1.86 eV, which is 0.2 eV lower than the calculated bulk band gap. Our estimate of the formation energy of Ga vacancy at (10 $\bar{1}$ 0) surface is 3.97 eV, which is 2.93 eV less than that at bulk *w*-GaN, under N-rich conditions. The defect formation energy of surface Ga vacancy in -1, -2 and -3 charged states are calculated to be 4.35, 4.62 and 7.92 eV, respectively. We find that under p-type growth conditions neutral gallium vacancy is the most stable while under n-type growth conditions Ga vacancy in -2 charged state has better stability, with a thermodynamic charge transition level of (0/2-) at 0.32 eV above surface VBM.

Our estimate of formation energy of N vacancy at (10 $\bar{1}$ 0) surface of *w*-GaN is 3.17 eV, which is 2.04 eV less than for bulk *w*-GaN. The estimated defect formation energy of surface N vacancy in +1, +2 and +3 charged states are 0.04, -1.31 and -2.86 eV, respectively. We find that under p-type growth conditions N-vacancy with +3 charged state while for n-type conditions +1 charged state are most stable. We also estimate that the Fermi level pins at 0.35 ± 0.02 eV below surface CBM. Further, to model the atomic steps in the side wall surface of nanowall network, we remove a line of N-atoms and performed the calculations. We find that proximal vacancies are more stable and promote clustering of vacancies. The surface electronic structure in these configurations

indicates metallic nature of the surface. EELS data suggests the presence of deep trap states with transition level at 2.2 eV as well as shallow states, which indicates N vacancies at the surface are responsible for high electrical conductivity as observed in GaN nanowall network.

The study of Mg incorporation in GaN nanowall network was motivated by the fact that in flat Mg-doped GaN thin films, the concentration of Mg incorporated on the surface is higher than in the bulk. Thus, we envisaged that GaN with the higher surface area can enable higher effective incorporation of Mg, by enhancing the solubility limit. Because of nanowall network with its porous structure has a very high surface to volume ratio, this morphology appeared to be a potential candidate for achieving high-quality p-GaN. We find that surface morphology of the grown films did not change upon Mg incorporation and the average pore dimension of all nanowall network remained unchanged. In our PL studies, we observed that the Near Band Edge is dominant in samples with relatively lower Mg incorporation and its intensity increases with increasing Mg:Ga flux with Donor-Acceptor Pair transition at 3.2 eV. For heavily doped samples, we find the blue luminescence (2.7-2.95 eV) dominates over other luminescence peaks. The intensity of BL is further seen to be sensitive to the annealing temperature of the samples. Raman spectroscopy revealed the Local Vibrational Mode of Mg-doped GaN appears at $\approx 657 \text{ cm}^{-1}$ due to the Mg-N stretching mode. The E_2 (high) mode shows a large variation and is sensitive to the concentration of Mg incorporation. The HR-XRD measurements suggest that FWHM of rocking curve of (0002) displays an “U” type behaviour with increasing Mg:Ga flux, whereas for (10 $\bar{1}$ 1) the values reduce as Mg incorporation increases which suggest that Mg incorporation reduces mosaicity in the films. X-ray Photoelectron Spectroscopy revealed that with increasing Mg:Ga ratio, the binding energy of Ga-3d and N-1s core-levels of samples are red shifted suggesting that there is a continuous downward shift of the Fermi level towards VBM with the increase in Mg concentration. Valence band spectra shows clearly that the $(E_F - E_{VBM})$ reduces from 2.42 eV (undoped sample) to 1.09 eV (highest doped samples) shows the formation of p-GaN nanowall network.

The microscopic origin of blue luminescence and the self-compensation effect in heavily doped GaN is intensely debated in the literature, however, no clear conclusions have

been deduced yet and has motivated us to investigate its microscopic origin. For this, we used a combination of experimental X-ray absorption near edge spectroscopy (XANES), *first-principles* calculations based on density functional theory and full multiple scattering theoretical analysis of various possible defect complexes. For the heavily doped sample, where 2.7 eV peak was noted, the absorption threshold of N K-edges is observed to shift $\approx 0.7\text{eV}$ towards higher energy, relative to that of undoped samples with a clear distortion of the peak K-edge, suggesting the formation of deep localized states. Our simulated N-K edge and Ga L_3 edge match a defect complex composed of Mg-substituted at Ga site (Mg_{Ga}) and Mg at interstitial site (Mg_{i}) is seen to be primarily responsible for the observed BL by Donor-Acceptor Pair transition (DAP) associated with a deep donor state in the gap. This correlates with a higher (lower) oxidation state of N (Ga) in heavily Mg-doped GaN than in its pristine structure which becomes evident in our experiments and calculations. Based on our observations and analysis we propose that synthesis of p-type GaN under lower Ga flux (Ga poor condition) will be more efficient than under Ga rich condition at lower substrate temperatures.

Finally, we study the growth and characterization of Mg-doped wurtzite phase GaN nanorods formed on silicon (111) substrate. We observe that incorporation of Mg in the nanorods strongly influence their morphology since the diameter of the nanorods (or surface coverage) increases with increase in Mg concentration in the films. Firstly, we investigate the microscopic origin of such enhanced radial growth using various experimental techniques and *first-principles* DFT calculations. We find that during early stages of growth nanorods are quite isolated but the nanorods tends to coalesce as growth proceeds and the critical height of coalescence is related to Mg concentration in the films which decreases with increase in Mg concentration. HRTEM imaging revealed the formation of tapered nanorods due to the formation of atomic steps as a consequence of growth with shadowing effect of neighbouring rods. From DFT calculations we note that upon Mg incorporation of 8.3% on $(10\bar{1}0)$ the diffusion barrier along $[11\bar{2}0]$ of Ga adatoms reduces by 26.6% in comparison to the pristine surface. This explains how this could be the influential factor for the enhanced radial growth of nanorods.

HR-XRD measurements show that “c” lattice parameter of GaN reduces upon Mg incorporation, contrary to the expectations, wherein the lattice parameters of GaN should

increase since the ionic radius of Mg is larger than that of Ga. This deviation is attributed to the formation of different defects or defect complexes, that modify the as the local strain. We note that the FWHM of GaN (0002) reflex obtained by ω -scan of undoped GaN nanorods is 2.94° , which is much higher than those in doped samples (0.70 - 0.99°), and is attributed to the reduction of mosaicity in the films by Mg incorporation. PL spectra of undoped nanorods revealed two optical transition peaks: a dominant Near Band Edge emission at ≈ 3.4 eV and a broad YL peak centred at ≈ 2.2 eV. PL spectra observed for GaN nanorods with Mg concentration is less than 6×10^{19} atoms cm^{-3} a green luminescence peak centred at ≈ 2.5 eV and a small peak at ≈ 3.2 eV along with Near Band Edge emission. With an increase in Mg concentration to $\approx 2.67 \times 10^{20}$ atoms cm^{-3} , a broad Near Band Edge peak and a broad 2.87 eV blue luminescence peak is seen in the photoluminescence spectra. Cathodoluminescence mapping study revealed that Near Band Edge is mainly localized at the tips of the nanorods, while the emission from the bottom of the nanorods is almost negligible. However, the Mg impurity is quite uniform by distributed throughout the length of nanorods. Raman spectroscopic study reveals a small change in the position of $E_2(\text{high})$ peak, whereas its FWHM increases with increase in Mg concentration. X-ray photoelectron spectroscopy study shows that the Ga-3d and N-1s core levels peaks shift to lower energy with increasing Mg incorporation. This is again interpreted as a consequence of a continuous downshift of the Fermi level towards the Valence band minima which is also evident from the valence band study in which the $E_{Fermi}-E_{VBM}$ is seen to reduce from 2.04 eV (undoped sample) to 1.41 eV (highest doped sample).

Thus, in its entirety, the thesis addresses several key issues that plague the exploitation of the enormous potential of GaN in commercialization. We show here that the nanowall network morphology of GaN can be the material that may help us obviate these limitations and be used for device fabrication with enhanced performance.

8.2 Highlights of the work

We list here the significant observation and inferences that have resulted from this work:

- An anisotropy in the diffusion barrier for adatoms on $(20\bar{2}1)$ faceted pyramid depending upon the width of the facets is shown to be the mechanism behind the shape transition that leads to the formation of the nanowall network.
- The band edge intensity of nanowall network in photoluminescence study is found to strongly increase with the average pore dimensions of the films. The nanowall with the largest pore size (≈ 215 nm) shows two orders of magnitude enhancement of integrated PL intensity compared to that of the GaN flat film and is attributed to the unique geometry that reduces total internal reflection.
- N-vacancies are identified as the primary reason behind the high electrical conductivity in GaN nanowall network. *First-principles* calculations suggest, surface nitrogen vacancies form spontaneously and give rise to the native n-type character of $(10\bar{1}0)$ surface. These nitrogen vacancies are found to result in a metallic electronic structure with the clustering of vacancies and Ga-Ga metallic bond formation.
- Despite heavy Mg incorporation in the GaN nanowall network, its morphology remains intact. We have found 3.2 times enhancement in Near Band Edge for samples with low Mg incorporation ($\text{Mg:Ga} < 0.04$), while higher Mg ($\text{Mg:Ga} > 0.06$) appreciably reduces Near Band Edge and increases the blue luminescence. XPS reveals that the nanowall network morphology, more than 10^{20} cm^{-3} Mg atoms can be incorporated in the sample while retaining its Near Band Edge emission.
- We uncovered the atomistic origin of blue luminescence (2.7 eV) peak in PL spectra. We find that defect complex with of Mg substitutional Ga site and Mg at an interstitial site result in blue luminescence.
- With an increase in the Mg concentration, the morphology of the GaN nanorods sample grown on Si (111) substrate is seen to vary. We establish that the reduction of the diffusion barrier and adsorption energy of the Ga adatoms on side wall surface of nanorods, due to the presence of Mg atoms promote the enhanced radial growth rate of Mg-doped GaN nanorods.

8.3 Limitations of the work and Future directions

The limitation of the work carried out in this thesis is discussed in this section. Suggestions for improved research and the future course of this work can take:

- The insight provided here on the atomistic mechanism involved in the formation of the nanowalls has to be exploited further to understand the morphological evolution due to the change in the kinetics of growth. A better understanding of the role of supersaturation and a thermodynamical description on the formation of the nanowalls is necessary.
- The electrical characteristics of the GaN nanowall structure is very poorly understood because of its porous nature and difficulties in making proper electrical measurements. One major challenge is making of an ohmic contact on such a porous structure, though the conductivity of the material is high. A comprehensive study of making contacts on these porous films will enable a better measure of the electrical properties that can yield more accurate values of carrier type, concentrations, etc by Hall measurements.
- The luminescence intensities from GaN nanowall is significantly high in comparison to flat GaN epilayer. So this should be intensely researched to use this morphology in making highly efficient light emission devices.
- Our preliminary DFT studies have employed semilocal approaches, and so the estimation of the formation energy of defects and thermodynamic transitions levels are at best qualitative. To obtain more accurate values, much-advanced DFT techniques such as hybrid functionals and/or quasi-particle GW need to be employed, to make the results more quantitative and reliable.
- The formation energies of the impurity on the surface of the material is seen to be lower in comparison to its bulk counterpart, thus material with more surface to volume ratio enhances solubility limits of dopants in the host. However, we could not quantify this behaviour from currently used experimental techniques. Scanning Kelvin Probe Microscopy or electrochemical capacitance-voltage profiling measurements might be able to further overcome this issue appropriately.

- Similar to the case of nanowall, a direct implementation of the nanorods to device configuration can enhance its usability to several real-world applications. The role of Mg incorporation in GaN nanorod to its structural properties and mosaicity is still not fully clear from this work. A systematic investigation of HR-XRD and TEM analysis at the interface is required for a better understanding of the issue.

Further work on band gap engineering of the nanowall network with varying Indium composition can yield this potential configuration with varying band gaps. Because of the high surface area to volume ratio and porous nature of GaN nanowall, it can be a suitable candidate for gas and bio sensing devices, solar cells and photochemical water splitting etc. The GaN nanowall can also be used as a template for two-step growth of nanowires, nanorods and flat epitaxial layers. Because of its high electrical conductivity and large transparency it also has the potential application as transparent conducting layers. The exploration of this unique morphology with multifunctional properties as a material for device fabrication can be exciting both scientifically and technologically.



Bibliography

- [1] A. G. Bhuiyan, K. Sugita, A. Hashimoto, and A. Yamamoto, *IEEE J. Photovoltaics* **2**, 276 (2012).
- [2] J. Wu, *J. Appl. Phys.* **106**, 5 (2009).
- [3] R. Juza and H. Hahn, *Zeitschrift für anorganische und allgemeine Chemie* **239**, 282 (1938).
- [4] H. G. Grimmeiss and H. Koelmans, *Nature (London)* **14a**, 264 (1959).
- [5] H. P. Maruska and J. J. Tietjen, *Appl. Phys. Lett.* **15**, 327 (1969).
- [6] H. Maruska, D. Stevenson, and J. Pankove, *Appl. Phys. Lett.* **22**, 303 (1973).
- [7] J. Pankove and H. Schade, *Appl. Phys. Lett.* **25**, 53 (1974).
- [8] M. Duffy, C. Wang, G. O'clock, S. McFarlane, and P. Zanzucchi, *J. Electron. Mater.* **2**, 359 (1973).
- [9] R. Dingle, K. Shaklee, R. Leheny, and R. Zetterstrom, *Appl. Phys. Lett.* **19**, 5 (1971).
- [10] J. Pankove, E. Miller, and J. Berkeyheiser, *Journal of Luminescence* **5**, 84 (1972).
- [11] S. Yoshida, S. Misawa, and S. Gonda, *Appl. Phys. Lett.* **42**, 427 (1983).
- [12] H. Amano, N. Sawaki, I. Akasaki, and Y. Toyoda, *Appl. Phys. Lett.* **48**, 353 (1986).
- [13] S. Nakamura, *Jpn. J. Appl. Phys.* **30**, L1705 (1991).
- [14] H. Amano, I. Akasaki, T. Kozawa, K. Hiramatsu, N. Sawaki, K. Ikeda, and Y. Ishii, *Journal of Luminescence* **40**, 121 (1988).
- [15] H. Amano, M. Kito, K. Hiramatsu, and I. Akasaki, *Jpn. J. Appl. Phys.* **28**, L2112 (1989).
- [16] S. Nakamura, T. Mukai, M. Senoh, and N. Iwasa, *Jpn. J. Appl. Phys.* **31**, L139 (1992).
- [17] S. Nakamura, M. Senoh, and T. Mukai, *Jpn. J. Appl. Phys.* **30**, L1708 (1991).
- [18] S. Nakamura, N. Iwasa, M. Senoh, and T. Mukai, *Jpn. J. Appl. Phys.* **31**, 1258 (1992).
- [19] J. Neugebauer and C. G. Van de Walle, *Phys. Rev. Lett.* **75**, 4452 (1995).
- [20] J. Neugebauer and C. G. Van de Walle, *Appl. Phys. Lett.* **68**, 1829 (1996).
- [21] S. Nakamura, *Jpn. J. Appl. Phys.* **31**, 1457 (1992).
- [22] S. Nakamura, M. Senoh, and T. Mukai, *Jpn. J. Appl. Phys.* **32**, L8 (1993).
- [23] S. Nakamura, T. Mukai, and M. Senoh, *Appl. Phys. Lett.* **64**, 1687 (1994).
- [24] J. Pankove, *Phys. Rev. Lett.* **9**, 283 (1962).
- [25] N. Holonyak Jr and S. Bevacqua, *Appl. Phys. Lett.* **1**, 82 (1962).
- [26] A. Setlur, *The Electrochemical Society Interface* **16**, 32 (2009).
- [27] V. Bachmann, *Studies on luminescence and quenching mechanisms in phosphors for light emitting diodes*, Ph.D. thesis, Utrecht University (2007).

- [28] S. Nakamura, MRS Bull. **34**, 101 (2009).
- [29] K. Katayama, H. Matsubara, F. Nakanishi, T. Nakamura, H. Doi, A. Saegusa, T. Mitsui, T. Matsumoto, M. Irikura, and T. Takebe, J. Cryst. Growth **214**, 1064 (2000).
- [30] T.-H. Wang and Y.-K. Kuo, Appl. Phys. Lett. **102**, 171112 (2013).
- [31] R. N. Hall, G. E. Fenner, J. Kingsley, T. Soltys, and R. Carlson, Phys. Rev. Lett. **9**, 366 (1962).
- [32] I. Akasaki, H. Amano, S. Sota, H. Sakai, T. Tanaka, and M. Koike, Jpn. J. Appl. Phys. **34**, L1517 (1995).
- [33] I. Akasaki, S. Sota, H. Sakai, T. Tanaka, M. Koike, and H. Amano, Electron. Lett. **32**, 1105 (1996).
- [34] S. Nakamura, Science **281**, 956 (1998).
- [35] S. Nakamura, M. Senoh, S.-i. Nagahama, N. Iwasa, T. Yamada, T. Matsushita, H. Kiyoku, and Y. Sugimoto, Jpn. J. Appl. Phys. **35**, L74 (1996).
- [36] S. Nakamura, M. Senoh, S.-i. Nagahama, N. Iwasa, T. Yamada, T. Matsushita, Y. Sugimoto, and H. Kiyoku, Appl. Phys. Lett. **70**, 868 (1997).
- [37] B. Baliga, J. Appl. Phys. **53**, 1759 (1982).
- [38] L. Shen, S. Heikman, B. Moran, R. Coffie, N.-Q. Zhang, D. Buttari, I. Smorchkova, S. Keller, S. DenBaars, and U. Mishra, IEEE Electron Device Lett. **22**, 457 (2001).
- [39] Y. Okamoto, Y. Ando, K. Hataya, T. Nakayama, H. Miyamoto, T. Inoue, M. Senda, K. Hirata, M. Kosaki, and N. Shibata, IEEE Trans. Microw. Theory Tech. **52**, 2536 (2004).
- [40] Y.-F. Wu, M. Moore, A. Saxler, T. Wisleder, and P. Parikh, in *2006 64th Device Research Conference* (IEEE, 2006) pp. 151–152.
- [41] K. Shinohara, D. Regan, A. Corrion, D. Brown, S. Burnham, P. Willadsen, I. Alvarado-Rodriguez, M. Cunningham, C. Butler, and A. Schmitz, in *Electron Devices Meeting (IEDM), 2011 IEEE International* (IEEE, 2011) pp. 19–1.
- [42] D. Brown, A. Williams, K. Shinohara, A. Kurdoghlian, I. Milosavljevic, P. Hashimoto, R. Grabar, S. Burnham, C. Butler, and P. Willadsen, in *Electron Devices Meeting (IEDM), 2011 IEEE International* (IEEE, 2011) pp. 19–3.
- [43] D. S. Lee, B. Lu, M. Azize, X. Gao, S. Guo, D. Kopp, P. Fay, and T. Palacios, in *Electron Devices Meeting (IEDM), 2011 IEEE International* (IEEE, 2011) pp. 19–2.
- [44] D. V. McLaughlin and J. M. Pearce, Metall. Mater. Trans. A **44**, 1947 (2013).
- [45] A. Marti and G. L. Araújo, Sol. Energ. Mat. Sol. Cells **43**, 203 (1996).
- [46] O. Jani, H. Yu, E. Trybus, B. Jampana, I. Ferguson, A. Doolittle, and C. Honsberg, in *22nd European Photovoltaic Solar Energy Conference* (2007) pp. 64–67.
- [47] C. Yang, X. Wang, H. Xiao, J. Ran, C. Wang, G. Hu, X. Wang, X. Zhang, J. Li, and J. Li, Phys. Status Solidi A **204**, 4288 (2007).
- [48] X.-m. Cai, S.-w. Zeng, and B.-p. Zhang, Appl. Phys. Lett. **95**, 173504 (2009).
- [49] B. R. Jampana, A. G. Melton, M. Jamil, N. N. Faleev, R. L. Opila, I. T. Ferguson, and C. B. Honsberg, IEEE Electron Device Lett. **31**, 32 (2010).

- [50] C. Boney, I. Hernandez, R. Pillai, D. Starikov, A. Bensaoula, M. Henini, M. Syperek, J. Misiewicz, and R. Kudrawiec, in *Photovoltaic Specialists Conference (PVSC), 2010 35th IEEE* (IEEE, 2010) pp. 003316–003321.
- [51] O. Jani, I. Ferguson, C. Honsberg, and S. Kurtz, *Appl. Phys. Lett.* **91**, 132117 (2007).
- [52] B. W. Liou, *Thin Solid Films* **520**, 1084 (2011).
- [53] A. M. Al-Amri, P.-H. Fu, K.-Y. Lai, H.-P. Wang, and L.-J. L. J.-H. He, *Sci. Rep.* **6**, 28571 (2016).
- [54] B. Kang, G. Louche, R. Duran, Y. Gnanou, S. Pearton, and F. Ren, *Solid-State Electronics* **48**, 851 (2004).
- [55] J. Schalwig, G. Müller, O. Ambacher, and M. Stutzmann, *Phys. Status Solidi A* **185**, 39 (2001).
- [56] S. J. Pearton, B. S. Kang, S. Kim, F. Ren, B. P. Gila, C. R. Abernathy, J. Lin, and S. N. G. Chu, *J. Phys. Condens. Matter* **16**, R961 (2004).
- [57] J. K. Furdyna, *J. Appl. Phys.* **64**, R29 (1988).
- [58] H. Ohno, *Science* **281**, 951 (1998).
- [59] T. Dietl, H. Ohno, F. Matsukura, J. Cibert, and D. Ferrand, *Science* **287**, 1019 (2000).
- [60] G. Das, B. Rao, and P. Jena, *Phys. Rev. B* **69**, 214422 (2004).
- [61] M. L. Reed, N. A. El-Masry, H. H. Stadelmaier, M. K. Rittums, M. J. Reed, C. A. Parker, J. C. Roberts, and S. M. Bedair, *Appl. Phys. Lett.* **79**, 3473 (2001).
- [62] D. S. Han, J. Park, K. W. Rhie, S. Kim, and J. Chang, *Appl. Phys. Lett.* **86**, 032506 (2005).
- [63] S. Sonoda, S. Shimizu, T. Sasaki, Y. Yamamoto, and H. Hori, *J. Cryst. Growth* **237**, 1358 (2002).
- [64] J. Chang, G. Kim, J. Lee, S. Han, H. Kim, W. Lee, M. Ham, K. Huh, and J. Myoung, *J. Appl. Phys.* **93**, 7858 (2003).
- [65] M. Park, K. Huh, J. Myoung, J. Lee, J. Chang, K. Lee, S. Han, and W. Lee, *Solid State Commun.* **124**, 11 (2002).
- [66] K. Kim, K. Lee, D. Kim, H. Kim, Y. Ihm, D. Djayaprawira, M. Takahashi, C. Kim, C. Kim, and S. Yoo, *Appl. Phys. Lett.* **82**, 1775 (2003).
- [67] G. Thaler, M. Overberg, B. Gila, R. Frazier, C. Abernathy, S. Pearton, J. Lee, S. Lee, Y. Park, and Z. Khim, *Appl. Phys. Lett.* **80**, 3964 (2002).
- [68] M. E. Overberg, C. R. Abernathy, S. J. Pearton, N. A. Theodoropoulou, K. T. McCarthy, and A. F. Hebard, *Appl. Phys. Lett.* **79**, 1312 (2001).
- [69] N. Theodoropoulou, A. Hebard, M. Overberg, C. Abernathy, S. Pearton, S. Chu, and R. Wilson, *Appl. Phys. Lett.* **78**, 3475 (2001).
- [70] I. Petrov, E. Mojab, R. Powell, J. Greene, L. Hultman, and J.-E. Sundgren, *Appl. Phys. Lett.* **60**, 2491 (1992).
- [71] H. Morkoç, *Handbook of nitride semiconductors and devices, Materials Properties, Physics and Growth*, Vol. 1 (John Wiley & Sons, 2009).
- [72] T. Lei, T. Moustakas, R. Graham, Y. He, and S. Berkowitz, *J. Appl. Phys.* **71**, 4933 (1992).

- [73] S. Strite, D. Chandrasekhar, D. J. Smith, J. Sariel, H. Chen, N. Teraguchi, and H. Morkoç, *J. Cryst. Growth* **127**, 204 (1993).
- [74] P. Schley, C. Napierala, R. Goldhahn, G. Gobsch, J. Schörmann, D. As, K. Lischka, M. Feneberg, K. Thonke, and F. Fuchs, *Phys. Status Solidi C* **5**, 2342 (2008).
- [75] Q. Xia, H. Xia, and A. L. Ruoff, *J. Appl. Phys.* **73**, 8198 (1993).
- [76] H. Xia, Q. Xia, and A. L. Ruoff, *Phys. Rev. B* **47**, 12925 (1993).
- [77] J. Ibáñez, A. Segura, F. Manjón, L. Artús, T. Yamaguchi, and Y. Nanishi, *Appl. Phys. Lett.* **96**, 201903 (2010).
- [78] B. Daudin, J. Rouvière, and M. Arlery, *Mater. Sci. Eng. B* **43**, 157 (1997).
- [79] T. Sasaki and T. Matsuoka, *J. Appl. Phys.* **64**, 4531 (1988).
- [80] F. Tuomisto, T. Suski, H. Teisseyre, M. Krysko, M. Leszczynski, B. Lucznik, I. Grzegory, S. Porowski, D. Wasik, and A. Witowski, *Phys. Status Solidi B* **240**, 289 (2003).
- [81] H. Morkoç, *Mater. Sci. Eng. R* **33**, 135 (2001).
- [82] L. Liu and J. H. Edgar, *Mater. Sci. Eng. R* **37**, 61 (2002).
- [83] X. Wang and A. Yoshikawa, *Prog. Cryst. Growth Charact. Mater.* **48**, 42 (2004).
- [84] P. Kung and M. Razeghi, *Opto-Electron. Rev.* **8**, 201 (2000).
- [85] S. King, R. Nemanich, and R. Davis, in *APS Meeting Abstracts*, Vol. 1 (2014) p. 45013.
- [86] M. Craven, S. Lim, F. Wu, J. Speck, and S. DenBaars, *Appl. Phys. Lett.* **81**, 469 (2002).
- [87] T. Paskova, V. Darakchieva, E. Valcheva, P. Paskov, B. Monemar, and M. Heuken, *J. Cryst. Growth* **257**, 1 (2003).
- [88] H. Craft, J. Ihlefeld, M. Losego, R. Collazo, Z. Sitar, and J. Maria, *Appl. Phys. Lett.* **88**, 212906 (2006).
- [89] Y. Nakada, I. Aksenov, and H. Okumura, *Appl. Phys. Lett.* **73**, 827 (1998).
- [90] A. Barski, U. Rössner, J. Rouviere, and M. Arlery, *MRS Internet J. Nitride Semicond. Res.* **1**, e21 (1996).
- [91] J. Wu, H. Yaguchi, K. Onabe, R. Ito, and Y. Shiraki, *Appl. Phys. Lett.* **71**, 2067 (1997).
- [92] Y. Iwahashi, H. Yaguchi, A. Nishimoto, M. Orihara, Y. Hijikata, and S. Yoshida, *Phys. Status Solidi C* **3**, 1515 (2006).
- [93] H. Okumura, K. Ohta, G. Feuillet, K. Balakrishnan, S. Chichibu, H. Hamaguchi, P. Hacke, and S. Yoshida, *J. Cryst. Growth* **178**, 113 (1997).
- [94] K. Pakuła, J. Baranowski, and J. Borysiuk, *Cryst. Res. Technol.* **42**, 1176 (2007).
- [95] S. W. King, E. Carlson, R. Therrien, J. Christman, R. J. Nemanich, and R. F. Davis, *J. Appl. Phys.* **86**, 5584 (1999).
- [96] H.-Y. Chen, H.-W. Lin, C.-H. Shen, and S. Gwo, *Appl. Phys. Lett.* **89**, 243105 (2006).
- [97] G. Calabrese, P. Corfdir, G. Gao, C. Pfüller, A. Trampert, O. Brandt, L. Geelhaar, and S. Fernández-Garrido, *Appl. Phys. Lett.* **108**, 202101 (2016).
- [98] J. Goldberger, R. He, Y. Zhang, S. Lee, H. Yan, H.-J. Choi, and P. Yang, *Nature* **422**, 599 (2003).

- [99] A. Milekhin, R. Meijers, T. Richter, R. Calarco, S. Montanari, H. Lüth, B. P. Sierra, and D. Zahn, *J. Phys. Condens. Matter* **18**, 5825 (2006).
- [100] S. Dhamodaran, D. S. Chander, and J. Ramkumar, *Appl. Surf. Sci.* **257**, 9612 (2011).
- [101] A. Lundskog, J. Palisaitis, C.-W. Hsu, M. Eriksson, K. Karlsson, L. Hultman, P. Å. Persson, U. Forsberg, P.-O. Holtz, and E. Janzén, *Nanotechnology* **23**, 305708 (2012).
- [102] X. Geng, B. K. Duan, D. A. Grismer, L. Zhao, and P. W. Bohn, *Semicond. Sci. Technol.* **28**, 065001 (2013).
- [103] J. Li, J. Liu, L.-S. Wang, and R. P. Chang, *Inorg. Chem.* **47**, 10325 (2008).
- [104] M. Lei, H. Yang, P. Li, and W. Tang, *Appl. Surf. Sci.* **254**, 1947 (2008).
- [105] S. Lester, F. Ponce, M. Craford, and D. Steigerwald, *Appl. Phys. Lett.* **66**, 1249 (1995).
- [106] S. Y. Karpov and Y. N. Makarov, *Appl. Phys. Lett.* **81**, 4721 (2002).
- [107] D.-S. Wu, H.-W. Wu, S.-T. Chen, T.-Y. Tsai, X. Zheng, and R.-H. Horng, *J. Cryst. Growth* **311**, 3063 (2009).
- [108] A. Roskowski, E. Preble, S. Einfeldt, P. Miraglia, J. Schuck, R. Grober, and R. Davis, *Opto-Electron. Rev.* , 261 (2002).
- [109] F. Ishida, K. Yoshimura, K. Hoshino, and K. Tadatomo, *Phys. Status Solidi C* **5**, 2083 (2008).
- [110] J.-T. Chen, W.-C. Lai, Y.-C. Chang, J.-K. Sheu, and W.-C. Sen, *Appl. Phys. Lett.* **101**, 131103 (2012).
- [111] C. Chèze, L. Geelhaar, O. Brandt, W. M. Weber, H. Riechert, S. Münch, R. Rothmund, S. Reitzenstein, A. Forchel, T. Kehagias, *et al.*, *Nano Research* **3**, 528 (2010).
- [112] C. Wiesmann, K. Bergenek, N. Linder, and U. T. Schwarz, *Laser Photonics Rev.* **3**, 262 (2009).
- [113] C.-F. Lin, Z.-J. Yang, B.-H. Chin, J.-H. Zheng, J.-J. Dai, B.-C. Shieh, and C.-C. Chang, *J. Electrochem. Soc.* **153**, G1020 (2006).
- [114] S. E. Brinkley, C. L. Keraly, J. Sonoda, C. Weisbuch, J. S. Speck, S. Nakamura, and S. P. DenBaars, *Appl. Phys. Express* **5**, 032104 (2012).
- [115] H. W. Choi, M. D. Dawson, P. R. Edwards, and R. W. Martin, *Appl. Phys. Lett.* **83**, 4483 (2003).
- [116] A. David, H. Benisty, and C. Weisbuch, *J. Disp. Technol.* **3**, 133 (2007).
- [117] J. J. Wierer, A. David, and M. M. Megens, *Nat. Photon.* **3**, 163 (2009).
- [118] J. K. Kim, S. Chhajed, M. F. Schubert, E. F. Schubert, A. J. Fischer, M. H. Crawford, J. Cho, H. Kim, and C. Sone, *Adv. Mater.* **20**, 801 (2008).
- [119] O. V. Bilousov, J. J. Carvajal, J. Mena, O. Martínez, J. Jiménez, H. Geaney, F. Díaz, M. Aguiló, and C. O'Dwyer, *CrystEngComm* **16**, 10255 (2014).
- [120] S. Chhajed, W. Lee, J. Cho, E. F. Schubert, and J. K. Kim, *Appl. Phys. Lett.* **98**, 071102 (2011).
- [121] C. B. Soh, C. B. Tay, R. J. N. Tan, a. P. Vajpeyi, I. P. Seetoh, K. K. Ansah-Antwi, and S. J. Chua, *J. Phys. D: Appl. Phys.* **46**, 365102 (2013).
- [122] H. K. Lee, Y. H. Ko, G. S. R. Raju, and J. S. Yu, *Opt. Express* **20**, 25058 (2012).

- [123] X.-H. Li, P. Zhu, G. Liu, J. Zhang, R. Song, Y.-K. Ee, P. Kumnorkaew, J. F. Gilchrist, and N. Tansu, *J. Display Technol.* **9**, 324 (2013).
- [124] J. M. Hwang, W. H. Hung, and H. L. Hwang, *IEEE Photonics Technol. Lett.* **20**, 608 (2008).
- [125] C.-F. Lin, J.-H. Zheng, Z.-J. Yang, J.-J. Dai, D.-Y. Lin, C.-Y. Chang, Z.-X. Lai, and C. Hong, *Appl. Phys. Lett.* **88**, 083121 (2006).
- [126] Z. Chen, Y. Jiang, D. R. Dunphy, D. P. Adams, C. Hodges, N. Liu, N. Zhang, G. Xomeritakis, X. Jin, N. R. Aluru, S. J. Gaik, H. W. Hillhouse, and C. J. Brinker, *Nat. Mater.* **9**, 667 (2010).
- [127] J. G. Rivas, D. Dau, A. Imhof, R. Sprik, B. Bret, P. Johnson, T. Hijmans, and A. Lagendijk, *Opt. Commun.* **220**, 17 (2003).
- [128] J. H. Lee, B. Lee, J. H. Kang, J. K. Lee, and S. W. Ryu, *Thin Solid Films* **525**, 84 (2012).
- [129] L. Golovan, P. Kashkarov, and V. Y. Timoshenko, *Crystallography Reports* **52**, 672 (2007).
- [130] Y. D. Wang, S. J. Chua, M. S. Sander, P. Chen, S. Tripathy, and C. G. Fonstad, *Appl. Phys. Lett.* **85**, 816 (2004).
- [131] J. Lian, W. Zhou, Q. M. Wei, L. M. Wang, L. a. Boatner, and R. C. Ewing, *Appl. Phys. Lett.* **88**, 093112 (2006).
- [132] S. Kucheyev, J. Williams, C. Jagadish, J. Zou, V. Craig, and G. Li, *Appl. Phys. Lett.* **77**, 1455 (2000).
- [133] S. Kucheyev, J. Williams, C. Jagadish, G. Li, and S. Pearton, *Appl. Phys. Lett.* **76**, 3899 (2000).
- [134] A. Zhong and K. Hane, *Nanoscale Res. Lett.* **7**, 686 (2012).
- [135] D. Poppitz, A. Lotnyk, J. W. Gerlach, and B. Rauschenbach, *Acta Mater.* **65**, 98 (2014).
- [136] O. V. Bilousov, H. Geaney, J. J. Carvajal, V. Z. Zubialevich, P. J. Parbrook, a. Giguere, D. Drouin, F. Diaz, M. Aguilo, and C. O'Dwyer, *Appl. Phys. Lett.* **103**, 112103 (2013).
- [137] M. Kesaria, S. Shetty, and S. M. Shivaprasad, *Cryst. Growth Des.* **11**, 4900 (2011).
- [138] V. Thakur, M. Kesaria, and S. Shivaprasad, *Solid State Commun.* **171**, 8 (2013).
- [139] C. Wu, D. Wu, P. Lin, T. Chen, and R. Horng, *Nanoscale Res. Lett.* **4**, 377 (2009).
- [140] R. B. Jain and H. P. Maruska, *Phys. Status Solidi A* **204**, 1970 (2007).
- [141] P. Born and D. Robertson, *J. Mater. Sci.* **15**, 3003 (1980).
- [142] B. Monemar, O. Lagerstedt, and H. Gislason, *J. Appl. Phys.* **51**, 625 (1980).
- [143] T. Tingberg, T. Ive, and A. Larsson, *J. Electron. Mater.* **46**, 4898 (2017).
- [144] J. Hsu, D. Lang, S. Richter, R. Kleiman, A. Sergent, and R. Molnar, *Appl. Phys. Lett.* **77**, 2873 (2000).
- [145] S. Goss, X. Sun, A. Young, L. Brillson, D. C. Look, and R. J. Molnar, *Appl. Phys. Lett.* **78**, 3630 (2001).
- [146] K. Kim, M. Cheong, H. Cho, E. Suh, and H. Lee, *Appl. Phys. Lett.* **80**, 799 (2002).
- [147] C. Mavroidis, J. Harris, M. Kappers, N. Sharma, C. Humphreys, and E. Thrush, *Appl. Phys. Lett.* **79**, 1121 (2001).

- [148] C. Mavroidis, J. Harris, M. Kappers, C. Humphreys, and Z. Bougrioua, *J. Appl. Phys.* **93**, 9095 (2003).
- [149] R. D. Elena, A. Leonid, and A. Lytvynov, “Sapphire: Material, manufacturing, applications,” (2009).
- [150] G. Koblmüller, F. Reurings, F. Tuomisto, and J. Speck, *Appl. Phys. Lett.* **97**, 191915 (2010).
- [151] C. G. Van De Walle and J. Neugebauer, *J. Appl. Phys.* **95**, 3851 (2004).
- [152] Q. Yan, A. Janotti, M. Scheffler, and C. G. Van de Walle, *Appl. Phys. Lett.* **100**, 142110 (2012).
- [153] J. Buckeridge, C. R. A. Catlow, D. Scanlon, T. Keal, P. Sherwood, M. Miskufova, A. Walsh, S. Woodley, and A. Sokol, *Phys. Rev. Lett.* **114**, 016405 (2015).
- [154] G. Miceli and A. Pasquarello, *Phys. Rev. B* **93**, 165207 (2016).
- [155] G. Makov and M. Payne, *Phys. Rev. B* **51**, 4014 (1995).
- [156] C. Freysoldt, J. Neugebauer, and C. G. Van de Walle, *Phys. Rev. Lett.* **102**, 016402 (2009).
- [157] H. P. Bhasker, S. Dhar, A. Sain, M. Kesaria, and S. M. Shivaprasad, *Appl. Phys. Lett.* **101**, 132109 (2012).
- [158] H. P. Bhasker, V. Thakur, S. M. Shivaprasad, and S. Dhar, *Solid State Commun.* **220**, 72 (2015).
- [159] H. Amano, M. Kito, K. Hiramatsu, and I. Akasaki, in *Institute of Physics: Conference Series* (1990) pp. 725–730.
- [160] J. A. Van Vechten, J. D. Zook, R. D. Horning, and B. Goldenberg, *Jpn. J. Appl. Phys.* **31**, 3662 (1992).
- [161] M. Zhang, P. Bhattacharya, W. Guo, and A. Banerjee, *Appl. Phys. Lett.* **96**, 132103 (2010).
- [162] C. G. Van de Walle, S. Limpijumnong, and J. Neugebauer, *Phys. Rev. B* **63**, 245205 (2001).
- [163] H. Wang, L. Tan, and E. Chor, *J. Cryst. Growth* **268**, 489 (2004).
- [164] A. Castiglia, J.-F. Carlin, and N. Grandjean, *Appl. Phys. Lett.* **98**, 213505 (2011).
- [165] E. Cimpoiasu, E. Stern, R. Klie, R. a. Munden, G. Cheng, and M. a. Reed, *Nanotechnology* **17**, 5735 (2006).
- [166] A. J. Ptak, L. J. Holbert, L. Ting, C. H. Swartz, M. Moldovan, N. C. Giles, T. H. Myers, P. Van Lierde, C. Tian, R. A. Hockett, S. Mitha, A. E. Wickenden, D. D. Koleske, and R. L. Henry, *Appl. Phys. Lett.* **79**, 2740 (2001).
- [167] S. M. Myers, A. F. Wright, G. A. Petersen, W. R. Wampler, C. H. Seager, M. H. Crawford, and J. Han, *J. Appl. Phys.* **89**, 3195 (2001).
- [168] G. Namkoong, E. Trybus, K. K. Lee, M. Moseley, W. A. Doolittle, and D. C. Look, *Appl. Phys. Lett.* **93**, 172112 (2008).
- [169] M. Malinverni, J.-M. Lamy, D. Martin, E. Feltn, J. Dorsaz, A. Castiglia, M. Rossetti, M. Duell, C. Vélez, and N. Grandjean, *Appl. Phys. Lett.* **105**, 241103 (2014).
- [170] S. Brochen, J. Brault, S. Chenot, A. Dussaigne, M. Leroux, and B. Damilano, *Appl. Phys. Lett.* **103**, 032102 (2013).
- [171] U. Kaufmann, P. Schlotter, H. Obloh, K. Köhler, and M. Maier, *Phys. Rev. B* **62**, 10867 (2000).

- [172] P. Kozodoy, S. Keller, S. DenBaars, and U. Mishra, *J. Cryst. Growth* **195**, 265 (1998).
- [173] U. Kaufmann, M. Kunzer, M. Maier, H. Obloh, A. Ramakrishnan, B. Santic, and P. Schlotter, *Appl. Phys. Lett.* **72**, 1326 (1998).
- [174] S. Hautakangas, J. Oila, M. Alatalo, K. Saarinen, L. Liskay, D. Seghier, and H. Gislason, *Phys. Rev. Lett.* **90**, 137402 (2003).
- [175] S. Hautakangas, K. Saarinen, L. Liskay, J. Freitas Jr, and R. Henry, *Phys. Rev. B* **72**, 165303 (2005).
- [176] G. Miceli and A. Pasquarello, *Phys. Rev. B* **93**, 165207 (2016).
- [177] U. Wahl, L. Amorim, V. Augustyns, A. Costa, E. David-Bosne, T. Lima, G. Lippertz, J. Correia, M. da Silva, M. Kappers, *et al.*, *Phys. Rev. Lett.* **118**, 095501 (2017).
- [178] M. A. Reshchikov, D. O. Demchenko, J. D. McNamara, S. Fernández-Garrido, and R. Calarco, *Phys. Rev. B* **90**, 035207 (2014).
- [179] U. Kaufmann, M. Kunzer, H. Obloh, M. Maier, C. Manz, A. Ramakrishnan, and B. Santic, *Phys. Rev. B* **59**, 5561 (1999).
- [180] Y. Koide, D. E. Walker, B. D. White, L. J. Brillson, M. Murakami, S. Kamiyama, H. Amano, and I. Akasaki, *J. Appl. Phys.* **92**, 3657 (2002).
- [181] M. Reshchikov, G.-C. Yi, and B. Wessels, *Phys. Rev. B* **59**, 13176 (1999).
- [182] J. L. Lyons, A. Janotti, and C. G. V. D. Walle, *Phys. Rev. Lett.* **108**, 156403 (2012).
- [183] Y. Nakano and T. Jimbo, *Phys. Status Solidi C* **442**, 438 (2002).
- [184] T. Hashizume, *J. Appl. Phys.* **94**, 431 (2003).
- [185] T. Cheng, S. Novikov, C. Foxon, and J. Orton, *Solid State Commun.* **109**, 439 (1999).
- [186] L. T. Romano, M. Kneissl, J. E. Northrup, C. G. Van De Walle, and D. W. Treat, *Appl. Phys. Lett.* **79**, 2734 (2001).
- [187] M. E. Groenert, C. W. Leitz, A. J. Pitera, V. Yang, H. Lee, R. J. Ram, and E. A. Fitzgerald, *J. Appl. Phys.* **93**, 362 (2003).
- [188] X. Chen and T. Uesugi, *Appl. Phys. Lett.* **88**, 031916 (2006).
- [189] B. Yang, A. Trampert, O. Brandt, B. Jenichen, and K. Ploog, *J. Appl. Phys.* **83**, 3800 (1998).
- [190] S. Eftychis, J. Kruse, T. Koukoula, T. Kehagias, P. Komninou, A. Adikimenakis, K. Tsagaraki, M. Androulidaki, P. Tzanetakis, E. Iliopoulos, *et al.*, *J. Cryst. Growth* **442**, 8 (2016).
- [191] T. Yodo, H. Ando, H. Tsuchiya, D. Nosei, M. Shimeno, and Y. Harada, *J. Cryst. Growth* **227**, 431 (2001).
- [192] M. Tamura, M. López-López, and T. Yodo, *Superficies y vacío* **13**, 80 (2001).
- [193] M. N. A. Rahman, Y. Yusuf, M. Mansor, and A. Shuhaimi, *Appl. Surf. Sci.* **362**, 572 (2016).
- [194] S.-G. Ihn, J.-I. Song, Y.-H. Kim, and J. Y. Lee, *Appl. Phys. Lett.* **89**, 053106 (2006).
- [195] L. Li, D. Guimard, M. Rajesh, and Y. Arakawa, *Appl. Phys. Lett.* **92**, 263105 (2008).
- [196] L. Cerutti, J. Ristić, S. Fernández-Garrido, E. Calleja, A. Trampert, K. Ploog, S. Lazic, and J. Calleja, *Appl. Phys. Lett.* **88**, 213114 (2006).

- [197] T. Mårtensson, C. P. T. Svensson, B. A. Wacaser, M. W. Larsson, W. Seifert, K. Deppert, A. Gustafsson, L. R. Wallenberg, and L. Samuelson, *Nano Lett.* **4**, 1987 (2004).
- [198] F. Glas, *Phys. Rev. B* **74**, 121302 (2006).
- [199] M. A. Verheijen, G. Immink, T. de Smet, M. T. Borgström, and E. P. Bakkers, *J. Am. Chem. Soc.* **128**, 1353 (2006).
- [200] W. Han, S. Fan, Q. Li, and Y. Hu, *Science* **277**, 1287 (1997).
- [201] G. Cheng, L. Zhang, Y. Zhu, G. Fei, L. Li, C. Mo, and Y. Mao, *Appl. Phys. Lett.* **75**, 2455 (1999).
- [202] L. Zhao, G. Meng, X. Peng, X. Zhang, and L. Zhang, *J. Cryst. Growth* **235**, 124 (2002).
- [203] H.-M. Kim, Y.-H. Cho, H. Lee, S. I. Kim, S. R. Ryu, D. Y. Kim, T. W. Kang, and K. S. Chung, *Nano Lett.* **4**, 1059 (2004).
- [204] H.-W. Lin, Y.-J. Lu, H.-Y. Chen, H.-M. Lee, , and S. Gwo, *Appl. Phys. Lett.* **97**, 073101 (2010).
- [205] A. Bengochea-Encabo, S. Albert, D. Lopez-Romero, P. Lefebvre, F. Barbagini, A. Torres-Pardo, J. M. González-Calbet, M. A. Sanchez-Garcia, and E. Calleja, *Nanotechnology* **25**, 435203 (2014).
- [206] C.-Y. Wang, L.-Y. Chen, C.-P. Chen, Y.-W. Cheng, M.-Y. Ke, M.-Y. Hsieh, H.-M. Wu, L.-H. Peng, and J. Huang, *Opt. Express* **16**, 10549 (2008).
- [207] H. P. T. Nguyen, S. Zhang, K. Cui, X. Han, S. Fatholouloumi, M. Couillard, G. Botton, and Z. Mi, *Nano Lett.* **11**, 1919 (2011).
- [208] T. Kuykendall, P. Ulrich, S. Aloni, and P. Yang, *Nat. Mater.* **6**, 951 (2007).
- [209] R. Armitage and K. Tsubaki, *Nanotechnology* **21**, 195202 (2010).
- [210] Y. J. Hong, C.-H. Lee, A. Yoon, M. Kim, H.-K. Seong, H. J. Chung, C. Sone, Y. J. Park, and G.-C. Yi, *Adv. Mater.* **23**, 3284 (2011).
- [211] W. Guo, M. Zhang, P. Bhattacharya, and J. Heo, *Nano Lett.* **11**, 1434 (2011).
- [212] C. Chiu, T.-C. Lu, H. Huang, C. Lai, C. Kao, J. Chu, C. Yu, H.-C. Kuo, S. Wang, C. Lin, *et al.*, *Nanotechnology* **18**, 445201 (2007).
- [213] P. Deb, H. Kim, V. Rawat, M. Oliver, S. Kim, M. Marshall, E. Stach, and T. Sands, *Nano Lett.* **5**, 1847 (2005).
- [214] S. D. Hersee, X. Sun, and X. Wang, *Nano Lett.* **6**, 1808 (2006).
- [215] F. Furtmayr, M. Vilemeyer, M. Stutzmann, J. Arbiol, S. Estradé, F. Peirò, J. R. Morante, and M. Eickhoff, *J. Appl. Phys.* **104**, 034309 (2008).
- [216] S. Li and A. Waag, *J. Appl. Phys.* **111**, 5 (2012).
- [217] J. Arbiol, S. Estradé, J. D. Prades, A. Cirera, F. Furtmayr, C. Stark, A. Laufer, M. Stutzmann, M. Eickhoff, M. H. Gass, *et al.*, *Nanotechnology* **20**, 145704 (2009).
- [218] D. Zhang, C. Xue, H. Zhuang, H. Sun, Y. Cao, Y. Huang, Z. Wang, and Y. Wang, *ChemPhysChem* **10**, 571 (2009).
- [219] Q. Wang, X. Liu, M. Kibria, S. Zhao, H. Nguyen, K. Li, Z. Mi, T. Gonzalez, and M. Andrews, *Nanoscale* **6**, 9970 (2014).

- [220] S.-Y. Bae, K. Lekhal, H.-J. Lee, J.-W. Min, D.-S. Lee, Y. Honda, and H. Amano, *Phys. Status Solidi B*, 1600722 (2017), 1600722.
- [221] J. D. Plummer, *Silicon VLSI technology: fundamentals, practice and modeling* (Pearson Education India, 2009).
- [222] P. Chabert and N. Braithwaite, *Physics of radio-frequency plasmas* (Cambridge University Press, 2011).
- [223] S. Averkin, A. Ershov, A. Orlikovsky, K. Rudenko, and Y. N. Sukhanov, *Russian Microelectronics* **32**, 292 (2003).
- [224] A. Fridman and L. Kennedy, *Plasma Physics and Engineering* (Francis Books, Inc, 2004).
- [225] M. A. Lieberman and A. J. Lichtenberg, *Principles of plasma discharges and materials processing* (John Wiley & Sons, 2005).
- [226] M. S. Silberberg, R. Duran, C. G. Haas, and A. D. Norman, *Chemistry: The molecular nature of matter and change*, Vol. 4 (McGraw-Hill New York, 2006).
- [227] A. V. Engel, *Ionized Gases Oxford* (Clarendon Press, 1955).
- [228] A. Ichimiya and P. I. Cohen, *Reflection high-energy electron diffraction* (Cambridge University Press, 2004).
- [229] C. Hammond, *Chemical Rubber Co., Cleveland, OH* **47** (2000).
- [230] A. Guinier, *X-ray diffraction in crystals, imperfect crystals, and amorphous bodies* (Courier Corporation, 1994).
- [231] H. Haug and S. W. Koch, *Quantum theory of the optical and electronic properties of semiconductors* (World Scientific Publishing Co Inc, 2009).
- [232] M. Kira, F. Jahnke, S. W. Koch, J. D. Berger, D. V. Wick, T. R. Nelson, G. Khitrova, and H. M. Gibbs, *Phys. Rev. Lett.* **79**, 5170 (1997).
- [233] D. A. Long and D. Long, *Raman spectroscopy* (McGraw-Hill New York, 1977).
- [234] H. Harima, *J. Phys. Condens. Matter* **14**, R967 (2002).
- [235] M. Suzuki and T. Uenoyama, *J. Appl. Phys.* **80**, 6868 (1996).
- [236] V. Y. Davydov, N. Averkiev, I. Goncharuk, D. Nelson, I. Nikitina, A. Polkovnikov, A. Smirnov, M. Jacobson, and O. Semchinova, *J. Appl. Phys.* **82**, 5097 (1997).
- [237] C. Kisielowski, J. Krüger, S. Ruvimov, T. Suski, J. Ager III, E. Jones, Z. Liliental-Weber, M. Rubin, E. Weber, M. Bremser, *et al.*, *Phys. Rev. B* **54**, 17745 (1996).
- [238] J. F. Watts and J. Wolstenholme, *An Introduction to Surface Analysis by XPS and AES*, by John F. Watts, John Wolstenholme, pp. 224. ISBN 0-470-84713-1. Wiley-VCH, May 2003. , 224 (2003).
- [239] S. Doniach and M. Sunjic, *J. Phys. C: Solid State Phys.* **3**, 285 (1970).
- [240] L. A. Bendersky and F. W. Gayle, *J. Res. Natl. Inst. Stand. Technol.* **106**, 997 (2001).
- [241] R. F. Egerton, *Electron energy-loss spectroscopy in the electron microscope* (Springer Science & Business Media, 2011).
- [242] J. Stöhr, *NEXAFS spectroscopy*, Vol. 25 (Springer Science & Business Media, 2013).

- [243] R. G. Wilson, F. A. Stevie, and C. W. Magee, *Secondary ion mass spectrometry: a practical handbook for depth profiling and bulk impurity analysis* (Wiley-Interscience, 1989).
- [244] K. S. Kunz and R. J. Luebbers, *The finite difference time domain method for electromagnetics* (CRC press, 1993).
- [245] P. Hohenberg and W. Kohn, Phys. Rev. **136**, B864 (1964).
- [246] R. M. Martin, *Electronic structure: basic theory and practical methods* (Cambridge university press, 2004).
- [247] K. Burke and L. O. Wagner, Int. J. Quantum Chem. **113**, 96 (2013).
- [248] J. P. Perdew and A. Zunger, Phys. Rev. B **23**, 5048 (1981).
- [249] P. A. Dirac, in *Mathematical Proceedings of the Cambridge Philosophical Society*, Vol. 26 (Cambridge Univ Press, 1930) pp. 376–385.
- [250] J. P. Perdew, J. A. Chevary, S. H. Vosko, K. A. Jackson, M. R. Pederson, D. J. Singh, and C. Fiolhais, Phys. Rev. B **46**, 6671 (1992).
- [251] A. D. Becke, Phys. Rev. A **38**, 3098 (1988).
- [252] J. Heyd, G. E. Scuseria, and M. Ernzerhof, Journal of Chemical Physics **118**, 8207 (2003).
- [253] A. L. Ankudinov, B. Ravel, J. J. Rehr, and S. D. Conradson, Phys. Rev. B **58**, 7565 (1998).
- [254] A. L. Ankudinov and J. Rehr, Phys. Rev. B **56**, R1712 (1997).
- [255] J. J. Rehr, J. J. Kas, F. D. Vila, M. P. Prange, and K. Jorissen, Phys. Chem. Chem. Phys. **12**, 5503 (2010).
- [256] J. J. Rehr and R. C. Albers, Rev. Mod. Phys. **72**, 621 (2000).
- [257] J. J. Rehr, J. J. Kas, F. D. Vila, M. P. Prange, and K. Jorissen, Phys. Chem. Chem. Phys. **12**, 5503 (2010).
- [258] M. Kesaria and S. Shivaprasad, Appl. Phys. Lett. **99**, 143105 (2011).
- [259] V. Thakur, M. Kesaria, and S. Shivaprasad, Solid State Commun. **171**, 8 (2013).
- [260] D. G. Zhao, D. S. Jiang, H. Yang, J. J. Zhu, Z. S. Liu, S. M. Zhang, J. W. Liang, X. Li, X. Y. Li, and H. M. Gong, Appl. Phys. Lett. **88**, 241917 (2006).
- [261] V. Thakur, S. K. Nayak, K. K. Nagaraja, and S. M. Shivaprasad, Electron. Mater. Lett. **11**, 398 (2015).
- [262] X. H. Zhang, Y. C. Liu, X. H. Wang, S. J. Chen, G. R. Wang, J. Y. Zhang, Y. M. Lu, D. Z. Shen, and X. W. Fan, J. Phys. Condens. Matter **17**, 3035 (2005).
- [263] G. Mie, Ann. Phys. **25**, 377 (1908).
- [264] A. Rastelli, M. Kummer, and H. Von Känel, Phys. Rev. Lett. **87**, 256101 (2001).
- [265] J. V. Barth, G. Costantini, and K. Kern, Nature **437**, 671 (2005).
- [266] J. Tersoff and R. Tromp, Phys. Rev. Lett. **70**, 2782 (1993).
- [267] H. Brune, M. Giovannini, K. Bromann, and K. Kern, Nature **394**, 451 (1998).
- [268] V. Consonni, M. Knélangen, L. Geelhaar, A. Trampert, and H. Riechert, Phys. Rev. B **81**, 085310 (2010).

- [269] V. A. Shchukin and D. Bimberg, *Rev. Mod. Phys.* **71**, 1125 (1999).
- [270] X. Li, C. Wang, and G. Yang, *Progress in Materials Science* **64**, 121 (2014).
- [271] A. Pimpinelli and J. Villain, *Physics of crystal growth*, Vol. 53 (Cambridge university press Cambridge, 1998).
- [272] V. Thakur, S. K. Nayak, K. K. Nagaraja, and S. M. Shivaprasad, *Electron. Mater. Lett.* **11**, 398 (2015).
- [273] S. K. Nayak, D. Shamoon, J. Ghatak, and S. M. Shivaprasad, *Phys. Status Solidi A* **214**, 1600300 (2017).
- [274] V. Thakur and S. M. Shivaprasad, *Appl. Surf. Sci.* **327**, 389 (2015).
- [275] A. Zhong and K. Hane, *Nanoscale Res. Lett.* **7**, 686 (2012).
- [276] A. Zhong and K. Hane, *Jpn. J. Appl. Phys.* **52**, 08JE13 (2013).
- [277] S. Kushvaha, C. Ramesh, P. Tyagi, A. Shukla, B. Yadav, N. Dilawar, K. Maurya, and M. S. Kumar, *J. Alloys Compd.* **703**, 466 (2017).
- [278] K. G. Libbrecht, arXiv preprint arXiv:1111.2786 (2011).
- [279] K. G. Libbrecht, arXiv preprint arXiv:1209.4932 (2012).
- [280] K. G. Libbrecht, *Annu. Rev. Mater. Res.* (2017).
- [281] J. M. Soler, E. Artacho, J. D. Gale, A. García, J. Junquera, P. Ordejón, and D. Sánchez-Portal, *J. Phys. Condens. Matter* **14**, 2745 (2002).
- [282] J. P. Perdew, K. Burke, and M. Ernzerhof, *Phys. Rev. Lett.* **77**, 3865 (1996).
- [283] J. D. Pack and H. J. Monkhorst, *Phys. Rev. B* **16**, 1748 (1977).
- [284] W.-J. Lee and Y.-S. Kim, *Phys. Rev. B* **84**, 115318 (2011).
- [285] G. Lukin, C. Röder, E. Niederschlag, Y. Shashev, U. Mühle, O. Pätzold, J. Kortus, D. Rafaja, and M. Stelter, *Cryst. Res. Technol.* **47**, 121 (2012).
- [286] F. Degave, P. Ruterana, G. Nouet, J. Je, and C. Kim, *Mater. Sci. Eng. B* **93**, 177 (2002).
- [287] M. Richards-Babb, S. Buczkowski, Z. Yu, and T. Myers, *MRS Online Proceedings Library Archive* **395** (1995).
- [288] D. Vanderbilt and L. Wickham, *MRS Online Proceedings Library Archive* **202** (1990).
- [289] M. A. Herman, W. Richter, and H. Sitter, *Epitaxy: physical principles and technical implementation*, Vol. 62 (Springer Science & Business Media, 2013).
- [290] M. Krishnamurthy, J. Drucker, and J. Venables, *J. Appl. Phys.* **69**, 6461 (1991).
- [291] J. Drucker, *Phys. Rev. B* **48**, 18203 (1993).
- [292] Z. Fang, J. Kang, W. Huang, H. Sun, M. Lu, J. Kong, and W. Shen, *J. Phys. Chem. C* **112**, 4925 (2008).
- [293] S. K. Nayak, D. Shamoon, J. Ghatak, and S. M. Shivaprasad, *Phys. Status Solidi A* **214**, 1600300 (2017).
- [294] C. E. Dreyer, A. Janotti, and C. G. Van de Walle, *Phys. Rev. B* **89**, 081305 (2014).
- [295] T. Nishinaga, *Handbook of Crystal Growth: Fundamentals* (Elsevier, 2014).

- [296] C. Stampfl and C. Van de Walle, *Phys. Rev. B* **59**, 5521 (1999).
- [297] F. Gao, E. J. Bylaska, and W. J. Weber, *Phys. Rev. B* **70**, 245208 (2004).
- [298] I. Gorczyca, A. Svane, and N. Christensen, *Phys. Rev. B* **60**, 8147 (1999).
- [299] J. Neugebauer and C. G. Van de Walle, *Phys. Rev. B* **50**, 8067 (1994).
- [300] J. S. Lee, J. D. Lim, Z. G. Khim, Y. D. Park, S. J. Pearton, and S. N. G. Chu, *J. Appl. Phys.* **93**, 4512 (2003).
- [301] L. Kronik, M. Jain, and J. R. Chelikowsky, *Physical Review B* **66**, 041203 (2002).
- [302] P. Dev, Y. Xue, and P. Zhang, *Phys. Rev. Lett.* **100**, 1 (2008).
- [303] A. Kuang, H. Yuan, and H. Chen, *Appl. Surf. Sci.* **256**, 6040 (2010).
- [304] P. Larson and S. Satpathy, *Phys. Rev. B* **76**, 245205 (2007).
- [305] Y. Li, W. Fan, H. Sun, X. Cheng, P. Li, X. Zhao, and M. Jiang, *J. Solid State Chem.* **183**, 2662 (2010).
- [306] T. Mattila and R. Nieminen, *Phys. Rev. B* **54**, 16676 (1996).
- [307] P. Boguslawski, E. L. Briggs, and J. Bernholc, *Phys. Rev. B* **51**, 17255 (1995).
- [308] H. Y. Xiao, X. T. Zu, F. Gao, and W. J. Weber, *J. Appl. Phys.* **103**, 123529 (2008).
- [309] H. Jin, Y. Dai, B. Huang, and M. H. Whangbo, *Appl. Phys. Lett.* **94**, 162505 (2009).
- [310] H. Bhasker, V. Thakur, M. Kesaria, S. Shivaprasad, and S. Dhar, in *AIP Conference Proceedings*, Vol. 1583 (AIP, 2014) pp. 252–258.
- [311] J. M. Soler, E. Artacho, J. D. Gale, A. Garcia, J. Junquera, P. Ordejon, and D. Sanchez-Portal, *J. Phys. Condens. Matter* **14**, 2745 (2001).
- [312] D. M. Ceperley and B. J. Alder, *Phys. Rev. Lett.* **45**, 566 (1980).
- [313] N. Troullier and J. L. Martins, *Phys. Rev. B* **43**, 1993 (1991).
- [314] L. Kleinman and D. M. Bylander, *Phys. Rev. Lett.* **48**, 1425 (1982).
- [315] S. G. Louie, S. Froyen, and M. L. Cohen, *Phys. Rev. B* **26**, 1738 (1982).
- [316] H. J. Monkhorst and J. D. Pack, *Phys. Rev. B* **13**, 5188 (1976).
- [317] S. B. Zhang and J. E. Northrup, *Phys. Rev. Lett.* **67**, 2339 (1991).
- [318] M. H. Naik and M. Jain, *Comput. Phys. Commun.* (2018).
- [319] M. Feneberg, S. Osterburg, K. Lange, C. Lidig, B. Garke, R. Goldhahn, E. Richter, C. Netzel, M. D. Neumann, N. Esser, *et al.*, *Phys. Rev. B* **90**, 075203 (2014).
- [320] T. Paskova, D. Hommel, P. P. Paskov, V. Darakchieva, B. Monemar, M. Bockowski, T. Suski, I. Grzegory, F. Tuomisto, K. Saarinen, N. Ashkenov, and M. Schubert, *Appl. Phys. Lett.* **88**, 2004 (2006).
- [321] Q. Yan, P. Rinke, A. Janotti, M. Scheffler, and C. G. V. D. Walle, *Phys. Rev. B* **90**, 125118 (2014).
- [322] R. González-Hernández, A. González-García, D. Barragán-Yani, and W. López-Pérez, *Appl. Surf. Sci.* **314**, 794 (2014).
- [323] S.-H. Wei and A. Zunger, *Appl. Phys. Lett.* **69**, 2719 (1996).
- [324] M. S. Hybertsen and S. G. Louie, *Physical Review B* **34**, 5390 (1986).

- [325] A. Rubio, J. L. Corkill, M. L. Cohen, E. L. Shirley, and S. G. Louie, *Physical Review B* **48**, 11810 (1993).
- [326] M. Suzuki, T. Uenoyama, and A. Yanase, *Phys. Rev. B* **52**, 8132 (1995).
- [327] B. Gil, O. Briot, and R.-L. Aulombard, *Phys. Rev. B* **52**, R17028 (1995).
- [328] S. L. Chuang and C. S. Chang, *Phys. Rev. B* **54**, 2491 (1996).
- [329] R. Dingle, D. D. Sell, S. E. Stokowski, and M. Ilegems, *Phys. Rev. B* **4**, 1211 (1971).
- [330] D. C. Reynolds, D. C. Look, W. Kim, O. Aktas, A. Botchkarev, A. Salvador, H. Morkoc, and D. N. Talwar, *J. Appl. Phys.* **80**, 594 (1996).
- [331] C. E. Dreyer, A. Janotti, and C. G. Van De Walle, *Appl. Phys. Lett.* **102**, 142105 (2013).
- [332] I. Vurgaftman and J. R. Meyer, *J. Appl. Phys.* **94**, 3675 (2003).
- [333] T. Schmidt, R. Miwa, W. Orellana, and H. Chacham, *Phys. Rev. B* **65**, 033205 (2002).
- [334] D. Carter and C. Stampfl, *Phys. Rev. B* **79**, 195302 (2009).
- [335] J. L. Lyons and C. G. Van de Walle, *NPJ Computational Materials* **3**, 1 (2017).
- [336] J. Neugebauer and C. G. Van De Walle, *Mater. Res. Soc. Symp. Proc.* **339**, 687 (1994).
- [337] A. Gulans, R. A. Evarestov, I. Tale, and C. C. Yang, *Phys. Status Solidi* **510**, 507 (2005).
- [338] P. Chao, S. Jun-Jie, Z. Yan, K. S. a. Butcher, T. L. Tansley, J. E. Downes, and S. Jia-Xiang, *Chinese Phys. Lett.* **24**, 2048 (2007).
- [339] Q. Yan, A. Janotti, M. Scheffler, and C. G. Van De Walle, *Appl. Phys. Lett.* **100**, 1 (2012).
- [340] X. M. Duan and C. Stampfl, *Phys. Rev. B* **77**, 115207 (2008).
- [341] Z. Xiong, L. Luo, J. Peng, and G. Liu, *J. Phys. Chem. Solids* **70**, 1223 (2009).
- [342] J. Northrup and J. Neugebauer, *Phys. Rev. B* **53**, R10477 (1996).
- [343] A. Filippetti, V. Fiorentini, G. Cappellini, and A. Bosin, *Phys. Rev. B* **59**, 8026 (1999).
- [344] V. Jindal and F. Shahedipour-Sandvik, *J. Appl. Phys.* **107**, 054907 (2010).
- [345] M. Landmann, E. Rauls, W. G. Schmidt, M. D. Neumann, E. Speiser, and N. Esser, *Phys. Rev. B* **91**, 035302 (2015).
- [346] Z. Wang, J. Li, F. Gao, and W. J. Weber, *J. Appl. Phys.* **108**, 44305 (2010).
- [347] I. Horcas, R. Fernández, J. Gomez-Rodriguez, J. Colchero, J. Gómez-Herrero, and A. Baro, *Rev. Sci. Instrum.* **78**, 013705 (2007).
- [348] G. Miceli and A. Pasquarello, *Microelectron. Eng.* **147**, 51 (2015).
- [349] K. Laaksonen, M. Ganchenkova, and R. Nieminen, *J. Phys. Condens. Matter* **21**, 015803 (2008).
- [350] J. Kioseoglou, V. Pontikis, P. Komninou, T. Pavludis, J. Chen, and T. Karakostas, *J. Phys. Condens. Matter* **27**, 125006 (2015).
- [351] S. Limpijumnong and C. G. Van de Walle, *Phys. Rev. B* **69**, 035207 (2004).
- [352] R. Tonner and N. Gaston, *Phys. Chem. Chem. Phys.* **16**, 24244 (2014).
- [353] I. P. Smorchkova, E. Haus, B. Heying, P. Kozodoy, P. Fini, J. P. Ibbetson, S. Keller, S. P. DenBaars, J. S. Speck, and U. K. Mishra, *Appl. Phys. Lett.* **76**, 718 (2000).

- [354] S. K. Nayak, D. Shamoan, J. Ghatak, and S. M. Shivaprasad, *Phys. Status Solidi A* **214**, 1600300 (2017), 1600300.
- [355] R. Kirste, M. P. Hoffmann, J. Tweedie, Z. Bryan, G. Callsen, T. Kure, C. Nenstiel, M. R. Wagner, R. Collazo, A. Hoffmann, and Z. Sitar, *J. Appl. Phys.* **113**, 103504 (2013).
- [356] O. Gelhausen, M. Phillips, E. Goldys, T. Paskova, B. Monemar, M. Strassburg, and A. Hoffmann, *Phys. Rev. B* **69**, 125210 (2004).
- [357] N. Zhang, Z. Liu, Z. Si, P. Ren, X.-D. Wang, X.-X. Feng, P. Dong, C.-X. Du, S.-X. Zhu, B.-L. Fu, H.-X. Lu, J.-M. Li, and J.-X. Wang, *Chinese Phys. Lett.* **30**, 087101 (2013).
- [358] M. Reshchikov, G.-C. Yi, and B. Wessels, *Phys. Rev. B* **59**, 13176 (1999).
- [359] B. Monemar, P. P. Paskov, G. Pozina, C. Hemmingsson, J. P. Bergman, S. Khromov, V. N. Izyumskaya, V. Avrutin, X. Li, H. Morkoc, H. Amano, M. Iwaya, and I. Akasaki, *J. Appl. Phys.* **115**, 053507 (2014).
- [360] U. Kaufmann, M. Kunzer, M. Maier, H. Obloh, A. Ramakrishnan, B. Santic, and P. Schlotter, *Appl. Phys. Lett.* **72**, 1326 (1998).
- [361] J. Buckeridge, C. R. A. Catlow, D. O. Scanlon, T. Keal, P. Sherwood, M. Miskufova, A. Walsh, S. M. Woodley, and A. A. Sokol, *Phys. Rev. Lett.* **114**, 016405 (2015), arXiv:arXiv:1412.1694v1 .
- [362] Y.-P. Sui and G.-H. Yu, *Chinese Phys. Lett.* **28**, 067807 (2011).
- [363] M. A. Reshchikov and H. Morko, *J. Appl. Phys.* **97**, 061301 (2005).
- [364] S. Hautakangas, K. Saarinen, L. Liskay, J. A. Freitas, and R. L. Henry, *Phys. Rev. B* **72**, 165303 (2005).
- [365] T. L. Williamson, D. J. Daz, P. W. Bohn, and R. J. Molnar, *J. Vac. Sci. Technol. B* **22**, 925 (2004).
- [366] M. A. Moram and M. E. Vickers, *Reports Prog. Phys.* **72**, 036502 (2009).
- [367] S. R. Ryu, S. D. G. Ram, S. J. Lee, H.-d. Cho, S. Lee, T. W. Kang, S. Kwon, W. Yang, S. Shin, and Y. Woo, *Appl. Surf. Sci.* **347**, 793 (2015).
- [368] Q. Sun, A. Selloni, T. H. Myers, and W. A. Doolittle, *Phys. Rev. B* **73**, 155337 (2006).
- [369] L. Romano, J. Northrup, A. Ptak, and T. Myers, *Appl. Phys. Lett.* **77**, 2479 (2000).
- [370] R. Nonoda, K. Shojiki, T. Tanikawa, S. Kuboya, R. Katayama, and T. Matsuoka, *Jpn. J. Appl. Phys.* **55**, 05FE01 (2016).
- [371] L. Eckey, U. von Gfug, J. Holst, a. Hoffmann, a. Kaschner, H. Siegle, C. Thomsen, B. Schineller, K. Heime, M. Heuken, O. Schon, and R. Beccard, *J. Appl. Phys.* **84**, 5828 (1998).
- [372] E. Oh, H. Park, and Y. Park, *Appl. Phys. Lett.* **72**, 70 (1998).
- [373] U. Kaufmann, P. Schlotter, H. Obloh, K. Köhler, and M. Maier, *Phys. Rev. B* **62**, 10867 (2000).
- [374] S. Hautakangas, V. Ranki, I. Makkonen, M. J. Puska, K. Saarinen, L. Liskay, D. Seghier, H. P. Gislason, J. A. Freitas, R. L. Henry, X. Xu, and D. C. Look, *Phys. B Condens. Matter* **376-377**, 424 (2006).
- [375] S. Hautakangas, K. Saarinen, L. Liskay, J. Freitas, and R. Henry, *Phys. Rev. B* **72**, 165303 (2005).
- [376] H. Wende, *Reports Prog. Phys.* **67**, 2105 (2004).

- [377] D. Phase, M. Gupta, S. Potdar, L. Behera, R. Sah, A. Gupta, C. Mnourli, D. Bhattacharyya, and S. Gadkari, in *AIP Conference Proceedings*, Vol. 1591 (AIP, 2014) pp. 685–686.
- [378] B. Ravel and M. Newville, *J. Synchrotron Radiat.* **12**, 537 (2005).
- [379] M. Leszczynski, I. Grzegory, H. Teisseyre, T. Suski, M. Bockowski, J. Jun, J. Baranowski, S. Porowski, and J. Domagala, *J. Cryst. Growth* **169**, 235 (1996).
- [380] G. Kresse and J. Furthmüller, *Phys. Rev. B* **54**, 11169 (1996).
- [381] S. K. Nayak, M. Gupta, and S. Shivaprasad, *RSC Advances* **7**, 25998 (2017).
- [382] W. R. L. Lambrecht, S. N. Rashkeev, B. Segall, K. LawniczakJablonska, T. Suski, E. M. Gullikson, J. H. Underwood, R. C. C. Perera, J. C. Rife, I. Grzegory, S. Porowski, and D. K. Wickenden, *Phys. Rev. B* **55**, 2612 (1997).
- [383] E. M. Bittar, C. Adriano, T. M. Garitezi, P. F. S. Rosa, L. Mendonça-Ferreira, F. Garcia, G. D. M. Azevedo, P. G. Pagliuso, and E. Granado, *Phys. Rev. Lett.* **107**, 267402 (2011), arXiv:1107.0962.
- [384] Y. C. Pan, S. F. Wang, W. H. Lee, W. C. Lin, C. I. Chiang, H. Chang, H. H. Hsieh, J. M. Chen, D. S. Lin, M. C. Lee, W. K. Chen, and W. H. Chen, *Solid State Commun.* **117**, 577 (2001).
- [385] M. S. Moreno, K. Jorissen, and J. J. Rehr, *Micron* **38**, 1 (2007).
- [386] M. A. Reshchikov, D. Demchenko, J. McNamara, S. Fernández-Garrido, and R. Calarco, *Phys. Rev. B* **90**, 035207 (2014).
- [387] C. G. Van de Walle, J. Neugebauer, C. Stampfl, M. McCluskey, and N. Johnson, *Acta. Phys. Pol. A* **96**, 613 (1999).
- [388] J. Neugebauer and C. G. V. de Walle (Proceedings of the Materials Research Symposia of Gallium Nitride and Related Materials, edited by R. D. Dupuis, J. A. Edmond, F. A. Ponce, and S. Nakamura (Materials Research Society, Pittsburgh, Pennsylvania, 1995)) p. 645.
- [389] H. Teisseyre, T. Suski, P. Perlin, I. Grzegory, M. Leszczynski, M. Bockowski, S. Porowski, J. A. Freitas, J. Henry R.L., A. E. Wickenden, and D. D. Koleske, *Phys. Rev. B* **62**, 10151 (2000).
- [390] D. O. Demchenko and M. A. Reshchikov, *Phys. Rev. Lett.* **115**, 029701 (2015).
- [391] J. L. Lyons, A. Alkauskas, A. Janotti, and C. G. Van de Walle, *Phys. Status Solidi B* **252**, 900 (2015).
- [392] U. Wahl, L. M. Amorim, V. Augustyns, A. Costa, E. David-Bosne, T. A. L. Lima, G. Lippertz, J. G. Correia, M. R. da Silva, M. J. Kappers, K. Temst, A. Vantomme, and L. M. C. Pereira, *Phys. Rev. Lett.* **118**, 095501 (2017).
- [393] D. Zhang, C. Xue, H. Zhuang, H. Sun, Y. Cao, Y. Huang, Z. Wang, and Y. Wang, *ChemPhysChem* **10**, 571 (2009).
- [394] L. Geelhaar, C. Cheze, B. Jenichen, O. Brandt, C. Pfueller, S. Münch, R. Rothmund, S. Reitzenstein, A. Forchel, T. Kehagias, *et al.*, *IEEE Journal of Selected Topics in Quantum Electronics* **17**, 878 (2011).
- [395] B. Jenichen, O. Brandt, C. Pfueller, P. Dogan, M. Knelangen, and A. Trampert, *Nanotechnology* **22**, 295714 (2011).

- [396] A. Wierzbicka, Z. Zytewicz, S. Kret, J. Borysiuk, P. Dluzewski, M. Sobanska, K. Klosek, A. Reszka, G. Tchutchulashvili, A. Cabaj, *et al.*, *Nanotechnology* **24**, 035703 (2012).
- [397] S. Fernández-Garrido, V. Kaganer, C. Hauswald, B. Jenichen, M. Ramsteiner, V. Consonni, L. Geelhaar, and O. Brandt, *Nanotechnology* **25**, 455702 (2014).
- [398] A. De and S. Shivaprasad, *J. Phys. D: Appl. Phys* **49**, 355304 (2016).
- [399] V. M. Kaganer, S. Fernandez-Garrido, P. Dogan, K. K. Sabelfeld, and O. Brandt, *Nano Lett.* **16**, 3717 (2016).
- [400] L. Lymperakis and J. Neugebauer, *Phys. Rev. B* **79**, 241308 (2009).
- [401] R. González-Hernández, A. González-García, D. Barragán-Yani, and W. López-Pérez, *Appl. Surf. Sci.* **314**, 794 (2014).
- [402] S. Nayak, M. H. Naik, M. Jain, U. Waghmare, and S. Shivaprasad, arXiv preprint arXiv:1710.05670 (2017).
- [403] M. Landmann, E. Rauls, W. Schmidt, M. Neumann, E. Speiser, and N. Esser, *Phys. Rev. B* **91**, 035302 (2015).
- [404] R. S. Mulliken, *J. Chem. Phys.* **23**, 1833 (1955).
- [405] M. A. Reshchikov and H. Morkoc, *J. Appl. Phys.* **97**, 061301 (2005).
- [406] M. A. Reshchikov, D. Demchenko, A. Usikov, H. Helava, and Y. Makarov, *Phys. Rev. B* **90**, 235203 (2014).
- [407] H. Lei, H. Leipner, J. Schreiber, J. Weyher, T. Wosiński, and I. Grzegory, *J. Appl. Phys.* **92**, 6666 (2002).
- [408] J. Neugebauer and C. G. Van de Walle, *Appl. Phys. Lett.* **69**, 503 (1996).
- [409] P. Perlin, T. Suski, H. Teisseyre, M. Leszczynski, I. Grzegory, J. Jun, S. Porowski, P. Bogusławski, J. Bernholc, J. Chervin, *et al.*, *Phys. Rev. Lett.* **75**, 296 (1995).
- [410] T. Mattila and R. M. Nieminen, *Phys. Rev. B* **55**, 9571 (1997).
- [411] D. Hofmann, D. Kovalev, G. Steude, B. Meyer, A. Hoffmann, L. Eckey, R. Heitz, T. Detchprom, H. Amano, and I. Akasaki, *Phys. Rev. B* **52**, 16702 (1995).
- [412] S. Nayak, M. Gupta, U. V. Waghmare, and S. Shivaprasad, arXiv preprint arXiv:1708.04036 (2017).
- [413] A. Kaschner, H. Siegle, G. Kaczmarczyk, M. Straßburg, A. Hoffmann, C. Thomsen, U. Birkle, S. Einfeldt, and D. Hommel, *Appl. Phys. Lett.* **74**, 3281 (1999).